MICRO-SCALE FATIGUE MECHANISMS IN METALS: AN *IN SITU* HIGH FREQUENCY EXPERIMENTAL APPROACH

by

Steven Lavenstein

A dissertation submitted to The Johns Hopkins University
in conformity with the requirements for the degree of
Doctor of Philosophy

Baltimore, Maryland
November 2019

Abstract

More than half of all mechanical failures in engineering structures are classified as fatigue failures. Regardless of the constituting material's strength, the limiting factor in service-life is the amount of cyclic damage that the material can accumulate before fracture. Since metals are the material-of-choice for most structural applications, scientists have strived to gain a fundamental understanding of the mechanisms that lead to their failure under cyclic loading, which is necessary for the design of novel and superior alloys. The reason fatigue of metals is such a challenging problem is that different microstructural features are involved and the controlling mechanisms span many length and time scales. In particular, the dislocation plasticity that precedes micro-crack initiation and the nature of micro-crack growth remain poorly understood.

Small-scale testing has recently emerged as a valuable methodology to understand micro-scale deformation. Over the past two decades, this method has made many breakthroughs in understanding the physics of dislocation plasticity. However, extending these methods to cyclic loading has been met with many difficulties. In this thesis, fundamental fatigue mechanisms in face-centered cubic metals at the micro-scale are explored. To achieve this, a novel high-frequency micro-fatigue experimental methodology is developed by combining aspects of electron microscopy, micro-mechanical testing, and acoustic emission detection. These experiments are designed to replicate stress states (e.g., bending and uniaxial) and cycle counts ($>10^7$) common in bulk fatigue

experiments, although at a ∼10 μm length scale. All experiments are performed *in situ* in a scanning electron microscope to acquire real-time observations of surface morphology changes that are not obtainable with bulk-scale fatigue experiments. Using this method, a transition from cyclic hardening to softening is found in nickel-base superalloys, which is attributed to the shearing of precipitates. Also, for the first time, persistent slip bands (PSB) were observed in pure nickel in micron-scale single crystals. However, the number of cycles to PSB nucleation was two orders of magnitude higher than those in bulk crystals, which was attributed to the high surface-to-volume ratio in the tested crystals. Additionally, the experiments have shown that PSBs nucleate locally and propagate in a way that current models in literature do not account for. A new mechanism-based model was proposed to capture these new observations. The PSBs were also found to promote micro-crack initiation in nickel and nickel-base superalloys. Finally, intermittent micro-crack propagation events and acoustic emissions associated with micro-plasticity were quantified and characterized statistically.

Readers:

Prof. Jaafar A. El-Awady (Advisor),

Prof. Kaliat T. Ramesh, Prof. Timothy P. Weihs

Thesis Committee

Primary Readers

Jaafar A. El-Awady (Advisor)
Associate Professor
Department of Mechanical Engineering
Johns Hopkins University

Kaliat T. Ramesh
Professor
Department of Mechanical Engineering
Johns Hopkins University

Timothy P. Weihs
Professor
Department of Materials Science
Johns Hopkins University

Acknowledgments

I would like to acknowledge that this research was possible due to funding from the Aerospace Materials for Extreme Environments Program (Program Manager Dr. Ali Sayir) at the U.S. Air Force Office for Scientific Research (AFOSR), through Grant No. FA9550-18-1-0071, to Johns Hopkins University. I also acknowledge partial funding support from the Air Force Research Laboratory, Structural Materials Division, Materials and Manufacturing Directorate.

I have been very fortunate in my graduate school career at JHU to have crossed paths with so many intelligent, helpful, and fun people.

Most importantly, I am very grateful to have had Professor Jaafar El-Awady as my PhD advisor. Prof. El-Awady has been a great mentor and has always made a point to make sure that his students are not only productive, but are enjoying their graduate school experience. He has given me the freedom to tackle problems in whatever way I see fit while also keeping me focused on the big picture in my research. This style of advising was very important in motivating me to work hard during my PhD.

Members of the El-Awady lab group at JHU, past and present, have been great colleagues and friends over the years. These include Kinshuk Srivastava, Quan Jiao, Dylan Madisetti, Yejun Gu, Mohammad Rafiei, Gidong Sim, Wei Li, Xiawa Wu, Mostafa Omar, Junjie Yang, Mohamed Hamza, Harsh, Ahmed Hussein, Zara Molaeinia, Amin Aramoon, and Haidong Fan. Also, a special

thanks to Dylan Madisetti for developing the image analysis codes used in Section 4.2.1.3 of this thesis. Another special thanks goes out to Yejun Gu for helping to flesh out some of the mathematics in Section 4.3.5 of this thesis. I would also like to mention undergraduate members of the El-Awady group who worked with me on a few research projects: Roshan Plamthottam and Sapreen Abbass.

In my first year as a PhD student, Lukasz Farbaniec, Nick Krywopusk, and Zafir Alam were very helpful to me in introducing the fundamentals of scanning electron microscopy (SEM) and electron backscatter diffraction (EBSD). David Eastman was crucial in helping to develop, maintain, and train me on the femtosecond laser milling system at HEMI. In addition, David has been a great friend.

A special thanks to Dr. Craig Johnson at the Centralized Research Facilities (CRF) in Drexel University. Since much of the focused ion beam (FIB) work in this thesis was performed at Drexel University, Craig was very helpful in maintaining the FIB as well as teaching me a lot about the physical and practical aspects of FIB milling. Also, Craig was pivotal in his assistance with TEM characterization in Chapter 4.

Shortly after I began my PhD at JHU, Bryan Crawford also began working at JHU as a lab manager for the Materials Science and Engineering Department. Since Bryan had brought with him years of experience in microactuation and nanoindentation at Nanomechanics, this could not have been more lucky for me. Bryan was very helpful in developing loading methodologies in this thesis as well as teaching me the fundamental inner-workings of the actuator, as opposed to treating it like a black box.

Many of my experiments in this thesis were performed in the Hopkins Extreme Materials Institute (HEMI) facilities in Malone Hall. This entailed many interactions with Matt Shaeffer and David Elbert of HEMI. Both were very helpful in tending to laboratory issues and in incorporating new devices

with the SEM.

The small-scale mechanical testing community is a very niche and tight-knit group. One of the difficulties in small-scale testing is that there are so few people that perform these types of experiments to ask for assistance. As such, having collaborators at the Air Force Research Laboratory (AFRL) was pivotal to my research since this lab contains some of the biggest names in micro-scale experimentation of metals. In particular, Dr. Paul Shade, Dr. Chris Woodward, and Dr. Mike Uchic were invaluable resources in developing the novel small-scale methodologies used in this thesis.

Also, a shoutout to the staff at the Mechanical Engineering Department and HEMI. I owe Mike Bernard a great debt of gratitude for helping to bring me to JHU. I have also enjoyed talking Orioles baseball with Mike and going to many ballgames with him. Also, Kevin Adams has been very helpful and I have enjoyed my conversations with him. Another acknowledgment goes to Shawna O'Brien and Cynthia Larichiuta for processing all of my travel reimbursement forms.

In addition to my groupmates and colleagues, I would like to mention all of the friends that I have met at Hopkins over the years. In particular, Jason Parker, Anindya Bhaduri, Gary Lin, Tracy Ling, Suhas Eswarappa Prameela, Kimmie Andes, Gianna Valentino, Anu Kaushik, Arunima Banerjee, Jibu Jose, Cristina Martin Linares, OJ Agarwal, Kelvin Xie, Debjoy Mallick, and Amy Dagro. I will never forget all of the conferences, MEGA socials, MechE BBQs, GRO events, softball games, summer schools, parties, and happy hours that we got to hang out at.

Finally, I would like to thank my family. My little sisters, Nicole and Tiffani, my mom, and my dad have been my biggest supporters for as long as I can remember. I love you all.

Contents

List of Tables

List of Figures

Chapter 1

Introduction and Background

Fatigue is the single most common form of mechanical failure in many engineering applications [2, 3]. It is estimated that 4% of the U.S. gross national product is lost in the form of components that have failed in fatigue [2]. Fatigue failure is also commonly connected to many catastrophic incidents that involve loss of life and/or multimillion dollar structures/equipment. While fatigue failure has been subject to intensive studies for over 150 years, one of the main difficulties in predicting fatigue failure is still the lack of a rigorous understanding of the complex mechanisms that lead to fatigue damage [4, 5]. The complexity of fatigue failure arises from being a multiscale phenomena, as well as its sensitivity to the loading conditions, material class and microstructure, and environmental conditions, among others [6, 7].

With a large fraction of structural materials being metals, a large research effort has been focused on characterizing the behavior of metals under cyclic loading. For metals, fatigue damage is often manifested in the form of irreversible motion of dislocations and their interactions. In contrast, reversible dislocation motion is erased upon completion of a cycle and does not accumulate. Over the course of many loading cycles, complex dislocation arrange-

Some parts of this chapter were published in a recent review article in Current Opinion in Solid State & Materials Science by S. Lavenstein and J.A. El-Awady [1].

ments develop, which subsequently lead to the nucleation of micro-cracks. The lifetime of a metal component can be broken down into the amount of cycles required to initiate a crack and the number of cycles to propagate the crack to the point of failure. Other microstructural features that are known to contribute to crack initiation in metals include grain boundaries, twins, precipitates, impurity atoms, interstitial atoms, vacancies, and voids [4].

In light of this, a complete understanding of fatigue failure of metals requires a fundamental understanding of dislocation mechanisms and their interactions with different microstructural features during cyclic loading. Classic studies that characterize deformation and damage evolution in fatigue have utilized various experimental and modeling techniques. By the early 1950's, load cells capable of imposing high frequency push-pull uniaxial loads were readily available [8], which led to a surge in experimental studies dedicated to identifying the fatigue mechanisms in metals. The earliest experimental studies characterized damage evolution simply through the observation of surface extrusions after cyclic loading (e.g., [9]). It was not until the 1960's when transmission electron microscopy (TEM) was utilized to observe the underlying dislocation structure in fatigued metals [10, 11, 12, 13, 14]. Furthermore, experimental analysis of point defect production during fatigue was identified using electrical resistivity measurements on cyclically loaded wires [15]. It was this union of single crystal growth techniques, high frequency cyclic loading setups, and high voltage electron microscopy that gave rise to the micro-scale fatigue mechanisms field of research in the 1960-1980's. Nevertheless, most traditional fatigue investigations have been limited to *post-mortem* characterization using microscopy on localized regions of interest (i.e., cracks or surface facets).

More recently, the availability of precision mechanical testing instruments along with state-of-the-art micro-fabrication techniques have paved the way for small-scale testing. Often, these experiments are performed *in situ*, which

allows local changes in sample geometry (e.g., slip bands, cracks, etc.) to be observed in real time. In a bulk specimen, the mechanical properties are governed by an ensemble of various sub-micron scale local events (e.g., dislocation slip) that collectively contribute to the overall response. With micro-scale experiments, the length scale of the specimen is often on the same or approximate scale of the mean free path of the defects that govern deformation. As a result, the mechanical response of micro-scale specimens often exhibits very abrupt strain bursts (or stress drops), large statistical scatter in test sample responses, and changes in active deformation mechanisms as compared to bulk-scale experiments [16].

With that in mind, the rationale for performing small-scale experiments as opposed to bulk-scale experiments varies depending on the material and the objective of the study. Oftentimes, it is the effect of size on mechanical response that is of interest. Size effects, such as "smaller is stronger" and intermittent plasticity have been well explored for monotonic deformation [17, 18, 19, 20]. In addition, many look to small-scale experiments as a tool for isolating and determining the mechanical contribution of different micro-scale mechanisms. The other intriguing aspect of small-scale experiments is that usually the sample size is commonly on the same length-scale as simulation cells typically modelled using meso-scale techniques, such as discrete dislocation dynamics (DDD) simulations. This provides an avenue to perform one-to-one validations/comparisons that cannot be made with bulk-scale experiments. Accordingly, micro-fatigue experiments hold great potential to provide unique insights into fatigue mechanisms that are not easily obtainable in bulk-scale materials.

Additionally, accurate modeling of the fatigue response of metals requires tracking the evolution of local damage during cyclic loading. Crystal plasticity finite element (CPFE) models present a practical method that is capable of simulating bulk-scale microstructures [21]. Various fatigue CPFE methods

have been able to incorporate certain aspects of fatigue, such as crack initiation [22], cyclic ratcheting [23], and evolution of dislocation density [24]. However, the physical phenomena in these models are abstracted to reduce the degrees of freedom and computational cost. Thus, the behavior observed in these models is mostly phenomenological and does not provide insight into specific mechanisms of fatigue. Nevertheless, CPFE does provide a way to translate small-scale fatigue experiments into bulk responses using statistical volume elements of the microstructure [25, 26, 27]. At a lower length scale, molecular dynamics (MD) provides a fundamental tool for modeling nano-scale cracks [28, 29] and dislocations [30], but is limited to size scales much less than a micron making it difficult to build any long-range dislocation structures, which are commonly observed in fatigued metals. On the other hand, meso-scale modeling provides a good compromise at an intermediate size scale of approximately 1-10 μm, and thus bridges the gap between atomistic and bulk scale models. Specifically, discrete dislocation dynamics (DDD) provides a physics-based framework for simulating large dislocation densities under different loading conditions. Such dislocation models are also useful for providing inputs to larger scale CPFE models.

This chapter provides a detailed review of fatigue mechanisms as well as recent advances in experimental techniques to study fatigue mechanisms at the micro-scale.

1.1 Recent Advances in Experimental Techniques for Studying Micro-scale Fatigue Mechanisms in Metals

Many of the earliest small-scale fatigue experiments were developed in the 1990's for quantifying the fatigue properties of thin films and micro-wires. This

was promoted in part by the increased interest in MEMS technologies and the availability of related fabrication methods (e.g., lithography and deposition) for the fabrication of thin films and micro-wires. One of the popular methods was to deposit a thin film on a much thicker flexible substrate and then imposing uniaxial tension-compression cyclic loading on the film without inducing damage to the substrate [31]. Other adaptations of MEMS into micro-scale fatigue experiments include electro-static micro-resonators [32, 33], a push-to-pull device [34], and electro-statically driven cantilevers [35].

Moving beyond the scope of specimens created using traditional MEMS-based fabrication techniques, focused ion beam (FIB) milling can subtractively micro-machine virtually any desired geometry in any metal, and has thus been pivotal in recent small-scale research. In the context of small-scale cyclic loading experiments, FIB has been used to fabricate specimens for cyclic tension [36, 37], bending [38, 39, 40, 41, 42, 43], and compression [44, 45] experiments. One of the caveats with FIB milling is its long fabrication time, especially for milling large volumes of material. Therefore, there is a need in the community to speed up the fabrication process of micro-samples.

In early small-scale fatigue experiments, electro-magnetic actuators were used to impose vibratory loads on the specimen [46, 47, 48]. In one of the earliest examples of this, fatigue loading was applied using a "hard bass loudspeaker" connected to a function generator [46]. Using this technique, cyclic loading was imposed uniaxially but with a tension-tension profile [46, 47, 48]. Additionally, since electro-magnetic actuators were already incorporated into the design of many commercial nanoindenters, this provided a convenient approach for conducting small-scale fatigue experiments. In particular, the continuous stiffness measurement (CSM) setup in many nanoindentation systems work by applying an oscillatory load with a very small amplitude at a very high frequency that is superimposed over the regular indentation load. This allows for continuously measuring the dynamic stiffness as a function of

depth [49]. This functionality was exploited by Schwaiger and Kraft (1999) to apply sinusoidal loads about a mean constant load to reach 2.4×10^6 cycles with a loading frequency of 45 Hz [50]. This technique was originally used to study fatigue of bilayer micro-beams (i.e., thin metal films on non-metallic substrates) and other samples that could be readily fabricated using MEMS techniques [50, 51]. More recently, this CSM-based cyclic loading methodology was also adapted to study ultrafine-grained Cu micro-pillar specimens under compression-compression cyclic loading [45]. In this study the specimens were fabricated using FIB milling and the experiments were conducted using a compact nanoindenter setup inside a scanning electron microscope (SEM).

In such (*in situ* or *ex situ*) nanoindenter-based small-scale fatigue experiments, the loading is imposed on the specimen often through the utilization of typical nanoindenter diamond tips (e.g., Berkovich, wedge, conical, flat-end, etc.) or specially fabricated tips. However, these tips do not allow for imposing tensile loading on the sample, and thus are only applicable for fatigue studies in compression-compression or cyclic loading around a mean bending load. To combat this, in some recent *in situ* SEM micro-beam fatigue studies a special gripper that can apply fully reversed tension-compression loading was utilized (Figure 1.1(a)) [38, 42, 39, 43, 52]. A similar gripper was also used in a recent uniaxial fatigue study of Cu micropillars [53]. However, one drawback of this type of gripper is that it is not always in contact with the specimen, and at high frequencies the tip of the gripper would impact the specimen when it re-engages the specimen on the reverse cycle.

Another interesting approach for micro-scale fatigue experiments is the utilization of non-contact, inertia-based methodologies [56, 54, 41, 57]. In one methodology micro-cantilever beams with a relatively large mass of material at its free-end were fabricated from a bulk sample, and then vibrational loads were imposed on the bulk sample using piezo actuation, with frequencies in the kHz regime [54]. Due to the inertia of the mass at the free-end of the micro-

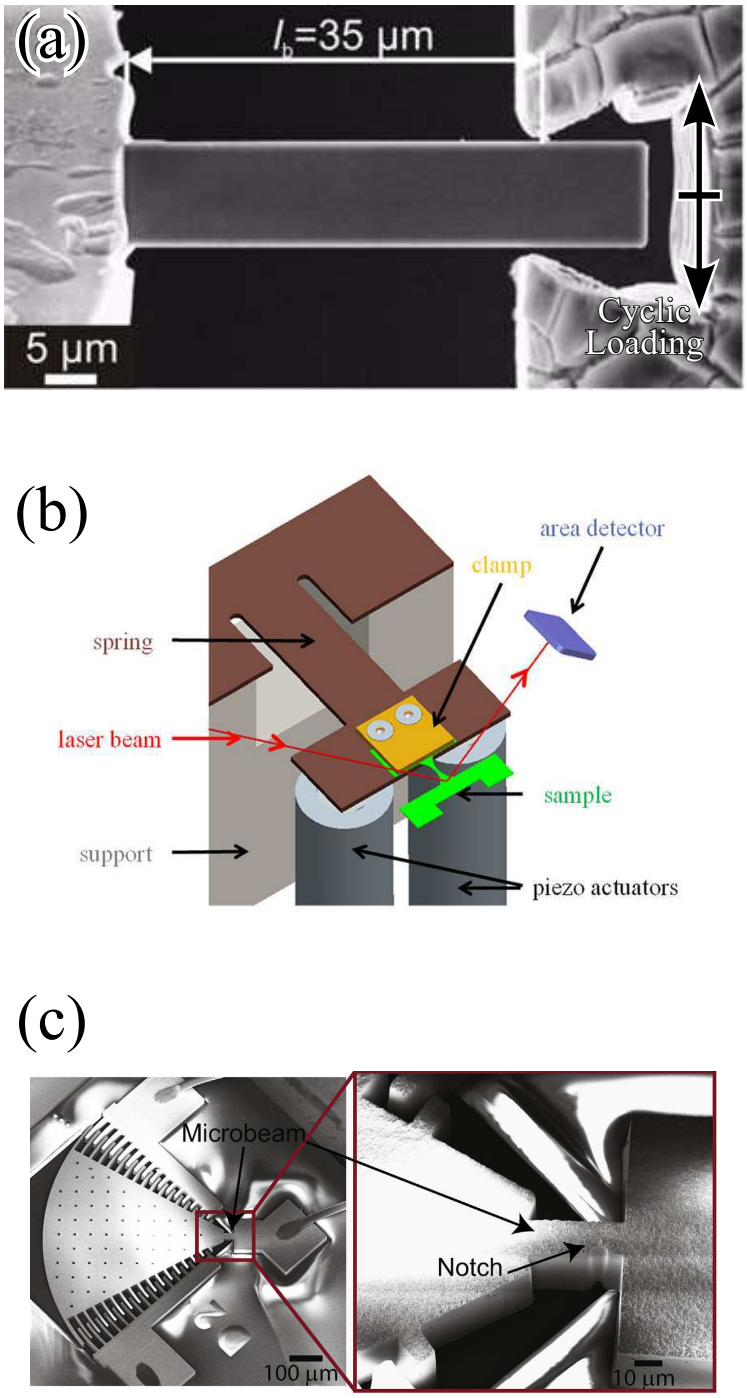

Figure 1.1: Scanning electron microscopy micrographs showing different setups for imposing fully reversible cyclic bending loads on micro-cantilevers by: (a) using a gripper with a fixed opening gap [38]; (b) piezo actuation on the bulk sample that results in deflections on the micro-cantilevers due to the inertia induced by the mass at the end of the micro-cantilever [54]; and (c) electrostatic comb drive actuator to provide high frequency bending excitation of a notched cantilever [55]. The individual images are reprints with permission.

cantilever (see Figure 1.1(c)) it will deflect, which results in the generation of cyclic stresses in the micro-cantilever. With this type of approach, testing frequencies must be performed at resonance to optimize the testing amplitude. Also, with this type of approach, finite element analysis is often utilized to characterize the stress state in the sample [54]. The sample geometry, the resonant frequency, and the fatigue amplitude are all correlated. Similar considerations must be taken as well for other resonance-based fatigue systems, such as electrostatic micro-resonators (Figure 1.1(d)) [32, 58, 55, 33]. It should be noted that these experiments must be performed at their respective resonance frequencies as defined by each sample's geometry and mass distribution. However, at a given frequency, a large range of fatigue amplitudes can still be probed. One other limitation is that these methods are currently limited to bending stress-states in the sample.

It should be noted that *in situ* SEM micro-scale fatigue experiments provide continuous imaging of the formation of slip traces, crack initiation, crack propagation, and other features (e.g., [38, 36, 44, 45, 43, 33]), which would be difficult to resolve in time using only destructive, *post-mortem* characterization. Micro-Laue diffraction has also been utilized to characterize the evolution of geometrically-necessary dislocation density during cyclic loading of micro-cantilever beams [39]. This was also used recently in larger length scale fatigue experiments [59]. Additionally, repeated tension cycles have been performed using *in situ* TEM with an electronically transparent test foil to monitor individual dislocation motion [37] and crack growth [60] during cyclic loading. Furthermore, x-ray diffraction has been used *in situ* to measure film stresses during cyclic deformation [31]. The ability to make such real-time observations of localized deformation events is one of the main strengths of conducting cyclic loading experiments at the micro-scale.

In recent years, advances in material characterization techniques have also enriched the field of micro-scale fatigue experiments. For example, electron

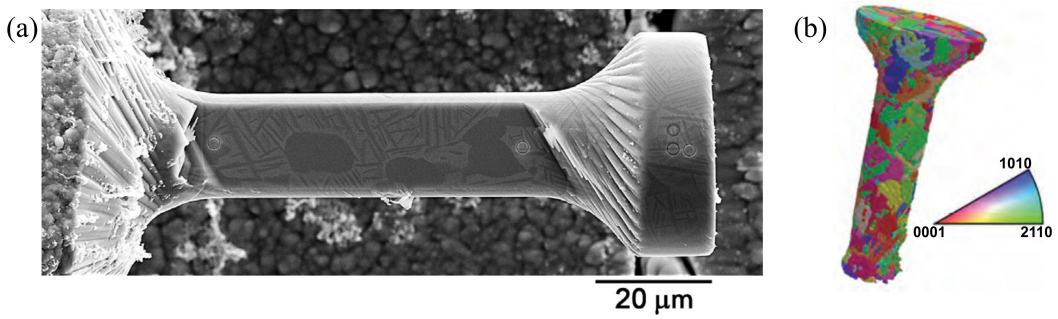

Figure 1.2: (a) A representative Ti micro-scale tension fatigue specimen [36]; and (b) 3D EBSD serial sectioning reconstruction of said specimen (orientations shown are in the tensile direction) [61]. The individual images are reprints with permission.

back-scatter diffraction (EBSD) was used to quantify lattice rotations in cyclically-loaded micro-pillars [44]. FIB tomography was used to produce 3D reconstructions of crack profiles after cyclic loading [43]. State-of-the-art EBSD and FIB serial sectioning also allowed for characterization of the 3D grain microstructure of cyclically loaded micropillars to quantify the active slip systems within each grain (see Figure 1.2) [61]. The combination of FIB lift-outs and TEM has been useful in extracting and examining site-specific foils of fatigued thin films [62, 63, 64]. However, TEM is not the only tool that can be used to observe dislocation structures. The emergence of electron channeling contrast imaging (ECCI) has also been used to observe dislocation structures in micro-fatigue using an SEM and without the need for sample thinning and preparation [65, 66, 67].

1.2 Quantifying the Origins of Dislocation Patterning During Cyclic Loading

The mechanical response of metals during cyclic loading is characterized by the motion and accumulation of dislocations. Due to cyclic loading, a portion of the plastic shear strain, γ_{pl}, induced by dislocation slip can be reversed with reversal of the loading, while a portion remains irreversible, $\gamma_{pl,irr}$. This

is quantified by defining a parameter of irreversibility, $p = \gamma_{pl,irr}/\gamma_{pl}$ [68]. If all dislocation plasticity were reversible during cyclic loading, then it would be expected that no plastic damage will accumulate from cycle to cycle. However, in bulk scale metals exposed to cyclic loading, every loading cycle in which plastic deformation is imposed, the dislocation structure, and accordingly plastic strain, is incrementally changed.

The evolving dislocation structure typically changes with increasing number of cycles, and these changes are unique for different imposed strain amplitudes. Furthermore, distinct dislocation structures develop in single crystals when saturation in the cyclic mechanical response is reached. At saturation, the fatigue hysteresis loops reach a steady-state and do not change appreciably with further cyclic loading. The dislocation structures found in cyclic saturation have been well characterized using TEM observations, which include vein, ladder, and elongated cell structures, as shown in Figure 1.3. The high dislocation density regions in these dislocation structures are referred to as "walls", and are constructed from a high density of edge dislocation dipoles. The low dislocation density regions are referred to as the "cell interior" and are composed of both screw dislocations and edge dipoles at a relatively much lower dislocation density.

The cellular structures form due to the activation of multiple slip systems, and thus, are also observed in multi-slip monotonic loading conditions. However, the vein and ladder structures are unique to cyclic loading since they are only observed after the accumulation of large plastic strains on a single slip system. In monotonic loading, it would not be possible to form such structures since dislocations on secondary slip planes would eventually activate at high enough stresses regardless of the crystallographic orientation.

The 3D ladder dislocation structure is commonly referred to as a persistent slip band (PSB) and is perhaps the most important dislocation structure with regard to crack initiation. The egress of a PSB at the crystal surface usually

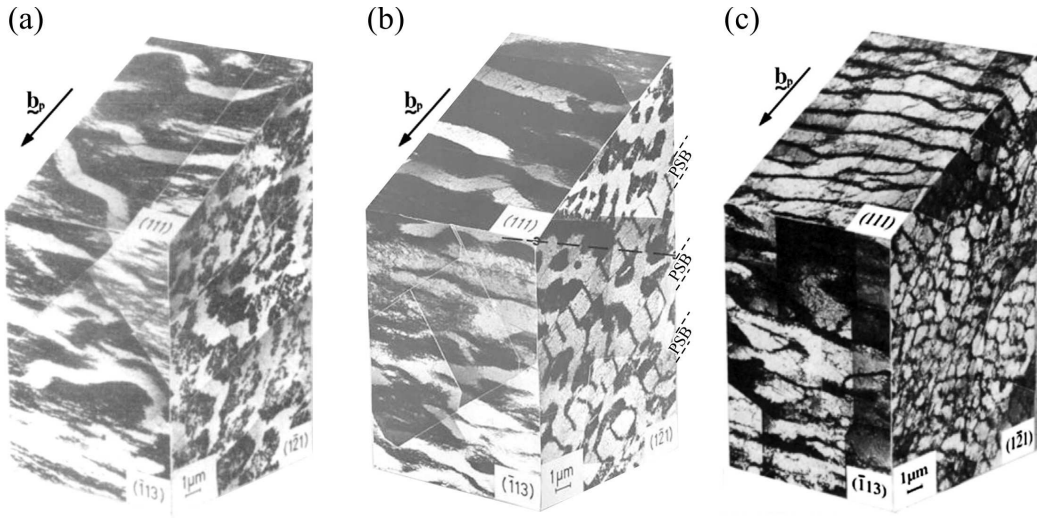

Figure 1.3: Common dislocation structures at saturation as observed in 3D using TEM from foils extracted on different planes: (a) veins [12]; (b) PSB ladder-vein composite [13]; and (c) elongated cells [14]. The individual images are reprints with permission.

takes the form of localized extrusions on the surface in the direction of the primary Burgers vector. Cracks commonly initiate at these surface features as well as at the intersection of a PSB with a crystallographic boundary (e.g., grain and twin boundaries) [69].

These distinct dislocation structures are typically rationalized using the low-energy dislocation structures (LEDS) theory, which hypothesizes that mobile dislocations within a crystal can minimize their energy per unit length by reducing their separation at localized regions of the crystal volume [70, 71, 72]. Thus, when a large enough irreversible plastic strain builds up in the material, the dislocation structure will self-organize and form patterns that minimize the energy of stored dislocations, while still accommodating the applied plastic strains [70, 71, 72]. This semi-periodic clustering of dislocations manifests in the crystal as long-range patterns, also known as self-organized dislocation structures.

This can be explained in a thermodynamic sense by considering a system enclosed by the surface of the crystal. If the stresses imposed on a crystal are large enough to cause plastic deformation but low enough to avoid fracture,

the work put into the crystal will be partially stored as internal energy and partially dissipated as heat energy. Additionally, the internal energy can also be expressed as follows:

$$U_{int} = VU_{El} + \rho VU_D \tag{1.1}$$

where U_{El} is the elastic strain energy density, V is the crystal volume, ρ is the dislocation density, and U_D is the dislocation energy per unit line length. The first term on the right hand side of Equation 1.1 is the elastic strain energy stored in the crystal, while the second term is the energy stored by the dislocation lines. An average value for the dislocation energy per unit line length, U_D, within the LEDS theory can be approximated by assuming an array of dislocations having an average spacing of R_{LEDS}, such that [71, 72]:

$$U_D \approx \mu b^2 \frac{1-\nu/2}{4\pi(1-\nu)} \ln\left(\frac{R_{LEDS}}{b}\right) \tag{1.2}$$

Equation 1.2 indicates that a dislocation array could lower its energy per unit length by reducing the distance between opposite-signed dislocation segments. Low energy dislocation configurations that accomplish this are dipolar loops, which consist of elongated edge segments of opposite signs on closely-spaced slip planes. Closely-spaced arrays of these edge dipoles constitute the dislocation clusters found in dislocation structures such as ladders.

Many computational efforts have also focused on characterizing the sequence of dislocation mechanisms that lead to self-organized structures, such as PSB ladders or cell walls. In one of the earliest dislocation-based models, Neumann (1987) investigated the relaxed configuration starting from a homogeneous distribution of infinitely long edge dislocations [73]. Upon reaching equilibrium, dislocation patterns, similar to the ladders and veins, were observed. This method allowed for the investigation of low energy dislocation

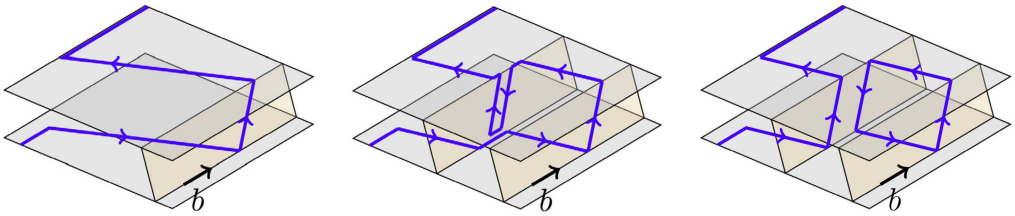

Figure 1.4: Schematic representation of the formation of an edge dislocation dipole as suggested by 3D DDD simulations [75]. A jogged dislocation forms parallel edge dislocations on two parallel planes. Local reorientation of the edge arms to a screw character followed by cross-slip and annihilation of the screw segments pinches-off a closed loop edge dislocation dipole and leaving behind a new jog. This process can successively produce prismatic dipole arrays. Reprint with permission from [75].

structures in fatigue without having to repeatedly apply loads to the simulation cell. These simulation results are in qualitative agreement with the LEDS theory.

To understand the formation of edge dislocation dipoles during cyclic loading, a dipole formation mechanism was proposed using 3D DDD simulations [74]. In these simulations, the dipoles were observed to form based on the cross-slip of screw dislocations, pile-up on neighboring planes, and then opposite-signed dislocations on closely-spaced planes would meet and become stable. This allows arrays of dipoles to be formed even with only one Frank-Read source inserted into the 3D simulation cell [74]. More recently, 3D DDD simulations also show that after a superjog is formed, either cross-slip or intersection with forest dislocations could result in the formation of prismatic dipole arrays [75]. The case of truncation by cross-slip is illustrated in Figure 1.4.

It has also been hypothesized that the subsequent clustering of edge dislocation dipoles leads to the formation of characteristic low energy dislocation structures during cyclic loading. One leading theory to explain this is based on the hypothesis that the backward and forward motion of long screw dislocations during cyclic loading would lead to the sweeping edge dipoles and their clustering in periodic patterns [76]. This hypothesis was tested using 3D DDD simulations by modeling the interactions of rigid edge dislocation dipoles in

a Ni micro-crystal with a perpendicular screw dislocation (see Figure 1.5(a)) [77]. It was shown that upon cycling loading, the dipolar loops are swept by the screw dislocation to form clusters as the dipoles mutually trap one another. Although only ∼20 cycles were performed in that study, these simulations support the idea that homogeneously-spaced dipole configurations would not be stable upon cyclic loading. Similar clustering of dipoles in a band was also observed in 3D DDD simulations of austenitic 316L steel surface grains [74].

On the other hand, a similar clustering of infinitely long edge dislocations into periodically regular walls was also observed in 2D DDD simulations (see Figure 1.5(b)) [78]. However, this clustering was induced purely by the cyclic loading only on the edge dislocation dipoles with no screw dislocations in the system [78]. While the dislocation configurations in such 2D DDD simulations are idealized, they indicate that the back and forth screw dislocation motion during cyclic loading might not be the only mechanism that explains the clustering phenomena. However, further large scale 3D DDD simulations of the response of arrays of finite length edge dislocation dipoles are still needed to provide further quantification of the role of the screw dislocations versus that of the long range stress field of the edge dipoles alone on the clustering response.

Additionally, it is commonly argued in literature that veins are a precursor to PSB formation [79, 68], although the reactions/mechanisms that lead to this transition are not entirely understood. Tabata et al. (1983) proposed that a vein can untangle via the annihilation of dislocations on secondary slip planes [79]. Once untangled, these dislocations are free to form dipoles and cluster as discussed above. This model is supported by TEM observations showing the gradual transition along the PSB from an irregular vein structure into a well-defined ladder structure, as shown in Figure 1.6. In support of this hypothesis, Amodeo et al. (1990) conducted 2D DDD simulations of cyclic loading on a vein microstructure constructed from infinitely long edge dislocations. These

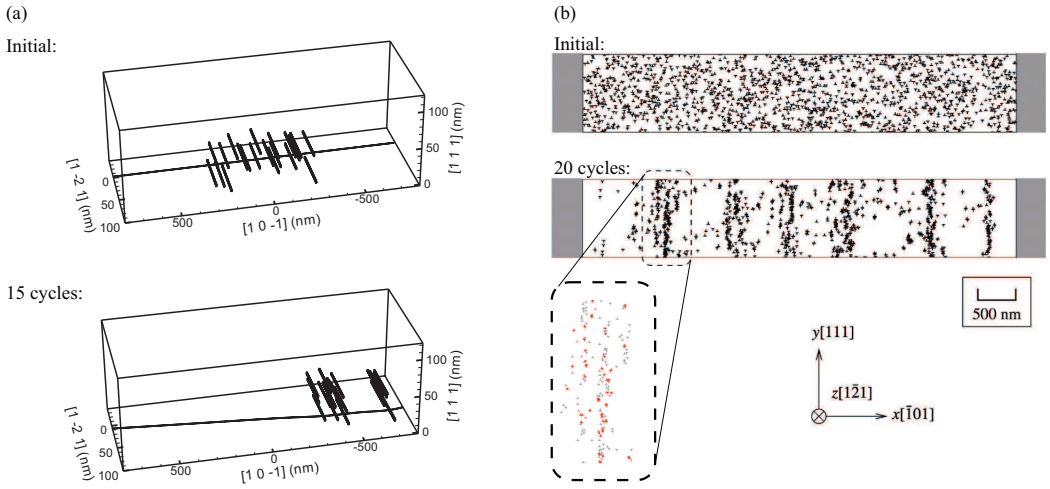

Figure 1.5: Initial dislocation distribution and those after 20 cycles as predicted from: (a) 3D DDD simulations showing the sweeping of edge dipoles by the forward and backward motion of a single screw dislocation [77]; (b) 2D DDD simulations showing the clustering of infinitely long edge dislocations due to the cyclic loading of a 5600 nm-thick copper "thin film" simulation cell [78]. The individual images are reprints with permission.

simulations showed that the vein structure can break down by dipole formation and dislocation annihilation of mobile dislocations within the vein resulting in the formation of wavy bands [80]. These results agree qualitatively with the hypothesis of Tabata et al. (1983) [79].

Another question of interest to the fatigue community is: What controls the saturation stress of a metal? In one of the earlier attempts to address this, Mughrabi (1983) evaluated the distribution of stresses within PSBs by measuring the local radii of curvature of screw and edge dislocations in the PSB channels, as observed in TEM micrographs of cyclically deformed Cu single crystals [81]. These measurements indicated that the stresses near the walls are considerably higher than the crystal saturation stress, while those in the channel are lower. Based on these measurements, Mughrabi (1983) proposed a composite model to correlate the relative contributions of the PSB walls and channels to the fatigue saturation stress [81]. In addition, the fatigue saturation stress was attributed to a number of factors, including: (i) the stress required for two screw dislocations of opposite signs on offset slip planes to

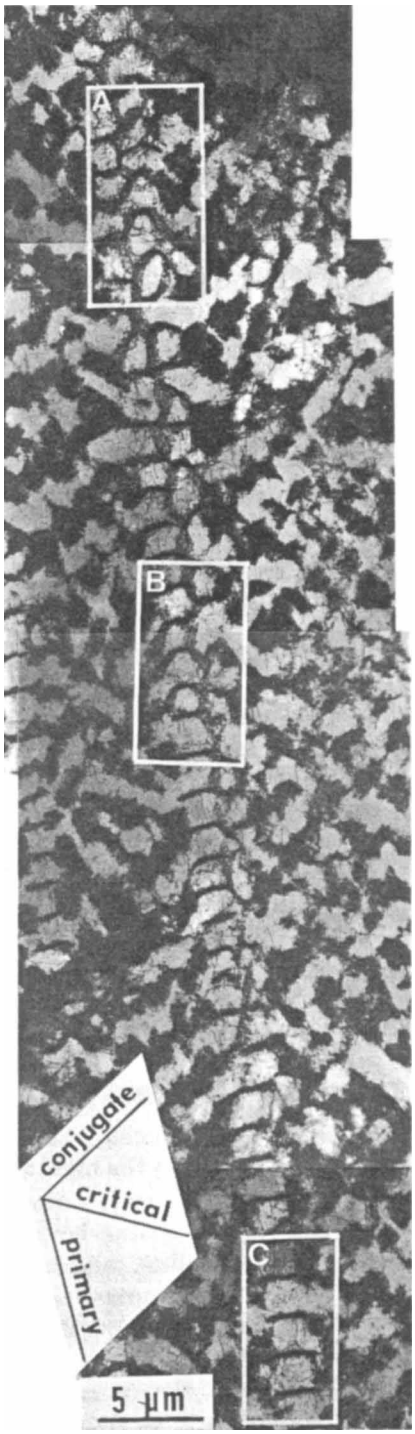

Figure 1.6: Development of a PSB ladder structure in a [123] cyclically loaded Cu single crystal after 5,000 cycles [79]. Boxed regions highlight: (A) poorly developed, (B) moderately developed, and (C) well developed regions within a single PSB structure. Reprint with permission from [79].

pass one another; (ii) the stress required for screw dislocations bowing in the PSB channel, and (iii) the long range internal stress field induced by the edge dislocation dipolar walls. However, a wide range of estimates and conclusions have been proposed in literature regarding the contribution of each to the saturation stress [82, 83, 84, 85, 86].

To address this, a number of 3D DDD simulations have been conducted to quantify the contribution of the different stresses on the saturation stress [87, 88, 89, 90, 91]. Schwarz and Mughrabi (2006) computed the passing stress and the bowing stress of two opposite screw dislocations on two parallel planes gliding in a confined channel [87]. However, these simulations overestimated the resolved shear stress in the channel of the PSB due to the lack of the far field stress induced by the dipolar walls. Subsequently, El-Awady et al. (2007) developed a PSB model in which the edge dislocation dipolar walls were approximated as rigid and infinitely long with periodic boundary condition in the direction of the primary Burgers vector [89]. From these simulations it was shown that the saturation stress is very sensitive to the local curvatures of the screw dislocations moving in the channel. Additionally, changing the density of edge dipoles in the PSB walls had a significant effect on the local curvatures, and thus the passing stress. This type of analysis is difficult to quantify experimentally and demonstrates the utility of 3D DDD in quantifying local stress values and connecting them to far-field stresses. A summary of various theoretical and computational calculations of the resolved shear stress in a PSB channel is shown in Figure 1.7.

More recently, a more complex 3D DDD simulation of a PSB was performed with 10% of the wall dislocation dipoles being mobile [91]. This allowed dislocations to occasionally permeate through the walls and bow into neighboring channels, as shown in Figure 1.8(a). One of the interesting findings from these simulations is that applying a plastic strain amplitude below the capacity of the PSB leads to the bowing out of edge segments from the wall into the chan-

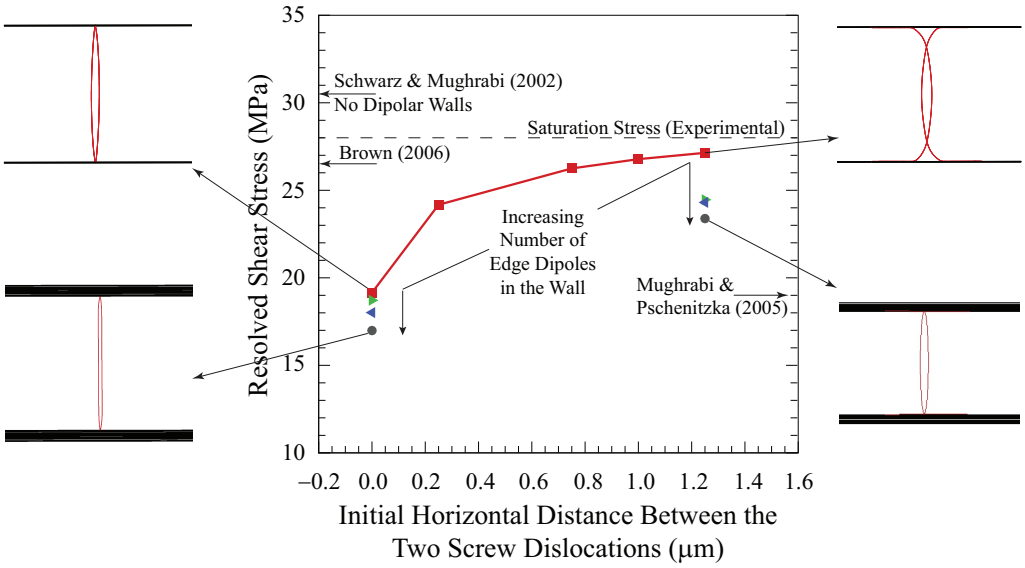

Figure 1.7: Resolved shear stress versus initial distance between screw dislocations in a PSB channel as predicted from 3D DDD simulations and other theoretical estimates [92, 85, 87, 89]. The symbols represent predictions from 3D DDD simulations reported in [89]. Similar symbols indicates calculations based on the same number of simulated edge dislocation dipoles in the walls. The resolved shear stress is observed to decrease with increasing number of edge dislocation dipoles in the walls. A snapshot of the screw dislocations in the channel and the edge dipoles in the walls are shown in the inserts for different conditions as indicated by the arrows. The 3D DDD results by Schwarz and Mughrabi (2006) do not account for the back stresses induced by the dipolar walls, which might explain the higher resolved shear stresses predicted [87]. The analytical results by Brown (2006) neglects the effect of the screw dislocations [85], while the results by Mughrabi and Pschenitzka (2005) account for the curvature [92].

nels, which greatly affects the shape of the hysteresis loop (see Figure 1.8(b) and (c)). Since plastic energy is still dissipated in this lower strain amplitude case, the PSB cannot be thought of as a reversible phase transition [91].

Other simulations have also been able to produce cellular dislocation structures that are commonly observed in cyclic loading of crystals oriented for multiple slip or at high strain amplitudes. From 2D DDD simulations, dislocation climb was shown to be a necessary mechanism for the formation of such cells in Ni-base superalloys (see Figure 1.9) [80, 94]. For the 2D simulations shown in Figure 1.9, the stress gradients at the interface between the precipitate and matrix provided the driving force for the diffusion and thus climb of dislocations along the interface to form enclosed cellular regions [94]. Similar cells were also observed from corresponding creep simulations in the same study [94]. This suggests that perhaps the loading and unloading in fatigue is not the only driving force for the development of cells and that the time for the thermally-activated climb mechanisms to proceed might be of importance too. Interestingly, 3D DDD simulations that do not incorporate climb have also predicted the formation of 3D dislocation cells during cyclic loading. However, in these later simulations the formation of the dislocation cells was attributed to cross-slip of screw dislocations [95].

1.3 Size Effects on the Cyclic Response of Microcrystals

The "smaller is stronger" phenomena observed for micro- and nano-scale metals has been well documented over the past two decades [96, 16, 97, 98]. Arguments used to explain the increase in strength with smaller volumes usually include the transition from dislocation forest hardening, to exhaustion hardening, to hardening induced by the truncation of dislocation sources, to disloca-

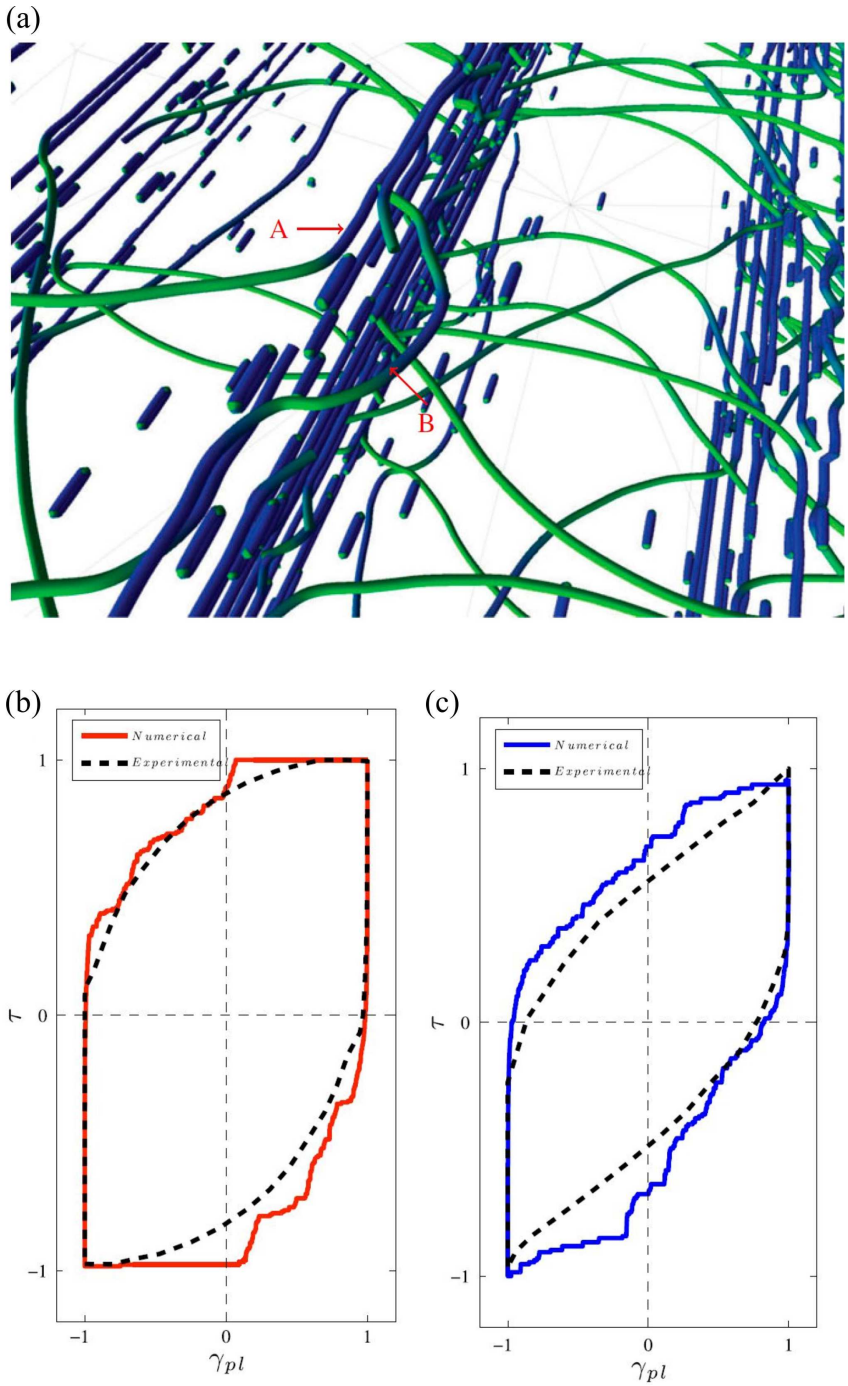

Figure 1.8: (a) Penetration of an edge dislocation "A" through the PSB wall due to the stress field induced by the glide of another edge dislocation "B" at the interface between the PSB wall and channel [91]. Loop "A" will subsequently expand in the neighboring channel. Screw and edge dislocations are colored by green and blue, respectively. The normalized hysteresis loops for PSB cyclically loaded at (b) $\gamma_p = 1 \times 10^{-3}$, and (c) $\gamma_p = 5 \times 10^{-3}$ [91]. Experimental data from [93] is also included for comparison. Reprint with permission from [91].

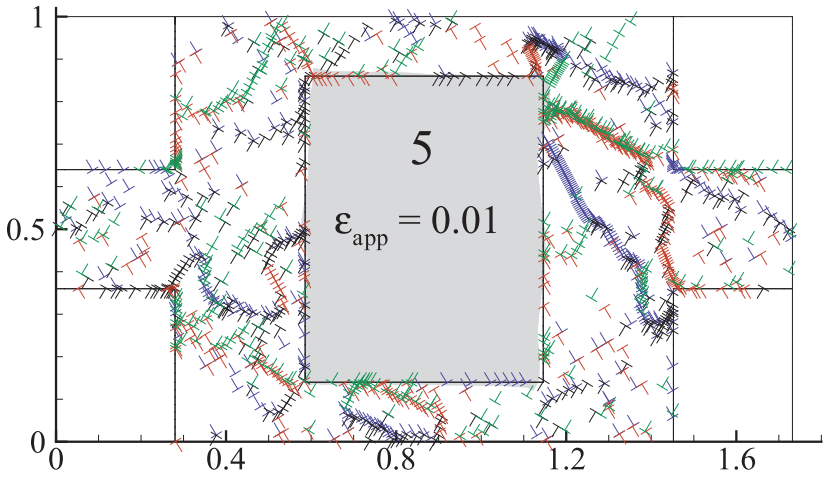

Figure 1.9: Dislocation structure as predicted from 2D DDD simulations in a 1 μm tall unit cell of Nickel-base superalloy with impenetrable precipitates. Microstructure shown is after 5 loading cycles with periodic boundary conditions at a strain amplitude of 0.01. The deformation of the central precipitate is indicated by the displacements magnified by a factor of 10. Slip systems are denoted using different colors. All dimensions are in μm. Reprint with permission from [94].

tion starvation at the nanoscale [99].

However, in fatigue, the fatigue strength of metals is not necessarily correlated with its monotonic strength. Fatigue strength, and accordingly the fatigue life, is characterized by how much damage accumulation a material can tolerate before it fails. In terms of plastic damage accumulation (i.e., irreversible dislocation motion), the size of the crystal affects its fatigue strength in two ways. On one hand, the long-range dislocation patterns associated with cyclic loading are strongly influenced by the size of the material. This is true for geometrically small crystals with free surfaces, as well as fined-grained polycrystals. On the other hand, surface roughness, characterized by extrusion heights and intrusion depths, relative to the material dimensions can strongly influence the fatigue life of the material. Thus, this section provides a summary of the current understanding of size effects on the fatigue strength, the fatigue life in metals, and the correlation with the size-dependent dislocation structure and surface roughness evolutions.

Figure 1.10 summarizes the effect of crystal size on the fatigue life of Cu,

which is one of the few metals where an abundance of fatigue life data is available over a range of sizes spanning from 50 nm to bulk under different cyclic loading conditions. This figure represents a composite plot from micro-scale experiments of different cyclic loading conditions (i.e., uniaxial loading and bending) and for different specimen geometries (i.e., thin films, micro-wires, and micro-beams). The available data from strain controlled experiments (i.e., constant strain amplitude) as well as those from stress controlled experiments (i.e., constant stress amplitude).

A number of general observations can be extracted from Figure 1.10. For thin films under uniaxial cyclic loading, three regimes can be identified. When the film thickness, t, is larger than a critical size, which is somewhere in the range $20 \lesssim t \lesssim 100$ μm , the fatigue life (and fatigue strength) decreases with decreasing thickness. This is evident in both single crystal (SC) thin films (cf. Kammuri et al. (2015) [105]) and polycrystalline ones having an average grain size larger than or equal to the film thickness (cf. Hong et al. (1997) [107], Reed et al. (1998) [106], and Judelewicz et al. (1994) [47]). On the other hand, when the film thickness is below this critical size, the reverse trend is observed with the fatigue life continuously increasing with decreasing thickness (cf. Kraft et al. (2001 and 2002) [102, 101], and Wang et al. (2008) [100]). However, when the film thickness decreases below 100 nm, no appreciable change in fatigue life was observed [100].

Similar trends are also observed in Cu micro-wires (Figure 1.10(b)). Below a critical size the fatigue life increases with decreasing wire diameter, while above it the life deceases with decreasing wire diameter (cf. [109, 67, 110, 46]). However, the available results in literature suggest different estimates for this critical size at which this transition happens. The micro-wires study by Khatibi et al. (2005) [67], Weiss et al. (2002) [109], and Yang et al. (2009) [110] suggest the critical size should be below 20-50 μm, while the experiments by Hofbeck et al. (1986) suggest this transition should happen at even larger

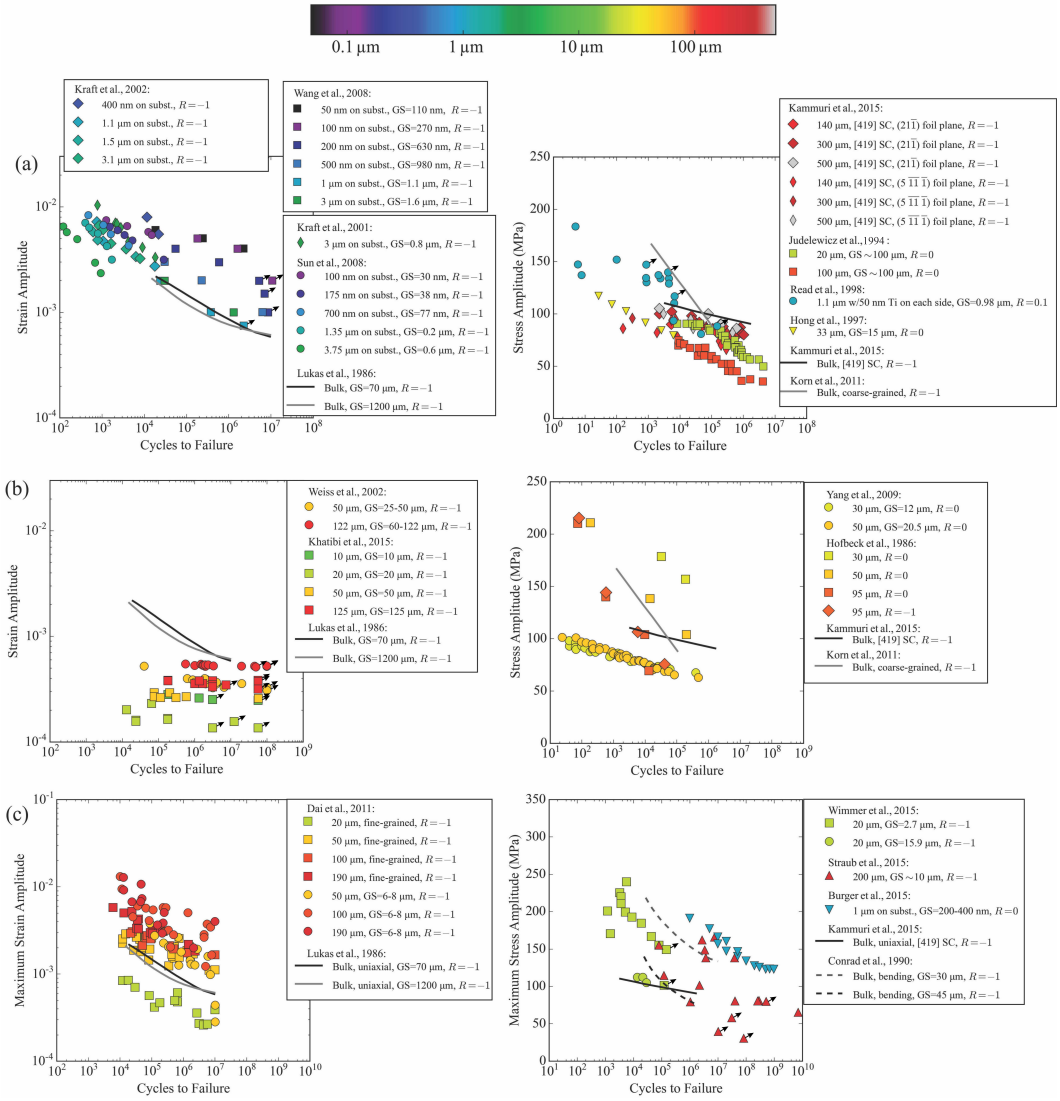

Figure 1.10: Composite plot from published experimental results summarizing the fatigue life of Cu under cyclic: (a) uniaxial loading of thin films [100, 101, 102, 103, 104, 105, 47, 106, 107, 108]; (b) uniaxial loading of micro-wires [109, 67, 104, 110, 46, 105, 108]; and (c) bending of micro-beams [111, 104, 52, 54, 112, 105, 113]. Symbol color indicates the size of the specimen as indicated by the legend. Bulk data is also included as solid and dashed lines for reference. Arrows indicate run-outs.

sizes (likely around 100 μm) [46].

The micro-bending fatigue life data for Cu are also summarized in Figure 1.10(c). However, to the author's knowledge, far less consistent studies are available in literature as compared to uniaxial loading of thin foils or micro-wires. Nevertheless, an inverse size effect for polycrystal thin foils in the range of $20 \leq t \leq 190$ μm beams [111]. It should be noted that in these experiments, the samples size is significantly larger than the average grain size (i.e., multiple grains span through the thickness of the foil). It is suggested that in experiments with such a larger thickness-to-grain-size ratio, the fatigue life may be dominated by the crack growth resistance since there would be significantly more grain boundaries that a crack would have to propagate along to fail the sample as compared to thin foils having thicknesses smaller than the average grain size [111]. Other stress amplitude controlled micro-bending fatigue life data on Cu is available; however, it is difficult to discern a clear size effect relative to bulk due to the lack of data. Perhaps the one exception would be bending of 1 μm films on a substrate which showed improved fatigue life over bulk [112]. Additional micro-bending studies have observed a dramatic increase in the number of cycles required to propagate cracks in polycrystalline Ni micro-beams having thickness of ∼20 μm and average grain size of 1-2 μm [33].

Another point that is evident from Figure 1.10 is that, unlike in size effects on the flow strength of metals in monotonic loading, the available size effects on fatigue life data is difficult to compare between different studies. Issues that may explain this include differences in sample geometry, material purity, and loading conditions. Also, grain size is another factor that varied throughout the compiled studies. Nevertheless, as discussed above interesting trends can be extracted from these data. To make definitive statements on size effects on fatigue life of microcrystals would likely require a fatigue setup capable of applying uniaxial, fully-reversed cyclic loading. Samples would ideally vary in

diameter from sub-micron to ∼100 μm with a constant aspect ratio. Furthermore, while the results discussed above are for Cu, similar observation were made for other metals [114, 115, 116].

In the following, a summary of the mechanisms responsible for the transition in the size effects on the fatigue life are discussed. Due to computational difficulties, there is a lack of DDD simulations investigating the mechanisms involved in the decrease of fatigue life with decreasing film thickness or microwire diameter above the critical size discussed above. However, experimentally, this was attributed to the slip markings on the surface of the thin foils relative to the foil thickness increases with decreasing thickness (or diameter) [67, 105].

Below the critical size, numerous DDD simulations and experimental observations have been made. The high fatigue strength and life of Cu thin films having thicknesses less than ∼2 to 3 μm was attributed to the lack of formation of dislocation structures in these films [117, 64]. Such dislocation structures are a common precursor to crack initiation and subsequent failure. When the film thickness decreases below 100 nm, dislocation plasticity mostly seizes, and crack initiation and propagation at grain boundaries, twin boundaries, or other interfaces were the only observed factors that determine the fatigue life [100].

When the film thickness is larger than ∼2 to 3 μm, accumulation of damage in the form of dislocation structures is commonly observed after cyclic deformation. The magnitude of the accumulated damage also increases with a further increase in thickness, which is correlated to a decrease in the fatigue life with increasing thickness [117]. This finding is qualitatively consistent with 2D DDD simulations of Cu thin films [78] and 3D DDD simulations of free standing single crystal Ni micropillars [95]. In the 2D DDD simulations, it was shown that dislocation structure formation is only observed for thin films with thickness larger than 1 μm [78]. This smaller critical thickness for dislocation structure formation as compared to experiment is likely a result

of the rigid boundary conditions enforced on the 2D simulation cells, which is in contrast to the free surface conditions in the experiments [78]. On the other hand, the 3D DDD simulations show that single crystal Ni microcrystals cyclically loaded in a multi-slip orientation do not show any dislocation density multiplication or cyclic hardening when the crystal size is below 2.0 μm [95]. In contrast, for crystals having larger sizes, significant dislocation density accumulation in in the form of cell-like dislocation structures and considerable cyclic hardening is observed [95]. These simulations also show that the dislocation cell size and wall thicknesses increase with increasing crystal size, as shown in Figure 1.11. These observations are in very good agreement with the experimental observations.

Another aspect to consider, in particular for cyclic studies of thin foils on a substrate, is that the diffusion and coalescence of vacancies at the film-substrate interface is also a common failure mechanism. When the film thickness decreases, vacancy diffusion length also decreases. Thus, vacancies can reach the free surface of the film more easily rather than localize at the film-substrate interface, and thus, the fatigue life can increase [62]. This is supported by lack of voids at the film-substrate interface in 0.4 μm films [62].

For surface failure, surface roughness has also been shown to be highly dependent on crystal size in multi-slip DDD cyclic loading simulations as seen in Figure 1.12 [118]. This is important because surface crack initiation is strongly influenced by surface features. It was reported that for simulated crystals having an edge length of 2.0 μm and smaller, surface roughness evolved in the form of bands while the remainder of the surface remained relatively smooth [118]. This is in contrast with larger crystals in which the roughness was more evenly distributed along the crystal surface. Also, as shown in Figure 1.12(e), the maximum step height scales with the size of the crystal according to a power law. The larger step heights in larger crystals would be expected to be more prone to crack initiation and thus failure. It should be pointed out

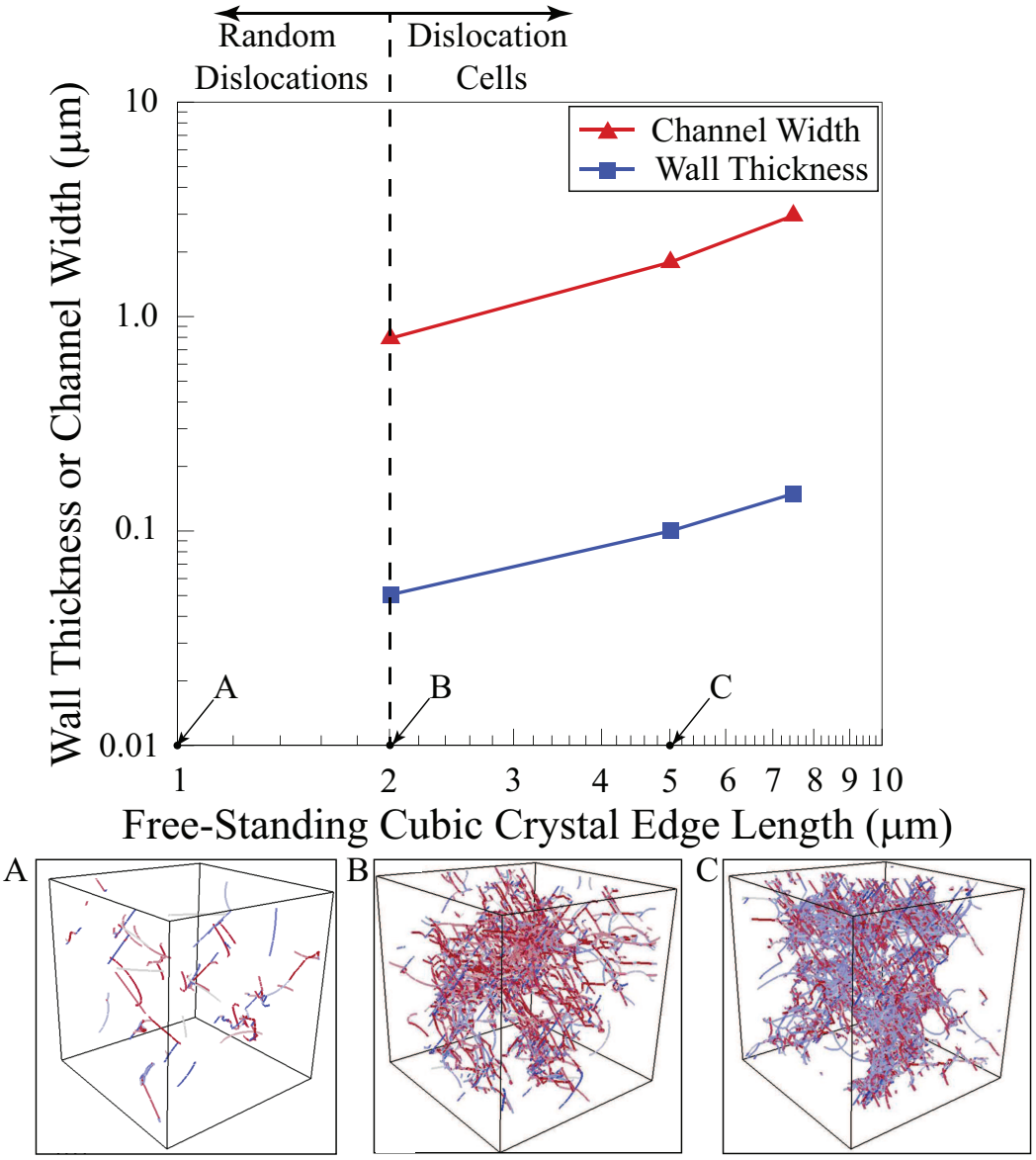

Figure 1.11: The effect of the crystal size on the average dislocation cell size and wall thickness as predicted from 3D DDD simulations of free standing Ni single crystals under uniaxial cyclic loading. The data is based on results published in [95]. Below a crystal size of 2 μm, only random unstructured dislocations are observed. The loading was strain controlled with fully reversed cyclic loading at a strain rate of $\dot{\varepsilon} = 200\ s^{-1}$ and a total strain amplitude of $\Delta\varepsilon = 0.4\%$ in the multi-slip crystallographic direction [001]. The inserts show the predicted dislocation structure after (A) 80 loading cycles for 1 μm, (B) 5 cycles for 2 μm, and (C) 2 cycles for 5 μm simulation cells.

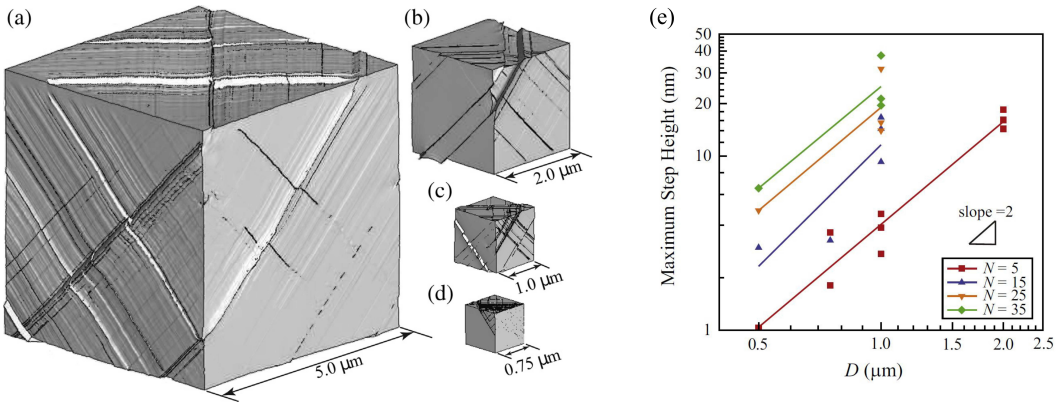

Figure 1.12: Reconstructions of the crystal surface morphology after 5 loading cycles for crystals having: (a) $D = 5.0$ μm and $\rho_0 = 10^{11}\ m^{-2}$; (b) $D = 2.0$ μm and $\rho_0 = 10^{12}\ m^{-2}$; (c) $D = 1.0$ μm and $\rho_0 = 10^{13}\ m^{-2}$; and (d) $D = 0.75$ μm and $\rho_0 = 10^{12}\ m^{-2}$. The surface displacement is magnified 10 times. (e) The maximum surface height versus crystal size for different numbers of loading cycles and a fixed initial dislocation density $\rho_0 = 10^{12}\ m^{-2}$. The individual images are reprints with permission from [118].

that the slip bands seen in Figure 1.12(a)-(d) are not due to the presence of PSBs in the crystal but rather a consequence of the heterogenous distribution of dislocations in the crystal.

In the presence of stress gradients in small volumes (e.g., bending of micro-beams), dislocations have been found to pile up at the line intersecting active slip planes and the neutral plane. This has been shown both with experiments as well as with DDD simulations [38, 39, 119, 120]. Kirchlechner et al. (2015) suggest that cross-slip at the neutral plane onto a secondary slip plane can lead to an irreversible accumulation of dislocations [39]. If the micro-beam is oriented such that cross-slip does not occur, the mechanical and microstructural response during cyclic loading stays relatively constant at least for ∼10 cycles, indicating almost complete reversibility [39]. In 3D DDD simulations of cyclic micro-bending, the dislocation densities fluctuate during each cycle in a corresponding manner with the load, but there is a gradual irreversible accumulation of dislocations from cycle to cycle [38]. It would seem that this effect, the cyclic pile-up and dissolving of dislocations at the neutral axis, is unique to small-scale, single-crystal beams. One potential reason for this is that the

distance between dislocation sources and the free surface for micro-scale specimens can be spanned in a single loading cycle. It has also been shown using 3D DDD of cyclic loading in micro-bending and micro-torsion that the size of the pile-up is limited by the thickness of the specimen, which further contributes to the size-effect [121]. Furthermore, the backstress of dislocations pile-ups at the neutral plane has also been shown to promote a Bauschinger effect.

1.4 Crack Initiation and Propagation

Fatigue damage in metals can also be manifested in the progressive emergence of cracks near locations of high stress concentrations, materials free surfaces, or at internal interfaces. The fatigue life can be divided into two stages: a crack initiation stage and a crack propagation stage. The percentage of life spent in either stage depends on the magnitude of the imposed stresses. In dealing with crack propagation at the bulk-scale, linear elastic fracture mechanics (LEFM) provides relations for the crack growth rate per cycle as a function of the stress intensity factor (i.e., the Paris law). On the other hand, the evolution of the dislocations and their interactions with free and internal surfaces are the primary factors that govern crack initiation and propagation in fatigue, and LEFM lacks the ability to predict the initiation of cracks or account for the evolution of the dislocation structure during cyclic loading. Accordingly, there is significant need to quantify crack initiation and propagation based on deformation mechanisms at the micron scales, which is difficult to assess from bulk scale experiments alone. Thus, DDD simulations and micro-experiments can provide ample understanding of the involved mechanisms in crack initiation.

For any model to truly capture the physics of crack initiation, the effects of surface roughness must be incorporated. A model developed by Essmann, Gösele, and Mughrabi (the EGM model) suggests that that static extrusions

form as a result of the increased volume in a PSB due to the annihilation of vacancy dipole loops [122]. As the dislocations within the PSB annihilate, the dislocations at the PSB-matrix interface exit the crystal and create a step. Using simple geometric arguments, this model can be used to calculate the extrusion height, h_e, as follows [122]:

$$h_e = \frac{C_V^{sat} D}{\cos \beta} \tag{1.3}$$

where the saturation vacancy concentration is C_V^{sat}, the crystal diameter is D, and the angle between the specimen axis and the primary slip plane is β. This equation can be approximated for Cu as:

$$h_e \approx 3 \times 10^{-4} D \tag{1.4}$$

Based on Equation 1.4, PSB extrusion heights would be on the order of micrometers for bulk-scale single crystals and on the order of nanometers for microcrystals. Using the same logic, the EGM model could also be used to explain intrusions induced by the annihilation of interstitial dipoles. To justify the observation that extrusions dominate over intrusions in PSBs, the EGM model reasons that the concentration of vacancy-type defects is much larger than for interstitial-type defects. The Polák model has contested that this has more to do with the relative mobility of vacancies and interstitial point defects [123, 124]. Polák argues that diffusion of vacancies from the PSB to the matrix results in a net transfer of matter and the build-up of interfacial stresses. A recent refinement of the Polák model states that the eventual plastic relaxation of these stresses results in intrusions that deepen and eventually initiate cracks [124]. The EGM model makes no distinction between these intrusions and stage-I micro-cracks.

It is interesting to note, that even without incorporating volume change due to dipole annihilation into their simulations, DDD simulations still predicts

an overall extrusion growth with increasing number of cycles [125, 118]. Upon simulating slip bands during cyclic loading using 3D DDD, it was reported that only 10% of surface extrusions remain stable over the course of the simulation [125]. However, the fact that such a high fraction of the extrusions (90%) are non-static indicates that the missing physical consideration of volume change may be necessary to accurately represent the localized surface changes induced by PSBs.

Déprés et al. (2004) also report that prismatic loops, which are present in slip bands, leave through the free surface of the crystal and are responsible for the extruded volume [125]. In a later study, it was noted that the dislocations at the interface between the slip band and the surrounding matrix assist in extrusion growth to a large extent [126]. Hussein et al. (2016) suggest a mechanism where double cross-slip at the surface of the crystal leads to the creation of enclosed step on the surface [118]. This mechanism allows for slip bands to grow and thicken as observed experimentally.

To quantify the effect of dislocation plasticity on crack growth, a cohesive surface method was coupled with 2D DDD simulations [127]. In these simulations, both cohesive constitutive relations, representing reversible separation (mimicking experiments in perfect vacuum), and irreversible separation (mimicking experiments in oxidizing environment) were employed [127]. These simulations suggested that continuous crack growth is governed by the irreversibility of dislocation motion. It was also shown that the fatigue crack growth threshold is sensitive to the irreversibility of the cohesive surface, with crack closure playing an important role in setting the fatigue threshold for an irreversible cohesive surface. It should be noted that these simulations did not account for stress concentrations that arise from surface extrusions and intrusions.

Brinckmann et al. (2007) extended this model and incorporated surface roughness in their 2D DDD simulations coupled with cohesive surface models

[128]. These simulations suggested that fatigue crack initiation at the free surface arises from the build-up of local stresses due to the evolving surface roughness induced by the evolving dislocation structure. In addition, these simulations showed that the opening of a cohesive surface is initially slow in the early stages of cyclic loading, then accelerates until reaching the critical opening after a certain number of cycles [128].

It should be noted that in these 2D DDD simulations, dislocation patterning, which is commonly observed in experiments, was not predicted. This is likely due to the lack of 3D mechanisms (e.g., dislocation cross-slip) and/or the small grain sizes modeled. Furthermore, in such simulations, the cohesive surface model requires prior knowledge of the location and path of the crack.

To address some of these limitations, 3D DDD simulations were also employed to study the crack initiation processes in 316L austenitic stainless steel surface grains. In these simulations a new criterion was developed to set a threshold for crack initiation that combines requirements for the extrusion shape as well as the local stress [125, 126, 129]. This allows the crack location to naturally occur alongside slip bands (see Figure 1.13(a)). Note that in Figure 1.13(a) the crack initiates at the interface between the PSB-like dislocation microstructure and the matrix, similar to what is observed experimentally. In addition to crack initiation, the dependence of crack growth rate as a function of grain size was also determined from these simulations (see Figure 1.13(b)). [126, 129]. Upon inserting a crack in simulations of grain sizes ranging from 10-20 μm, the crack extension is quantified using a parameter called the crack tip slip displacement ($CTSD$), which is measured using the average displacement by dislocations at the crack tip. It was shown that smaller grains exhibit faster crack growth rates since the applied plastic strain was more concentrated as compared to larger grains. However, upon normalizing the crack growth rate by the grain size, the ratio was approximately constant with respect to grain size for crack lengths less than half the grain size. For larger cracks the CTSD

drops dramatically as the effects of the grain boundary causes the crack tip to blunt as shown in Figure 1.13(c).

Based on these simulations, a reverse exponential relation was developed to predict the ratio of the crack growth to the grain size [126, 129]:

$$\frac{CTSD}{D_g} \approx \varepsilon_p \left(1 - \exp\left(-\frac{\lambda}{\varepsilon_p}\frac{b}{D_g}\left(1 - \frac{a}{D_g}\right)\right)\right) \tag{1.5}$$

where D_g is the grain size, b is the Burgers vector, a is the crack length, ε_p is the plastic strain amplitude, and $\lambda = 25$ is a fitting parameter.

While as indicated earlier that fatigue crack propagation in bulk scale is commonly described using LEFM, the issue with applying these relations to micro-cracks is the stress intensity factor assumes a negligibly small process zone relative to the crack size. Thus, for small crack sizes, these assumptions break down and LEFM cannot accurately predict crack propagation rates [130]. Inside the process zone, various micro-scale failure mechanisms contribute to the overall crack propagation [4]. Accordingly, small-scale experiments are uniquely suited to characterize the physics that drive short crack growth, since the crack size, process zone radius, and sample width are all on similar length scales.

In fatigued Cu micro-wires, crack initiation was observed along slip bands that later propagated along and through grain boundaries [67]. As evidenced by the SEM micrograph in Figure 1.14, there is a clear transition from a stage-I crack along the slip band to a stage II crack that propagates such that it is parallel to the grain boundary. The thicker wires were found to exhibit a zig-zag crack path, which could possibly explain the improvement in fatigue life for thicker wires in this study. It is interesting to note that the crack initiation sites were found to have a vein, cell, or elongated cell structure. However, no PSBs were found, which would normally be expected at crack initiation sites.

Another consideration when dealing with cracks in micro-beams is the

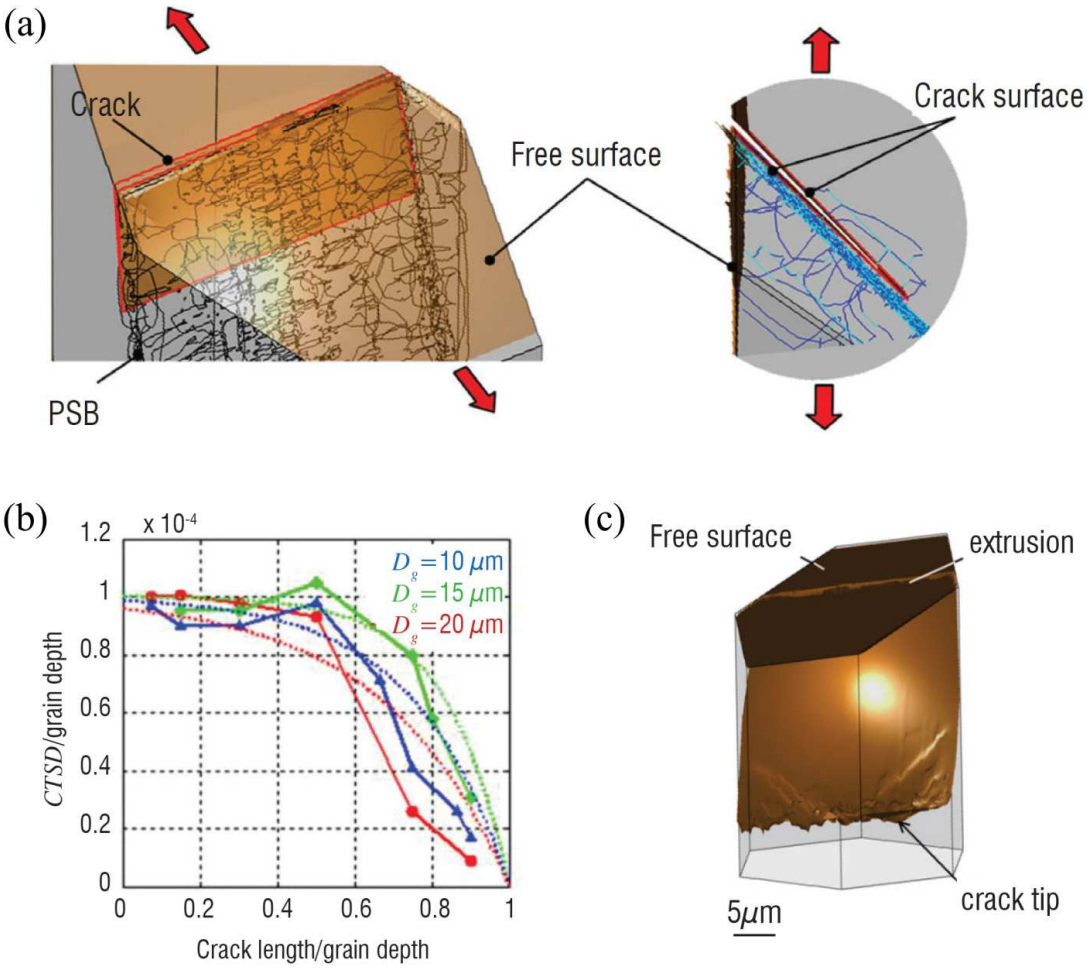

Figure 1.13: The simulation of a crack in 316L stainless steel using 3D DDD: (a) Dislocation structure. (b) Normalized crack tip slip displacement, $CTSD$, versus normalized crack length for different grain sizes. Note that in the early stages of crack growth, there is relatively little variation in $CTSD$ for different grain sizes. Also note the exponential decay of CTSD as the crack goes through the grain depth. The dashed lines are from Equation 1.5. (c) Surface of a crack that nucleated along an extrusion. Note the blunting of the crack tip as it approaches grain boundary and plasticity is dispersed on more slip systems. The individual images are reprints with permission from [129].

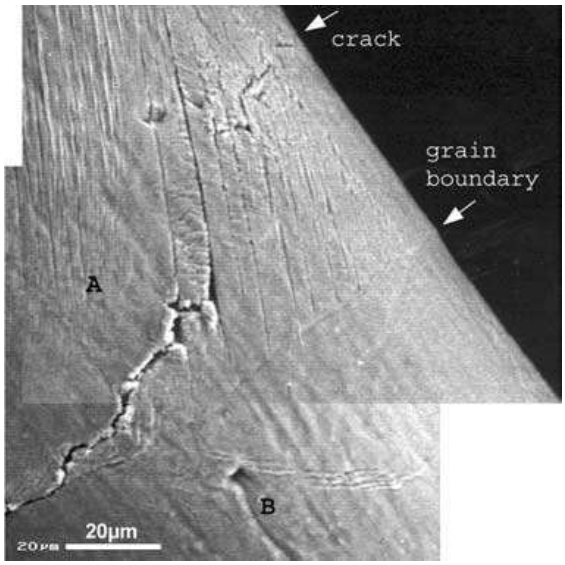

Figure 1.14: SEM micrograph after 6 $\times 10^6$ cycles of a crack site in a bamboo-structured Cu microwire having 125 μm diameter and exposed to a strain amplitude of 3.5 $\times 10^{-4}$. Slip traces correspond to the primary slip system of the grain. It is suggested that cracks initiated along the slip bands and propagated to become a stage II crack with further cyclic loading. Reprint with permission from [67].

stress gradients induced by the loading boundary conditions as opposed to those around the crack tip. Ultra-low crack growth rates were reported in Ni micro-beam fatigue experiments and were attributed to a reduction in stress concentration at the crack tip due to the stress gradient across the beam width [33]. This is unique to the micro-scale bending since only at these length scales would the stress gradient be comparable to the stress gradient present at a crack tip. Further work to quantify the effect of stress gradients on fatigue life of micro-beams was also conducted [131, 132]. It was found that by increasing the stress gradient, η from 17% to 36%, a ten-fold reduction in crack growth rate was observed where η is defined as

$$\eta = \frac{1}{\sigma_{max}} \frac{d\sigma}{dx} \tag{1.6}$$

Pre-cracks and notches were also often introduced in micro-fatigue specimens to accelerate the initiation of a crack so that subsequent crack propaga-

tion studies can be performed. In micro-samples, FIB is sometimes used to create a notch in order to promote crack initiation [133, 40, 43]. For example FIB has been used to mill a notch along the primary slip plane in single crystal Ni superalloy micro-beams [43]. Of course, these notches are not atomically-sharp and cannot be treated as a crack. As such, it generally takes a certain number of cycles to initiate a crack from these stress concentrations. Also, even though the presence of these notches simulate the stress concentration effects of an intrusion alongside a slip band, the dislocation microstructure near the crack tip is much different than what would be obtained if the crack would have nucleated naturally. From 3D DDD simulations, it was found that if a crack is inserted at the beginning of a simulation before any slip bands had formed, the crack would blunt upon cyclic loading [129]. Contrasting this with a crack alongside a slip band (see Figure 1.13(a)), the crack would propagate in a planar manner and maintain its sharpness [129]. This finding serves as a reminder that cracks obtained using notches are not directly comparable to cracks that initiate alongside slip bands.

The presence of grain and twin boundaries are also known to promote crack initiation in fatigue in bulk and small-scale studies [134]. Cracks have been observed to nucleate along grain and twin boundaries in thin 200 nm Cu films [63]. In 3.0 μm Cu films, fatigue cracks are also seen at grain and twin boundaries. However, it is the interaction between extrusions and the boundaries that cause cracks to form [64]. Besides grain boundaries, interfaces of any kind would almost certainly help in the accumulation of damage and subsequent crack initiation. Many fatigue studies of thin films confined with a substrate on one side, and voids at the film-substrate interface have been shown to promote crack initiation under cyclic loading in submicron film thicknesses [135]. Due to the complex nature of the interaction between interfaces and dislocations, DDD simulations have not yet been able to capture the physics of crack initiation along grain boundaries, twin boundaries, or multi-phase

materials.

In micro-fatigue of fine-grained polycrystals, the grain size becomes the characteristic length scale that governs short crack growth. In one such study, an AISI 4340 steel microbeam was FIB-milled with a notch size on the same order of the grain size [40]. The study was done *in situ*, which allowed for observation of crack propagation mechanisms. The crack was observed to deflect (Figure 1.15), branch, and bridge with nano-scale cracks in response to the presence of grain boundaries. This resulted in a discontinuous crack growth whereby the crack was arrested at times and did not grow at all for a certain number of cycles. This is in agreement with 3D DDD simulations, which indicate that when a crack approaches a grain boundary, the tip of the crack blunts which leads to a reduction in the crack propagation rate [129]. Grain growth is another mechanism that has been observed experimentally to effect crack growth in nano-crystalline materials [60].

Finally, it should be noted that given that the crack length in small-scale studies is often on the same order as the size of the plastic zone at the crack tip, that this has profound impacts on the propagation behavior of these micro-cracks. In one case, striations are observed on the fracture surface which signifies a repetitive blunting and resharpening mechanism of crack propagation [133]. This same effect is replicated computationally in [136] using the aforementioned 2D cohesive surface DDD framework. In the previously discussed inclined notch beam experiment [43], crack propagation was seen to alternate directions according to different slip planes. This effect is attributed to the pile-up of dislocations along the neutral axis (similar to the one discussed in Section 1.2) and the resulting backstresses imposed on the crack [43]. Both of these mentioned studies observed significantly lower crack growth rates than those observed in bulk.

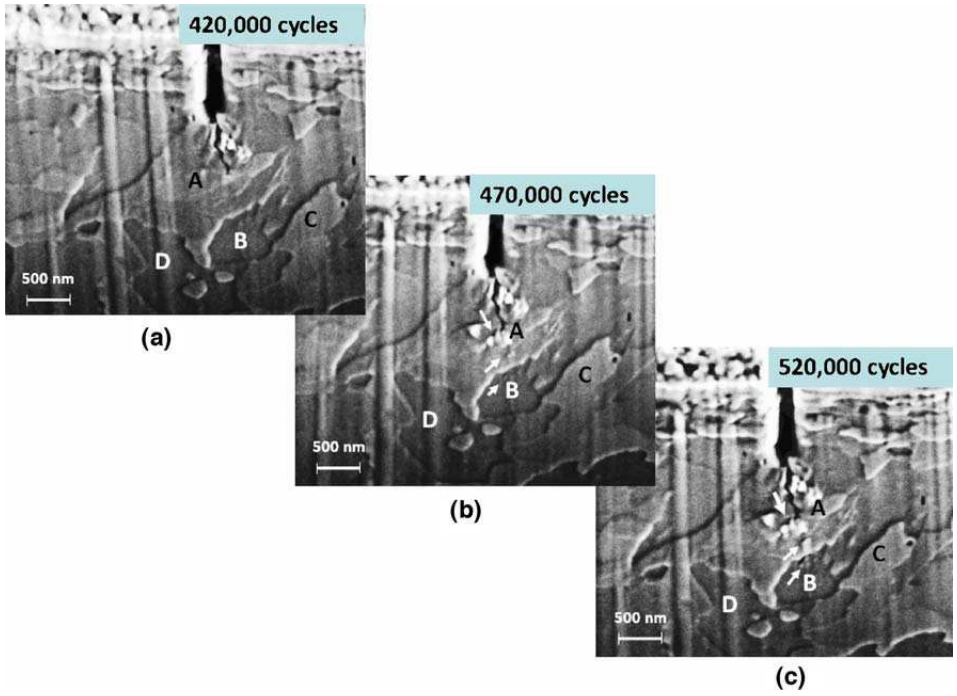

Figure 1.15: (a) to (c) The fatigue crack deflection process at the grain boundary of AISI 4340 microbeam (the white arrows show nano-scale fatigue cracks induced by the major fatigue crack). The crack patch deflects as it transmits through grain A. Note the surface "indents" that appear ahead of the crack tip at the opposite boundary of grain A and along the boundary of grain B. Reprint with permission from [40].

1.5 Present State of Micro-scale Fatigue Research

Fatigue damage, manifested as dislocation evolution, slip localization, crack initiation, crack propagation, then complete failure, is a complex phenomenon that has captured the attention of many scientists for years. However, many open questions remain unanswered due to complexity of the mechanisms involved. While most of the current understanding of fatigue damage evolution is based on post-deformation observations (e.g., optical and electron microscopy) from bulk scale experiments at different stages of the life of a sample, it is difficult to quantify from these "static" observations, with high certainty, the mechanisms that are attributed to the evolving fatigue damage. In addition, dislocation observations by means of TEM usually provide a 2D view of a thin foil extracted from the material.

Micro-scale fatigue experiments provide unique opportunities to directly focus on the appropriate length scales involved in fatigue damage. Also, combining these experiments with discrete dislocation dynamics simulations provides an avenue to isolate and quantify different mechanisms at the appropriate length scale. However, up until now, experimental limitations have greatly limited progress in micro-fatigue.

Interestingly, while the first small-scale fatigue experiments have been conducted over two decades ago, there is still a significant lack of systematic studies for any material system, at varying crystal sizes, and under specific cyclic loading conditions. A composite plot summarizing from literature the various methodologies that have been used to study small-scale fatigue for different metals, the length scale studied, and maximum number of cycles reached, is shown in Figure 1.16. It is interesting to note that there is relatively small number of studies on the plot, while this plot summarizes most of the published small-scale fatigue experiments over the past two decades. The lack of

extensive small-scale fatigue studies might be due to the difficulties associated with fabricating the samples and conducting the experiments. Furthermore, while some studies have been able to reach the very high cycle and even the ultra-high cycle fatigue regimes, these are usually methodologies that induce stress gradients as opposed to uniaxial methods. There appears to be a notable lack of uniaxial studies for samples having sizes in the range of 3-10 μm. It would be interesting to study the effect of crystal size on dislocation structures in this relatively unexplored size scale. Khatibi et al. observed cells and veins using fully reversed uniaxial fatigue as low as 10 μm but did not report PSBs [67]. Perhaps the size requirements to develop a PSB and other dislocation structures can be found using small scale fatigue testing of single crystal samples in the ∼1-10 μm size scale. Although, sizes as low as 50 nm have been explored, the vast majority of uniaxial fatigue studies below 1 μm have been on thin films on a substrate. To make generalizable statements about the fatigue mechanisms in submicron crystals, micro-fatigue methods that do not incorporate a substrate should be pursued.

Micro-fatigue experiments also have the potential to help characterize short crack growth under cyclic loading. The sensitivity of small-scale testing equipment is much better suited than bulk setups to detect crack growth events for physically small cracks. Performing these experiments *in situ* may also allow for measurement of crack growth rates.

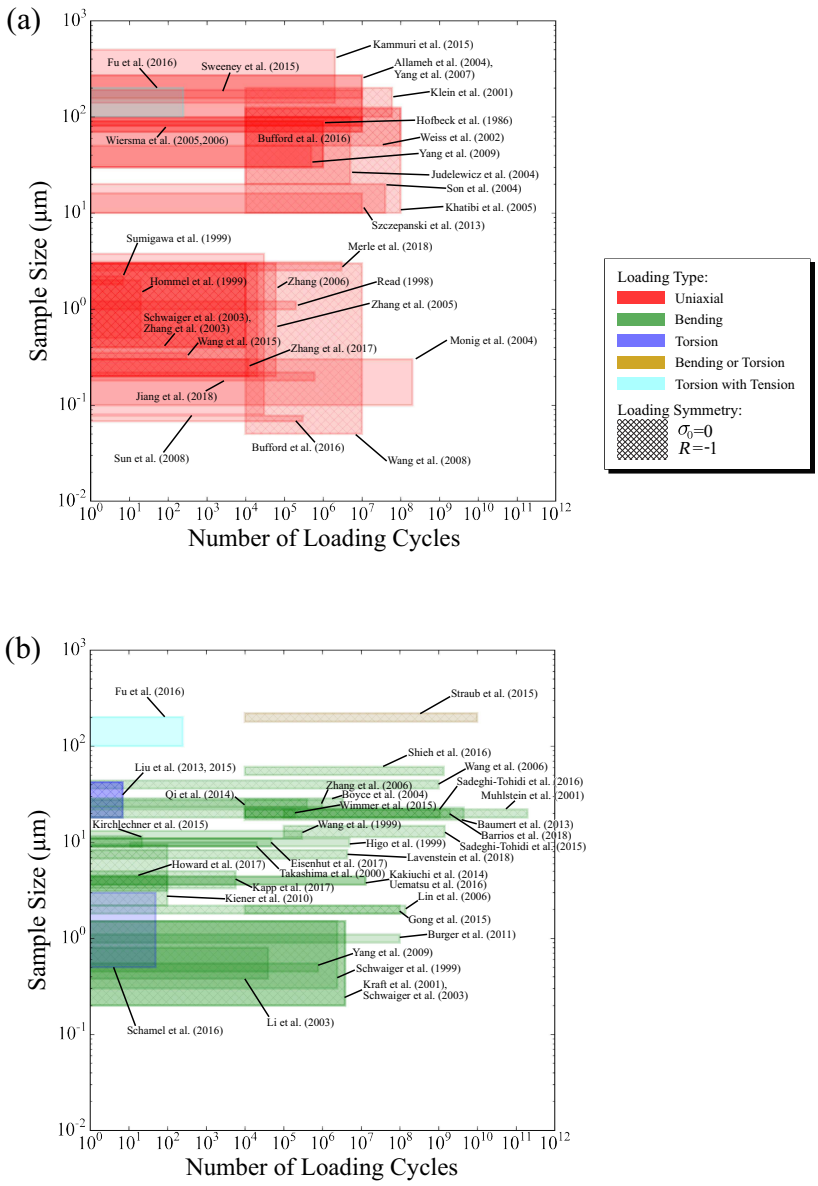

Figure 1.16: Composite plot summarizing a wide (although likely not comprehensive) survey of micro-scale cyclic loading experiments published to date [46, 47, 31, 48, 50, 133, 137, 32, 109, 62, 117, 138, 135, 139, 140, 63, 141, 67, 141, 116, 64, 142, 143, 100, 40, 110, 38, 144, 36, 35, 105, 145, 37, 54, 146, 41, 39, 52, 44, 147, 148, 45, 43, 34, 42, 149, 33, 150, 60, 131, 58, 55, 151, 152] showing the range of sample sizes and the number of cycles reached for: (a) uniaxial loading; and (b) non-uniaxial loading. Hatched boxes denote fully reversed symmetric loading. Appropriate lower bounds for cycles probed were selected based on the testing frequencies. For studies where only one size was reported, 10% was added to the upper and lower bounds of the size scale for visibility on the plot.

1.6 Thesis Objectives and Organization

The objectives of this thesis are to (1) expand the capabilities of micro-fatigue studies by developing a new high frequency, *in situ* small-scale cyclic loading methodology; (2) explore fatigue mechanisms (e.g., dislocation evolution and fracture) mechanisms at the micro-scale in face-centered cubic metals; and (3) provide micro-fatigue data to the mesoscale modeling community (i.e., dislocation dynamics simulations) so that validations on a comparable size scale can be made.

The remainder of the thesis is organized as follows. Chapter 2 provides details about the developed of a new developed methodology for micro-fatigue experiments and associated data analysis procedures. Ni-base superalloy microbeams under high frequency cyclic loading are studied in Chapter 3. The method is expanded to pure Ni and uniaxial stress states in Chapter 4. The incorporation of acoustic emission detection with this method is demonstrated in Chapter 5. Finally, the thesis is summarized and future directions are discussed in Chapter 6.

Chapter 2

Materials, Methods, and Procedures

The small-scale methods developed throughout this thesis are a combination of various experimental techniques. In the following, a description of all experimental methods, materials used, sample preparation, and data analysis procedures are discussed in detail.

2.1 General Experimental Methods

2.1.1 Materials

2.1.1.1 René-N5 Sample Preparation

The material used in Chapter 3 is a single-crystal René-N5 Ni-base superalloy acquired from General Electric Aviation. The composition of the alloy by atomic percentage is 63% Ni, 7% Cr, 7.5% Co, 1.5% Mo, 5% W, 6.5% Ta, 6.2% Al, 0.05% C, 0.004% B, 0.15% Hf, 3% Re, and 0.015% Y [153]. The alloy has a two-phase microstructure that consists of a γ matrix (Ni solid solution) and an ordered array of cuboidal γ' precipitates (Ni_3Al) as shown in Figure 2.1. The γ' phase constitutes the majority of the alloy by volume

fraction and the precipitates are approximately ∼300-500 nm in size [154]. Rectangular samples were prepared from the as-received bulk single crystal by slicing $6 \times 5 \times 12$ mm^3 sections using wire electrical discharge machining (EDM), followed by mechanical polishing of the surface using silicon carbide metallurgical papers.

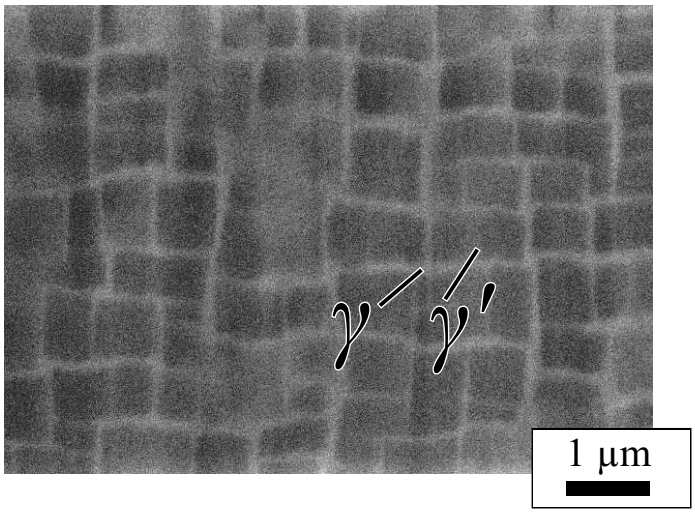

Figure 2.1: High contrast scanning electron micrograph of the {101} surface of a René-N5 microstructure.

2.1.1.2 Nickel Sample Preparation

The material used in Chapters 4 and 5 is a single crystal Nickel (Ni) with 99.999% purity obtained from Goodfellow Corporation, USA. The obtained Ni bar was cut into multiple cuboidal pieces with dimensions $3.3 \times 3.3 \times 9.0$ mm^3 using wire electrical discharge machining (EDM). One of the cuboids was then mechanically polished to a 6 μm finish on all sides with metallurgical paper, then heat treated at a temperature of 1365°C in Argon at a back pressure of 1 psi for 2 weeks.

The cuboid was once again sectioned using wire EDM along with a goniometer to orient the crystal such that the $[\bar{3}5\bar{2}]$ crystallographic direction was normal to the newly-created top face. Consequently, this was the loading

direction used for all studies in Chapters 4 and 5. This orientation was chosen to achieve single slip deformation under uniaxial stresses. The Schmid factor for the associated primary slip system in this case is 0.45 while that for the coplanar and conjugate slip systems were both 0.33.

2.1.2 Scanning Electron Microscopy (SEM)

Almost every aspect of the fabrication, testing, and characterization performed in this thesis relies on scanning electron microscopy (SEM). All experiments are performed *in situ*, meaning that the material being tested is observed in real time under the SEM. Therefore, a basic understanding of the theoretical and practical considerations of SEM is necessary to understand the experimental observations reported in this thesis.

The basic principle of SEM is to radiate a flux of electrons onto a focused region of the sample surface [155]. The incident electrons interact with the surface of the sample and reflect back secondary electrons, backscattered electrons, X-rays, and Auger electrons. Almost all SEM surface imaging performed in this thesis is done using a secondary electron detector. Variations in secondary electron yield provide the contrast for surface image analysis in SEM.

In this thesis, all general SEM imaging and *in situ* experiments are conducted using a TESCAN Mira3 SEM (Figure 2.2) [156]. The Mira3 SEM features a Schottky field emission electron gun and various beam settings can be adjusted to optimize the SEM imaging. The electron accelerating voltage determines the amount of energy that is used to accelerate the electrons. A higher accelerating voltage increases the interaction volume as well as the resolution of the scan. The beam intensity is related to the number of electrons flowing per unit time. For the Mira3 SEM, beam intensity is set using a scale of 1-20 (no units) with higher numbers correlating with higher intensities. To

further tune the SEM resolution settings, various preset lens imaging modes are available with the Mira3: resolution, depth, field, and wide field. Resolution provides the best spatial resolution (i.e., smallest spot size) and is used for almost all imaging in the present thesis. Depth and field modes sacrifice resolution so that more of the depth of a surface is in focus (i.e., a higher depth of focus). Wide field mode provides a very large field of view and is useful for initial alignment of samples at low magnifications.

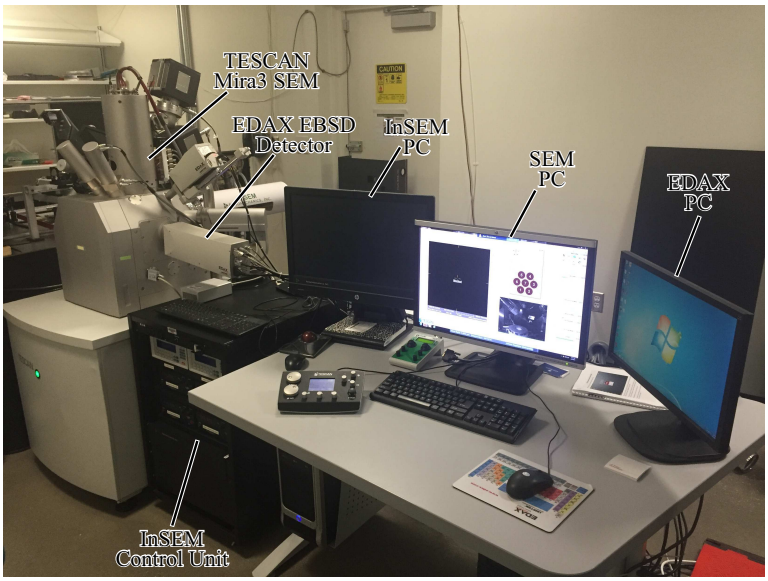

Figure 2.2: SEM characterization and testing facility. Image courtesy of Hopkins Extreme Materials Institute (HEMI).

All SEM imaging in this thesis is performed under vacuum. SEM imaging also requires that samples be conductive and grounded so that they do not build up a charge. Charge build-up in turn results in erratic behavior during SEM imaging. In this thesis, all samples are metals and thus conductivity is not a significant issue. However, in Chapter 5, conductivity is purposely limited to reduce electrical noise detected by acoustic emission sensors. For general imaging, carbon tape is used to attach samples to SEM stubs. For applications that require a less compliant adhesive (i.e., micro-mechanical testing), 5-minute epoxy is mixed with graphite powder to mount samples and

provide a conductive path to the SEM ground.

2.1.3 Transmission Electron Microscopy (TEM)

To characterize the dislocation microstructure of samples in Chapter 4, bright field transmission electron microscopy (TEM) was used. A JEOL 2100 with a FEG source at 200 kV was used in bright field mode to obtain TEM micrographs. This TEM facility is a part of the Centralized Research Facilities (CRF) at Drexel University.

2.1.4 Electron Backscatter Diffraction (EBSD)

Electron backscatter diffraction (EBSD) detectors interface with SEM to acquire orientation information at a localized region of a crystalline material [157]. An EBSD detector is usually mounted in on the side ports of an SEM chamber. During EBSD, the sample is tilted to increase the yield of backscattered electrons to the detector while the incident electron beam is focused on the material surface. Since the backscattered electrons come from deep inside the sample surface, they contain information about the crystal orientation of the material. The EBSD detector is capable of sensing the angular distribution of electrons in the form of diffraction bands (i.e., Kikuchi patterns). With the crystal structure known, these patterns can be indexed to obtain the crystal orientation relative to the stage coordinates. This can be repeated with a scanning pattern to obtain a spatial map of orientations for a section.

In this thesis, an EDAX EBSD is used to obtain crystallographic orientation information. For example, since this thesis uses exclusively single crystals, EBSD is useful for ensuring that the desired orientation is being tested. Also, in Chapter 4, EBSD is used to characterize how the fatigue dislocation microstructure affects the crystallographic texture of cyclically loaded Ni single crystals.

2.1.5 Focused Ion Beam (FIB)

Focused Ion Beam (FIB) has been a useful tool in materials science research since the 1990s [158]. FIB is appealing due to the ability to micro-machine samples with high precision. The most common application of FIB is to extract and thin site-specific TEM samples. This requires an instrument that combines the FIB with an SEM beam, micro-manipulators, and gas injection systems (e.g., the FIB/SEM in Figure 2.3). In this thesis, FIB is used primarily as a tool for fabricating final micro-sample geometries. FIB is also used in Chapter 4 to extract TEM samples from cyclically deformed micro-samples. FIB is also occasionally used for imaging in Chapter 5.

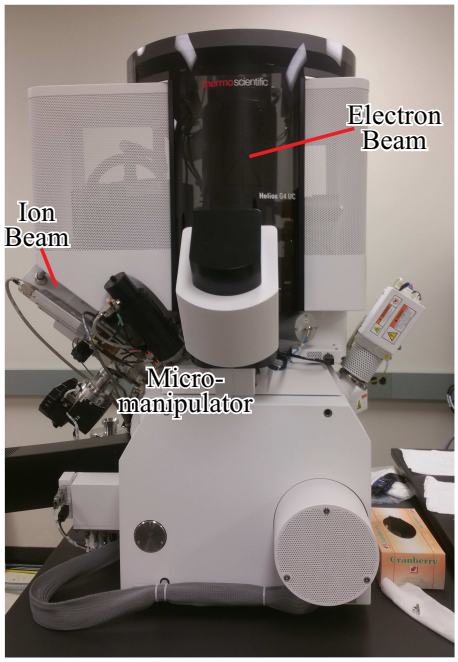

Figure 2.3: Thermo Scientific Helios DualBeam FIB/SEM at JHU.

The general concept of FIB is that it accelerates a stream of ions and directs it towards a spot on a solid material. Once the energized ions reach the material, various physical processes can occur. For micro-machining, sputtering is the most important of these processes. Sputtering is the ejection of atoms from the surface of the target material due to the incident ions. By

focusing the ion beam and deflecting it, complex patterns can be sputtered from the surface of the target material. By simply performing more pattern repetitions, more depth can be milled from the sample surface.

An FEI DualBeam 235 located at the CRF at Drexel University was used for all FIB work in Chapters 3 and 4, while a Thermo Scientific Helios DualBeam at JHU (see Figure 2.3) was used for fabricating the micropillars studied in Chapter 5. Both FIBs use a gallium (Ga) liquid metal ion source (LMIS). The Ga is contained in a W needle source. By heating the source, a small amount of liquid Ga wets the needle tip. Then, a series of electrostatic lenses and deflectors are used to extract, focus, and aim the ions at a specified target. The most important beam settings with respect to milling quality are the ion accelerating voltage and the beam current. Both of these settings affect the resulting spot size, penetration depth, and sputtering rate. A 30 kV accelerating voltage is used for most milling applications in this thesis while 5 kV is used for surface cleanup of TEM samples. Nominal beam currents can be set by selecting installed ion apertures. A maximum beam current of 21 nA is used for coarse cuts in this thesis. Beam currents as low as 2.5 nA are used for final surface mills of micro-samples. For near final surface mills of TEM samples, 100 pA is used. For final TEM surface cleanup, 50 pA is used. For general FIB imaging and alignment, 30 pA is used. Other important settings are related to FIB scan patterns. When the FIB scans over a region, each spot is milled for a set amount of time: the dwell time. Also, for two neighboring points, the percentage of the spot diameters that overlap is known as the overlap. For this thesis, typical settings for dwell time and overlap used for general FIB milling are 1.0 μs and 50%, respectively.

2.1.5.1 FIB Fabrication Considerations

Although the general idea of FIB milling is straightforward, there are many deviations from ideal milling behavior that must be considered (see Figure

2.4). This section provides a guide for many of the difficulties that may be faced during FIB milling and best practices to combat them. Most of the following are based on anecdotal findings from the author's experience.

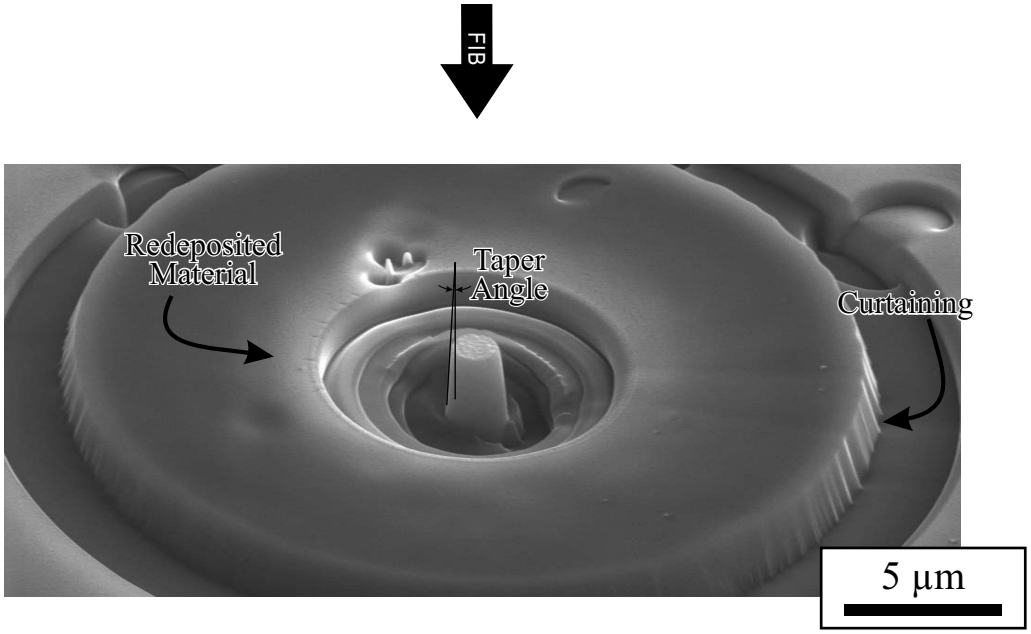

Figure 2.4: SEM micrograph during annular FIB milling of a Mg micropillar. Non-ideal FIB features are denoted.

Perhaps one of the most notable difficulties is sidewall taper angles when milling into the depth of a material. Depending on the beam current used, there is typically about a 3° sidewall taper in FIB when milling into the depth of a surface. The cause for this taper is related to the Gaussian beam profile. In other words, the center of the beam yields the highest sputtering rate; however, the tails of the beam profile mill more slowly. The result is an inclined sidewall. One simple way to combat this effect when straight sidewalls are desired is simply to offset the stage tilt to compensate for the taper. However, this is not always practical, especially for circular geometries (e.g., cylindrical micropillars).

In addition to taper, "curtaining" is another deleterious FIB effect that can affect the final surface roughness of the desired geometry (see Figure 2.4). If

the edge of a sample is not smooth, applying an ion beam to the sidewall can result in uneven milling rates along the edge that cause a linear roughness in the final milled sidewall (similar to the ripples in a curtain). Curtaining can be especially prominent when dealing with very deep mills. One precautionary measure to limit curtaining is to ensure that the top surface of the sample is as smooth as possible before milling the sidewalls. Another precautionary approach is to use a progressively smaller mill box and beam current as the final sidewall is approached. If after these measures curtaining is still present on the final sidewall, a first approach to eliminating it would be to use a fine mill box at the very edge of the sample to smooth the surface. However, it is often the case that the presence of the curtaining does not allow for a uniform sputter rate and the curtaining may persists. If this is the case, it may be necessary to move the milling region into the sample a few 100 nm to create a new smooth surface.

Another important consideration during FIB milling is the redeposition of sputtered material (also shown in Figure 2.4). Redeposition is when sputtered atoms land on the region being milled. One effect of this is a lower overall sputtering rate since more passes are required to achieve a given depth. This is one reason why edges tend to mill at a higher rate than the interior of samples in FIB. Since the edge of a sample is less likely to capture a redeposited atom, their overall sputter rate is higher. It should be noted that this "edge effect" is also partially due to lateral sputtering induced by atoms traveling through the sample volume [158]. Another reason to be conscious of redeposition is because if the sample surface becomes covered with a significant amount of redeposited material, this could affect its mechanical response. For this reason, the sample surface should always be the last step of any milling pattern. Also, this last step should ideally be performed with a small pattern region and at a low beam current.

One final, but crucial, element of FIB fabrication is the surface damage left

on FIB-machined surfaces. This damage can be in the form of amorphization, interstitial defects, vacancies, or dislocation nucleation [158]. The thickness of the damage layer is different for each material; however, for Si the damage layer due to amorphization is less than 100 nm [159, 160, 161]. For the ∼10 μm size scale of the micro-samples considered in this study, it is not expected that a damage layer on the order of ∼100 nm would have a significant effect on the monotonic mechanical response [162]. However, for fatigue, surface quality is very important and this damage layer should be kept in mind when interpreting results. For TEM foils (typically less than 200 nm thick), this damage layer can also be very important. Thus, for thinning of TEM foils, a low voltage (5 kV) is used to remove damage on both sides of the foils.

In addition to the factors discussed in this section, there are many other variables that one may encounter during FIB. For example there is sample charging/drift, mechanical drift, and limited viewing angles, among others. All of the factors listed in this section make it challenging to consistently reproduce sample geometries with FIB.

2.1.5.2 FIB Liftout

As previously mentioned, one of the most common uses of FIB is to extract site-specific TEM samples. This is especially useful in the case of micro-samples where the deformation is localized in a very small region. However, extraction of these samples is different from traditional bulk liftout. Specifically, in Chapter 4, the TEM foils had to be extracted from the gage section of Ni hammerhead micro-samples. While the section of interest (i.e., the gage region) is on the order of ∼10 μm, the hammerhead region is an order of magnitude larger. Lifting out the entire sample would be very difficult and unnecessary. Therefore, for all hammerheads TEM samples in Chapter 4, the hammerhead region was first cut off from the gage region using FIB. The liftout process is outlined with a series of micrographs in Figure 2.5.

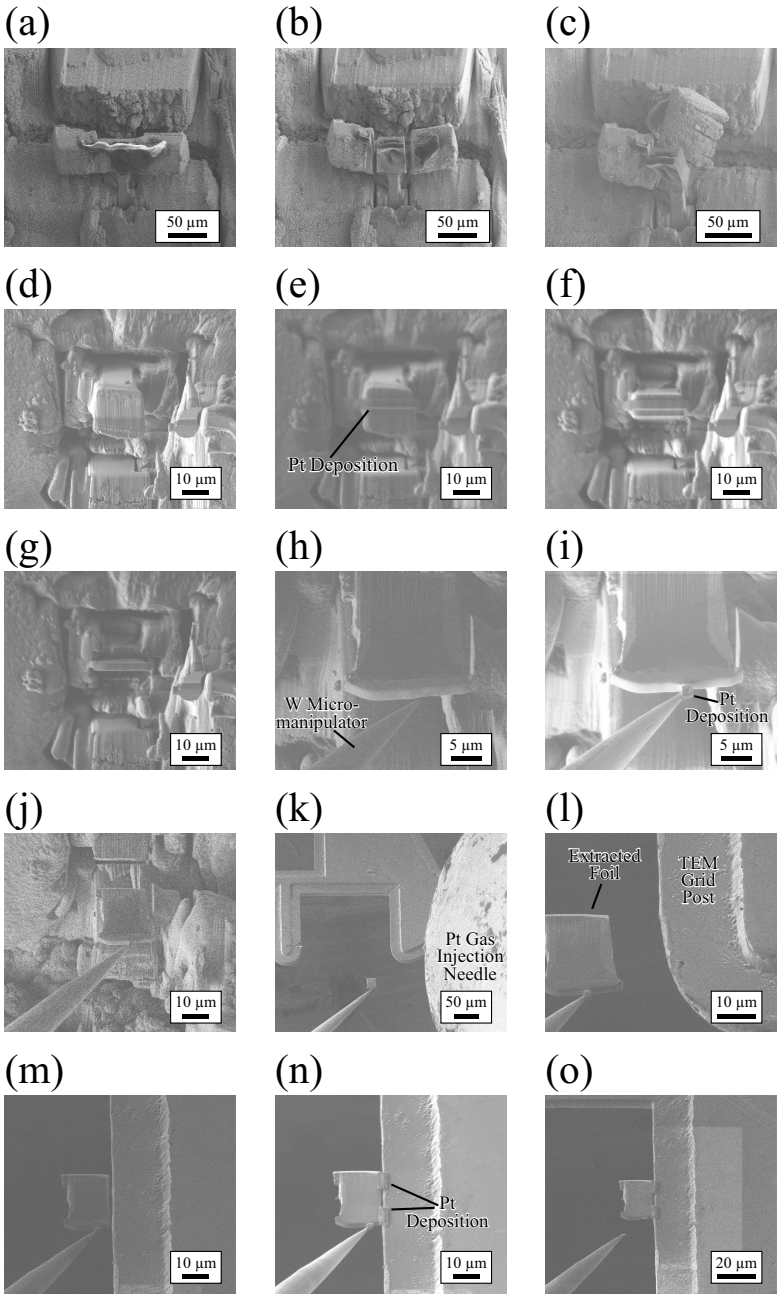

Figure 2.5: Micrographs of FIB liftout process for TEM samples of cyclically deformed Ni hammerhead micro-sample: (a) Ni hammerhead after testing; (b) - (c) FIB is used to cut off the hammerhead region of the sample. (d) The top of the gage region after the hammerhead region is cut free and falls off. (e) A protective Pt layer is deposited on the top of the gage region. (f)-(g) The gage region is thinned down to $\sim$1 µm in thickness. (h) The W micro-manipulation needle is lowered over the thinned foil. FIB is used to cut approximately 80% of the gage width free from the substrate. (i) Pt deposition is used to attach the sample to the W needle. (j) FIB is used to cut the remaining gage width so that the foil is completely free. (k)-(m) The extracted sample is lined up with a TEM grid post. (n) Pt deposition is used to adhere the sample to the TEM grid post. (o) FIB is used to detach the sample from the W needle. The extracted foil is now ready for further thinning before TEM analysis.

2.1.6 Femtosecond Laser Milling

Although FIB is the only fabrication method that provides the precision and flexibility required to make the micro-scale samples tested in this thesis, it can be very time consuming. This is especially true for milling large trenches (typically ∼100 μm in size) to provide room for samples to be tested without risking contact between the test probe and the sidewalls. Since it is not necessary for these large trenches to be as well defined as the test sample, using FIB to mill these large volumes would be an inefficient approach. Femtosecond laser milling provides a much coarser milling technique capable of removing material 4-6 orders of magnitude faster than FIB [163]. For example, the laser coarse mills shown in Figure 2.6 each took less than 10 minutes to mill (not including time for sample setup and positioning).

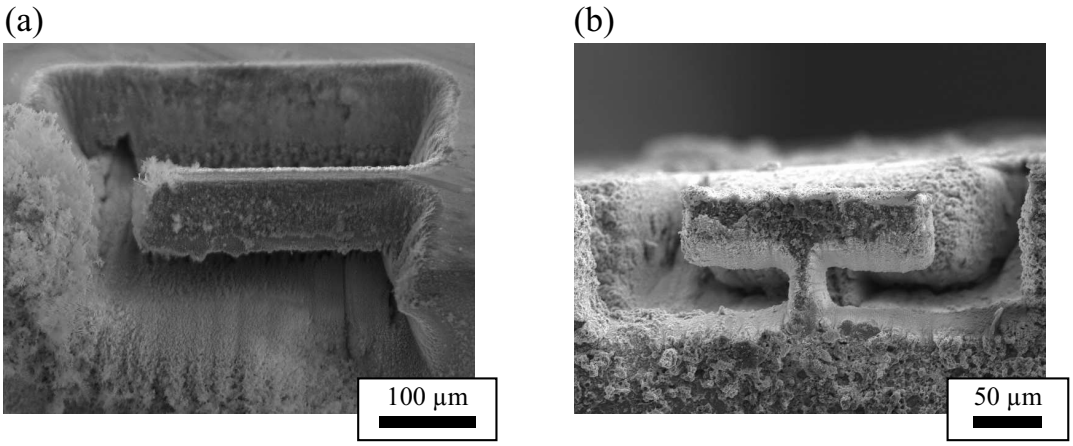

Figure 2.6: Coarse femtosecond laser-milled samples before FIB: (a) René-N5 micro-beam; (b) Ni hammerhead micro-sample.

The mechanism for material ablation with femtosecond laser milling is as follows [164]. The ultra-short laser pulse reaches the material and the energy is absorbed as electron thermal energy. If the Fermi energy is reached, the electrons are able to escape the material. This in turn creates an electric field that accelerates ions away from the material. Another consequence of this is that the duration of the pulse is much shorter than the timescale of

electron-phonon interactions. The result of this is minimal damage to the surface microstructure from shock waves or heat transfer.

A Clark MXR femtosecond laser was used to fabricate rough geometries for microsamples in this thesis. The laser passes through a polarizer, a series of mirrors, an aperture, and an objective lens. Further details about the setup can be found elsewhere [165]. The laser power, polarizer, and aperture are adjusted to achieve a laser energy of $\sim$40 μJ with a spot size of 20-30 μm for all milling in the present thesis. The laser wavelength was 780 nm and a pulse repetition rate was 1.0 kHz. During the ablation, the laser beam is stationary and the bulk material is repositioned using an Aerotech ANT-95 XY nanopositioning stage. The stage features subnanometer resolution and two linear axes of control. Multiple passes are generally needed to achieve the required dimensions.

Figure 2.6 shows two examples of how the laser can remove most of the required material before reaching the final sample geometry. However, one clear drawback of femtosecond laser milling is the surface roughness left on the remaining material. Clearly visible in Figure 2.6 is the $>$1 μm surface roughness due to variations in the beam profile. However, there is also a sub-micron surface roughness, known as Laser Induced Periodic Surface Structures (LIPSS), which are ripple-like structures that are generally unavoidable in laser milling [166]. They are characterized by a wavy line texture with a $\sim$100 nm spacing. Additionally, the Gaussian profile of the beam results in tapered sidewalls. Finally, ablated debris (see Figure 2.6), is often redeposited on the laser-machined surface which degrades the sample finish quality. For these reasons, subsequent fabrication/finishing steps (i.e., FIB milling/cleaning) are needed before the desired geometries can be achieved.

2.2 Micro-scale Sample Fabrication Methodology

2.2.1 René-N5 Micro-beam Fabrication

For Chapter 3, cantilever-like micro-beams were fabricated on the top edge of the single crystal sample such that the side and top surfaces of each micro-beam can be directly viewed in the SEM during testing. Each micro-beam was oriented such that the [100] and [001] crystallographic directions of the FCC lattice were parallel to the micro-beam length and loading directions, respectively. The cross-section of each micro-beam was rectangular with approximate dimensions of 8.5×8.5 μm^2, and the length was $\sim$125 μm from the fixed end to the loading end of the micro-beam. A fabricated micro-beam is shown in Figure 2.7.

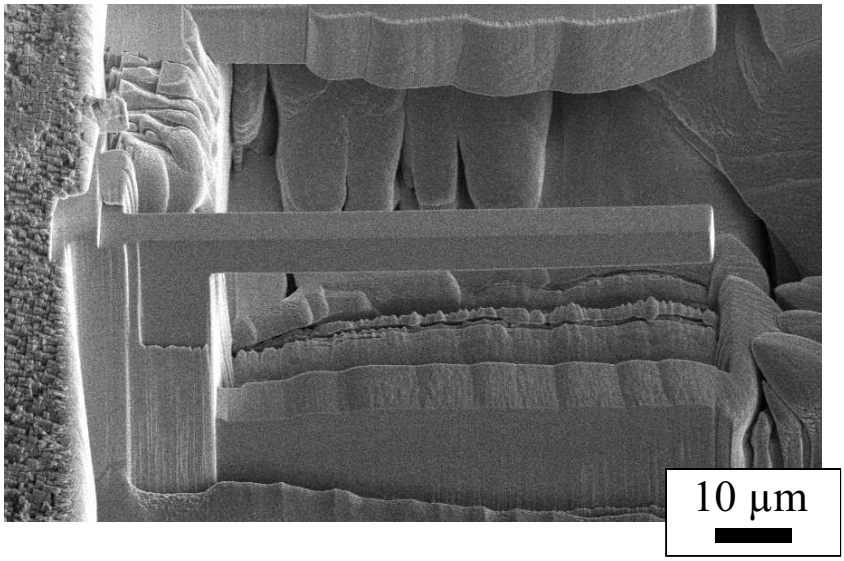

Figure 2.7: René-N5 cantilever micro-beam after fabrication.

The micro-beam fabrication was conducted in two steps. Initially, the [001] direction was laser-milled to obtain a lamella of approximately 15 μm in thickness and 120 μm in depth. The bulk single crystal was then rotated 90°

such that the [100] direction was in line with the laser and the under-side of the micro-beam was milled. Second, after the rough laser-milling (see Figure 2.6), the final dimensions of the micro-beams were attained using FIB as follows. An ion-beam current of 20 nA was used to remove the surface roughness produced during the laser milling step and reduce the micro-beam dimensions to within $\sim$ 4 μm of the final desired dimensions. An ion-beam current of 5 nA was then used to achieve the final dimensions of the micro-beams. A schematic of the laser and FIB milling steps is shown in Figure 2.8.

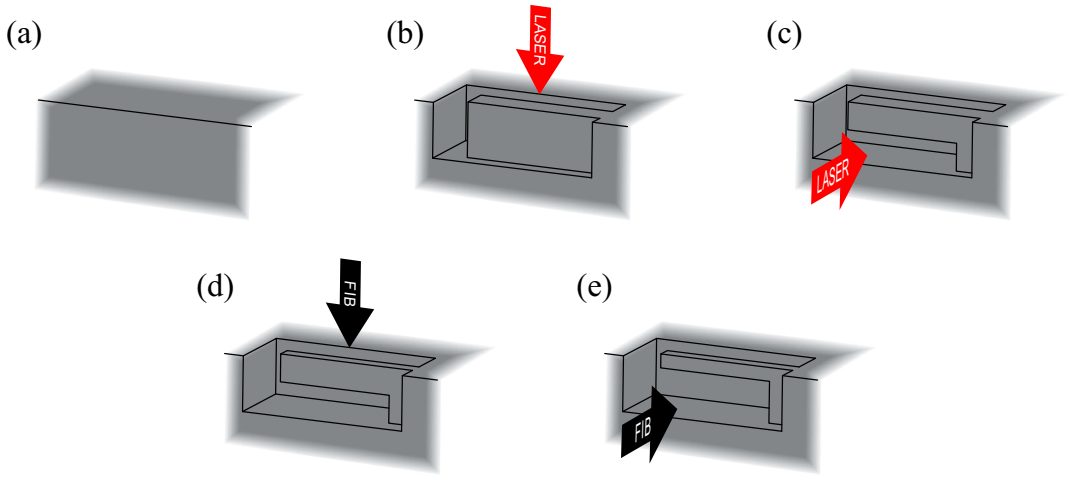

Figure 2.8: Schematic of cantilever micro-beam fabrication procedure: (a) material edge before fabrication; (b)-(c) coarse laser mills; (d)-(e) fine FIB mills.

2.2.2 Nickel Hammerhead Fabrication

For Chapter 4, a novel hammerhead micro-specimen geometry was designed as shown in Figure 2.9. This micro-specimen consists of a gage region with a much wider hammerhead region above it. The gage section of the hammerheads were rectangular in cross-section with approximate dimensions of 12×13 μm^2, while the gage lengths were approximately 27 μm. The hammerhead region was approximately 200 μm in width and approximately the same thickness as the gage region towards the center of the sample. The hammerhead region allows a relatively large area to adhere the probe to the micro-specimen so that tensile

and compressive loads can be imposed. The wider area is necessary to decrease the stress on the adhesive while maximizing the stresses that can be imposed on the gage region.

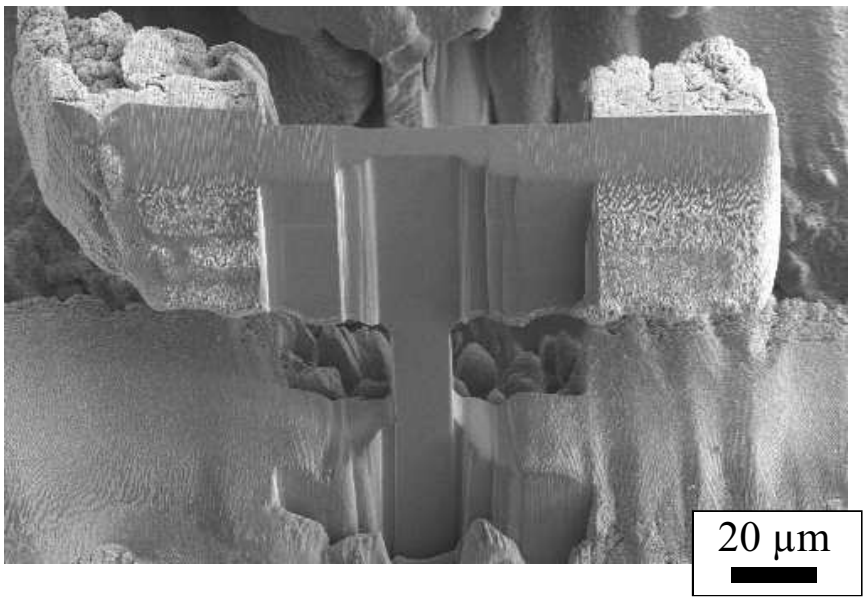

Figure 2.9: Ni hammerhead sample after fabrication

Micro-specimens were fabricated at the top edge of the sample so that the top and front views of the hammerheads were not impeded by the bulk of the sample. The fabrication of hammerheads was performed using a combination of femtosecond laser milling and FIB. The steps of the fabrication process are shown schematically in Figure 2.10.

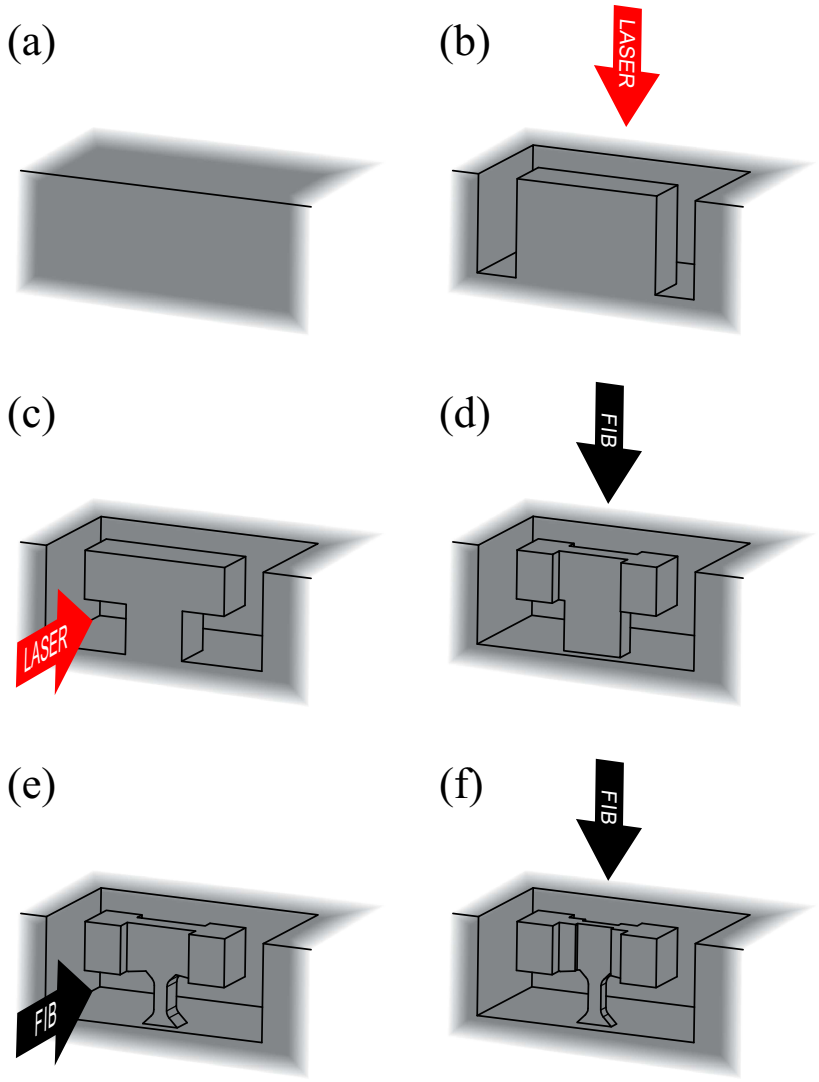

Figure 2.10: Schematic of hammerhead micro-sample fabrication procedure: (a) material edge before fabrication; (b)-(c) coarse laser mills; (d)-(f) fine FIB mills.

2.2.3 Nickel Micropillar Fabrication

For Chapter 5, Ni micropillars were used for all micro-compression experiments. The micropillars all had nominal diameters of 10 μm and height-to-diameter aspect ratios of ∼2-3. These micropillars were fabricated using a FIB-based "lathe-milling" technique similar to that developed by Uchic and Dimiduk (2005) [167]. This is in contrast with conventional annular milling techniques that typically result in a micropillar with a few degrees of taper

[168]. The main difference between the two techniques is that annular milling is performed with the FIB beam oriented normal to the sample surface with circular scans used to mill material until the desired depth/height is reached. On the other hand, lathe-milling is performed with the beam at an angle relative to the sample surface such that the sidewall of the pillar is milled. Lathe-milling requires successive stage rotations about the pillar center axis in order to achieve a circular geometry. Lathe-milling results in virtually no micropillar taper; however, it typically takes several times longer than annular-milled pillars. Examples of micropillars fabricated in Chapter 5 using lathe milling are shown in Figure 2.11.

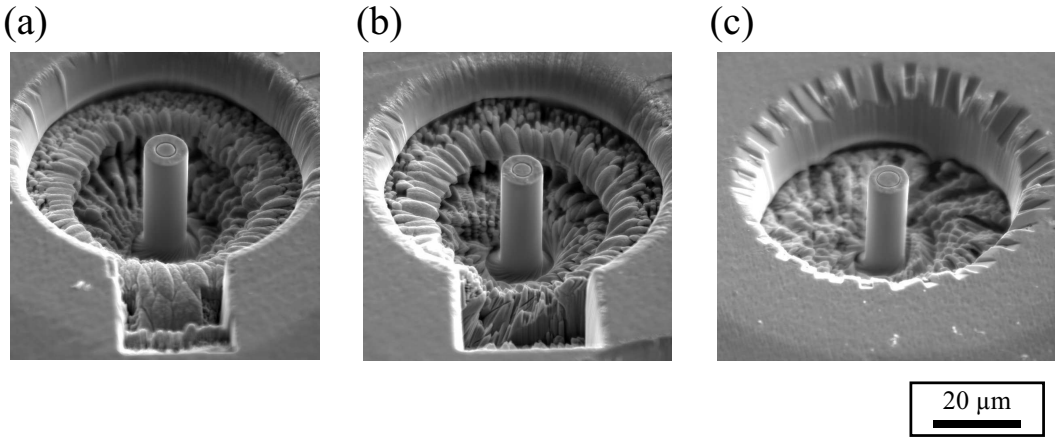

Figure 2.11: (a)-(c) SEM micrographs of Ni Micropillars after fabrication. Stage is tilted 45°. Note that in (a) and (b), rectangular regions are also milled at the edge of the trench to allow for a larger viewing region during *in situ* micro-compression.

Images taken using the FIB beam during lathe milling are shown in Figure 2.12.

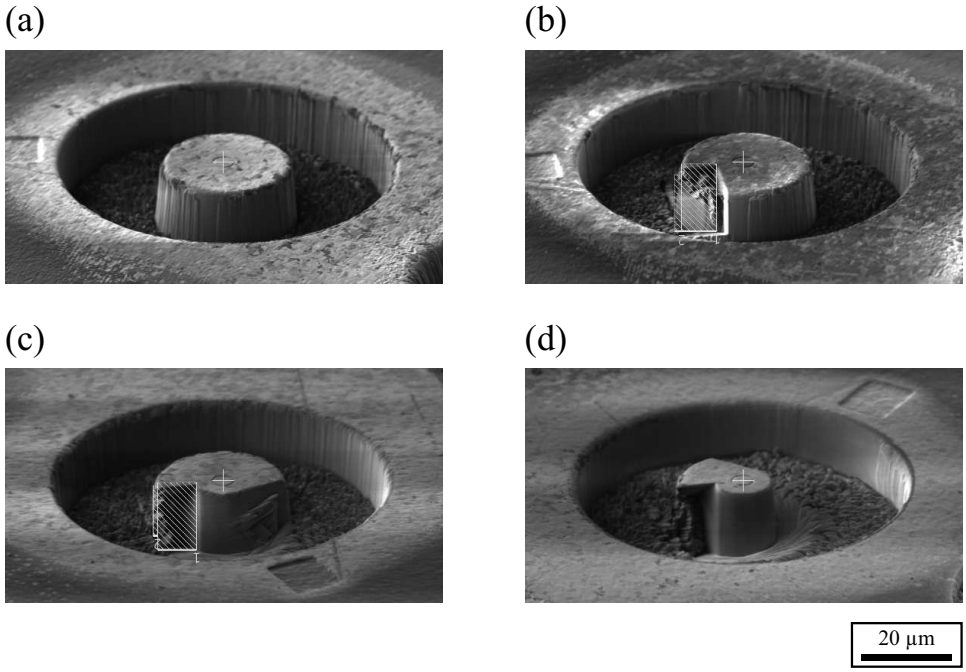

Figure 2.12: (a)-(d) FIB micrographs of steps during lathe-milling procedure at different stage rotations about the circular fiducial mark. Micrographs (b) and (c) show the boxed regions used to mill the sidewalls.

A schematic of the micropillar fabrication procedure is shown in Figure 2.13. The procedure for micropillar fabrications was as follows. First, annular milling was used to create a coarse trench for the micropillars. Then, lathe-milling was used to mill the pillar to its final diameter and height. A beam current of 21 nA was used for the annular milling step and 2.5 nA was used for lathe milling steps. Typically, two lathe milling revolutions are used with a finer mill box used for the second revolution. For all lathe-milling, the stage was tilted such that the FIB was angled 62° from the sample normal. Also, the mill box was rotated 0.4-0.5° to make the sidewalls straight.

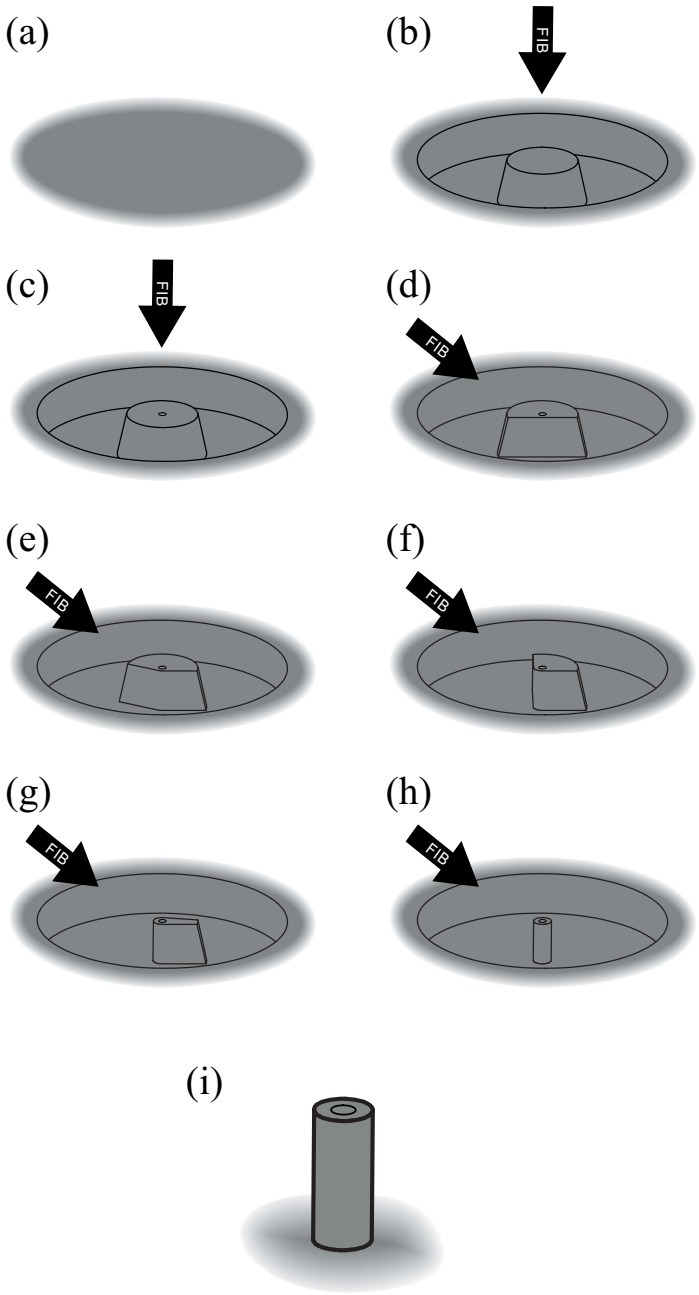

Figure 2.13: Schematic of the micropillar fabrication procedure: (a) sample top before fabrication; (b) coarse annular FIB milling micropillar trench; (c) FIB milling of circular fiducial mark; (d)-(h) lathe milling of micropillar sidewalls with successive clockwise stage rotations about the center of the fiducial mark; (i) final micropillar up close.

2.3 *In situ* Loading Methodology

2.3.1 Micro-actuator Loading Methodology

All *in situ* experiments performed in this thesis were conducted using a Nanomechanics (now a subsidiary of KLA Corporation) InSEM system, as pictured in Figure 2.14. The system features an InForce 1000 actuator mounted on a cradle and attaches to the stage of the Tescan Mira3 SEM at JHU. The cradle also exhibits a micro-positioner stage on which the sample of interest is mounted. This system allows for accurate and precise loading at a scale appropriate for the micro-specimens considered in this thesis. Additionally, the system fits inside an SEM chamber so that the micro-samples can be viewed in real time during testing.

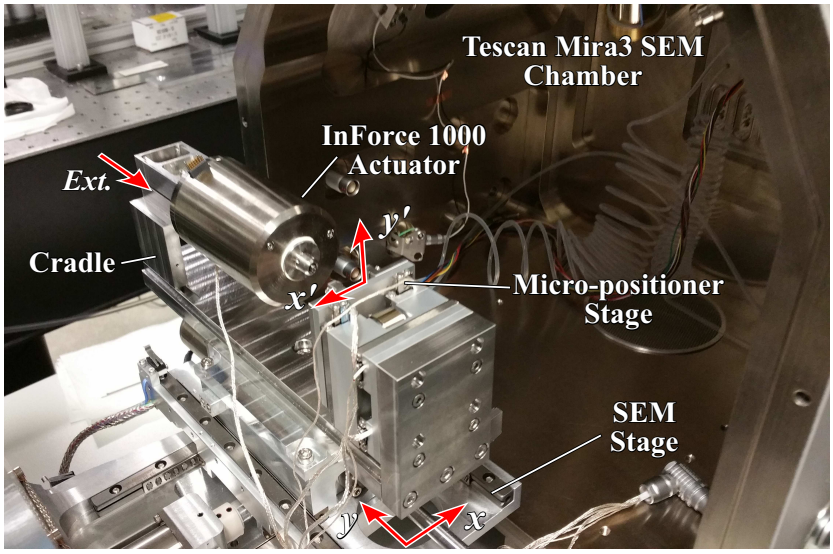

Figure 2.14: Photograph of the InSEM testing apparatus used for all *in situ* micromechanical experiments in this thesis. The coordinate systems for the SEM stage (non-primed) and the InSEM micro-positioner stage (primed) are as denoted. Note that the SEM chamber door is open and the stage is pulled out of the chamber. The SEM beam, and thus the viewing direction, is in the vertical direction. Under normal testing conditions, the SEM column would be in line with the sample on the micro-positioner stage while being probed by the actuator.

The InSEM cradle replaces the rotating stage normally used in the SEM so the setup cannot be rotated about the beam direction during *in situ* exper-

iments. However, x translations, y translations, and tilts about the x-axis are still possible (see Figure 2.14), granted there are no clearance issues with other instruments in the chamber. In addition to the SEM stage degrees of freedom, the micro-positioner stage also provides two translational degrees of freedom (x' and y' in Figure 2.14) to align the micro-specimen with the actuator. The actuator is brought closer to the sample using the extension (*Ext.* in Figure 2.14). The adjustment of the cradle's x', y', and extension positions are all piezo-actuated for precise alignment.

The InForce 1000 micro-actuator is used for all loading in this thesis. A schematic of the actuator is shown in Figure 2.15. The InForce 1000 micro-actuator has a loading capacity of 1.0 N, a displacement range of 80 μm, and is capable of imposing large dynamic loads. The load resolution is rated at 6 nN and the displacement resolution is 0.04 nm [169].

The basic principle of the actuator is relatively straightforward [170]. A force is applied to the central column using an electro-magnetic coil. The probe, attached to the end of the column moves in response to the applied force. This displacement is detected using a capacitive displacement sensors. The actuator frame holds the central column using leaf springs that have a known stiffness: k_{act}. Note that k_{act} is not constant but calibrated as a function of the actuator displacement. This is done by varying the load cell force, measuring the displacement, and computing the stiffness value at each displacement value. There are also damping effects in the load frame, with a damping coefficient of c_{act}. This damping can be cause by either drag resistance or Eddy currents in the electro-magnetic coil. Since all experiments are performed under vacuum ($\sim 10^{-3}$-10^{-2} Pa), the effects of drag are believed to be negligible. These damping effects are only significant at high velocities, such as those in high frequency fatigue experiments.

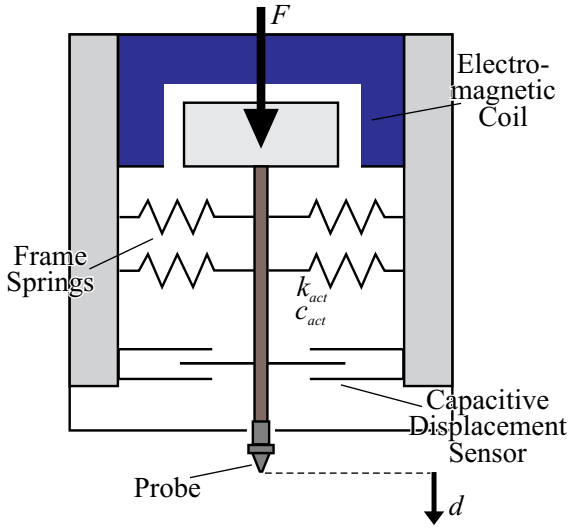

Figure 2.15: Schematic of the micro-actuator used for all loading in this thesis.

2.3.1.1 Force Application

The micro-actuator used in this thesis is an inherently force-controlled device [170]. The force is not measured directly; rather, it is assumed that the electro-magnetic force is the same as the raw force (i.e., the force applied to the sample and the springs). The only reason this would not be the case is if the actuator damping (with coefficient c_{act}) were significantly high. In the case of high velocity cyclic loading, this assumption may no longer be valid.

For the electro-magnetic actuator, the raw force, F, is proportional to the current, I, applied to the coil:

$$F = K_{em} I \tag{2.1}$$

where K_{em} is a known proportionality constant calibrated by the manufacturer using NIST traceable weights.

To obtain the load on the sample, P, Equation 2.2 is used.

$$P(t) = F(t) - F(t=0) - k_{act}(d(t) - d(t=0)) \tag{2.2}$$

where d is the raw displacement signal.

Before starting a test, it is required that no load is applied by the actuator. Mathematically speaking, $P(t = 0) = 0$; otherwise, load calculations during the test will not be correct. In the case of gluing samples, the force value when adhering the tip to the sample is noted. This value is used as the starting value at the beginning of each test since it corresponds to zero load applied on the sample.

2.3.1.2 Displacement Measurement

The displacement in the micro-actuator is detected using a capacitive displacement gauge [171]. The capacitor is depicted in Figure 2.15 and the middle plate of the capacitor moves with the actuator tip, while the top and bottom plates are stationary. The device converts tip displacement to a voltage signal as shown in Figure 2.16. At all times, two alternating current (AC) signals with sinusoidally varying voltages are applied to the top and bottom plates. The signals are separated with a phase angle of 180°. The detected AC voltage at the middle plate is then sent to a demodulator, which converts the sinusoidal signal into a constant direct current (DC) voltage average. This voltage value is calibrated such that a displacement can be obtained for any detected output voltage, V_{out}. This calibration is performed by the manufacturer and is done by measuring the displacement using a laser interferometer for different V_{out} values. When the middle plate is positioned exactly halfway between the two plates, the two signals cancel out and the output voltage is zero. Bias to either side changes the detected voltage, which is how displacement is detected.

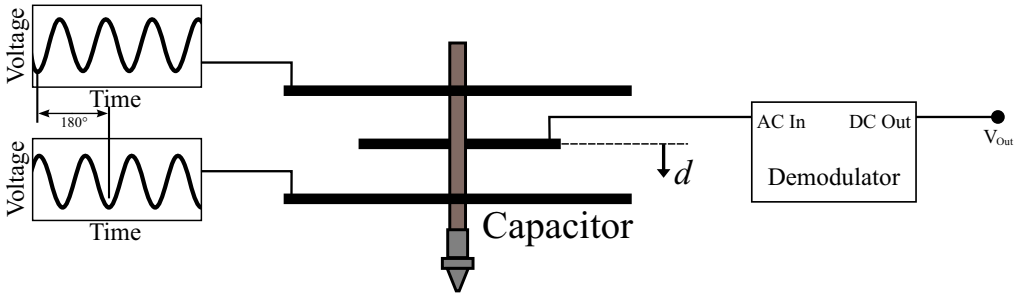

Figure 2.16: Schematic of the capacitive displacement gauge in the micro-actuator.

With the raw displacement signal, d, the displacement into the sample can be calculated as follows:

$$h(t) = d(t) - d(t=0) - \frac{F(t) - F(t=0)}{k_{frame}} \tag{2.3}$$

Here, k_{frame} is introduced as the stiffness of the test frame. This value is calibrated before testing by indenting fused silica with a Berkovich tip. The value k_{frame} is adjusted to obtain the known mechanical properties of the material. Also, for Equation 2.3 to be accurate, the tip must just be making contact with the sample at the beginning of the test (i.e., $h(t=0) = 0$). This is usually accomplished by detecting the surface, labeling this data point as the surface index, and then setting this point in time as $t = 0$. Note that Equation 2.3 does not account for displacement drift from thermal expansion. To apply drift correction, an additional term would have to be subtracted from Equation 2.3. For the present thesis, drift correction is not applied since this correction generally relies on questionable assumptions. For all cyclic loading studies in Chapters 3 and 4, it is very unlikely that significant drift would have occurred within the span of time required to complete a loading cycle since the velocities are so high. For the micropillar compression in Chapter 5, drift is not corrected for since displacement bursts are of interest, not the overall displacement values at any given point during the test.

2.3.1.3 Data Acquisition and Time Constants

All sensing of the load and displacement signals are performed onboard the InSEM control unit. The data is stored in an onboard buffer and periodically, the data is transferred to a PC. The communication between the control unit and PC is the limiting factor in the data acquisition rate of the system, which is 1 kHz at its maximum. This limitation is due to the rate that data can be transferred through the USB cables that connect the control unit to the PC.

Regardless of the data acquisition rate, the fidelity of the raw signal buffer is determined by the time constant of the detection device. The time constant is defined as the time required for 63.2% of an instantaneous step function to be detected. In essence, the time constant is the electronic delay of the device. A shorter time constant is desirable because it provides better temporal fidelity in the signal. A large time constant will be less noisy, but is more likely to miss fast changes. Between the force and displacement signals in the device, the displacement is the bottleneck. This electronic delay is attributed to the time required for the demodulator (see Figure 2.16), to output a DC voltage. The time constant for the displacement signal in the inForce 1000 micro-actuator used in this thesis is 20 μs. While this low time constant may seem unnecessary since the data acquisition rate is much slower, this high fidelity is still very important for many onboard calculations performed on buffer data in the control unit. This is especially important when performing dynamic calculations (see Section 2.3.2) in which the displacement is oscillating at a high frequency. Also, the onboard buffer data is used to calculate time derivatives with low noise levels.

2.3.1.4 Control Loop

The actuator is controlled by the method files in a proprietary Nanomechanics format (.NMD file extension). The method files can be created and altered us-

ing the InView software package for PC. The basic structure of the method files are built on a Test Sequence. The sequence includes a series of actuator control commands, actuator configuration commands, calculations, for loops, if statements, video capture commands, input prompts, micro-positioner movement commands, and message outputs. A test sequence object may include an end condition (e.g., a change in time or a target displacement) that moves the test onto the next object in the sequence. The sequence objects reference various sample calculation variables, which include data collected from the instrument as well as data calculated using the raw instrument data.

As previously stated, the InSEM control unit communicates with the InView software on the PC. Regardless of the set data acquisition rate, this exchange of information occurs at a rate of 1 kHz. When actuator control commands are set with InView, this communication rate is the fastest the commands can be sent. Also, for values that are calculated during the test, this is the rate that the values are updated.

Actuator control commands allow the user to set a control channel, mode, and value. Since the actuator is inherently force-controlled, the Control Channel should almost always be set to Force. The Control Mode can be set to control the value, rate of increase, rate of decrease, or to simply hold the current value. The value can be set to a calculation variable defined by the user. In addition, the actuator control command allows the dynamic force to be set to a user defined variable. Finally, actuator control commands also allow the data acquisition rate to be selected.

2.3.2 High Frequency Cyclic Loading Methodology

The InForce 1000 micro-actuator features dynamic capabilities within the control unit. Namely, the unit is capable of applying oscillating force signals on the electro-magnetic coil and measuring the resulting displacement amplitude

as well as the phase angle between the force and displacement signals. This functionality is typically used in conventional nanoindentation for a technique called continuous stiffness measurement (CSM). CSM allows the stiffness of the sample/contact surface to be monitored at any given point during loading. This works by applying a small dynamic load over the imposed indentation load and then measuring the resulting dynamic displacement. While the present thesis does not use the CSM method for surface indentation, one of the novel features of the experiments shown here is the use of this dynamic capability to perform high frequency cyclic loading experiments.

In the current study, the imposed oscillating force on the micro-beam tip is a periodic sinusoidal load with a driving frequency, ω, and a loading amplitude, F_{amp}, such that $F(t) = F_{amp} \sin \omega t$. Due to the damping effects in the nanoindenter's electromagnetic coil, the resulting displacement amplitude is strongly dependent on the loading frequency. The nanoindenter load frame and the sample can be modeled as a one-dimensional forced spring-mass-damper system and the complex representations of the imposed force and the resulting displacement as a function of time can be expressed as follows

$$F(t) = F_{amp} e^{i\omega t} \tag{2.4}$$

$$d(t) = d_{amp} e^{i(\omega t - \phi)} \tag{2.5}$$

where d_{amp} is the resulting displacement amplitude. A schematic of the steady-state imposed force and displacement response are shown in Figures 2.17(a) and 2.17(b), respectively.

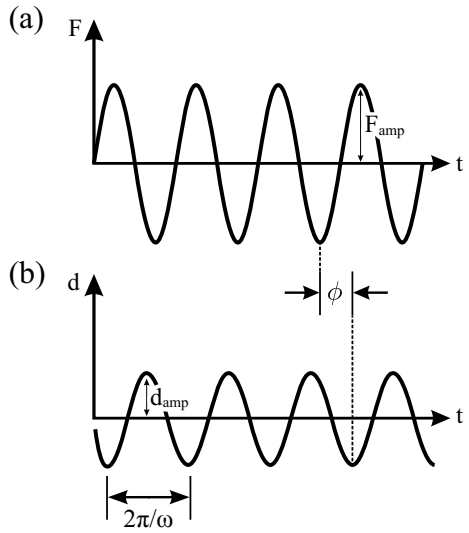

Figure 2.17: Schematic of the (a) dynamic force, and (b) dynamic displacement response as a function of time.

The resulting phase difference between the load and displacement response, ϕ, is shown schematically in Figure 2.18.

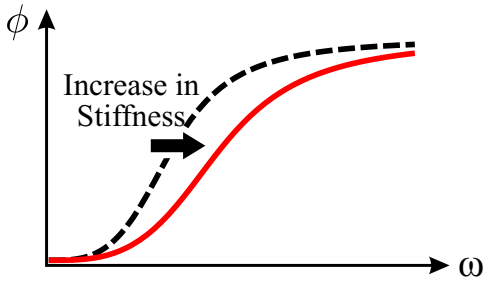

Figure 2.18: Schematic of the phase angle as a function of the driving frequency, ω for a driven harmonic osillator [172]. The dashed line represents the initial stiffness and the red solid line represents the final stiffness.

The resonance frequency coincides with a phase angle of 90° and a frequency equal to the natural frequency, $\omega_0 = \sqrt{k/m}$, where k and m are the system's effective stiffness and mass, respectively. At very high frequencies the damping effects cause the phase angle between the load and displacement to reach 180°. If the stiffness of the system were to increase (i.e., the natural frequency increases while the damping ratio decreases), the phase angle curve would move to the right. Likewise, a decrease in stiffness would move the

curve to the left. Since the curve at the natural frequency is steep, even a small change in stiffness would have a profound impact on the phase angle given that the driving frequency is held constant. Thus, near resonance, the phase angle of the system provides a very sensitive way to quantify changes in mechanical properties while applying a harmonic load.

On the other hand, to relate these dynamic signals to mechanical properties, the dynamic stiffness is used. The dynamic stiffness is defined as the real portion of the ratio between the applied load and the resulting displacement and takes the form:

$$S_{dyn} = \text{Real}\left[\frac{F(t)}{d(t)}\right] = \frac{F_{max}}{d_{max}}\cos\phi \tag{2.6}$$

Here, the cosine in equation (2.6) leads to a High sensitivity of the dynamic stiffness with respect to changes in the phase angle. If the system is driven near resonance, this results in maximum sensitivity to changes in the micro-sample's stiffness. The resonant frequency for the micro-beams in Chapter 3 was found to be in the range of 40 to 50 Hz. The maximum operating frequency is limited by how quickly the actuator can oscillate before damping effects become too restrictive to allow the target displacement amplitude to be reached. In practice, this limit is found to be approximately 300 Hz for a dynamic displacement of 10.5 μm (i.e., a velocity of ∼13 mm/s). It should be noted, however, that Nanomechanics reports a maximum actuator velocity of 130 mm/s.

In the context of this thesis, the term "dynamic stiffness" is used to refer to cyclic hardening or softening; however, this is somewhat of a misnomer. Stiffness, in the context of solid mechanics, is used to refer to the elastic region of a material's response to a load. In this thesis, dynamic stiffness is calculated by measuring the dynamic properties of materials undergoing cyclic loading. In a given cycle, there are both elastic and plastic contributions to the total

deformation. If the material were to harden, then a larger dynamic force would be required to maintain the same dynamic displacement and the dynamic stiffness would increase. Also, for a given dynamic displacement, cyclic hardening would decrease the area of the hysteresis loops and thus decrease the phase angle. From Equation 2.6 it clear that both of these changes would increase the dynamic stiffness for hardening or increases in elastic stiffness. The opposite would be true for softening or increases in elastic compliance. Thus, the term "dynamic stiffness" is used to describe changes in the flow stress as well as modulus in this thesis.

One other consideration for dynamic loading is the inertia of the actuator column. Since all of the load calculations assume equilibrium, they are not valid if inertia of the effective column mass is significant. This is not a concern for displacement controlled experiments (such as in Chapter 3) since only the displacement amplitude signal is used to calculate the strains. However, in Chapter 4, the load is needed to correct for the tip compliance. For a sinusoidal load, the magnitude of the maximum acceleration is given by $a_{amp} = \omega^2 d_{amp}$. Assuming high amplitude conditions, a_{amp} ~0.2-0.4 m/s^2 such as those used in Chapter 4, and given that the inertia term is ma_{amp} where the column mass is m =184 mg for the Nanomechanics InSEM. Accordingly, the inertia term will be less than 0.4 mN. Thus, this is considered negligible for this thesis.

The InSEM control unit utilizes a phase lock-in amplifier to extract the displacement signal at the driving frequency and filter out any unwanted noise corresponding to other frequencies. A fast Fourier transform (FFT) is performed on the filtered displacement signal over a period of time to determine the displacement amplitude along with the phase angle between the displacement and force signals. These dynamic parameters are continuously measured and recorded during dynamic loading. Thus, the dynamic stiffness can be continuously calculated from Equation (2.6). The period of time used for the FFT is termed the dynamic time constant. This value, similar to the displace-

ment time constant, is a measure of the temporal precision of the dynamic signals. A short dynamic time constant is useful for obtaining better temporal resolution. However, to limit noise in the dynamic signals, it is recommended that this value be set to at least 5 times the time period of one full loading cycle (i.e., $> 5 \times 2\pi/\omega$). Typical values for the dynamic time constant in this thesis are in the range of 20-100 ms.

Even though the phase lock-in amplifier is onboard the control unit, the PC still controls the dynamic amplitudes by continually updating the dynamic force at a control rate of 1 kHz. This configuration allows the system to perform these intensive FFT calculations but still receive control commands from the PC. Each fatigue method used in this thesis works by controlling the force amplitude, monitoring the resulting displacement amplitude, performing the necessary calculations (e.g., strain), and then updating the force amplitude accordingly. This is done in the form of a proportional control, where the error between the target displacement amplitude and the measured displacement amplitude are calculated at each control step. This error is then multiplied by a gain value, K_p. In the next control step, this product, $K_p(d_{target} - d_{amp})$ is added to the imposed force amplitude. This is shown mathematically in Equation 2.7. For a given control step, i, this equation is used to updated the force amplitude.

$$F_{amp}\left(t = \frac{i}{1000}\right) = K_p\left(d_{target} - d_{amp}\left(t = \frac{i-1}{1000}\right)\right) + F_{amp}\left(t = \frac{i-1}{1000}\right) \quad (2.7)$$

For cyclic loading experiments in this thesis, the value for K_p is tuned such that the target fatigue amplitude is reached within a few minutes. High gain values are avoided to prevent overshooting the target amplitude. Also, F_{amp} is initialized to zero at $t = 0$ for every experiment. For the fatigue work in this thesis, the vast majority of experiments are designed to control F_{amp} such that either the normal or shear strain on a slip system is maintained at a preset

value. This is done so that cyclic hardening does not significantly reduce the load amplitude and thus slow down the accumulation of damage in the fatigue samples.

Finally, there is an important distinction in terminology that must be paid attention to by anyone performing these cyclic loading experiments. For dynamic calculations in the InView software, the amplitudes are typically referred to as "Dynamic Force" and "Dynamic Displacement". These values are root mean squared (RMS) values, not amplitude values. To obtain the amplitude value of the force, the RMS value must be inserted into the equation: $F_{amp} = \sqrt{2}F_{RMS}$. Since the force amplitude is always a sine wave, this formula is always valid. For displacement amplitude, only if the displacement profile is a symmetric sinusoidal wave can the following equation be used: $d_{amp} = \sqrt{2}d_{RMS}$. If this is not the case, the general formula for the RMS displacement amplitude of a periodic signal can be used:

$$d_{RMS} = \sqrt{\frac{1}{2\pi}\int_0^{2\pi}[d(\tau)]^2 d\tau} \tag{2.8}$$

where $\tau = \omega t$.

2.3.3 Micro-probes

In order to manipulate the small-scale samples in this thesis, various types of micro-probes are required. Throughout this thesis, three different types of probes were used, two of which were custom fabricated. These probes are shown schematically in Figure 2.19.

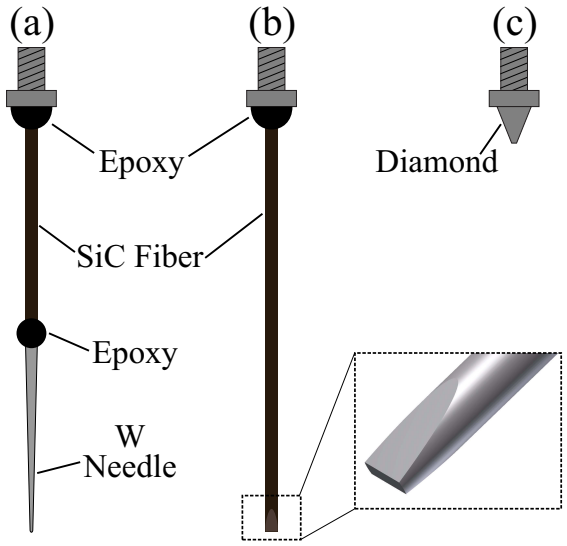

Figure 2.19: Schematic drawings of different microprobes used in this thesis: (a) Micro-beam probe used for bending fatigue in Chapter 3; (b) Hammerhead probe used for uniaxial fatigue in Chapter 4; (c) Flat-punch probe used for micro-compression in Chapter 5.

For probing micro-beams in Chapter 3, a sharp W needle tip (see Figure 2.19(a)) was used to apply a load to the free end. These tips were made using three basic components: an M0.8 threaded screw (Micro Star Tech IH-0340 holder), a SiC fiber, and a W needle. A hole was drilled into the threaded screw. A SiC fiber with a length of ∼1 cm, a diameter of 140 μm diameter, and a 30 μm diameter W core was inserted into the drilled hole. To adhere the SiC fiber, a bead of 5-minute epoxy mixed with graphite powder (for conductivity) was used. A tungsten Omniprobe micro-manipulation needle was used for the tip. The needle was blunted using metallurgical paper until the tip was approximately ∼20 μm in diameter. Then the needle was shortened to ∼5 mm in length using a low speed diamond wheel saw. The needle was then glued to the SiC fiber using 5-minute epoxy with graphite.

For probing the hammerhead micro-samples in Chapter 4, a long SiC fiber with a wedge-shaped geometry was used (see Figure 2.19(b)). The probe is made by mounting a 100 μm diameter SiC fiber with a W core onto an M0.8 threaded screw. Then, the tip of the probe was machined using a femtosecond

laser to give it a tapered profile, similar to that of a flathead screwdriver (see inset of Figure 2.19(b)). This probe geometry was designed so that the flat front can face the electron beam and thus provide a large area for the SEM glue to spread onto and cure.

The high aspect ratio of the micro-beam and hammerhead probes provide more lateral compliance as compared to the diamond probe. This is important for limiting the effects of tip friction where lateral constraints have been shown to influence the mechanical response and deformation morphology of micro-samples [173].

For micropillars compression studies in Chapter 5, a conductive diamond conical probe with a flat punch tip was used. Unlike the other custom-made probes, this probe was purchased from the company Synton. The tip exhibits a 13.5 μm diameter flat region. The relatively small flat region is preferable since larger probes would obstruct the electron beam view of the micropillar surface as it is being compressed.

2.3.4 SEM Glue

Many of the micro-fatigue experiments performed in this study were made possible by a novel polymer-based SEM glue developed by Kleindiek Nanotechnik [174]. The glue (SEMGlu^{TM}), allows the micro-probe to be adhered to micro-samples, thus allowing for fully reversible tension/compression loading while maintaining contact with the micro-sample.

Other small-scale experimental approaches to achieving fully reversed loading have incorporated double-sided sample grips [38, 175]. The downside of that method is that the probe loses contact with the sample when reversing the load each cycle. During high frequency loading, this loss of contact results in repeated impacts between the sample and the probe, which induces a more complicated stress state and greatly limits the number of cycles that can be

achieved. Also, this double-grip method has only been shown to be effective for bending fatigue.

Before curing, the SEMGlu^{TM} is a viscous resin. Upon imposing a focused, high intensity electron radiation on the glue, the monomer chains polymerize, thus, hardening the glue [174]. Another effect of electron irradiation is that the SEMGlu^{TM} spreads to increase its surface area.

The procedure for applying and curing the glue in the SEM is shown in Figure 2.20 for the case of gluing a W probe to a René-N5 micro-beam free end. Before handling the uncured SEM glue, the SEM is set to an accelerating voltage of 20 kV and a beam intensity of 3 (see Section 2.1.2). Then, the indenter tip is inserted into the SEMGlu^{TM}. This is done using the cradle extension and micro-positioning stage controllers (see Section 2.3.1). Note that image quality in Figure 2.20(a)-(f) is very noisy due to the low beam intensity to prevent premature glue curing. In practice, it is found that the best way to obtain a large amount of glue on the probe tip is to dip the tip into the glue using the extension controller and then move the y' micro-positioner in the negative direction to scoop up a large volume of glue (see Figure 2.14 for coordinate systems). Once the tip is wet with glue (see Figure 2.20(d)), the tip is lowered to be in contact with the end of the micro-beam resulting in a very small downwards deflection of no more than $\sim$2 μm (Figure 2.20(e)-(f)). For hammerhead gluing, the tip is lowered until contact is detected by observing a sudden change in the displacement reading ($<$1 μm). The SEM raster box is then positioned onto the glue and beam end (see Figure 2.20(g)) and the electron beam intensity is increased to cure and harden the SEMGlu^{TM} (see Figure 2.20(h)-(i)). This is done by ramping up the beam intensity; however, to prevent unwanted glue spreading (e.g., the glue covering the gage section of the sample), this is done a slow manner as follows. The beam intensity is incrementally increased until the first sign of spreading of the SEM glue. Once the spreading has stabilized and a few minutes have passed,

the beam intensity is once again increased. This process is repeated until a beam intensity of 20 is reached. The goal is for the glue cover the desired region and stabilize (i.e., stop spreading) at approximately the same time. In practice, it is found that higher scan speeds promote faster curing, while lower scan speeds promote faster spreading. For micro-beams, approximately 20 minutes is required after the glue stabilizes for the electron irradiation to fully cure the glue. For hammerhead micro-samples, at least an hour is needed for the glue to fully cure. A quasi-static loading cycle is performed on the micro-sample and if it does not exhibit any significant tension-compression asymmetry, the glue is considered to be hardened. It should also be noted that the SEM glue likely also contributes to the damping of the system; however, if the glue is fully hardened, this level of damping is assumed to be constant for the duration of a fatigue experiment.

For cantilever micro-beams in this thesis (see Figure 2.21), the high aspect ratio allows large stresses to be imposed on the fixed end without having to apply large loads that exceed the glue bond strength. For hammerhead micro-samples (see Figure 2.22), the wide hammerhead area allows for large stresses to be imposed on the relatively narrow gage section. For the W probe adhered to a micro-beam, a fully hardened SEMGlu^{TM} bond is typically able to carry a tensile load up to $\sim$3 mN before breaking. For the SiC hammerhead tip adhered to a hammerhead (see Section 2.3.3) tip is able to scoop up more glue due to its larger size. Also, the larger area provides more room for the glue to spread onto. After curing the glue is typically able to carry a tensile load up to $\sim$20-30 mN before breaking.

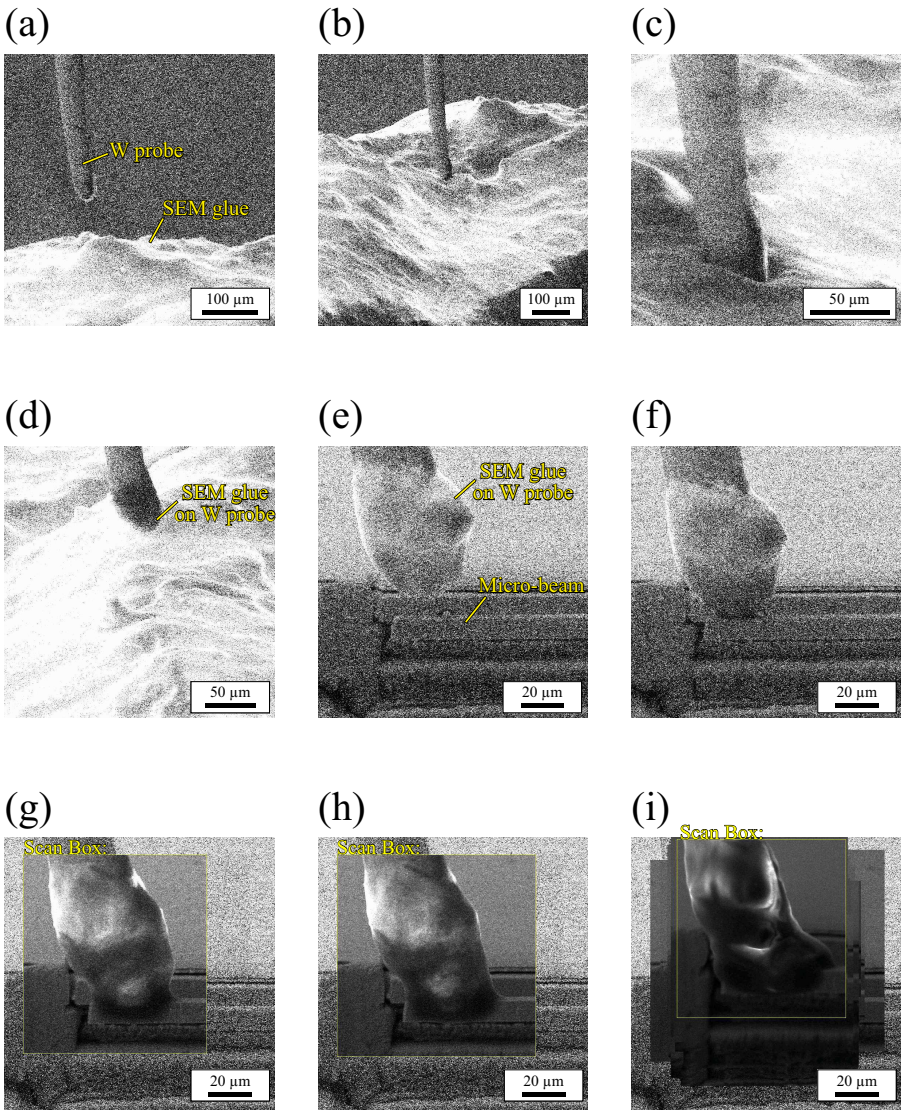

Figure 2.20: Sequence of steps for gluing the test probe to a micro-cantilever beam: (a)-(b) Test probe (W probe shown here) is lined up with the SEM glue. (c) Test probe is dipped into the glue, while the micro-positioner stage is moved in the lateral direction. (d) Test probe with the SEM glue on its tip. (e) Test probe is lined up with the cantilever micro-beam. (f) Test probe is placed in contact with micro-beam. (g)-(i) Using a smaller scan box, the beam intensity is ramped up to harden the SEM glue. Note how the glue spreads to cover a larger surface area as the beam intensity is increased.

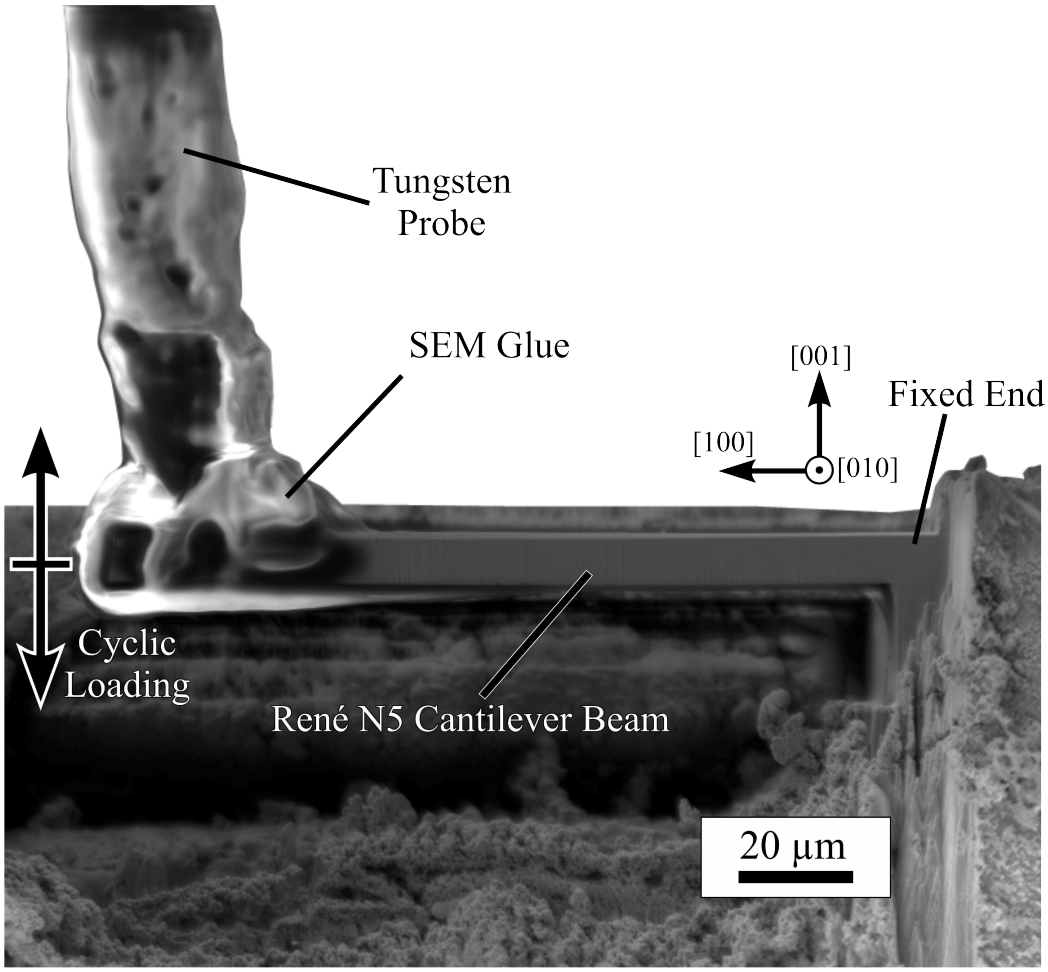

Figure 2.21: Micro-fatigue testing setup for René-N5 cantilever micro-beam tested in Chapter 3. SEM glue adheres the free end to a tungsten probe. Crystallographic coordinate system for the single crystal superalloy is denoted.

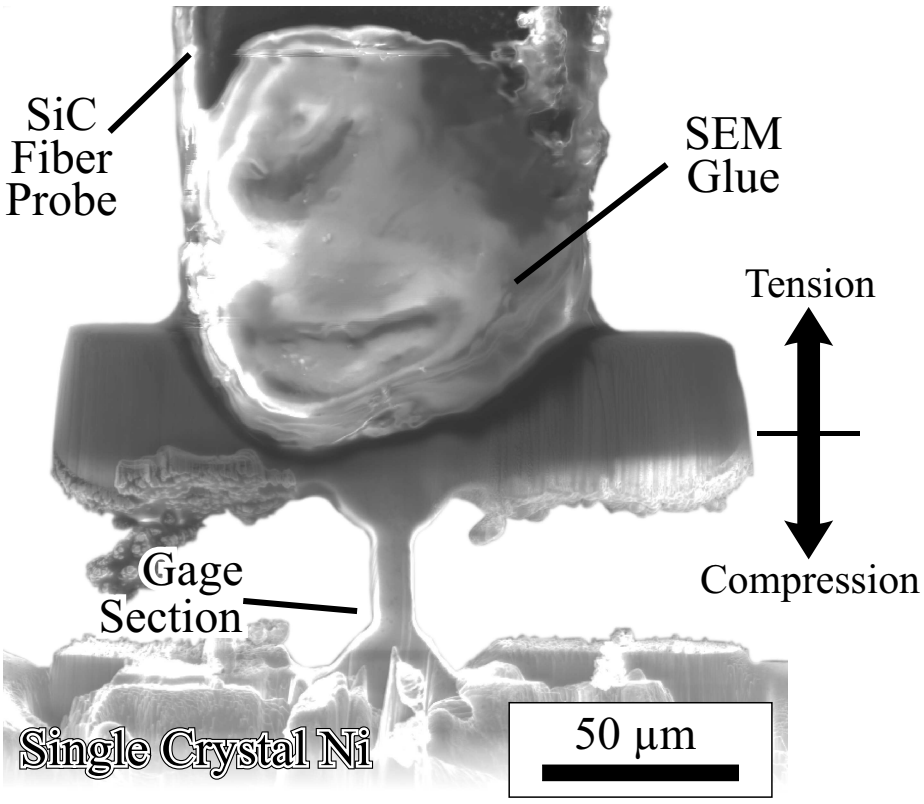

Figure 2.22: Ni hammerhead sample and the *in situ* micro-fatigue setup.

2.3.5 Strain Calculations

2.3.5.1 René-N5 Micro-beam Strain Amplitude Calculations

In Chapter 3, the strain amplitude is predicted using the ABAQUS finite element simulation software package (version 6.13) [176]. An elastic-plastic isotropic material model is assumed with elastic properties $E = 128$ GPa and $\nu = 0.28$ [153]. For all plastic material behavior, the stress-strain data are based on a 10 µm single crystal René-N5 micropillar compression experiment [154] to relate the strain deformation to stress values. The model geometries used for each beam were simple rectangular prisms with the dimensions adjusted to match the SEM-measured dimensions for each beam. The length of each beam is measured from the fixed end to the centroid of the indenter

tip. The boundary conditions imposed were a fixed boundary on one end of the rectangular prism and a vertical displacement boundary condition in the [001] direction on the opposite end. The vertical displacement is the maximum displacement imposed by the indenter (i.e., the displacement amplitude). The loading-end of the beam was not prescribed any displacement boundary conditions in the [100] or [010] directions to allow for rotational displacement at the tip. All stress and strain data reported are the effective values at the notch of the beam as computed from these simulations.

2.3.5.2 Nickel Hammerhead Shear Strain Calculations

In Chapter 4, the resolved shear strain amplitude on the primary slip system is controlled. The strain amplitude is as follows [4]:

$$\gamma_R = \frac{1}{\cos\phi_0}\left[\sqrt{\left(\frac{\ell}{\ell_0}\right)^2 - \sin^2\lambda_0} - \cos\lambda_0\right] \tag{2.9}$$

where ϕ_0 is the angle between the loading direction and the slip plane normal, λ_0 is the angle between the loading direction and the Burgers vector, ℓ_0 is the initial length of the sample, and ℓ is the maximum deformed length of the sample. The deformed length is simply $\ell = \ell_0 + d_{amp} - F_{amp}/k_{tip}$ where k_{tip} is the tip stiffness. The tip stiffness is measured before each test by compressing the bulk of the material near the sample to be tested. It is assumed that the compressive stiffness of the tip is equal to the tensile stiffness of the tip. It should be noted that due to experimental difficulties (e.g., misalignment and the quantification of glue compliance), the values obtained are approximate upper bounds of the resolved shear strain amplitudes.

2.4 Acoustic Emission Detection

Acoustic emission (AE) is a physical phenomenon where transient elastic stress waves propagate from a source in a solid material [177]. The sources are local regions of irreversible change within the material volume and can take the form of crack growth [178], dislocation motion [179, 180], phase transformations [181], and twinning [182], among others. Usually, an external stimulus of some sort, such as stress, is required to activate the AE source. When these stress waves reach the surface, they are characterized by a surface displacement. With very sensitive sensors, these AE waves can be detected in the form of a change in the electrical signal output [183]. The raw data obtained by AE detection is the variation of this signal with time. It should be noted that AE detection is not currently capable of quantifying the surface displacement. Rather AE detection is used to detect fast changes in a material's structure and obtain a signature (i.e., a waveform) for the event [184].

AE detection is a useful tool for non-destructive evaluation (NDE) of materials in structural applications [185]. Traditional AE for will monitor either the number of AE events per unit time, or simply the voltage amplitude of the AE signal [186]. Having established a baseline behavior for the structure, abnormal behavior can be identified before failure.

An AE response of a system is a not only a function of the physics within the material but is also highly sensitive to the AE setup conditions [187]. For example, sensor placement, sensor response, and material boundary conditions all play a role in the final detected AE signal. Thus, while AE detection can be useful to detect changes in a system, these are not directly comparable with the behavior of another AE system.

The following details an effort to incorporate such AE measurements with small-scale mechanical experiments. The results of this AE setup are discussed in Chapter 5 of this thesis.

2.4.1 Acoustic Sensors

AE sensors are transducer devices that convert elastic deformation into electrical voltage [183]. To accomplish this, these sensors incorporate either piezoelectric or ferroelectric ceramic. Piezoelectric transducers are most common; however, sensors that are also ferroelectric tend to provide a stronger electrical signal in response to deformation [188].

Due to the differences in size, mass, and material, each AE sensor exhibits a different response as a function of the driving frequency. For an ideal, single crystal transducer element, the response exhibits the highest sensitivity at the element's resonance frequency. For more complicated polycrystalline transducer elements, instead of a single resonance frequency, the frequency response is much more complicated. For example, the frequency response of the HD2WD sensor, used in Chapter 5, is shown in Figure 2.23. Clearly, the highest sensitivity is in the 0.3-1 MHz range, and the response is relatively uniform in this region. Towards the upper and lower frequency bounds of the sensors, sensitivity is dramatically reduced. Also, note the various peaks and valleys in the frequency response. These frequency response curves are very important in selecting a sensor for an AE application. In applications where the characteristic frequency range of interest is known *a priori*, it is desirable that the response of the sensor be uniform and highly sensitive in this range.

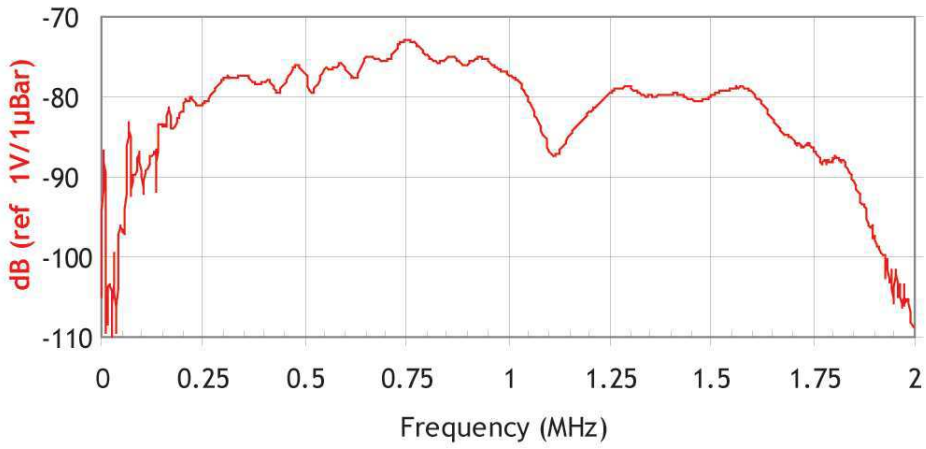

Figure 2.23: Frequency response of HD2WD AE sensor. Figure courtesy of Mistras.

The raw voltage detected by the sensors is very small. In order for the signal to be detectable, the sensor signal first goes through a preamplifier via a coaxial cable (see Figure 2.24). Here, the signal is amplified 60 dB before reaching the PCI-2 data acquisition board. The PCI-2 board is housed in a PC where it can be further analyzed.

Figure 2.24: AE Connection Diagram.

One important note is that these coaxial connections should be through high quality cables; otherwise, deleterious effects such as signal attenuation and electrical noise may be observed.

2.4.2 Acoustic Interface with *in situ* Experiments

To adapt the AE detection technique to the small-scale experimental methods outlined in Section 2.1, various modifications had to be made. This experimental setup is unique from most typical AE applications since the deformation being sensed is at a very localized region of the material. Also, the

loads applied in these experiments are very small (<50 mN). In conventional AE, there is usually a large stimulus and various AE sources active at any given point in time. With this in mind, the primary concern was mounting the sensor as close as possible to the micro-sample and to limit attenuation. It was decided to mount the AE sensor directly under the sample material to provide a direct path for the stress waves to travel. Thus, the experiment is designed such that the micro-sample, located on the material surface, is loaded and emits stress waves radially. The stress waves travel through the bulk of the material and then cross the interface to the sensor where they are detected.

A crucial step in improving reducing attenuation between the sample and AE sensor was the method used to couple these two components. Adhesives such as super glue were found to be undesirable for sample mounting since they were found to emit a low level of continuous AE noise. Therefore, a special ring clamp was designed (see Figure 2.25). The clamp applies pressure between the sample and AE sensor. This holds the sensor in place and holds the sample in direct contact with the sensor. Note that the sample is held in the ring portion of the clamp using a set screw. The base of the clamp is a plate that screws into the InSEM cradle (detailed in Section 2.3.1).

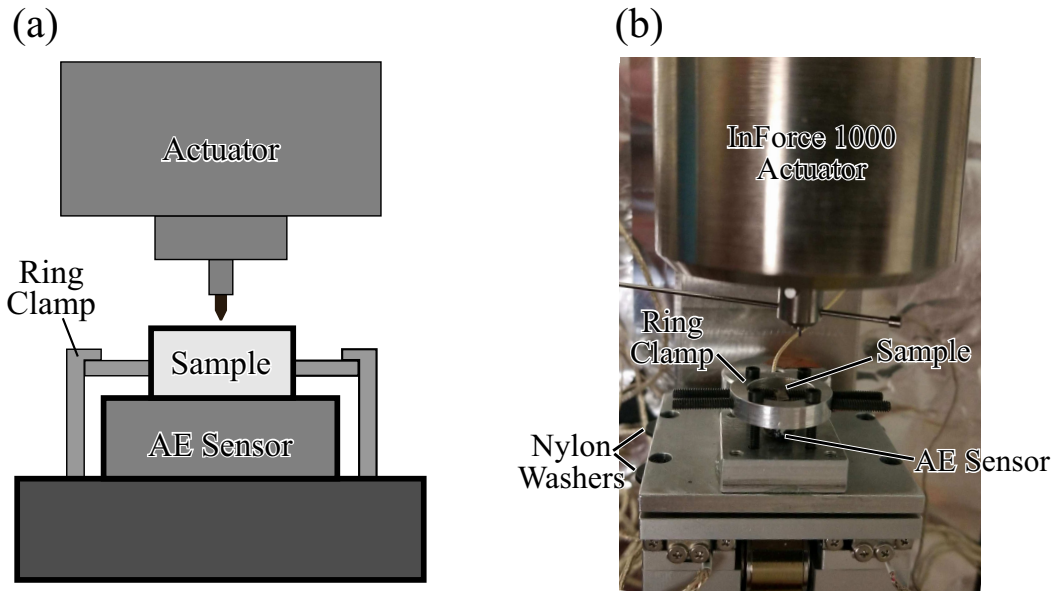

Figure 2.25: (a) Schematic and (b) photograph of the InSEM setup for an AE experiment The AE sensor is mounted under the sample and is held in place using a ring clamp.

Another experimental challenge faced in adapting this methodology to the InSEM was reducing electrical noise. In practice, it was found that if there was a conductive path between the AE sensor and the SEM ground, this resulted in an increase in AE noise detected. To reduce this, insulating material had to be used to prevent any contact with the SEM ground. For example, nylon screws and washers, a shown in Figure 2.25, were used as spacers between the sample plate and the InSEM cradle. Also, the vacuum port used to channel the coaxial cables from the sensor was shielded so that the SEM chamber wall did not make electrical contact with the connection. Finally, all metal contacts of the cables were shielded with electrical tape. Doing this resulted in a reduction in electrical noise.

2.4.3 Acoustic Data Acquisition and Filters

The raw AE voltage signal is acquired on the PCI-2 data acquisition board. The board features a very high data acquisition rate (20 MHz), and thus

has outstanding temporal resolution that is 4 orders higher than the InSEM system. While this high resolution is useful, continuous storage of this data would result in large and intractable file sizes. Traditional AE combats this by using a thresholding scheme. This scheme stores AE data in the form of short intervals of data known as hits. The beginning of a hit is triggered by the amplitude reaching a set threshold. The amplitude is defined in decibels using the logarithmic relation:

$$A_{dB} = 20 \log_{10} \left(\frac{V_{max}}{V_{min}} \right) - P \tag{2.10}$$

where V_{max} is the peak voltage of a hit, V_{min} is a minimum detectable voltage (1 μV for all AE in this thesis), and P is the amount of gain set for the analog preamplifier. The value of P must match that manually set gain to obtain a corrected amplitude value. Three other timing parameters also define the hit data: peak definition time (PDT), hit definition time (HDT), and hit lockout time (HLT). PDT is the amount of time after a local maximum that the system will wait before labeling this as the peak of the hit. If a greater local maximum is found during the PDT, this local maximum is newly labeled the peak and the peak timer starts again. The HDT is the amount of time after a threshold crossing that they system will wait before labeling a hit as having ended. If a threshold crossing occurs during the HDT, the timer is restarted once again. The HLT defines the minimum time that must pass after the end of a hit before the system can start a new hit. From a hit, various features can be obtained, as will be discussed in the next section; however, the raw waveform can be stored as well. The waveform is simply voltage versus time data during the defined hit. For waveform acquisition, an amount of time preceding a waveform can be stored by defining a pre-trigger time.

When acquiring data, one other setting that the user can define are frequency ranges. These are done by applying either a digital filter, an analog

filter, or both. Frequency filters can be useful to attenuate frequency ranges that are not of interest, as well as to limit the effect of room and electrical noise. Most room noises have a characteristic frequency <100 kHz whereas physical deformation events are typically >100 kHz. Therefore, it is often desirable to use a high pass filter to reduce these low frequency signals. One final note regarding frequencies: the data acquisition rate should be set at least twice the highest waveform frequency (i.e., the Nyquist frequency) to avoid waveform aliasing.

2.4.4 Waveform Feature Extraction

Even with the thresholding scheme outlined in the previous section, the waveform data of hits is not particularly useful in its raw format. If is desirable to reduce the dataset of voltage versus time values to waveform features for each hit. These features allow for physical interpretation of the AE data. Additionally, these features can be used to cluster, classify, and filter hits using data analytics techniques. These features can be extracted from the voltage versus time data (as shown in Figure 2.26(a)) or from the spectral data by performing a fast Fourier transform (FFT) (see Figure 2.26)(b)).

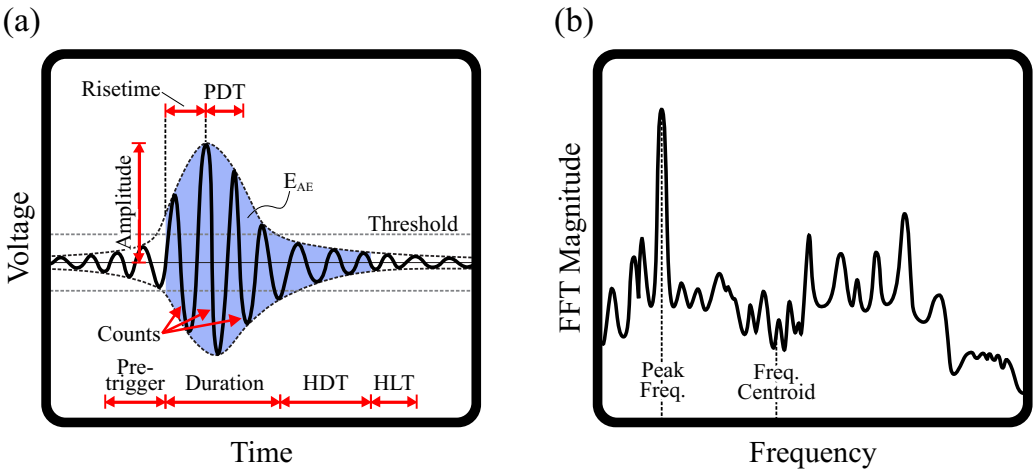

Figure 2.26: Schematic of (a) temporal waveforms and (b) spectral FFT of an AE hit event. Typical features of interest are denoted. Also, hit timing parameters (PDT, HDT, and HLT) are also denoted.

Conventional AE standards [189] specify specific definitions for these features. Amplitude, as previously defined in Equation 2.10, is related to the peak voltage amplitude of a hit. The duration of a hit is time between the first and last threshold crossing. Counts are the number of times the waveform crosses the threshold in one hit. The risetime is the time from the first threshold crossing to the peak voltage amplitude. To obtain a signature for the energy detected by an AE event, various definitions are available. The energy, E_{AE}, is simply the area under the rectified voltage signal during the hit. For this calculation, the final value is reported as an integer and is dependent on an energy reference gain value. Signal strength (S) is calculated in the same way, however, it is scaled to have volt-second units. Alternatively, for an energy in physical units (aJ), the absolute energy is defined as the electrical energy during a waveform:

$$E_{ABS} = \frac{1}{R}\int_{t_0}^{t_f} V^2(t)dt \tag{2.11}$$

where R is a known resistance value. Note that E_{ABS} is obtained by integrating over the length of a waveform while E_{AE} is only during the duration of a hit. These temporal features are typically calculated in real time during data acquisition, depending on pre-test configurations.

For the spectral data, the peaks and values are much more erratic and difficult to characterize. Simple calculations, such as the frequency with the highest FFT magnitude (peak frequency) and the frequency centroid of the FFT can be readily obtained. One common technique for extracting features from the FFT is to define partial power frequency ranges. The power spectrum of the FFT is summed for each partial power range. This provides a way to characterize the frequency distribution of each hit with relatively few features.

2.4.5 Correlation between AE and Micro-actuator Data

One unique aspect of the *in situ* AE micro-mechanical experiments designed in this thesis is the one-to-one correlation of discrete deformation events with AE hits. In bulk-scale AE, this type of analysis is not possible since many deformation events occur at the same time and at various locations in the material. Small-scale allows for interrogation of a localized region such that these events each happen one at a time. For example, in monotonic small-scale testing, intermittent motion of dislocation ensembles is known as strain bursts. As will be shown in Chapter 5, these strain bursts can be identified from micro-actuator velocity data. The strength of the methodology shown here is the ability to associate each individual AE hit with a strain burst event.

The AE system and micro-actuator have their own control units with proprietary data formats. Therefore, one of the challenges in this thesis has been to synchronize the two data sources. This was accomplished by pinging each control unit with a common external stimulus. However, for some experiments in Chapter 5, there is up to 3 seconds of delay between the two datasets which is corrected using the following post-processing procedure. First, the AE time intervals and micro-actuator strain burst time intervals (details in Section 2.5) are determined. Then, a square wave signal is generated for both the AE and micro-actuator event data using a simple one-hot convention. If an event is occurring at a given time value, the associated signal is one, otherwise it is zero. Then, a discrete convolution is applied as [190]:

$$y[n] = \sum_{k=-\infty}^{\infty} f[k]g[n-k] \tag{2.12}$$

Here, f denotes the micro-actuator one-hot signal and g denotes the AE one-hot signal. A peak in this convolution indicates good overlap between the two signals at an optimal n. The time difference associate with this value of n is used as the time lag correction. This value is no more than 3 seconds for all

experiments in Chapter 5.

Since the data acquisition rate for the AE system is 4 orders of magnitude higher than that for the micro-actuator, several AE events may occur during the time for one strain burst. Therefore, sometimes one strain burst event is correlated with multiple AE hits. Since the energy calculations are integrated over a time interval, all AE energy values are added for a strain burst event that is correlated with multiple hits.

2.4.6 AE Event Classification and Noise Filtering

Assuming that the timing parameters are well-defined, each hit should correspond to a physical AE event. Ideally, the AE signature of each event can be used to determine the physical mechanism (e.g., plasticity or fracture) of the source. Additionally, similar analysis can be used to distinguish AE signals of interest from noise signals. This is done by establishing a baseline for each test where the test conditions are replicated as closely as possible, except no loading is applied. Comparing this dataset to the experiment dataset provides a way to filter noise that is common to both the experiment and the baseline.

In dealing with large hit/feature datasets, it is not always practical to manually determine the feature criteria for classifying hits. For this, there are various preprocessing techniques to reduce dimensionality (e.g., principal component analysis) as well as classification techniques (e.g., support vector machines) to categorize each hit. For the present thesis, however, the number of hits is relatively manageable since the source of AE is very localized.

2.5 Burst Data Analysis

In Chapters 4 and 5, intermittent events (crack growth and plasticity) are obtained using the following thresholding procedure.

In Chapter 4, a low-pass Wiener filter was applied to get rid of noise in the displacement amplitude signal. A filter window size of 47.1 seconds was found to be optimal. This window region is used for obtaining local mean and standard deviation information.

With the filtered displacement amplitude signal, a running linear regression was performed to obtain a numerical approximation for the time derivative. A running 0.714 second interval of data was curve-fit to a line and the resulting slope was stored as the time derivative at each time step. To account for local variations in time derivative, a running average with a window size of 143 seconds was subtracted from the time derivative data.

Burst events were identified by determining local increases in the local time derivative of the dynamic displacement. This was done using a threshold-based analysis. Anytime the local time derivative of the dynamic displacement exceeded the threshold, an event was said to have started. Once the derivative went back below the set threshold, this was considered the end of the event. The difference in displacement amplitude between the start and end of each event comprised the burst dataset used in subsequent analysis.

Curve-fitting of the burst data was performed using the powerlaw Python package [191]. Specific mathematical details about the curve-fitting method can be found elsewhere [192]. In summary, the method binned the burst size data using an optimized logarithmic binning scheme and then curve-fit the data to a power-law. The power-law fitting was determined using a maximum likelihood estimator (MLE) and the following probability distribution function:

$$p(x) = Cx^{-\alpha} \tag{2.13}$$

where C and α are constants. Since C can be determined trivially from the normalization condition, α is the only fitting parameter of interest.

The only hyperparameter for the curve-fitting was the lower bound cutoff

for data used in the fitting process, x_{min}. The x_{min} hyperparameter was varied while both the standard error (SE) and the resulting goodness-of-fit parameter (D) were minimized. The standard error was defined as the width of the likelihood maximum [192]. The goodness-of-fit statistic, D, was the maximum distance between the cumulative distribution function of the data above x_{min} and the CDF for the best-fitting power-law in this region [192]. This parameter, D, is referred to as the Kolmogorov-Smirnov statistic. The final result of this analysis, is a power-law exponent, α.

Chapter 3

High frequency *in situ* fatigue response of René-N5 micro-beams

3.1 Introduction

A fundamental understanding of fatigue mechanisms is essential to predict the usable life of engineering components in aerospace applications. The fatigue life of turbine engine components, for instance, has a major influence on the cost of maintaining an aircraft fleet. The turbine blades experience low cycle thermomechanical fatigue loading from their start-up/shut-down cycles. High cycle fatigue is also induced on turbine blades via smaller vibrational loads. To maximize the fatigue and creep resistance of these integral components, turbine blades in modern jet engines are fabricated from predominately single crystal Ni-base superalloys [193].

The fatigue behavior of Ni-base superalloys has been well-characterized at both room temperature and high temperature testing conditions [194, 195,

Some parts of this chapter were published in Acta Materialia by S. Lavenstein et al. [149].

196]. Fatigue cracks in these superalloy blades have been found to initiate both at the leading edge of the blade and in the attachment region [197, 198]. Superalloys, with their characteristic $\gamma - \gamma'$ microstructures, have been shown to exhibit both cyclic hardening and cyclic softening in fatigue [194]. At room temperature the cyclic hardening is attributed to an increase in the density of slip bands [199], while cyclic softening has been attributed to the dissolution, disordering, and the shearing of γ' precipitates [194, 195].

While conventional bulk scale fatigue tests provide a way to quantify the fatigue life of materials, specific microstructural features that result in failure are difficult to ascertain. This motivates researchers to investigate the underlying mechanisms of fatigue failure as opposed to taking a stochastic approach in predicting the fatigue life of engineering components. One approach to accomplish this is to cyclically test small volumes of materials. Small material dimensions allow for a more fundamental investigation of the microstructural features that contribute to fatigue failures.

Further motivation for micro-scale fatigue testing is to characterize crack growth in ductile materials. Such findings can be used to investigate the rate of crack growth at various crack length scales. Stable crack propagation experiments have proven to be difficult for several reasons. First, notches made using conventional microfabrication methods are generally not atomically sharp and have a large plastic zone in ductile materials. Blunting effects inhibit the crack growth and promote yielding behavior at notch tips. Second, inertial effects from large strain bursts make it difficult to control the strain on the sample once a crack initiates which often results in catastrophic fracture.

Several studies have made progress in the field of micro-scale fatigue testing [200, 201, 38, 175, 202, 203]. Schwaiger and Kraft performed a fatigue study on thin Ag films on SiO_2 substrates [201]. Cantilever micro-beams were fabricated using a combination of sputter deposition and photolithography. The micro-beams were then tested by imposing a sinusoidal load superimposed over a

mean load. This methodology was unique in its utilization of the continuous stiffness measurement (CSM) method built into many nanoindenter systems. However, with this experimental methodology it was not possible to maintain a zero mean stress and the experiments were limited to film-substrate sample geometries.

More recently, Kiener et. al. performed *in situ* low cycle fatigue experiments in a scanning electron microscope (SEM) on micro-beams under bending [38]. In this approach, fully reversed loading (i.e., zero mean stress) was achieved using a custom-made W indenter probe. The probe was able to push and pull on the micro-beam loading end but in between half-cycles the grip would lose contact with the specimen. The method was able to reveal deformation mechanisms during fatigue; however, it was unable to exceed 100 cycles. Kirchlechner et. al. have also performed *in situ* micro-beam bending while performing Laue diffraction to characterize the dislocation motion during fatigue; however, they were also limited to cycle counts on the order of $\sim$10 [175].

Some researchers have taken the approach of performing *in situ* microscale uniaxial fatigue experiments [202, 203]. These experiments have exhibited differences in hardening/softening behavior when compared to their monotonic loading behavior. Possible explanations for this behavior include friction between the testing tip and the sample or perhaps the lateral stiffness of the loading frame. High load frame stiffness perpendicular to the loading direction has been shown to cause lattice rotation and thus alter the active slip systems. This effect has been mitigated using high aspect ratio fibers to attach the testing tip to the load frame of the test setup [203, 204]. This also helps to reduce the effects of misalignment. These small-scale cyclic loading studies are significant because they allow a fundamental and deterministic way to identify fatigue mechanisms. Also, they are necessary for the validation of physics-based fatigue simulations that are limited to small volumes of material

[205, 206].

Investigations of fatigued materials have found that crack initiation is most commonly observed at high-angle grain boundaries, twin boundaries, and alongside surface extrusions (i.e., intrusions) [207, 208, 209]. Thin film fatigue studies have found that for larger film thicknesses ($\geq$3 μm) the dominant mechanism for crack initiation is surface intrusions [210, 211]. When the film thickness is decreased to the submicron level, cracks are almost exclusively found at twin boundaries and grain boundaries. It is argued that for submicron film thicknesses, size-effects inhibit the ability of the microcrystals to accumulate plasticity. Less plasticity means less dislocation dipole annihilation which is believed to lead to surface extrusions/intrusions [212]. Also, void formation at the interface between the film and substrate has been found to be a major contributor to crack initiation [213]. Despite the breadth of studies carried out, there is still relatively little known about crack initiation, and further small-volume studies are necessary to elucidate the mechanisms that lead to crack initiation.

The motivation of the work in this chapter is to characterize plasticity, crack initiation, and fatigue life of single-crystal, Ni-base superalloy René-N5 cantilever micro-beams. In that attempt, an *in situ* SEM methodology is developed that uses high frequency actuator dynamics built into a nanoindenter to apply a cyclic load at high frequencies. The novel experimental procedure was outlined in detail in Chapter 2, Section 2.1. Micro-beams were fabricated such that the <100> directions of the crystal were normal to each face of the beam (see Figure 2.21). The approximate dimensions of each beam were $8.5 \times 8.5 \times 125$ μm^3. The experimental results showing the effect of the imposed strain amplitude on the fatigue life and deformation mechanisms are examined in Section 3.2. In Section 3.3 further insights regarding the deformation mechanisms and the fracture surface morphology are discussed. Finally, a summary and concluding remarks are made in Section 3.4.

3.2 Results

3.2.1 Fatigue Life

For all fatigue tests performed here, failure is defined as the point at which the micro-beam completely fractures from the fixed end. The cycles to failure as a function of the maximum strain amplitude at the notch from all samples tested are summarized in Figure 3.1. The results are also fitted to a Coffin-Manson power law [214]:

$$\frac{\Delta\varepsilon}{2} = \frac{\sigma_f}{E}(2N_f)^b + \varepsilon_f(2N_f)^c \tag{3.1}$$

with a fatigue ductility coefficient $\varepsilon_f = 1.02$, a fatigue ductility exponent $c = -0.688$, a fatigue strength coefficient $\sigma_f = 2.09$ GPa, and an Basquin exponent $b = -0.067$. The predicted fatigue ductility exponent from the current experiments is within the range of values typically reported for metals ($-0.5 \leq c \leq -0.7$).

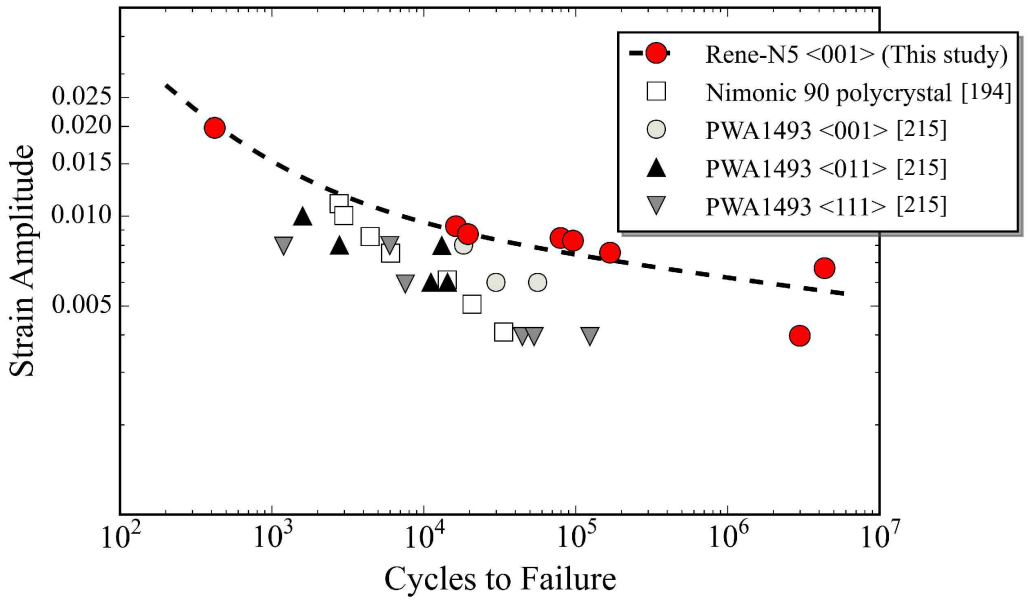

Figure 3.1: Cycles to failure as predicted from the current experiments for René-N5 micro-beams having a [100] orientation along the beam length. The dashed line represents the Coffin-Manson power law curve-fit to the data. Room temperature fatigue life results from other studies are also shown [194, 215].

In addition, the fatigue life measured for different bulk Ni-based single crystal superalloys during uniaxial fatigue experiments [194, 215] are also shown in Figure 3.1 for comparison. It should be noted that the stress concentration at the fixed end of the beam in the current study plays a big role in determining the fatigue life of the micro-beams. These types of stress localizations are not present in uniaxial bulk fatigue tests, and as such, comparisons with the bulk results can only be made in a qualitative manner. Nevertheless, even with the stress concentration in the present study, the micro-beams show an increase in the overall fatigue life when compared to bulk specimens, which can be attributed to sample size effects. This size effect has also been observed in small-scale fatigue tests of wire specimens [216]. Khatibi et. al. observed a Hall-Petch like behavior in varying the diameter of fatigue wire specimens [217]. Although there are various mechanisms used to explain the size effect, it is well established that metals having micro-scale dimensions are stronger. This would mean that for a given strain amplitude, there is a reduction in plastic strain for such micron-scale metals, as compared to their bulk counterparts. Since plastic strain is strongly correlated to fatigue life, this would indicate that smaller sizes should yield longer fatigue life. Another possible explanation is that these smaller volumes sample a fewer number of processing and fabrication defects as compared to bulk. With fewer defects to promote crack initiation, longer overall fatigue lifetimes would be expected.

It should also be noted that in the high cycle fatigue regime there is more scatter than that observed in the low cycle fatigue regime, althought the number of samples, 2, is very small. This can perhaps be attributed to the fact that in the high cycle regime the sample life is significantly affected by preexisting defects (e.g. casting defects, surface roughness, etc.) in the sample [218]. In microcrystal testing, the spacing between defects is expected to be larger than the sample size. Thus, a statistical approach with a larger number of test samples is required to characterize the fatigue life of micro-scale specimens in

the high cycle and ultra-high cycle regime.

3.2.2 Large Cyclic Strain Amplitude Response

Figure 3.2(a) shows the dynamic stiffness for a fatigue test conducted at a strain amplitude of 9.26×10^{-3}. During the experiment the evolution of the surface morphology near the micro-beam's fixed end is continually monitored and the SEM micrographs during testing at different cycle numbers of this test are shown in Figure 3.3. A movie of this experiment is also available online (https://www.youtube.com/watch?v=4gD8UdWwJbo). These results are representative for all tested samples at a strain amplitude larger than 7×10^{-3}.

As clearly observed from the insert in Figure 3.2(a), a periodic oscillatory noise is superimposed on a mean dynamic stiffness value. The phase angle does not exhibit this behavior. The oscillatory noise occurs predominantly due to small overshoots of the target displacement amplitude, where the control loop for the load amplitude never settles on a constant value but rather oscillates about the required load amplitude for the entirety of the fatigue test. This noise, although very small, becomes amplified in the calculated dynamic stiffness since the vibrational frequency is very close to resonance. For this reason, a moving average with a time constant of 4 seconds (equivalent to 200 data points) is used to smooth the dynamic stiffness curves. This is achieved by using a discrete convolution algorithm on the raw dynamic stiffness curves. The result of this procedure is shown in Figure 3.2(b). By comparing Figures 3.2(a) and 3.2(b) it is clear that all trends are directly captured after the smoothing step.

It is also important to note that at the beginning of the test, there is a temporary spike in the dynamic stiffness due to the transient nature of the damped harmonic oscillators. This transient behavior typically decays quickly

within ∼10-20 seconds.

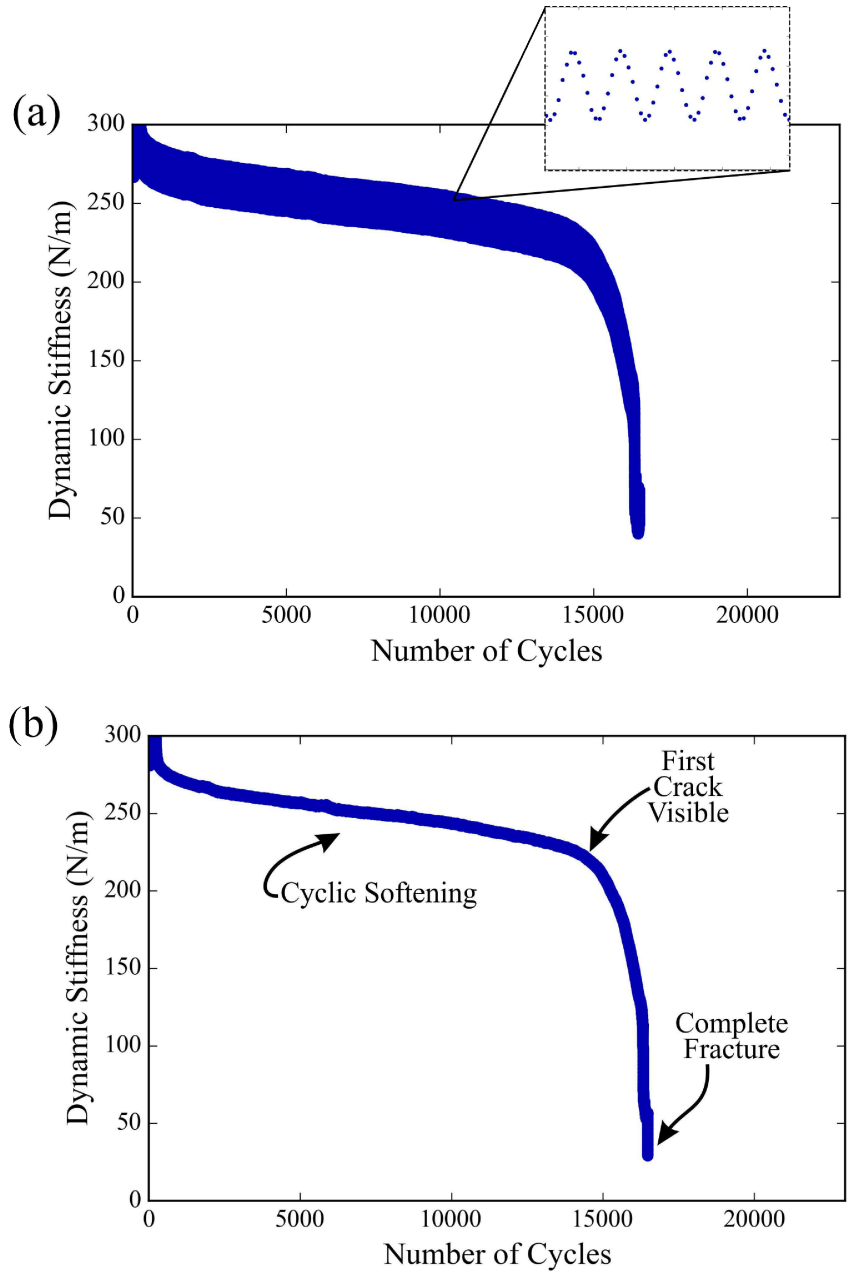

Figure 3.2: (a) The dynamic stiffness versus number of cycles for a strain amplitude of 9.26×10^{-3}. (b) The results in (a) with a 4 second running average cleanup applied.

Figure 3.2(b) indicates that for the majority of the fatigue life of the micro-beam, the dynamic stiffness gradually decays as the number of cycles increases. This is an indication of cyclic softening occurring in the sample. Towards

the end of the life of the micro-beam (i.e., after ∼14,620 cycles), a dramatic decrease in the dynamic stiffness is observed.

From the surface morphology images as a function of number of cycles it is observed that early on during the deformation visible extrusions form on the top and bottom edges of the micro-beam as shown in Figure 3.3(a) after 6,840 cycles. Slip trace analysis indicates that these extrusions coincide with {111} slip planes. As the number of cycles increases, more extrusions are formed and become longer and more pronounced (Figure 3.3(b)). After 14,620 cycles the first stages of crack nucleation become visible at the lower corner of the fixed end (Figure 3.3(c)). This lower corner is a preferred site for crack nucleation due to the stress concentration at this point. Once the crack nucleates the dynamic stiffness is observed to dramatically decrease as observed in Figure 3.2(b) as the crack propagates along the width of the beam until it spans the entire width resulting in complete fracture at the fixed end (see Figure 3.3(d)-(f)). The dramatic decrease in the dynamic stiffness observed during the crack propagation stage is mostly due to the dramatic decrease in the cross-sectional area at the fixed end of the micro-beam. It is interesting to note that from the first observable crack nucleation event to complete fracture spans a total of $1,680$ loading cycles, which is ∼10% of the micro-beam's life.

3.2.3 Small Cyclic Strain Amplitude Response

The dynamic stiffness versus cycle number for a micro-beam cyclically deformed with a strain amplitude of 6.7×10^{-3} is shown in Figure 3.4(a). This is representative for samples cyclically deformed at a strain amplitude less than 7×10^{-3}. Unlike the response under larger cyclic strain amplitudes, the dynamic stiffness exhibits a gradual increase by 45% with increasing number of cycles. This indicates cyclic hardening in the micro-beam. After the onset of crack initiation ($\sim 3.95 \times 10^6$ cycles) the dynamic stiffness decreases gradu-

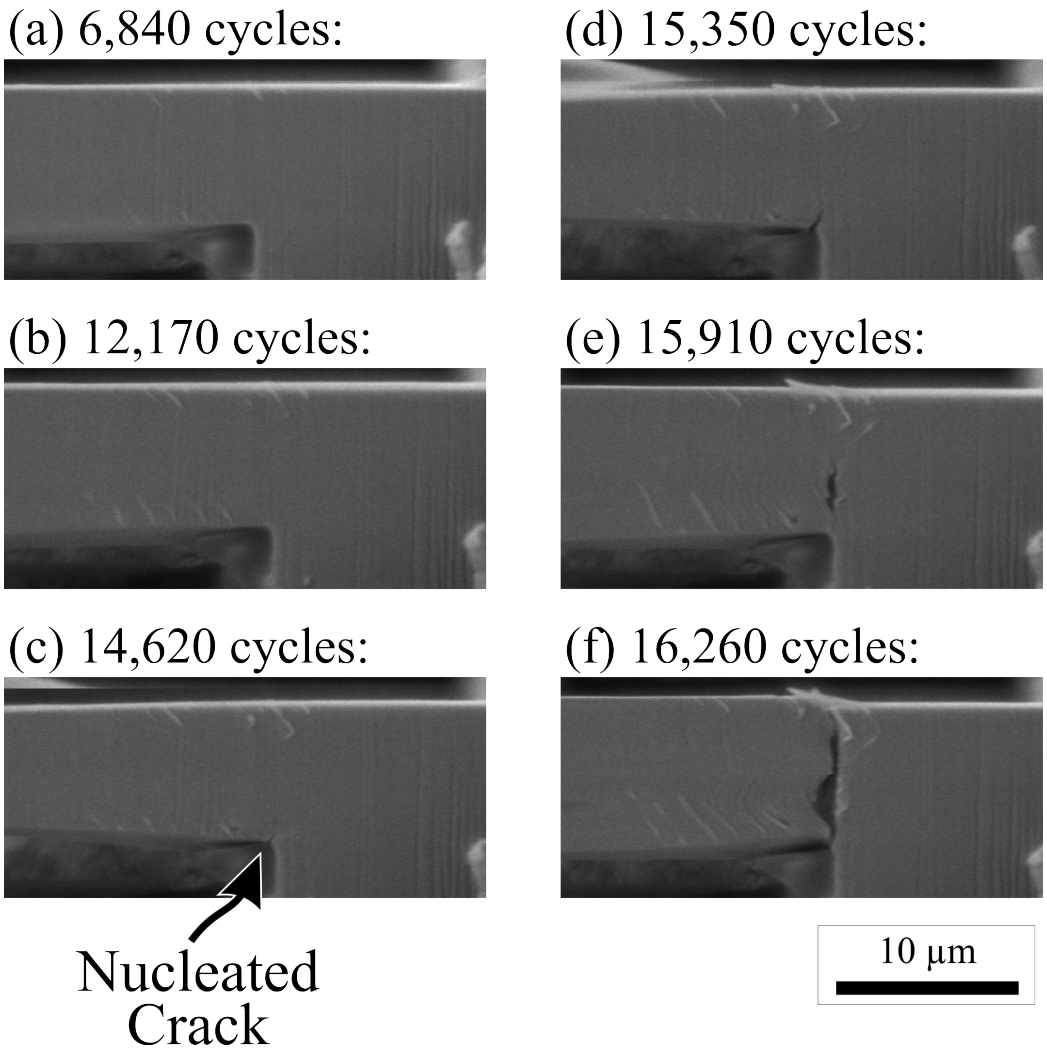

Figure 3.3: SEM micrographs of the surface morphology near the fixed end of a cyclically loaded micro-beam with a strain amplitude of 9.26×10^{-3}. Note that the distortion in the images is due to the high-frequency motion of the beam tip.

ally over the next 2.28×10^5 cycles. When the crack reaches a critical length, steady crack propagation commences and the dynamic stiffness dramatically decreases. The dynamic stiffness during the last 1.35×10^5 cycles is shown in Figure 3.4(b) with the inflection points denoted in the dynamic stiffness curves indicating two regimes with different rates of decrease after crack initiation. The first regime represents the nascent stages of crack growth, which corresponds to short-crack growth. In this regime the rate of decrease in the dynamic stiffness is relatively small since the crack growth rate is relatively slow. Once the crack reaches a critical size, the rate of decrease in dynamic stiffness increases significantly, which corresponds to a faster crack growth rate. The transition from a short-crack to a large crack response is predicted from an experiment with a strain amplitude of 4×10^{-3} to commence when the crack length is $\sim$18% of the micro-beam width.

In addition, two discontinuities are observed in Figure 3.4(a) and can be explained as follows. The first discontinuity after $\sim1.6\times10^6$ cycles is a result of an adjustment of the driving frequency from 40 Hz to 45 Hz to account for the change in the resonance frequency of the system due to the drastic cyclic hardening. This guarantees that the phase angle is always close to 90°, which leads to maximum sensitivity to changes in the micro-beam's stiffness. A higher driving frequency results in higher velocities, and thus higher damping effects, which explains the jump in the dynamic stiffness. On the other hand, a second small discontinuity is observed after $\sim2.8\times10^6$ cycles; this is commonly observed whenever the experiment is stopped then restarted at the same driving frequency. Due to the transient nature of damped harmonic oscillators, it generally takes several minutes to recover steady state behavior; however, sometimes there are small jumps in dynamic values between tests. It is not entirely clear why this happens or what circumstances lead to this initial discrepancy. Nevertheless, after a short period the overall shape of the dynamic stiffness is recovered.

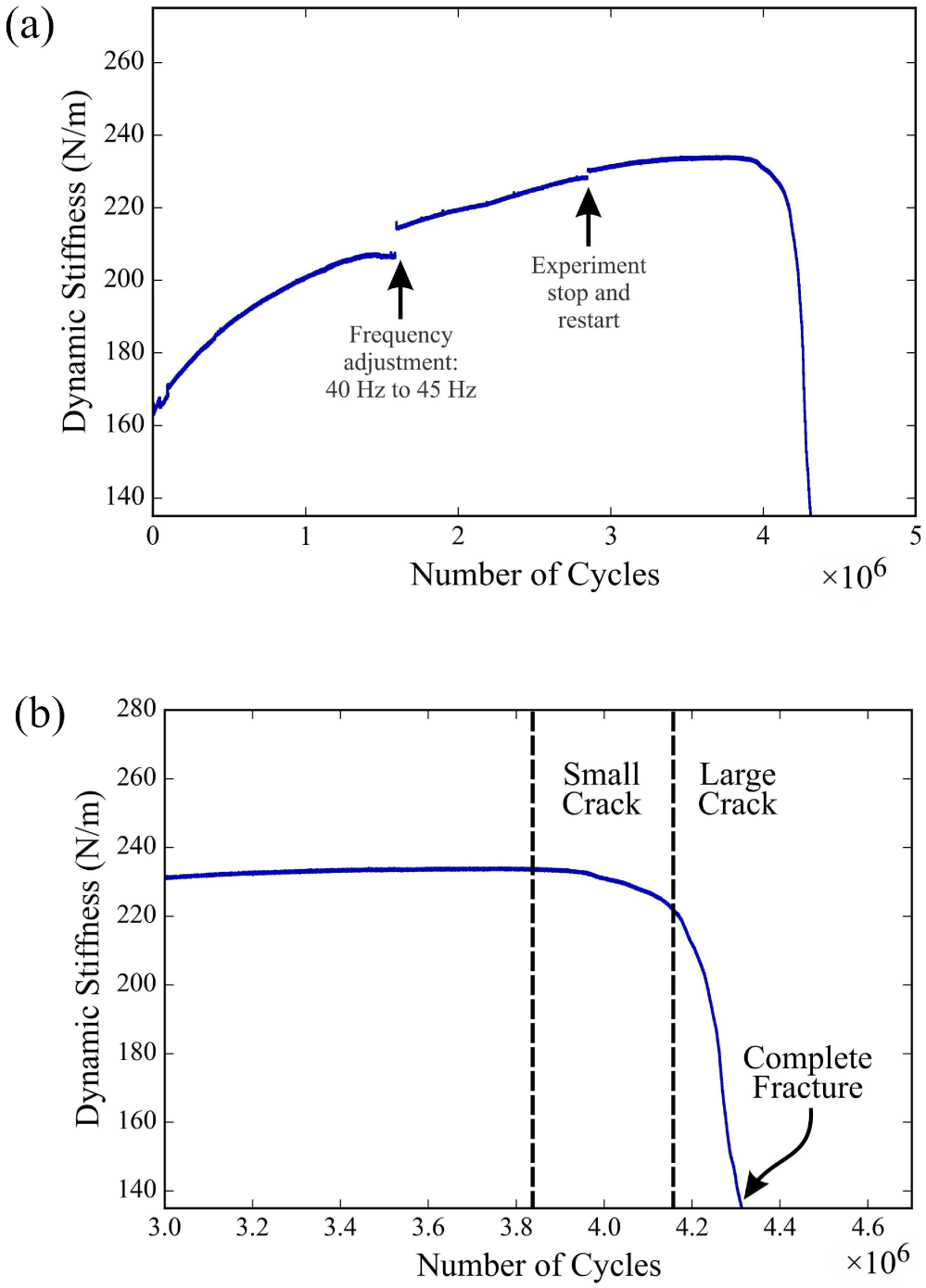

Figure 3.4: (a) The dynamic stiffness versus number of cycles for 6.70×10^{-3} strain amplitude micro-fatigue test of René-N5. A running average cleanup with a 4 second interval is applied. The first discontinuity is due to an adjustment in the loading frequency. The second small discontinuity is due to a stop/restart of the cyclic loading. (b) A closeup of the last 1.35×10^{5} cycles of (a) showing the two regimes of crack propagation.

To further quantify the hardening observed in the dynamic stiffness measurement, the high-frequency loading was interrupted regularly during an experiment with a strain amplitude of 3.97×10^{-3} to conduct quasi-static loading and determine the normalized load-displacement hysteresis loops at different cycles. The hysteresis loops for select cycle numbers are shown in Figure 3.5. Up to 1.1×10^6 cycles, the mechanical response shows a dramatic increase in the peak load. The increase in the peak load between cycles 1.1×10^6 and 2.9×10^6 is much less significant but still noticeable. After this point, a crack nucleates and the peak load gradually decreases only on the side of the beam that corresponds to the crack being in tension, as shown in Figure 3.5(b). When the crack is in compression, the peak load is almost unchanged since the crack is completely closed. As the crack propagates, the curve becomes more asymmetric with the peak load continuously decreasing until the micro-beam completely fractures.

Figure 3.6 shows the surface morphology at different cycles for an experiment performed at a strain amplitude of 3.97×10^{-3}. No significant surface roughening is observed near the fixed end of the beam and the crack nucleates on the bottom of the beam and propagates until the beam is completely fractured. It is worth noting that two separate cracks nucleated during this experiment. One nucleates at approximately 2.5×10^6 cycles but does not grow more than $\sim$1 μm in length. A separate crack nucleates closer to the fixed end at 2.90×10^6 cycles. This crack ends up propagating along the entire width of the beam and ultimately leads to failure. It is interesting to note that from the first observable crack nucleation event to complete fracture spans a total of 7.81×10^4 loading cycles, which is 2.6% of the micro-beam's life.

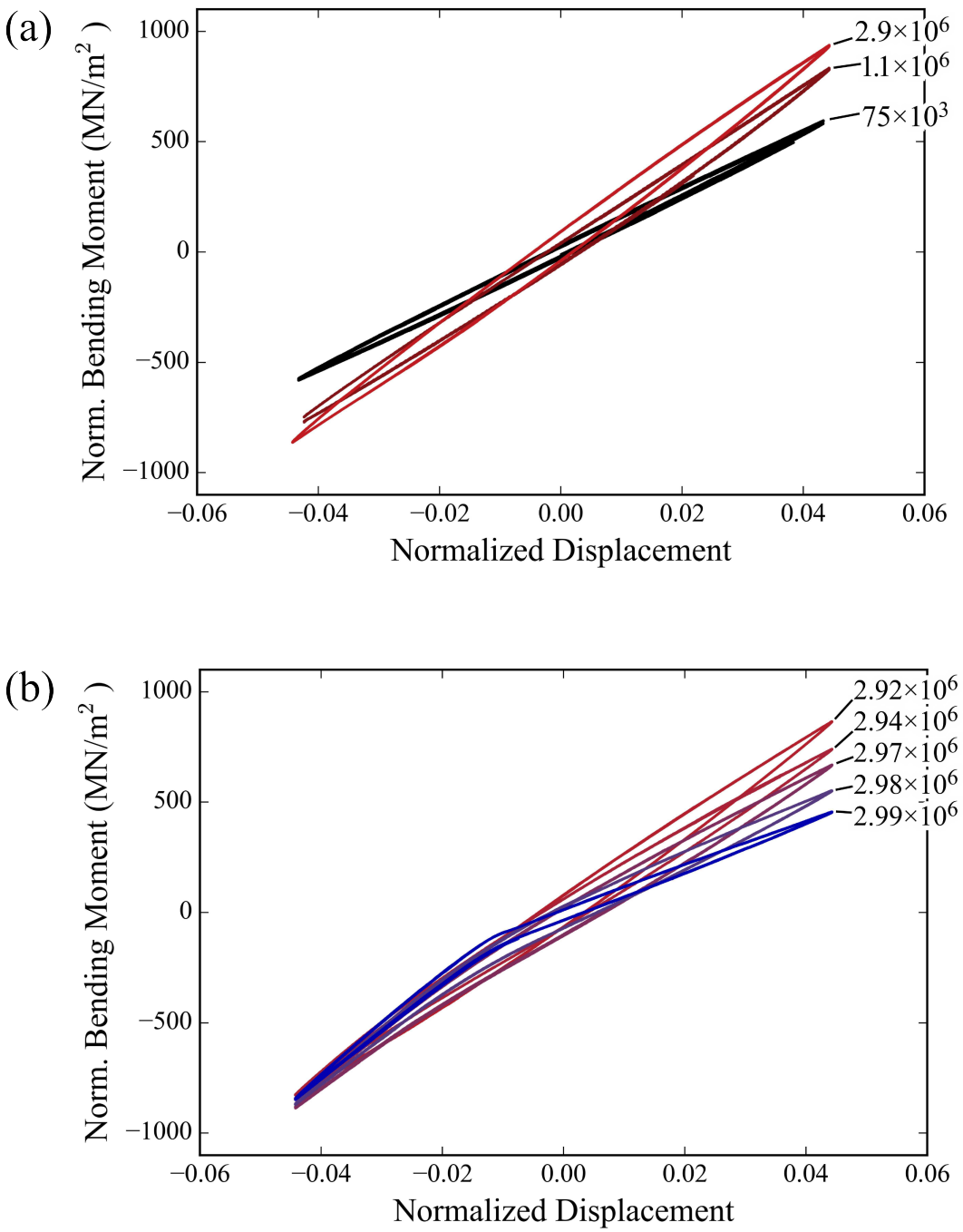

Figure 3.5: Hysteresis loops for a micro-beam cyclically loaded with a strain amplitude of 3.97×10^{-3} collected during periodic interruptions of the cyclic loading experiment. (a) Select number of hysteresis loops during the first $2.9{\times}10^6$ cycles indicating cyclic hardening. (b) Select number of hysteresis loops after crack initiation indicating compliance reduction. The normalized moment is defined as FL/bh^2 and the normalized displacement is defined as d/L, where F is the load on the beam, d is the displacement of the beam end, L is the distance between the fixed and the free end where the load is applied, b is the cross-sectional width of the beam, and h is the cross-sectional height of the beam.

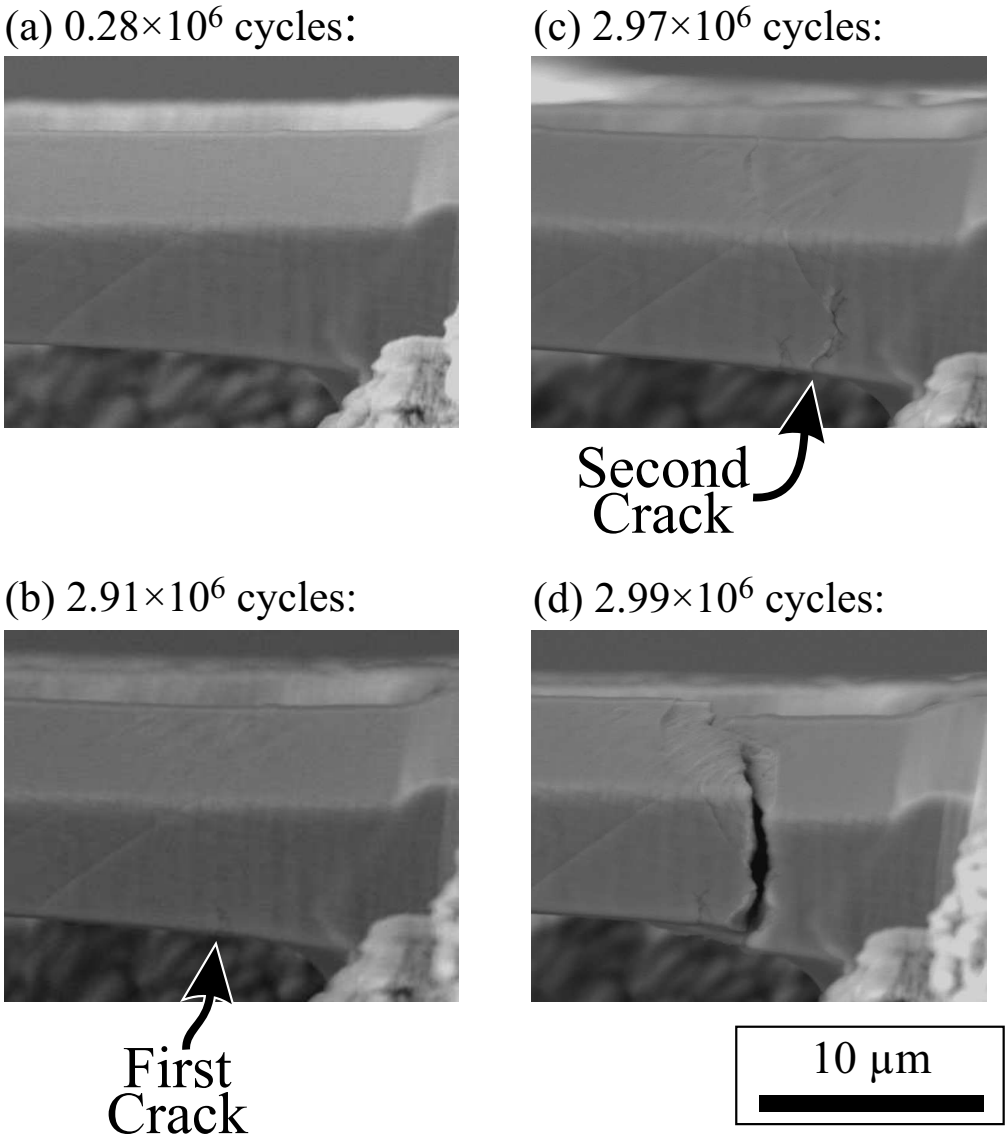

Figure 3.6: Scanning electron microscope micrographs showing the surface morphology near the fixed end of a cyclically loaded micro-beam with a strain amplitude of 3.97×10^{-3}.

3.3 Discussion

3.3.1 Mechanisms Leading to the Observed Cyclic Hardening/Softening at Different Strain Amplitudes

As shown by the surface morphologies in Figure 3.3, there is significant plastic deformation accumulating over the course of the cyclic loading in all samples tested at a strain amplitude larger than 7×10^{-3}. In contrast, samples tested below this strain amplitude show very little surface roughening throughout the sample lifetime. Since no cracks are seen in this early stage of fatigue, this would lead one to believe that the cyclic softening observed during this early stage of fatigue is related to dislocation motion. It has been shown that dislocation slip in these René-N5 alloys is associated with the shearing of γ' precipitates [219]. It has also been established that the shearing of precipitates in Ni-base superalloys is a known fatigue softening mechanism [220, 221]. In light of the observations in the present study, along with those in the literature, one can surmise that the cyclic softening of René-N5 at high strain amplitudes in the present is likely due to dislocation shearing of the γ' precipitates. This mechanism is further supported by the following analysis.

The resolved shear stress required to shear a γ' precipitate by a superdislocation is [222]

$$\tau_a = \frac{\Gamma_{\mathrm{APB}}}{2b} \tag{3.2}$$

where Γ_{APB} is the anti-phase boundary energy, and $b = 2.52$ Å is the magnitude of the Burgers vector for Ni_3Al. It should be noted that Equation (3.2) is limited to the ideal case of a single infinitely-long dislocation shearing through an infinitely-long precipitate and represents an upper bound of the actual value of τ_a. Experimentally-determined values for Γ_{APB} reported in literature and the corresponding predicted APB shearing stresses based on Equation (3.2) are indicated on Figure 3.7 [223, 224]. In addition, the max-

imum resolved shear stresses as predicted from the FEM simulations of the current experiments are shown in Figure 3.7. In the current experiments the $(111)[10\bar{1}]$ slip system exhibits the maximum Schmid factor. Different markers are used to indicate whether cyclic hardening or softening was predominant during the sample life.

Comparing the predicted critical shearing stress in Figure 3.7 with the critical resolved shear stress required to shear a precipitate, it would seem highly likely that the transition from cyclic hardening to cyclic softening can be attributed to stress required to shear precipitates in the superalloy when $\Gamma_{\mathrm{APB}} < 0.2\ \mathrm{J/m^2}$. Nevertheless, given that the predictions from Equation (3.2) represent an upper limit and in real crystals τ_a can be lower [222], it can be argued that when the applied strain amplitude is larger than 7×10^{-3} softening is expected due to precipitate shearing. When the applied strain amplitude is lower than this threshold, shearing is not expected and dislocation hardening would dominate due to dislocation interactions in the γ phase and pile up at the γ' interface.

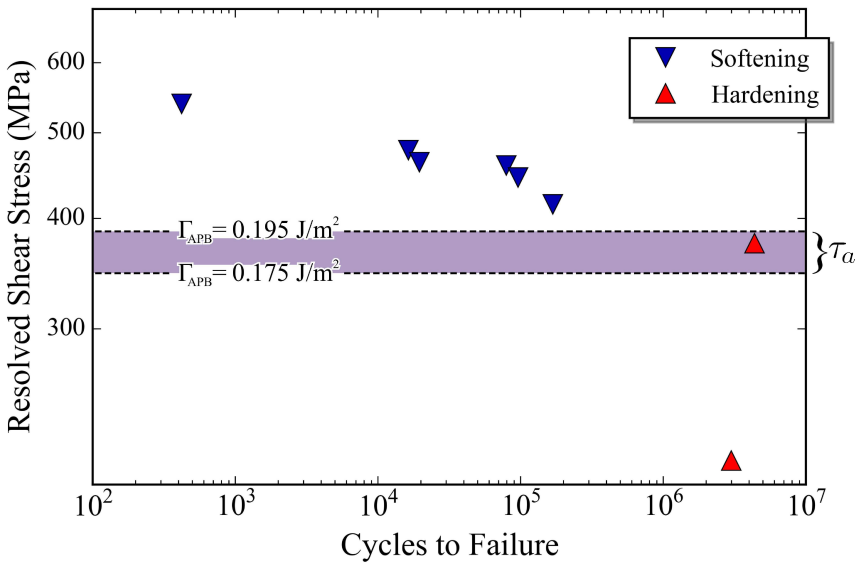

Figure 3.7: Calculated resolved shear stress values on the (111) $[10\bar{1}]$ slip system versus the number of cycles to failure for all tested cases in the current study. Dashed lines denote precipitate shearing stresses as calculated by Equation 3.2 for various values of Γ_{APB}.

3.3.2 Crack Initiation

Due to the small volumes, all tested specimens are assumed to contain no pre-existing cracks. The vast majority of the fatigue life for all tested samples was spent nucleating a crack and once the crack was present, the number of cycles to reach complete failure was relatively small. Understanding the micro-scale mechanisms that lead to crack initiation would provide great insight into quantifying the lifetimes of engineering materials.

The slip bands observed for strain amplitudes larger than 7×10^{-3} are typical for cyclically loaded Ni-base superalloys [225]. Though these slip bands are distinct from persistent slip bands observed in single phase FCC metals, they still contain a characteristic ladder structure of edge dislocation dipoles [225]. These slip bands are known to lead to crack-like openings at the interface between the slip band and surrounding matrix. Various models in the literature attempt to explain this phenomena (e.g., EGM and the Polák) and how these slip bands lead to crack initiation [122, 123]. There is some disagreement about whether these early crack-like openings are local vacancy clusters (i.e., intrusions) or in fact embryonic cracks.

Figure 3.8 shows the progression of slip bands during a micro-beam fatigue experiment with a strain amplitude of 7.85×10^{-3}. It is clear that the crack-like openings do not form until there are distinct extrusions. Interestingly, the crack-like openings reach approximately the same depth as the initially present extrusions. It could be argued that these openings form once vacancies in the slip bands have enough time to diffuse to the matrix (see Figure 3.8(c)). However, this distinction between cracks and intrusions could be not be delineated with the *in situ* surface observations in the present study. Nevertheless, these crack-like openings are very consequential in the context of fatigue crack initiation because they have been known to deepen, sharpen, and eventually form a large crack [209]. Crack-like openings are also clearly

apparent in the *post-mortem* SEM micrographs of the fractured surface shown in Figure 3.9.

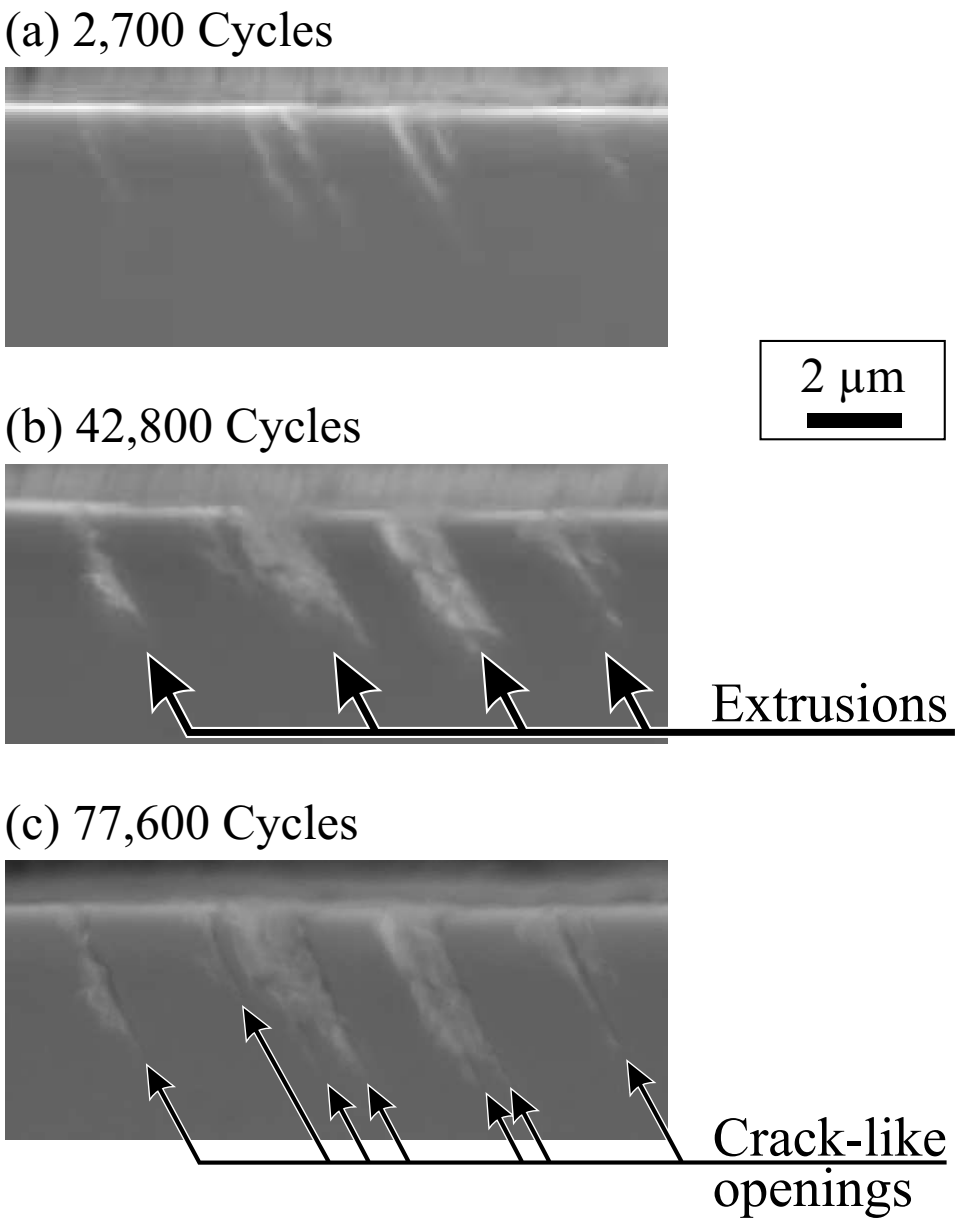

Figure 3.8: SEM micrographs of slip band formation near the fixed end of a cyclically loaded micro-beam with a strain amplitude of 7.85×10^{-3} showing: (a) the early stages of slip band formation; (b) fully developed slip band extrusions; (c) crack-like openings alongside each slip band.

3.3.3 Fracture Surface Morphology

In all tested micro-beams, the dominant crack that leads to failure always initiated at or near the lower corner of the micro-beam since the corner leads to a stress concentration. Surface extrusions along the {111} slip planes were also observed as preferred sites for crack nucleation in micro-beams that failed in less than 10^6 cycles. In most tested micro-beams, failure was dominated by the propagation of the crack from the bottom corner vertically upward along the (100) fixed end plane. However, in some cases the crack deviated from the fixed end plane and connected to a crack initiating along extrusions on the top surface, as shown by the morphology of the fractured surface in Figure 3.9. In this experiment the strain amplitude was 8.28×10^{-3} and the micro-beam completely fractured after 9.6×10^4 cycles. A combination of crack along the {111} slip planes on the top surface and a crack approximately along the (100) plane contributed to this failure. Figure 3.9(a) reveals the texture of the fracture surface of the beam along its cross-section. Towards the top half of the micro-beam, the fracture surface is relatively smooth and the crack surfaces correspond to {111} slip planes in the FCC crystal. Towards the bottom half, the {100} fracture surface is relatively rough since this surface does not follow any specific slip system. This contrast in fracture surface roughness could indicate that the cracks along the {111} slip plane may be intrusion surfaces, distinct from the rough {100} cracks towards the bottom.

The more oblique viewing angle in Figure 3.9(b) clearly shows the intersecting slip traces from the $(\bar{1}11)$ and $(11\bar{1})$ planes on the top surface. The fracture surface at the top of the beam creates a vertex where the two {111} cracks intersect. Note also that the sides of the micro-beam show a significant amount of extruded material.

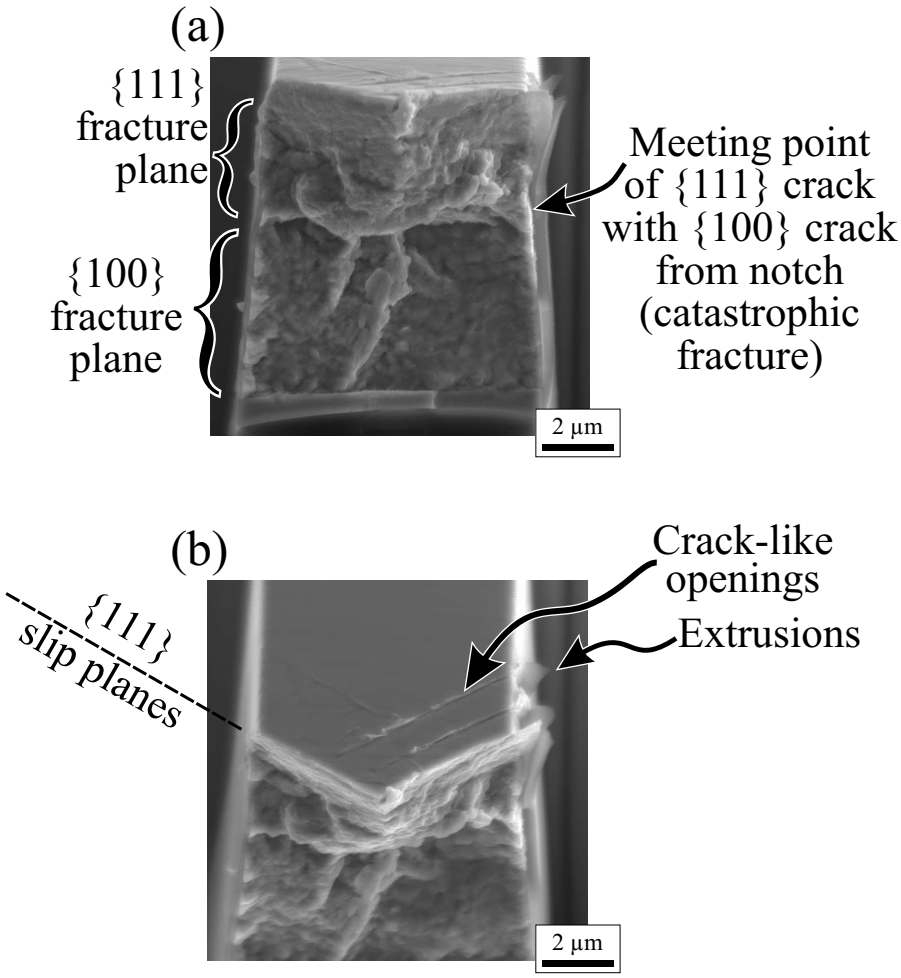

Figure 3.9: *Post-mortem* SEM micrograph of the fracture surface of a micro-beam cyclically loaded at a strain amplitude of 8.28×10^{-3}.(a) A 10° tilt view of the fracture surface relative to the [100] direction. (b) A 30° tilt view of the same fractured surface relative to the [100] direction.

3.4 Conclusions

In this chapter, the new micro-fatigue testing methodology discussed in Section 2.1 was utilized to perform high cycle fatigue tests *in situ* on small volumes of material. Micro-fatigue experiments were conducted on single-crystal René-N5 Ni-base superalloy micro-beams at zero mean strain with total strain amplitudes ranging from 3.97×10^{-3} to 1.98×10^{-2}. The method was shown to

be able to probe fatigue lives spanning 5 orders of magnitude. The small-scale fatigue life results reported here were observed to be superior to bulk superalloy fatigue studies. Real time *in situ* SEM viewing allowed for observations of the cause and location of fatigue failures. By tracking the dynamic stiffness during cyclic loading, it was found that high displacement amplitude tests exhibited softening from the very start of the test until complete failure. Tests conducted below a strain amplitude of 7×10^{-3} cyclically hardened for the vast majority of the fatigue life until eventually a crack formed and caused failure. This is attributed to a transition from dislocation accumulation in γ channels to shearing of the γ' precipitates as the dominant hardening and softening mechanisms, respectively. High strain amplitude fatigue tests show surface extrusions and slip traces forming near the fixed end. Cracks formed at stress concentrations as well as along surface extrusions. For low amplitude tests, two regimes of softening were observed possibly indicating a transition between short and large crack growth. Such observations could allow further characterization of the nature of short crack growth.

Chapter 4

Uniaxial fatigue of Ni microcrystals

4.1 Introduction

Nickel (Ni) forms the base of many important engineering alloys, most notably in Ni-base superalloys, which have been a staple in the aviation and energy industries for the past 7 decades [226]. To further understand how to improve the service life of these metals, a fundamental understanding of dislocation microstructure evolution during cyclic loading is necessary. Instead of investigating various candidate alloys (i.e., trial-and-error), an alternative approach is to first gain a fundamental understanding of the single-phase base material (Ni) then subsequently incorporate the effects of alloying elements and secondary phases.

For single slip oriented metal single crystals, the early stages of fatigue are characterized by the clustering of dislocations into patches (i.e., veins). With further cyclic loading, these patches have been found to break down into ladder dislocation structures (as discussed in Chapter 1). Ladder dislocation structures, more commonly referred to as persistent slip bands (PSBs), are

perhaps the most consequential of these structures with regards to fatigue crack initiation. PSBs take the form of regularly-spaced, dislocation-dense walls constructed of edge dislocation dipoles with dislocation-sparse channels separating them into a structure resembling a ladder (see Figure 1.3(b)). They are typically observed in wavy slip metals (e.g., copper and nickel), in large grains/crystals oriented for single slip, with a symmetrically applied tension-compression loading profile, and form along the slip plane with the highest resolved shear stress [227, 228]. The dislocation walls organize along the direction of the slip plane where the atoms are most closely packed (i.e., the Burgers vector direction) and egress from the free surface of the crystal in the direction of the Burgers vector as surface steps known as persistent slip markings (PSMs). PSBs have been found to promote micro-crack initiation at the crystal free surfaces along the interface between the PSB and the surrounding matrix [69], or in at the intersection of PSBs with high angle grain boundaries since dislocations are blocked by these boundaries.

The precise mechanisms that lead to fracture along a PSB-matrix interface is still the subject of debate. One of the leading models is that the extrusions that form on the free surface create stress concentrations that lead to localized micro-crack initiation. This model is commonly known as the EGM model after the authors who originally proposed it [229]. In a modification to this model, it was proposed that the diffusion of vacancies from the interior of the PSB to the PSB-matrix interface and their subsequent coalescence at the free surface (or grain boundary) leads to the formation of openings that are crack-like in appearance, but technically different from cracks (i.e., intrusions) [123]. These intrusions may thus serve as stress concentrations that lead to crack initiation.

PSBs are generally classified as long-range features that occur in bulk single crystal or polycrystalline metals. While they have been observed in bulk polycrystalline metals having grains sizes as small as tens of microns, they have

never been reported in single crystals having sizes smaller then a few hundred micrometers [106, 230, 53]. Additionally, only relatively recently has *in situ* small-scale cyclic testing been able to reach a large number of cycles [149, 33, 36, 54, 41]. These *in situ* methods are useful since most polycrystalline or bulk single crystal studies on the formation of PSBs have been limited to *post-mortem* characterization of polycrystals and bulk single crystals with very few exceptions (e.g., [231]).

With an increase in plastic strain amplitude, secondary slip systems start to play a more active role, and thus the planar PSBs become unstable. The PSBs gradually transform into cell dislocation structures with irregular shaped walls [232, 14]. Compared to PSB walls, these cell walls contain dislocations with several Burgers vectors in addition to the primary slip system [233]. The cellular dislocation structure is associated with a secondary hardening region of cyclic saturation and exhibits higher saturation stresses. Although this behavior has been well established for pure, bulk single crystals, there has been limited work on microcrystals at high strain amplitudes. One study reported elongated cellular dislocation structures in select grains of Cu polycrystalline micro-wires after cyclic loading [67]. However, details regarding the diameter and crystallographic orientation of these grains were not provided.

While the role of PSBs in crack initiation is well documented [69], the role of dislocation cells on fracture is less understood. It has been suggested that intergranular fracture is a dominant crack initiation mechanism since the cellular microstructure in single crystals leads to slight misorientations between neighboring cells [234]. The boundary between cells under plastic deformation is the site for many dislocation pileups and annihilation events, thus making it a viable candidate for eventual fatigue crack initiation. With so few fracture mechanisms available at these high strain amplitudes, it would seem that surface conditions (i.e., surface roughness) would be a large factor in the resulting fatigue life of single crystals. This makes the idea of lowering

the surface-to-volume ratio (i.e., small-scale fatigue samples) very intriguing.

Accordingly, the aim of this chapter is to provide unprecedented *in situ* observations and characterization of Ni microcrystals under cyclic loading. This is done by applying the high frequency (45-300 Hz) micro-fatigue method detailed in Section 2.3.2. Novel hammerhead micro-samples (see Figure 2.22) are developed and used throughout this chapter. This method allows for fully reversed tension-compression uniaxial fatigue of microcrystals with rectangular cross-section ∼12 μm in gage width and height-to-width aspect ratios of ∼2.5. Cyclic strains are applied along the $[\bar{3}5\bar{2}]$ crystallographic direction (see Section 2.1.1.2) to obtain single slip plastic deformation. The strain amplitudes are varied to observe the different regimes of dislocation structures under fatigue.

4.2 Results

4.2.1 Low Shear Strain Amplitudes ($\leq 1.5\times10^{-2}$)

4.2.1.1 Evolution of Surface Morphology

Sequential scanning electron microscopy (SEM) micrographs of the evolution of the surface morphology of a single crystal Ni microcrystal cyclically loaded at a shear strain amplitude of 6.3×10^{-3} are shown in Figure 4.1(a)-(o). The experiment was conducted under a constant shear strain amplitude of 6.3×10^{-3}. The dynamic stiffness as a function of the number of cycles is also shown in 4.1(q). The observations from this experiment are common for all experiments conducted below a shear strain amplitudes of $\sim1.5\times10^{-2}$. Within the first 8 loading cycles, a number of faint slip traces are observed to form on the edge plane (see Figure 4.1(b)). Subsequently, the surface morphology remains relatively unchanged for the next 2.5×10^{6} cycles. Nevertheless, the dynamic stiffness continuously increases during this stage, which correlates with cyclic hardening [149]. After a critical number of cycles is reached (typically more

than 10^6 cycles), slip band markings nucleate sequentially on the edge plane somewhere along the different slip traces that had formed in the first ∼10 cycles (see inset in Figure 4.1(c)).

It is interesting to note that these slip band markings do not appear along the entire slip plane at once. Instead, they first nucleate at a localized region of a slip plane then spread in both directions perpendicular to the primary Burgers vector on the slip plane until the slip band extends the entire gage width. Each slip band marking is approximately 1 μm in thickness (in the direction perpendicular to the original slip trace). As the slip band markings sequentially nucleate with increasing number of cycles, the rate of increase in the dynamic stiffness decreases until it reaches a steady state value when no new slip band markings are observed, which corresponds to "cyclic saturation". It should also be noted that the area fraction of the gage section occupied by these slip band markings scales with the applied strain amplitude.

Closer examination of the micro-sample (Figure 4.1(p)) provides a more clear view of the surface morphology of both the edge and screw planes after testing. This angled view shows that the surface topography of the slip band markings are composed of extrusions and intrusions. Also, a FIB cross-section of the sample in Figure 4.2 reveals that some of these intrusions extend deep into the sample and can be considered Stage I micro-cracks. It should be noted that in all the SEM micrographs intruded regions appear darker in contrast than the extrusions. Furthermore, observations indicate that surface intrusions form on the screw plane well after the formation of a fully-developed slip band marking on the edge plane and appear more gradually rather than the abrupt nucleation event observed on the edge plane.

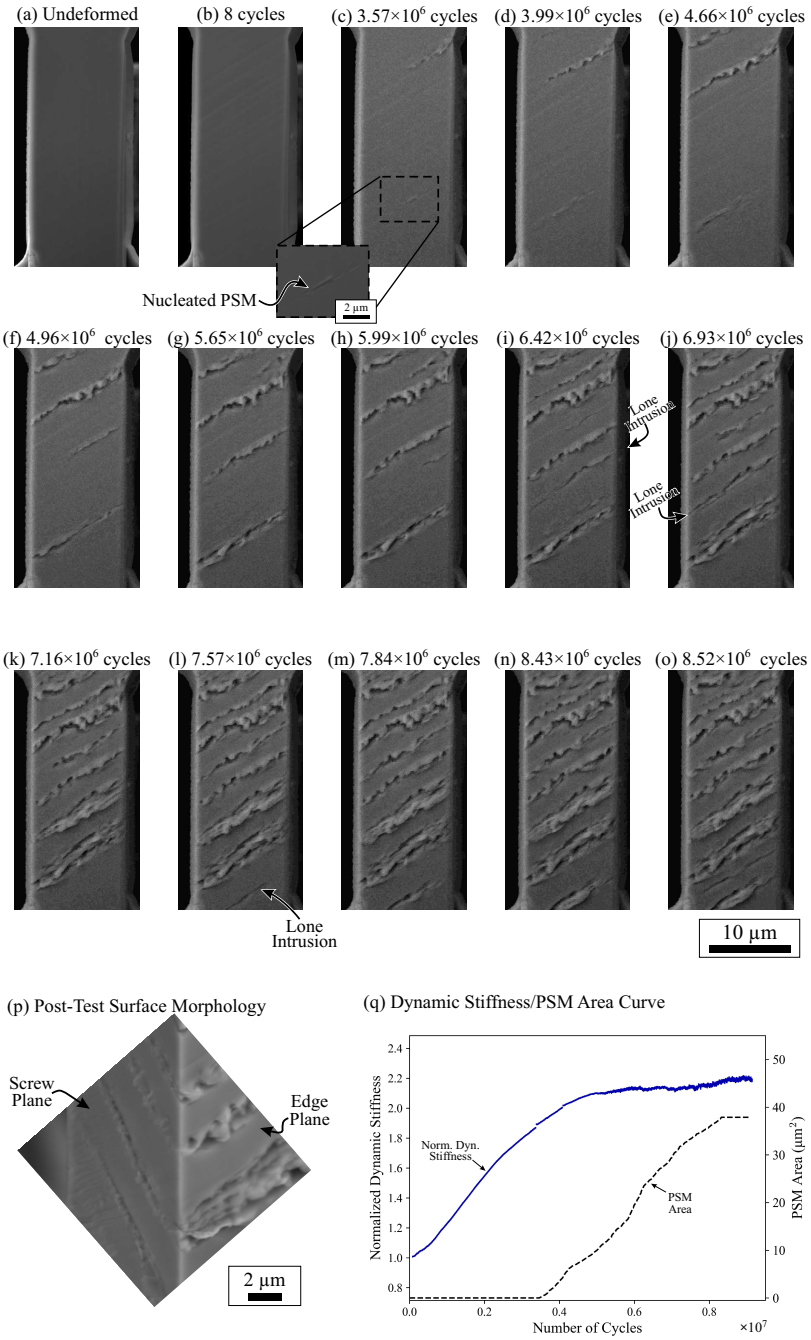

Figure 4.1: (a)-(o) SEM micrographs of the evolving surface morphology on the edge plane of a Ni microcrystal cyclically loaded at a shear strain amplitude of 6.3×10^{-3}. The microcrystal has a rectangular cross-section with dimensions 12 × 13 μm and gage length of 27 μm. (p) Three-dimensional view of the surface morphology after testing showing both the edge and screw planes. (q) The dynamic stiffness and the area of four analyzed persistent slip markings on the edge plane versus the number of loading cycles. In these *in situ* micrographs, extrusions and crack-like openings (i.e., intrusions) can clearly be discerned based on the contrast. The crack-like openings are associated with the dark regions on the surface of the micro-sample. This is confirmed by the close-up SEM micrographs of the surface (p).

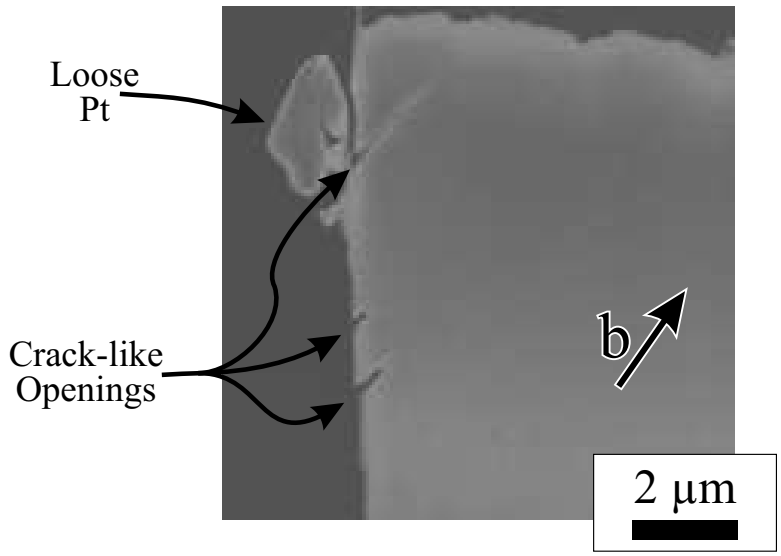

Figure 4.2: FIB cross-section of screw plane of Ni microcrystal cyclically loaded at a shear strain amplitude of 6.3×10^{-3}. Note that a piece of the protective Pt on the top left came loose during FIB thinning.

4.2.1.2 Characterization of the Dislocation Microstructure

Cross-sectional FIB lift-out foils from the deformed specimens were extracted from the interior of the gage sections in order to characterize the dislocation microstructure using transmission electron microscopy (TEM). A screw-plane view of the dislocation microstructure for a microcrystal cyclically deformed at a shear strain amplitude of 1.1×10^{-3} for 10^4 cycles then 6.9×10^{-3} for 1.45×10^7 cycles is shown in Figure 4.3. The observed dislocation microstructure exhibits characteristic ladder-like dislocation structures with regularly spaced dislocation walls separated by dislocation-sparse channels. The dislocation walls organize along the Burgers vector direction with a mean spacing between the walls on the order of 1 μm. These observations are characteristic features of PSBs in pure bulk Ni at room temperature [235, 236]. The observation of multiple neighboring PSBs in Figure 4.3(a) also resembles macro-PSBs observed in bulk FCC single crystals [123]. These observations indicate that the slip markings observed in the current experiments are PSMs. However, it should be

pointed out that the observed PSBs in the present study are less well-defined than many seen in bulk-scale fatigue studies of FCC metals [237, 235]. Namely, the ladder rungs are not as straight and evenly spaced. This difference with bulk observations will be addressed in the Discussion section.

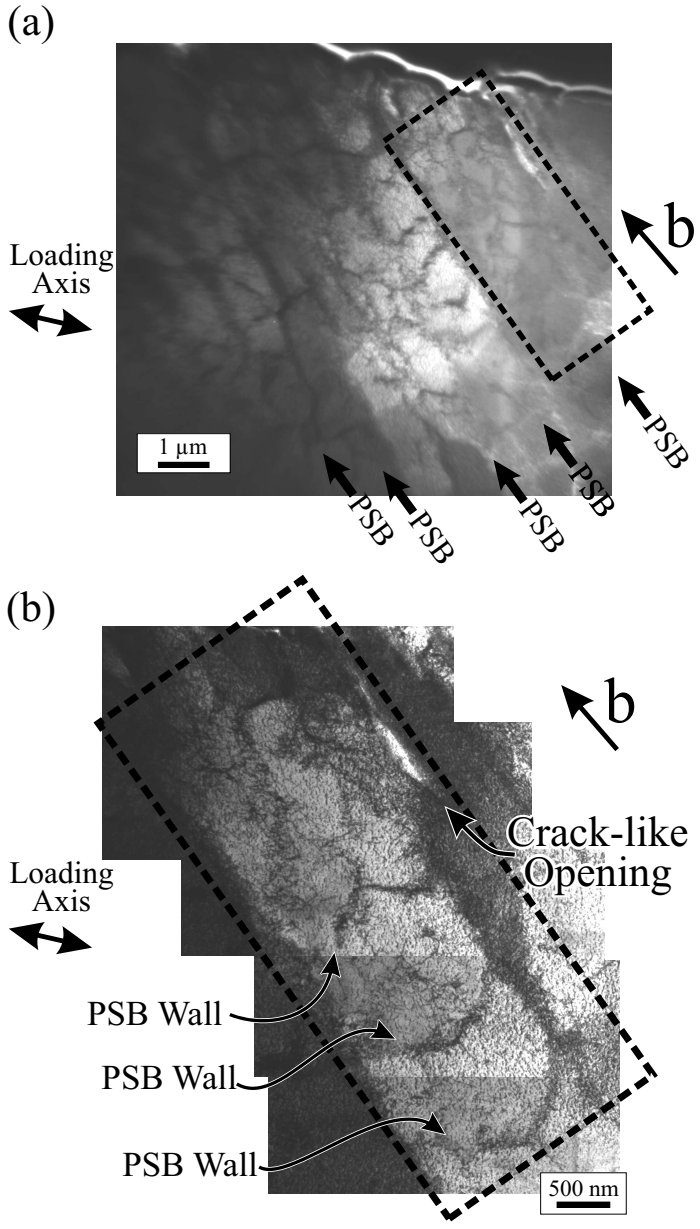

Figure 4.3: Dislocation microstructure of screw plane of a Ni microcrystal cyclically loaded at a shear strain amplitudes of 1.1×10^{-3} for 10^4 cycles then 6.9×10^{-3} for 1.45×10^7 cycles. (a) A macro-PSB is clear with a group of several PSBs clustered alongside one another. (b) A higher magnification of the dashed box shown in (a) showing a PSB with a crack-like opening along one side of the PSB-matrix interface.

The SEM micrograph of the screw plane surface morphology of a cyclically deformed microcrystal at a strain amplitude of 4.1×10^{-3} after 6.43×10^{6} cycles is shown in Figure 4.4(a). In this case, a single PSM that has propagated through the thickness of the microcrystal is observed. The TEM micrographs at different locations of a cross-sectional FIB lift-out foils are shown in Figure 4.4(b)-(f). Below the surface marking (Figure 4.4(d)) the early phase of development of a ladder-like dislocation structure is observed, namely, some walls have relatively few dislocations and are less straight as compared to walls further along the PSB. The surrounding matrix exhibits many dislocation tangles, but not as dense clusters (see Figure 4.4(b)). These dislocations are surmised to be on primary and secondary slip systems. Additionally, while dislocation "veins" are also sometimes observed (see Figure 4.4(b) and (f)), they are much more sporadic than the relatively consistent vein structures observed in bulk Ni studies (where approximately half of the matrix is occupied by veins) [235, 238, 236]. An additional observation in Figures 4.4(c) and (d) are the long dislocation segments both between the channels of the PSB as well as in neighboring regions. These long segments are presumed to be screw dislocations on the primary slip plane, although this could not be confirmed. However, since the segments are in line with the primary Burgers vector and screw dislocations have been observed in the channels of PSBs in previous studies [81, 239] the assumption of screw character is reasonable. It appears that the screw dislocations are entangled with secondary dislocations. In bulk PSBs, it is typical to see screw dislocations gliding between the channels of the PSBs. However, the observation that secondary dislocations entangle the screw segments indicates that the PSB is at an early stage of development. It is important to note these entangled screw dislocations were not observed in more well-formed PSBs such as the ones shown in Figure 4.3. Dislocation tangles have also been observed in bulk fatigue at the interface of the vein and PSB structures [79]; but the authors of that study assumed that these

are predominately edge multipoles on the primary and secondary slip systems. It has been argued that these loosen via secondary dislocation annihilation, which frees the primary dislocations and subsequently leads to the formation of PSB walls [79]. Based on the observations in Figure 4.4, it would seem that primary screws are also an important component of these tangles. Furthermore, recent dislocation simulations show that primary screws interact with secondary dislocations to form the edge dipoles in PSB walls [75].

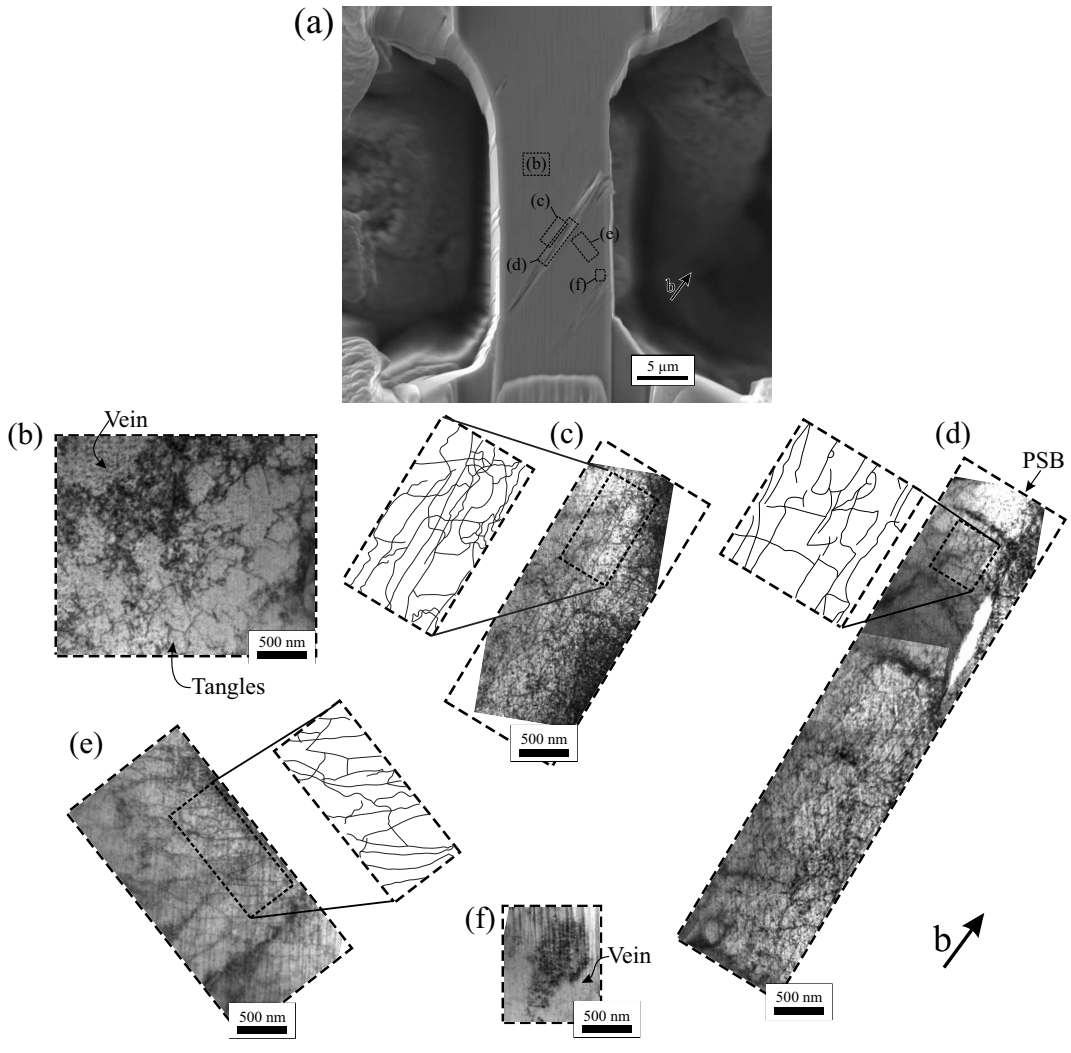

Figure 4.4: Ni microcrystal cyclic loaded at a shear strain amplitude of 4.2×10^{-3} for 6.43×10^{6} loading cycles: (a) SEM micrograph of the surface morphology on the screw plane; and (b)-(f) TEM micrographs of the dislocation microstructure in the screw plane. Refer to the dashed boxes in (a) for locations of (b)-(f). In (c)-(e), dislocation tangles are interpreted in a Bézier curve format in addition to the TEM micrographs.

4.2.1.3 PSM Embryonic Width and Propagation Profile

To extract the PSM propagation speeds and embryonic widths, image analysis was used. The following details the steps in the data analysis of the *in situ* videos. Codes used for this procedure are open source and available on Github [240].

The analysis of a given PSM starts with the entire gage section as shown in Figure 4.5(a). A shear transformation is first imposed to rotate the PSMs horizontally (Figure 4.5(b)). The band angles (and thus the shear angles) were determined by finding the vector direction that maximized the contrast gradient. The angles of shear used were within 3-4° of the crystallographically expected value (31° for the slip system having the highest Schmid factor).

Individual boxed regions approximately 10-15 μm wide by 1-2 μm thick were then used to select individual PSMs (Figure 4.5(c)). Within a given box, a row of pixels spanning the entire width of the box is then considered with respect to time (Figure 4.5(d)). The pixel dimensions ranged from 52-59 nm per pixel. For each pixel, the cycle number at which the surface changes from smooth to slip markings is determined by using a contrast threshold. This is done by determining a point in time that a given pixel crosses the threshold in contrast and is thus considered a PSM region. A Canny Edge Detection preprocessing filter is used to make these events more evident. Then, Otsu's method is used to determine when nucleation occurs [241], where the nucleation cycle, j, is determined by finding the cycle number that maximizes the following function:

$$\Delta\sigma = |(Stdev(I_{cycle=0} \rightarrow I_{cycle=j}) - (Stdev(I_{cycle=j+1} \rightarrow I_{cycle=N})| \qquad (4.1)$$

where I is the intensity and N is the total number of cycles. This process is repeated for each row of pixels in the boxed region.

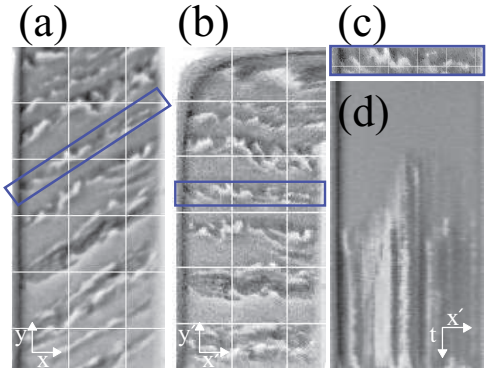

Figure 4.5: The process of extracting a PSM profile from a video of an *in situ* experiment (6.3×10^{-3} shear strain amplitude). (a) A PSM is selected in the final frame of the experiment (boxed in blue) (b) The same frame as (a) is sheared such that the PSM is horizontal (c) The cropped PSB from (b). (d) The PSM profile position versus time plot as obtained for the PSM in (c).

Once a nucleation point is obtained for each pixel in each row, the points for the entire boxed region are then considered collectively (see Figure 4.6), and to eliminate the noise along the thickness of the band the minimum envelope (the blue line in Figure 4.6) is used as the PSM profile.

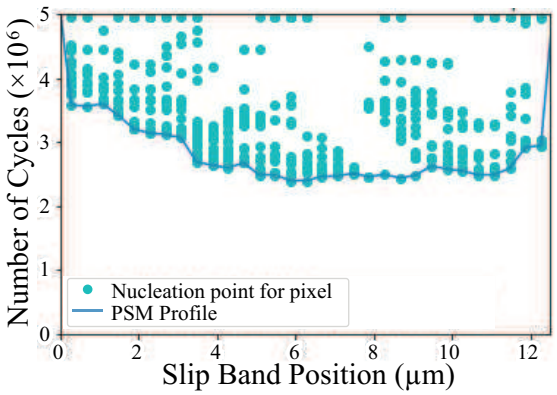

Figure 4.6: Nucleation points plotted for each pixel within the boxed region of Figure 4.5. Lower bounds is outlined which is constitutes the unfiltered PSM profile.

As a final step to remove noise, a post-processing filter was then applied to the PSM profiles. The first step is to apply a binning along the width of the PSM profiles to smooth them. Variable bin widths were used to optimize the profile. In the second filtering step, a moving window was applied along the minimum profile and the confidence of each point belonging to the window was

computed. Since values in a given window should not be random, it follows that strong false positives should be distinct from the other points. As such, if a given point differs from all the points in the running window by more than 95%, it is considered a false positive and is removed for profile visualization. Note that embryonic width and propagation speed calculations continue to use all datapoints. This procedure was performed for each PSM profile and the optimal bin size for each profile was found. The optimal bin size was determined to be the one which resulted in a lower convex hull with the fewest support points (see Figure 4.7). From this, a filtered PSM profile is obtained as shown in Figure 4.8.

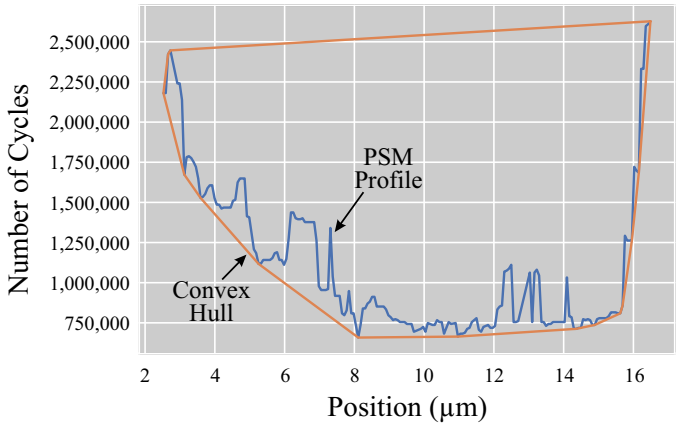

Figure 4.7: Nucleation points plotted for each pixel within the boxed region of Figure 4.5. Convex hull is outlined.

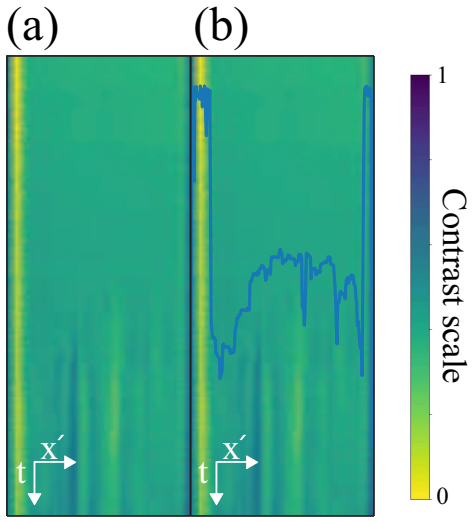

Figure 4.8: The average colorized PSM profile position-time image extracted from the analysis of a select PSM. The axes of the image are pixels, which are then accordingly scaled for further analysis. The blue line denotes the profile extracted from the image. Further smoothing (i.e., a running average) is generally performed to get rid of noise.

In an idealized case, a PSM may nucleate at a single point along the slip plane as depicted, then propagate with a certain velocity, in Figure 4.9(a). However, from the current experiments it is observed in practice that the PSM does not nucleate at a point on the surface, but rather a nucleation band with a specific width is observed (see schematic in Figure 4.9(b)). It is expected that the partially developed band emerges simultaneously since the PSB dislocation structure already has a width by the time it reaches the surface. This width is termed the embryonic width of the PSM. The embryo of the PSM is considered the group of consecutive points that most likely appear simultaneously.

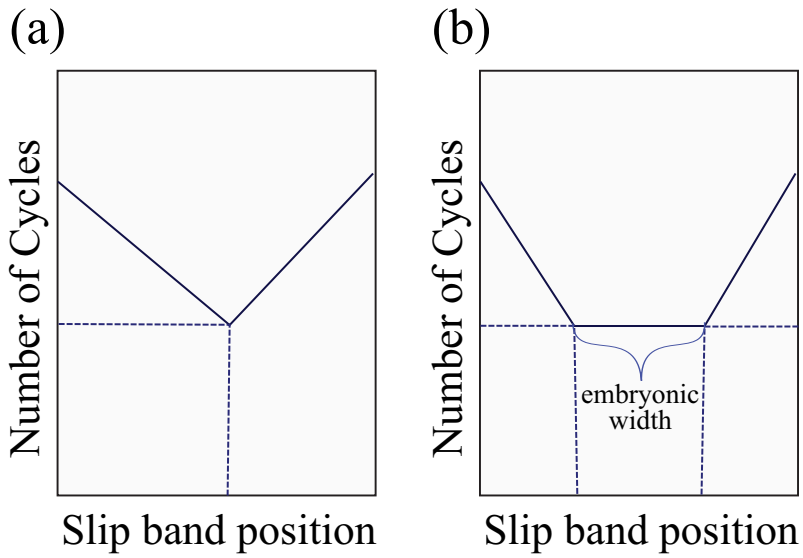

Figure 4.9: Schematic PSM postion-time profiles: (a) an idealized case for a PSM nucleating at a singular point on the surface; (b) in practice the PSM nucleates with a finite width (termed the embryonic width).

Due to the noise in the PSM profile data, the embryonic width is assumed to be the region of the front of the PSM profile that best resembles random Gaussian noise. To identify this region, various candidate embryo regions are considered. The first candidate embryo consists of just the very first few points of the PSM front. Subsequent data sets for the embryo are generated by expanding the previous set by the next events. All sets are then compared against a Gaussian distribution. The set that provides the most Gaussian-like distribution is considered the embryo (i.e., the highest correlation coefficient, R^2, of a curve fit to a normal distribution). The width of this set is termed the embryonic width of the PSM.

Once the profile for the PSMs were extracted, the speed of the PSM propagation can be readily obtained. To do this, data on either side of the PSM embryo were selected and the profile position-time data were curve-fit to a line. The slope of this line provides the speed of the PSM propagation (see Figure 4.10).

Figure 4.10: Shows how the slope of part of a profile can provide a "speed" for the propagation of a PSB for an experiment performed at a strain amplitude of $6.3\times\ 10^{-3}$.

Propagation profiles of select slip band markings for Ni microcrystals cyclically loaded at different shear strain amplitudes are shown in Figure 4.11. The first cycle at which a slip band marking is detected is labeled cycle zero. These profiles are nonuniform and are typical of slip band marking profiles observed in the current study. This nonuniform profile is likely correlated with the nonuniformity with which the underlying dislocation structure develops within the microcrystal. The embryonic widths from all the slip band markings profiles studied here were in the range of 2.6 to 8.3 μm. The propagation velocities were found to range from 1.89 to 8.63 pm/cycle.

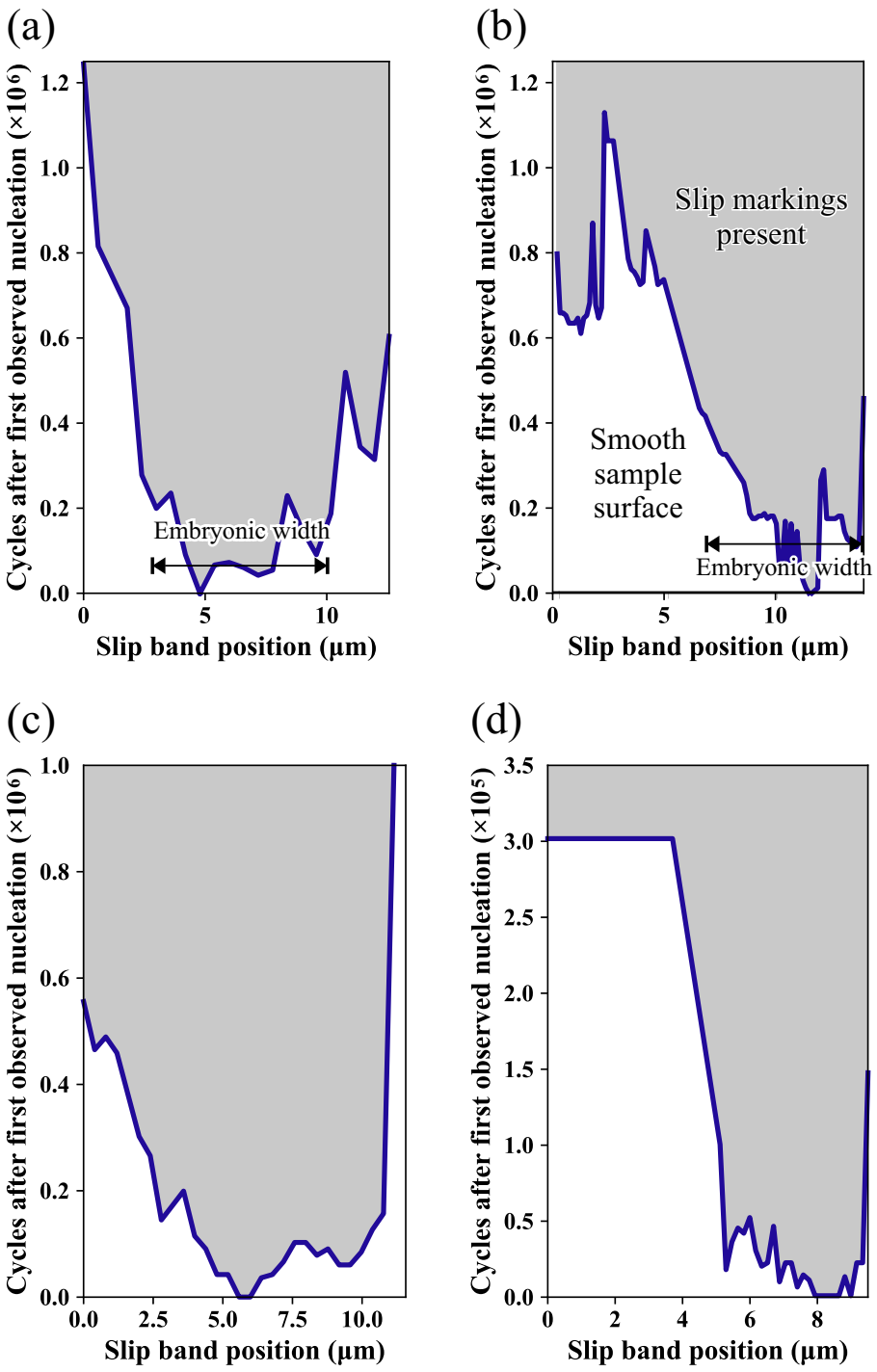

Figure 4.11: Propagation profiles of select slip band markings for Ni microcrystals cyclically loaded at a shear strain amplitudes of (a)-(c) 6.3×10^{-3} and (d) 1.2×10^{-2}. The PSB egresses at the surface with a relatively flat profile with a width presumably equal to the width of the leading edge of the slip band nucleus (termed the embryonic width).

The wide variation in the observed embryonic widths indicate that the PSM nucleus likely develops somewhere within the crystal volume at a certain depth from the surface before propagating to the surface of the sample. Thus, the observed width is likely correlated with the depth of the slip band nucleation event. On the other hand the wide variation in the propagation speed is likely correlated to the nonuniformity with which the underlying dislocation structure develops within the microcrystal.

4.2.2 High Shear Strain Amplitudes ($>1.5\times10^{-2}$)

4.2.2.1 Evolution of Surface Morphology

SEM micrographs at different cycle numbers of a Ni micro-fatigue experiment conducted at a strain amplitude of 1.6×10^{-2} are shown in in Figure 4.12. The dynamic stiffness as a function of number of cycles for this experiment was also monitored during cyclic loading using the dynamic stiffness parameter (Equation 2.6) and shown in Figure 4.13.

The experiment began at a cyclic frequency of 75 Hz. Within 1.85×10^{5} cycles, PSMs with extrusions and intrusions are evident on the edge plane (see Figure 4.12(d)). This is associated with rapid cyclic hardening in the dynamic stiffness (see Figure 4.13). The fraction of the gage area with PSMs increases with further cyclic loading until the entire region is saturated. Interestingly, this is not associated with a saturation in the dynamic stiffness indicating that the dislocation microstructure is continuously evolving. At approximately 1.22×10^{7} cycles, the dynamic stiffness begins to exhibit cyclic softening. Cyclic softening after a maximum in cyclic stress has been observed in bulk Ni at high strain amplitudes [242, 238]. However, this is normally followed by a plateau in cyclic stress. Instead, the hardening continues and a true plateau is never reached. The increase in dynamic stiffness after 1.53×10^{7} may very well be the result from the refinement of the cell size [232, 243]. By the time 1.94×10^{7}

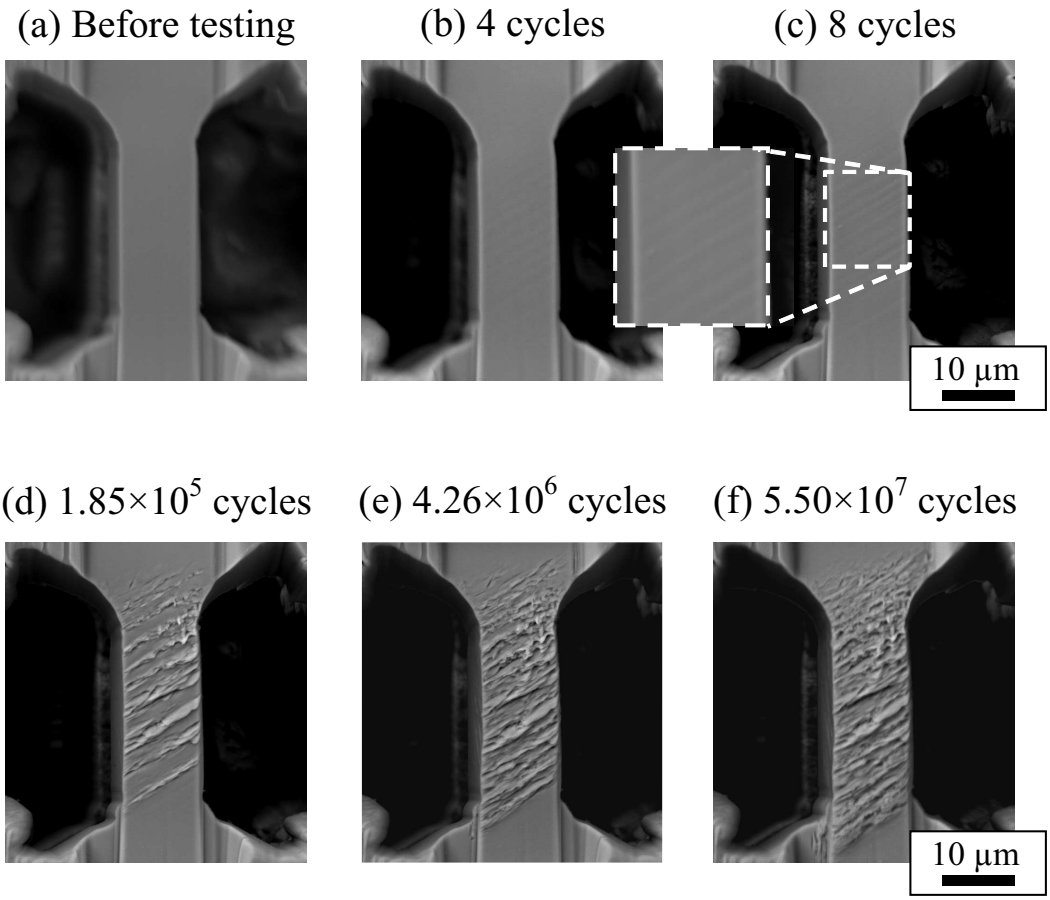

Figure 4.12: SEM micrographs of micro-fatigue experiments taken at various stages between cyclic loading. Cyclic loading was performed at a shear strain amplitude of 1.6×10^{-2}. Each SEM micrograph was taken during brief pauses in cyclic loading. Discontinuities are denoted with arrows. For the first 1.94×10^{7} cycles, the experiment was performed at a cyclic frequency of 75 Hz, after which it was increased to 300 Hz.

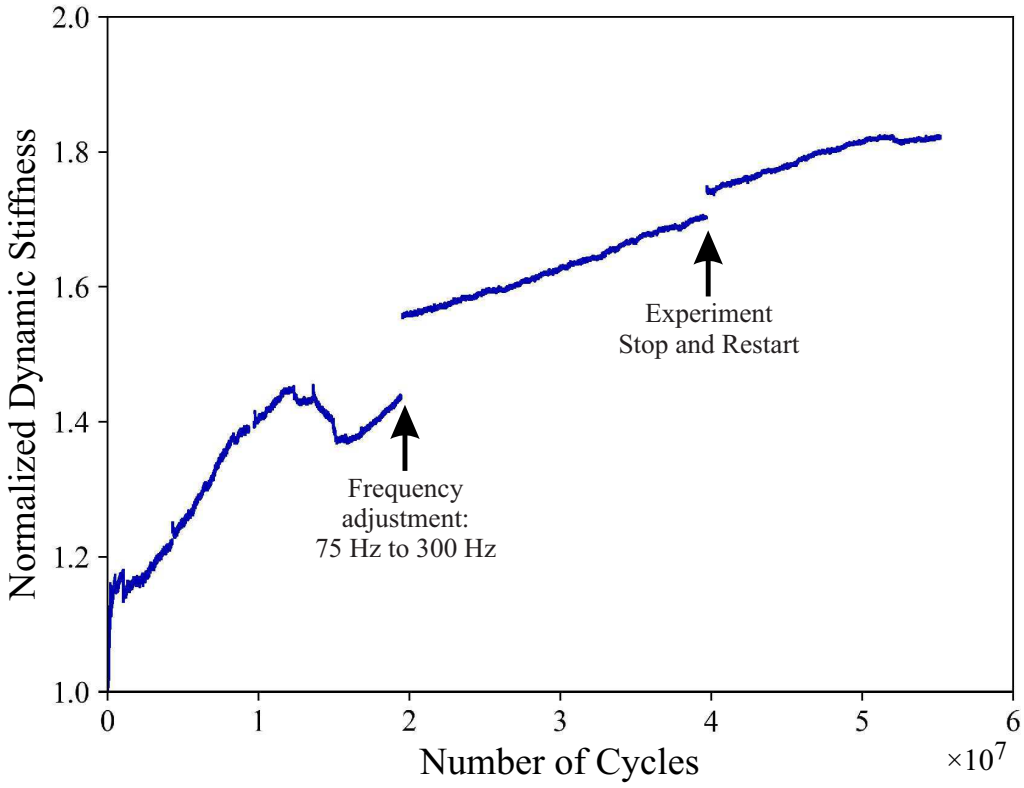

Figure 4.13: Normalized dynamic stiffness versus number of cycles for a hammerhead micro-fatigue experiments performed at a shear strain amplitude of 1.6×10^{-2} at a frequency of 75 Hz.

cycles were reached, the cyclic frequency was increased from 75 Hz to 300 Hz to induce failure more quickly. However, the sample never fractured and the experiment had to be stopped at 5.52×10^7 cycles.

As with low strain amplitudes, the slip bands at high strain amplitudes form along the first present slip traces. Also, the slip markings appear in a non-homogeneous manner. However, here, the slip bands fully propagate within 10^5 cycles. This is approximately 1-2 orders of magnitude faster than the low strain amplitude PSMs in Section 4.2.1.3. This indicates that PSM propagation is highly dependent on strain amplitude. Also, for this higher strain amplitude, many PSMs appear simultaneously, as opposed to one at a time for lower strain amplitudes.

4.2.2.2 Response During Fracture

Although these micro-samples proved to be very difficult to fail, occasional cases were observed where fabrication defects assisted in crack initiation. One experiment that exemplifies this is shown in Figures 4.14 and the measured dynamic properties are displayed in Figure 4.15.

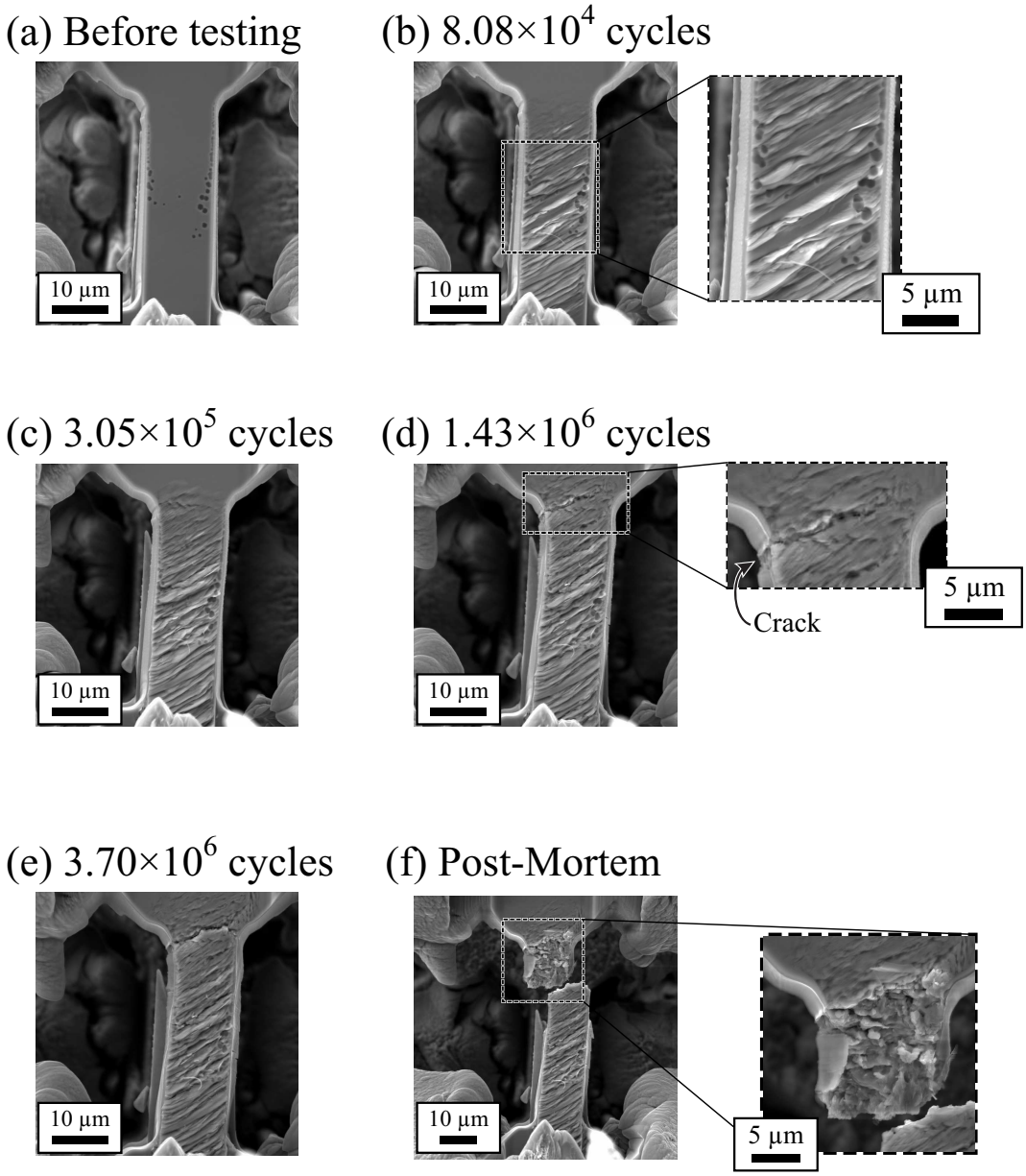

Figure 4.14: SEM micrographs of *in situ* Ni hammerhead experiment taken at various stages between cyclic loading tests (i.e., with no loading applied). The first part of the test is performed at a resolved shear strain amplitude of approximately 2×10^{-2} at 75 Hz. After 3.5×10^6 cycles, the engineering stress amplitude is controlled and ramped up from 172 MPa to 185 MPa at 1 Hz. Note that crater-like defects are evident on the surface of the gage section before testing. These do not have any apparent effect on the experiment.

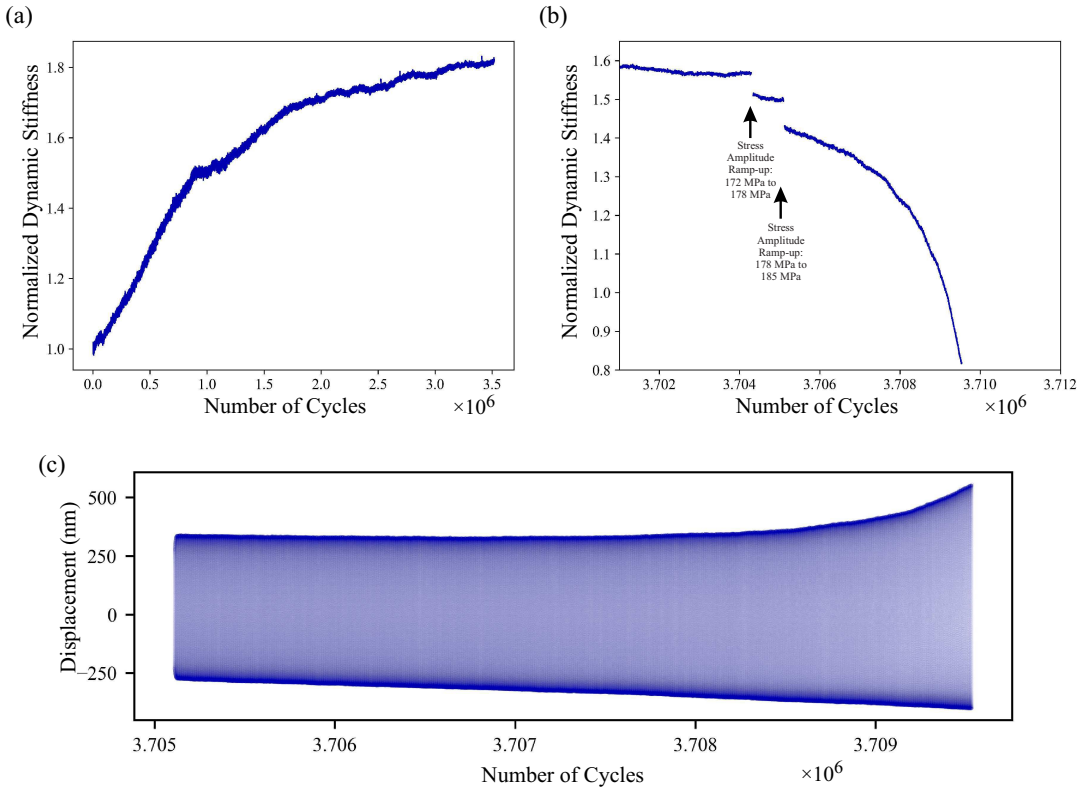

Figure 4.15: Cyclic mechanical properties during fatigue test of Ni hammerhead shown in Figure 4.14: (a) The dynamic stiffness during the first 3.5×10^6 cycles of the test at a resolved shear strain amplitude of approximately 2×10^{-2}. This first part of the test is performed at 75 Hz cyclic loading. (b) After 3.5×10^6 cycles, the engineering stress amplitude is controlled and ramped up from 172 MPa to 185 MPa. This portion of the test is performed at 1 Hz cyclic loading. (c) The displacement versus number of cycles during fracture and stress-controlled fatigue (the tensile direction is positive). Note the increase in displacement amplitude as well as the increased asymmetry as the crack propagates.

The micro-fatigue experiment shown here was initially conducted at a constant displacement amplitude (shear strain amplitude is estimated to be 2×10^{-2}). Note that the surface of the hammerhead gage section appears to exhibit some small crater-shaped defects that were somehow created after FIB fabrication. After 3.05×10^5 cycles, a crack nucleates on the upper left corner at an apparent stress concentrator left after fabrication. At the same time, PSMs start nucleating in the gage region. By the time 1.4×10^6 cycles are reached, the PSMs occupy the entire gage region and the crack has grown to approximately half the gage width, based on surface observations. As the

crack propagates to the right, the uneven load distribution causes the sample to bend to the right. Even with the presence of this crack, the dynamic stiffness (see Figure 4.15 (a)) exhibits hardening behavior with a gradually decreasing cyclic hardening rate. It is not clear what the mechanism is for this gradual decrease in cyclic hardening rate; however, it is likely in large part due to the reduced cross-sectional area of the sample. Other possible contributors are perhaps dislocation microstructure saturation or the increased compliance of the bent sample. This trend of crack propagation and bending continues until the dynamic stiffness plateaus. At this point, the loading method is changed to stress control to drive the crack (corresponding dynamic stiffness curve shown in Figure 4.15(b)). Also, the frequency is lowered to 1 Hz, which results in lower micro-actuator damping and thus a slightly decreased dynamic stiffness. Upon loading with an engineering stress amplitude of 172 MPa there is now a gradual decline in the dynamic stiffness, clearly associated with the crack growth. When the dynamic response appears to stabilize, the stress is ramped up to further drive the crack. Upon ramping up to 185 MPa, the crack now steadily grows and the dynamic stiffness decreases. This decrease continues until the hammerhead completely fractures (see Figure 4.14). The displacement amplitude increases as the crack gets larger and the sample becomes more compliant. As can be seen from the displacement profile in Figure 4.15(c), it is clear that the majority of the increase in compliance occurs on the tension side as the crack opens.

4.2.2.3 Characterization of the Dislocation Microstructure

FIB liftouts from the sample shown in Figure 4.12 were extracted after 5.50×10^6 loading cycles for TEM analysis of the dislocation structure. One liftout was made parallel to the screw plane (i.e., with the primary Burgers vector in plane) and one was made parallel to the edge plane. Bright field TEM of both liftouts are as a shown in Figure 4.16

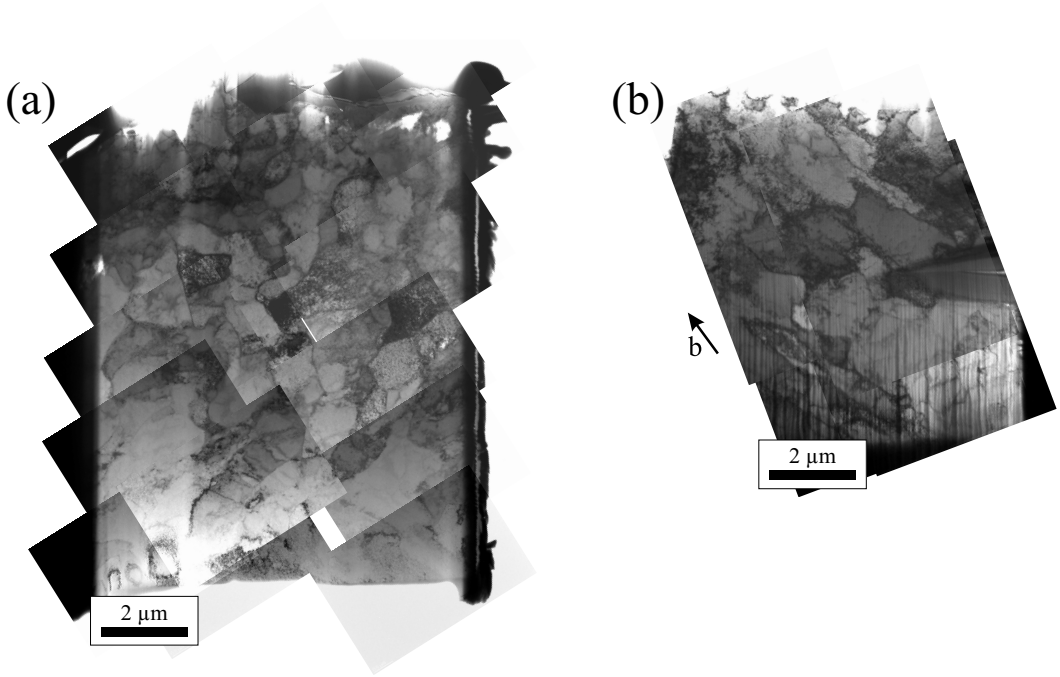

Figure 4.16: (a) Edge plane and (b) screw plane bright field TEM micrographs of cellular dislocation structure of Ni microcrystal after 5.50 $\times 10^7$ cycles at a shear strain amplitude of 1.6×10^{-2}.

It is observed that the dislocation microstructure exhibits many irregular-shaped dislocation walls that are characteristic of a cellular dislocation structure. This is evident in both the screw and edge plane views. The dark walls indicate high dislocation density relative to the practically dislocation-free cell interiors. The slight variations in contrast from cell to cell are a result of slight misorientations as also observed in bulk [239].

The cellular dislocation structure appears to occupy the entire volume of gage section with no PSBs as observed at lower strain amplitudes. The cellular structures on the edge plane appear equiaxial and resemble cellular structures seen in bulk FCC fatigue experiments at high strain amplitudes. Nevertheless, it is not clear that the cells exhibit any elongation in the direction of the Burgers vector as sometimes observed in single slip oriented bulk FCC crystals [14].

Additional *post-mortem* analysis were conducted on the fractured gage

section of the experiment shown in Figures 4.14 and 4.15 to characterize the dislocation microstructure. Once again, TEM was used to to identify the cellular dislocation microstructure on the screw plane (see Figure 4.17(a)). In addition, EBSD was used to obtain orientation data of the TEM foil and the inverse pole figure is shown in Figure 4.17(b) (the fracture surface is at the top of the micrograph). The individual cells are evident by the irregular shaped regions of different orientations. Towards the bottom of the samples (i.e., far from the fracture surface), the misorientations between neighboring cell are relatively small. Interestingly, there is a gradient in orientation of cells towards the fracture surface. A vector is drawn (see arrow in Figure 4.17(b)) and the corresponding relative misorientation is plotted in Figure 4.17(c). This very clearly shows the stepwise manner in which the cells rotated relative to one another to accommodate the bending deformation. Each cell wall serves as a low angle tilt boundary [81]. Along the profile, approximately 30° of misorientation was measured as a result of the bending deformation associated with the crack propagation. The bending, promoted by the non-uniform stress profile, cause the reorientation to occur about normal axis of the edge plane. The cell wall dislocations provide a low energy mechanism to accommodate this deformation [70]. This finding serves as an interesting example of how the multi-slip dislocations in the cell walls are able accommodate generalized deformation.

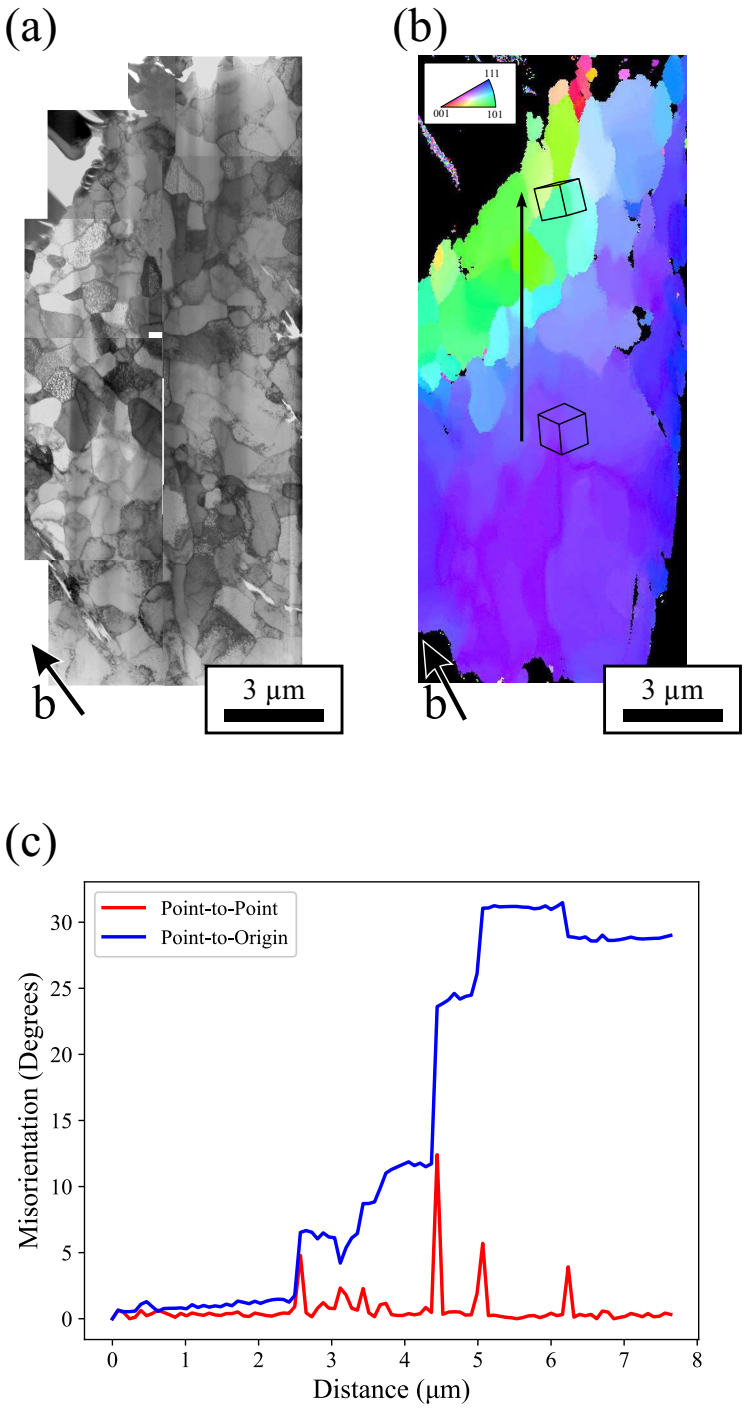

Figure 4.17: Screw plane microstructural analysis of dislocation cells in sample in Figure 4.14 after cyclic loading and fracture: (a) bright-field TEM micrographs showing cellular dislocation microstructure; (b) EBSD inverse pole figure showing out-of-plane orientations; (c) relative misorientation profile along the vector drawn in (b). Note that the fracture surface is at the top of the micrographs in (a) and (b).

4.3 Discussion

4.3.1 PSB Nucleation and Propagation

The *in situ* micro-fatigue experiments at low strain amplitudes in this chapter provide an unprecedented view of the evolution of PSMs: from the very instant of surface nucleation to full propagation. The PSM width along the slip plane have been observed to be as small as 2.6 μm or as large as 8.3 μm at the very first visible surface nucleation event. Additionally, the PSMs are observed to propagate in both directions perpendicular to the Burgers vectors on the primary slip plane. Although PSMs less than 10 μm in width have been observed in bulk fatigue tests [244, 245], the real-time observations of the present study confirm that these PSMs do in fact grow into larger PSMs upon further cylic loading and thus can be considered embryonic PSMs. This gradual evolution suggests certain refinements to conventional PSB models that idealize extrusion formation as a "rapid growth" process [246].

A schematic representation of the nucleation and propagation of a PSB and the resulting surface morphology based on the current *in situ* microcrystal cyclic loading experiments is shown in Figure 4.18(a). Upon the first few cycles of loading, the weakest slip planes in the gage length will activate to accommodate the applied strains. Each of these initially-activated slip planes is now a candidate site for the formation of a PSB. These initial surface slip traces, as seen in the experiments, likely are a result of the activation and escape of the weakest dislocation sources dislocations near the free surface of the microcrystal in the first few cycles. These slip traces are initially stable because the dislocations farther into the interior of the crystal do not move far enough to escape the free surface due to the small strain amplitude imposed on the crystal.

With further cyclic loading, dislocation tangles, such as those seen experimentally in Figure 4.4(b), form throughout the microcrystal with the highest

dislocation density tangles occurring around the softest slip planes. The transition from slip traces to PSMs is directly related to the transition in dislocation structure from tangles to PSBs. Based on the surface observations in the present study, this appears to happen locally along a lamellar slip region adjacent to the initial slip traces. For this to happen, secondary dislocations would have to disentangle and allow the primary dislocations to move freely. Based on discrete dislocation dynamics studies [77, 78, 74, 89, 75], it is well established that these primary dislocations will form dipoles and cluster upon cyclic loading, as depicted in Figure 4.18. Note that now the ladder structure forms and the egress of this embryonic PSB to the surface causes the slip markings to grow.

Once a small region of crystal exhibits a PSB with its own correspondingly small PSM, the observations of the present study suggest that the PSB will grow along the lamellar slip region as depicted in Figure 4.18. This growth would have to be associated with the widening of the ladder rungs. The extrusion height increasing would have to be associated with more ladder rungs forming in the direction of the Burgers vector. Once the PSB widens and fully occupies the entire slip region, the PSM is stable upon further cyclic loading (Figure 4.18(a)(vi)).

Upon analyzing the notion of PSB propagation, it would make sense to consider separately the concepts of PSB lengthening (parallel to the Burgers vector) versus PSB widening (perpendicular to the Burgers vector). The PSB propagation observed *in situ* on the surface of the micro-sample and shown in Figure 4.1 is PSB widening. PSB widening would be related to irreversible dislocation motion through PSB channels that extend the dipolar walls with edge dislocations. PSB lengthening is more difficult to evaluate based on surface features since the screw plane does not form distinct extrusions upon the nucleation of a PSB. However, TEM studies of PSBs have observed a gradient along the Burgers vector from a well-formed ladder dislocation structure to a

matrix dislocation structure [79]. Here, the authors characterize this transition as an untangling of dislocations and thus production of edge dipoles on the primary slip system. Also, the observation that PSBs have been able to transmit across low angle grain boundaries [247] gives credence to the idea that the a PSB will tend to lengthen in the direction of the Burgers vector.

In determining the dislocation mechanisms happening within the crystal volume, various discrete dislocation dynamics (DDD) studies of the early stages of PSB formation are published in the literature. There seems to be a general consensus from such simulations that randomly distributed edge dislocation dipoles will eventually cluster into periodic wall structures upon cyclic loading of a single slip system [77, 78, 248]. This has been shown using parametric dislocation dynamics of dipolar loops [77], 2D dislocation dynamics of edge dislocations [78], and 3D DDD simulations [248]. The main takeaway from these simulations is that randomly spaced dislocations become unstable upon cyclic loading and thus a periodic structure will form with alternating regions of high and low dislocation density. Further theoretical support for this clustering phenomena can be found by referring to the low energy dislocation structures theory [72].

Due to the stochastic nature of initial dislocation microstructures, it would seem unlikely that this clustering phenomena would progress at an equal rate across large length scales. Furthermore, the idealization of a uniform stress field across a slip plane is a very uncommon condition. In materials, there are often stress gradients due to the applied loading conditions. Also, local stress concentrations can be induced by geometric factors, whether due to grain or sample geometry. Areas with higher stresses would be expected to exhibit higher dislocation activity in fatigue and thus be more likely to nucleate PSBs. Once a PSB embryo is present, it could be argued that less cycles would be required for the PSB region to propagate than for another nucleation event to occur independently. The preferential formation of PSBs at stress

concentrations has also been observed in bulk cuboidal samples near corners [249]. Also, the local stresses induced near twin boundaries have also been found to promote PSB formation parallel to the twin boundary [250, 251, 252].

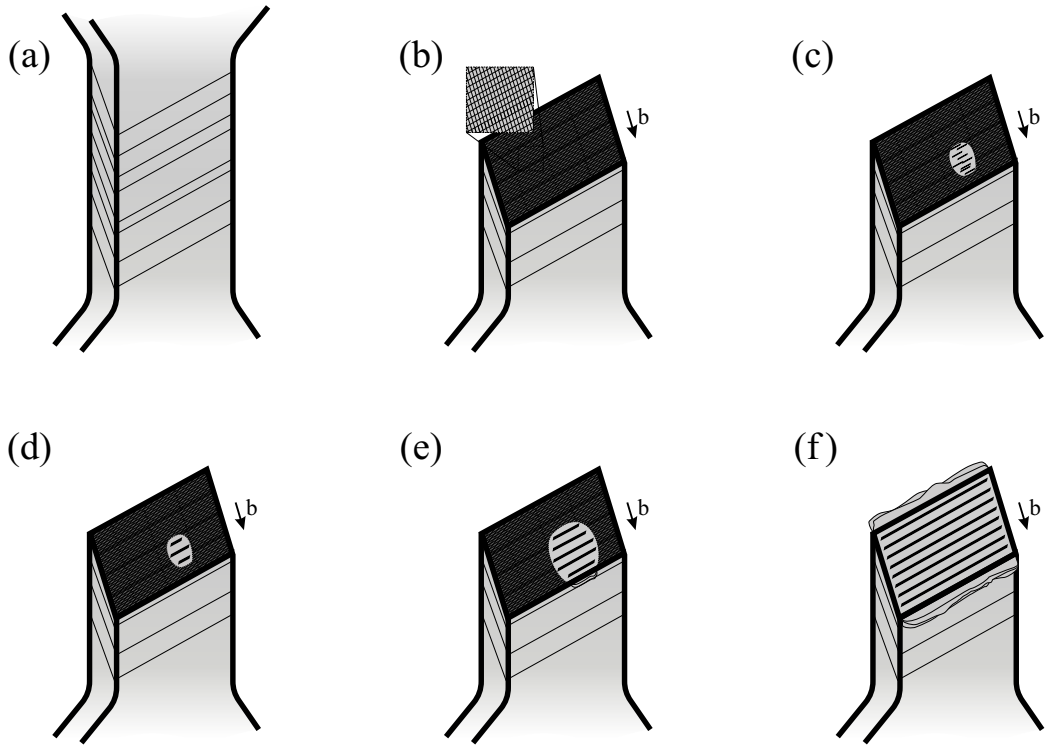

Figure 4.18: Schematic of the proposed PSB nucleation model in microcrystal: (a) Within the first few loading cycles the softest slip planes in the gage length are activated. Dislocations near the surface escape the micro-crystal creating surface steps on the plane with the highest resolved shear stress as defected by the straight lines. (b) After further cycling, dislocation tangles are produced on the primary slip planes in the activated slip regions. These dislocations are also entangled with secondary dislocations (not pictured). (c) At a critical number of cycles, tangles break free in the form of primary edge dipoles. (d) The dipoles cluster into a ladder structure and constitute a PSB nucleus. (e) The PSB nucleus widens and lengthens as dislocations from the surrounding matrix disentangle and become part of the PSB ladder structure due to the to-fro glide of screw dislocations. The egress of this nucleus takes the form of surface markings in the direction of the primary Burgers vector. (f) The propagation continues until the PSB occupies the entire slip region resulting in a more pronounced and stabilize surface markings.

4.3.2 Comparison with PSB Models

The real-time *in situ* observations in the present study provide unique insights with respect to PSB formation and fatigue crack initiation. Although various

PSB models have been proposed in literature, the EGM model is arguably the basis on which most other models build on. In the EGM model, PSMs are predominantly surface extrusions and surface crack initiation is induced by the stress concentration at the interface of the PSM extrusion. For this to be true, extrusions have to precede crack initiation. While the present study exhibits extrusions preceding intrusions, there are also several observations where this is not the case. For example in Figure 4.1(i), an intrusion propagated until it filled the entire gage width and then only later did adjacent extrusions appear all at once as opposed to propagating manner seen for the other PSMs (see Figures 4.1(i)-(k)). Thus, these features must be considered intrusions as opposed to a stress-initiated crack. A very similar observation of individual intrusions preceding extrusions have also been reported in bulk fatigue [253].

The other detail that this study sheds light on is the evolution of surface roughness associated with PSMs. The EGM model predicts that after the static extrusion is present, gradual roughening (i.e., statistical roughening) will occur as the PSB is cyclically loaded. However, this is not observed in the present study. Instead, the PSM seems to have an inherent surface roughness immediately upon formation. After fully propagating, the roughness of a PSM remains stable with further cyclic loading.

4.3.3 Slip Trace Analysis: Early Cycle Versus High Cycle

To further elucidate the origin of PSBs and how they nucleate, the *in situ* observations in this study provide some unique insight. The location of the slip planes that will eventually nucleate PSBs appear to be determined within the first few cycles. This is shown in Figure 4.19 which compares the micro-sample surface morphology for a sample during the early stages of fatigue with the surface after the PSBs have nucleated and propagated. This coincidence of slip traces and PSBs locations is also consistent with observations from bulk

Cu cyclic loading studies [79] and likely indicates that these are the weakest planes in the gage length of the micro-crystal. One interesting finding that the present study seems to add to this is that the cracks/intrusions of the eventual PSBs seem to line up with the slip traces while the PSM extrusions appear to occupy the spaces in between the initial slip traces. For any three adjacent slip traces, the PSMs are most likely to form first between the two that are more closely spaced together. In bulk Ni, slip traces within the first ∼10 cycles have also been observed to coincide with initiated cracks with further cycling [254].

The observation that crack-like openings alongside PSBs coincide with the most active slip planes early in the fatigue life of the specimens can be reasoned by considering the diffusion of vacancies from the PSB to the surrounding matrix [244]. If these early slip regions are believed to contain a higher initial dislocation density, they would attract vacancies since dislocations are known to act as sinks for vacancies. The accumulation of vacancies could form a crack-like opening along the PSB-matrix boundary (i.e., an intrusion).

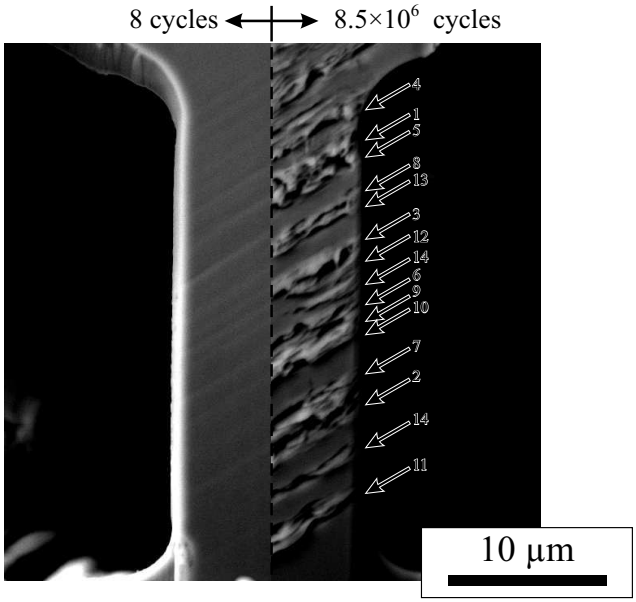

Figure 4.19: High contrast SEM micrograph of the surface morphology of a Ni hammerhead cyclically loaded at a shear strain amplitude of 6.3×10^{-3} after 8 cycles (left side) and 8.5×10^{6} cycles (right side). The numbers indicate the observed order with which the PSMs emerged from the surface (excluding PSMs not in the field of view during testing).

4.3.4 Size-effects at Low Strain Amplitudes

High dislocation density veins are characteristic dislocation microstructures that are generally observed in bulk cyclic loading experiments. These veins usually constitute the matrix that proceed PSB nucleation. Furthermore, once PSBs form, a saturation in the cyclic mechanical response is reached and no further hardening is observed. At room temperature, this saturation is achieved after $\sim$100 to 10^4 loading cycles [255, 238].

One curious aspect of the dislocation microstructure observed in the current study that contrasts with bulk studies is the lack of high dislocation density veins in the matrix. Although veins were observed on local regions of samples cyclically loaded at low shear strain amplitudes (see Figure 4.4(b) and (f)), they were not seen nearly as consistently as those found in bulk studies of fatigued Ni or Cu [237, 235]. Also, the veins observed here have much less dislocation density and much smaller size as compared to those observed in bulk. Instead, the matrix is mostly composed of dislocation tangles. The dislocation density distribution of these tangles seemed to be very heterogeneous with a higher density near PSBs and a lower density far from the PSBs or surrounding vein structures (see Figure 4.4(b)). Thus, we hypothesize that the loosening of these dislocation tangles is a necessary precursor for generating free dipoles that eventually cluster into dislocation walls. The fact that similar dislocation tangles were found within PSB channels (see Figure 4.4(d)) could mean that there are still more dislocations that could untangle upon further cyclic loading. This is consistent with the model proposed by Tabata et al. [79] for bulk crystals, where it was proposed that for a PSB wall to form primary edge dislocations have to be untangled from secondary dislocations so that they could cluster. These tangles also resemble those observed in DDD fatigue studies [248, 75]. Such DDD simulations suggest that dislocation tangles were very immobile relative to dipolar loops [248]. Thus, the limiting step in

nucleating a PSB may be the number of cycles required to disentangle these dislocations and create dipolar loops. The subsequent clustering process likely happens relatively quickly after disentanglement as shown in DDD simulations [77, 78, 74, 75].

Explanations for why veins may not be prevalent at this size scale could be attributed to the high surface to volume ratio as compared to bulk single crystals or polycrystals [95]. In the case of cyclic loading, the free surface would make it more difficult for the interior of the micro-crystal to accumulate dislocations. Since high dislocation densities are necessary to produce veins, this would inhibit their formation. Additional evidence for this can be found by observing the dynamic stiffness curve in Figure 4.1(q). This lack of veins would greatly limit the number of sources for a PSB to nucleate. This could explain the large number of cycles ($>10^6$) necessary to nucleate a PSB, and correspondingly, the extreme fatigue lifetimes exhibited in this study.

Another potential consequence of this finding is that veins may not be a necessary condition to produce PSBs even though they are often found in the surrounding matrix of PSB-matrix microstructures [237, 235]. A more general requirement for the nucleation of PSBs would be the presence of enough dense dislocation tangles. Veins would meet this requirement, but it could be argued that the dense clustering that is characteristic of veins is not a necessity. In past studies, matrix regions of fatigued FCC metals without the typical vein pattern have also been observed in bulk Cu [245] and austenitic steel [245].

4.3.5 Probabilistic Model of PSB Formation

The physical source from which PSBs nucleate are primary dislocations that have untangled from dislocations on secondary slip systems. As suggested by the current results, this can take the form of veins or dislocation tangles. Small volumes significantly reduce the likelihood that a possible nucleation event will

occur since fewer sources are available to nucleate a PSB. For example, in bulk with a large density of veins, there are many sources to nucleate a PSB from, whereas planar dislocation tangles are less likely to nucleate a PSB.

Based on the PSB nucleation mechanism proposed in Section 4.3, in the following a statistical approach is proposed to predict the number of cycles required for PSB formation in single crystals as a function of the crystal size. The limiting step is the formation of a local nucleus in a lamellar slip region of relatively high dislocation activity. The subsequent propagation occurs shortly after the formation of a PSB nucleus. A larger slip plane area would be expected to result in an increase in the probability of PSB nucleation and thus a reduction in the number of cycles required for nucleation. To describe this, a Poisson point process distribution is chosen to represent the random nature of nucleation in a 2D region. Using this distribution, the probability of m nucleation events occurring between cycle N_i and cycle N_j is

$$P(m, N_i, N_j, D) = \frac{f^m(N_i, N_j, D) \exp[-f(N_i, N_j, D)]}{m!}, \tag{4.2}$$

where $f(N_i, N_j, D)$ is the number of nucleation sources generated from cycle N_ith to cycle N_j and D is the area edge length. The assumption is that in the lower limit of D, the PSB nucleation rate would be proportional to the area of the slip region (i.e., $f(0, m', D) \propto D^2$). However, a quadratic form for $f(0, m', D)$ would cause the nucleation rate to go to infinity at the bulk-scale (i.e., large D), which is not physical. Thus, to set a lower bound for the cycles required to nucleate a PSB, an exponential function of the following form is chosen for f:

$$f(0, m', D) = \lambda_0 m' \left(1 - \exp\left(-\frac{D^2}{D_0^2}\right)\right) \tag{4.3}$$

where λ_0 is dependent on the material, crystallographic orientation, and strain

amplitude. Using this functional form, $f(0, m', D) \approx \lambda_0 D^2$ for small D and $f(0, m', D) \to \lambda_0$ as $D \to \infty$. Here the length scale at which bulk behavior is recovered, D_0, is another parameter in this functional form. Note that this form for f is one of various forms that could be used to capture this phenomenological behavior.

The corresponding expected number of cycles to the first nucleation event for the functional form in Equation 4.3 is given by

$$E_{cyc}[m'] = \sum_{m'=0}^{\infty} \exp[-f(0, m', D)] = 1 + \frac{1}{\exp(\lambda_0(1 - \exp(-D^2/D_0^2))) - 1}. \tag{4.4}$$

Equation 4.4 is plotted versus D in Figure 4.20 for $\lambda_0 = 10^{-3}$ since this value corresponds to 10^3 cycles to nucleation, which corresponds to the bulk response. Various values of D_0 are plotted.

Data from the Ni hammerheads in the present chapter are included as well as data from bulk scale Ni fatigue studies[255]. Since the onset of cyclic saturation is associated with the number of cycles required to nucleate a PSB, approximate values for cycles to saturation using the following analysis procedure on dynamic stiffness curves and cyclic stress curves (from the literature). First, for the initial cyclic hardening, the linear region was identified and the associated hardening rate was determined. Then, the region was expanded to include later cycles and the overall hardening rate of this new region was repeatedly determined. Once the cyclic hardening rate started to bend and no longer exhibit linear behavior, the overall hardening rate decreased. The first cycle number where the overall hardening rate reached 90% of the initial linear value was considered to be the onset of cyclic saturation. This criteria was defined so that the onset of saturation could be consistently identified. The 90% criteria was selected because higher values yielded false positives due to experimental scatter. Lower values yield overly conservative values for the

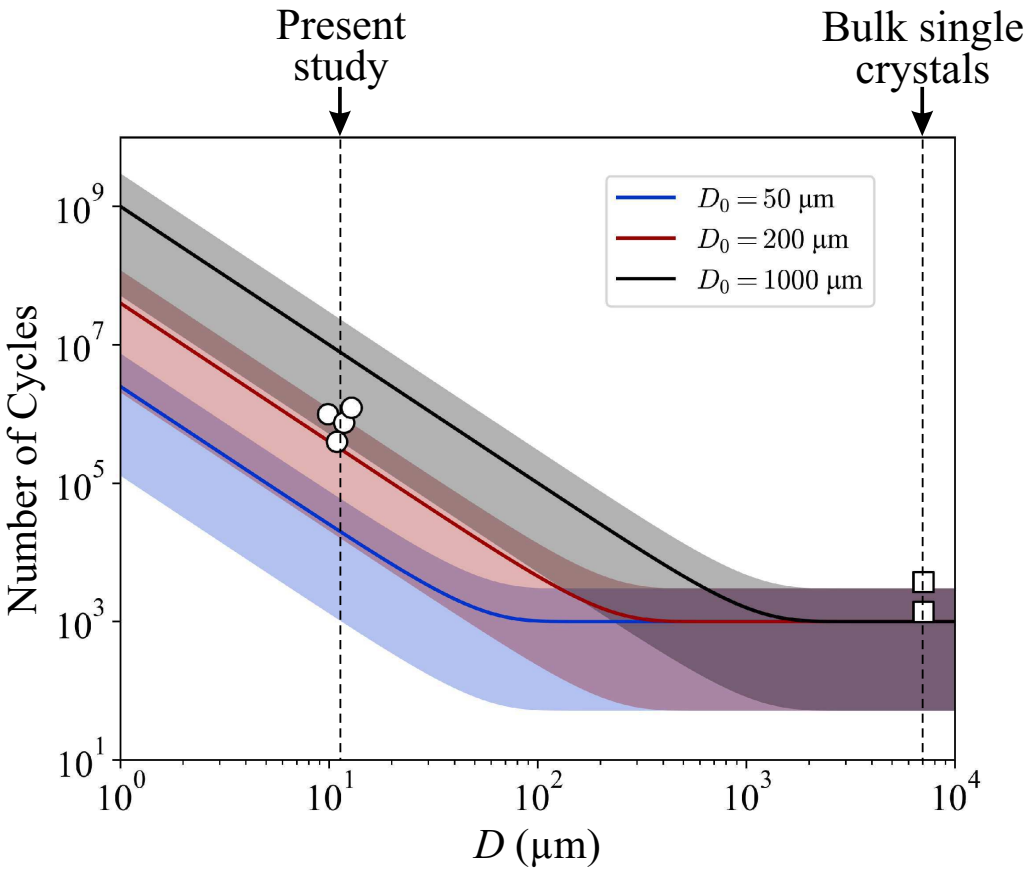

Figure 4.20: Curves shown are the expected number of cycles for the first PSB nucleation event in a single crystal versus crystal size, D as described by Equation 4.4 for $\lambda_0 = 10^{-3}$. Shaded regions are the 90% confidence intervals. The experimentally observed numbers of cycles for the onset of saturation (which is related to the onset of PSB formation) are are also included for the microcrystals studied here as well as for bulk crystals reported in literature. Resolved shear strain amplitudes for data in the present study range from 3.5×10^{-3} to 6.3×10^{-3}. Bulk data is reported for Ni single crystals with an orientation of $[\bar{1}49]$ (single slip) with resolved shear strain amplitudes at the onset of saturation of 3.3×10^{-3} (the upper square data point) and 4.7×10^{-3} (the lower square data point) [255]. For rectangular samples, the effective D is reported.

onset of saturation.

The proposed nucleation model clearly captures the effect of size on the number of cycles required for PSB nucleation. Also, the convergence to the bulk response can be seen above D_0. It would appear that a D_0 of $\sim$200 μm agrees closely with the values and scatter for the strain amplitudes considered in the present study. However, data at intermediate size scales is needed to clearly identify this transition from bulk to size-affected behavior. It should be noted that for the bulk data, the range of values for the reported data are due to the changes in strain amplitude. Larger strain amplitudes saturate more quickly than lower strain amplitudes. For this reason, the samples considered for Figure 4.20 have comparable strain amplitudes. In the current model the effect of strain amplitude on the nucleation rate is implicitly incorporated in the parameter λ_0.

4.3.6 Size Effects on the Fatigue Response at High Strain Amplitudes

In bulk Cu single crystals at high strain amplitudes, $<10^5$ cycles are needed for the cyclic mechanical response to saturate [256]. At high shear strain amplitude (1.6×10^{-2}) the fact that the sample continues to harden well after 10^7 cycles (see Figure 4.13) is surmised to mean the dislocation density increases at a much lower rate than in bulk. Thus, the micro-samples harden over the course of a much longer number of cycles. This could be explained by the high surface-to-volume ratio of the samples in the present study. It has been shown with dislocation dynamics simulations of Ni that smaller volumes lose dislocations to free surfaces and thus require more cycles to accumulate dislocation density [95].

Having established that dislocation microstructure is in a state of transition for the entire 5.50×10^7 cycles of the experiment, it is interesting that the

surface morphology stabilizes and is relatively constant for the vast majority of this time after the gage section has been entirely occupied by slip traces. This would suggest that the plastic deformation occurring within the microcrystal is homogenous, consistent with bulk findings [14].

A consequence of this homogeneous deformation is the lack of crack initiation mechanisms. Fatigue crack initiation generally requires localized strain incompatibilities for a fatigue micro-crack to nucleate [69]. The uniformity of dislocation motion makes crack initiation difficult [14, 239]. While crack initiation mechanisms similar to intergranular fracture could still occur [234], it is hypothesized that the small misorientation angles between fatigue cells make this unlikely to occur. This could very well explain the lack of fatigue cracks, even though micro-cracks have been seen in small-scale micro-fatigue experiments at lower strain amplitudes. With conventional fatigue crack initiation mechanisms unavailable with dislocation cell microstructures, it would seem that the limiting factor in fatigue lifetime would be related to fabrication defects on the sample surface.

4.3.7 The Effect of Crack Growth on the Phase Angle During High Frequency Cyclic Loading

The dynamic stiffness is dependent on the load amplitude, displacement amplitude, and the phase angle, ϕ (see Equation 2.6). When ϕ is close to 90° (i.e., resonance), the $\cos(\phi)$ term is the dominant contributor when there are changes in sample stiffness or plastic behavior. However, when ϕ is small, $\cos(\phi)$ is approximately 1 and the load and displacement amplitude signals are more dominant in the dynamic stiffness. However, looking at $\tan(\phi)$ separately from the dynamic stiffness provides information that otherwise would be difficult to extract from the load or displacement amplitude.

As shown in Chapter 2, changes in ϕ depend on the elastic stiffness and well

as the damping properties from both the loading apparatus and the sample. For example, during cyclic loading of the Renè-N5 cantilever beams in Chapter 3, ϕ increased monotonically during crack growth and was the dominant contributor to changes observed in the dynamic stiffness. This was true even in cases where changes in the force amplitude were small because of the high degree of load cell damping.

The only physical mechanisms that could explain an increase in ϕ is either an increase in damping or a decrease in the elastic stiffness of the sample. At a constant strain or load amplitude, it would be expected that the plastic strain would decrease as the number of cycles increases (i.e., decrease in damping). Thus, it is assumed that the increases in ϕ are directly attributable to crack growth and the resulting reduction in cross-sectional area of the sample.

In Figure 4.21, various $\tan(\phi)$ curves are shown for Ni micro-samples cyclically loaded at different shear strain amplitudes. All of the Ni micro-samples exhibit a steady decrease in $\tan(\phi)$ at least during the initial stages of fatigue life. This is presumably due to the reduced plasticity as the sample cyclically hardens. The reduction in rate of decrease of $\tan(\phi)$ can possibly be attributed to the reorganization of the dislocation structure from random tangles to low energy dislocation structures such as PSBs and cells.

Later in the fatigue life, the behavior of $\tan(\phi)$ is much more erratic and less consistent between experiments. Often, although not always, $\tan(\phi)$ increases toward the later stages of fatigue life as can be seen at strain amplitudes ranging from 4.5×10^{-3} to 1.1×10^{-2} in Figure 4.21. This effect is most pronounced for the 6.3×10^{-3} shear strain amplitude experiment where $\tan(\phi)$ increases at a steady rate for almost the entire second half of the fatigue life and nearly recovers the initial value upon cyclic loading. In contrast, for experiments performed at shear strain amplitudes of 4.5×10^{-3} and 1.1×10^{-3}, an abrupt increase is sometimes observed, but not always maintained. As displayed in Figure 4.21, experiments that exhibit these increases in $\tan(\phi)$ are also those

Shear strain amp.	tan(ϕ) during fatigue tests	Electron micrographs of samples after fatigue testing	Cracks visible?
4.2×10^{-3}	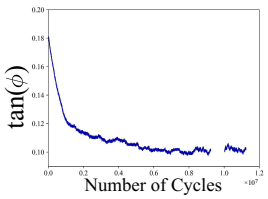	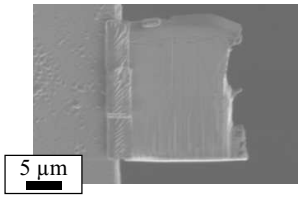	✗
4.5×10^{-3}	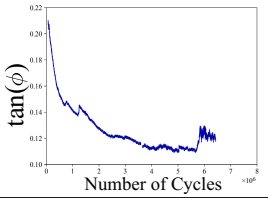	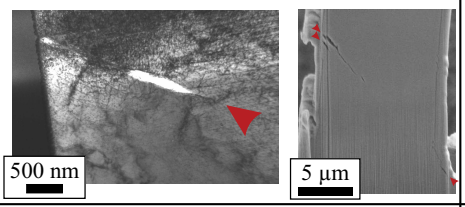	✓
5.2×10^{-3} to 7.8×10^{-3}	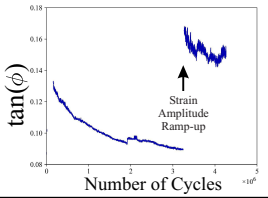	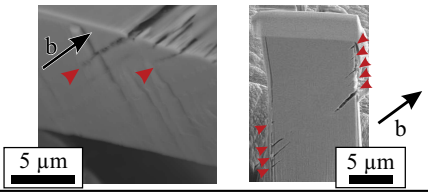	✓
6.3×10^{-3}	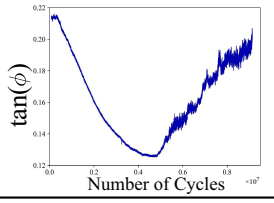	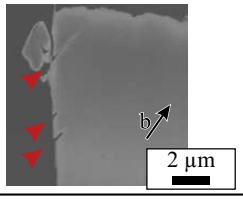	✓
1.1×10^{-2}	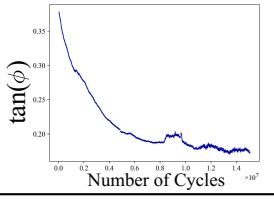	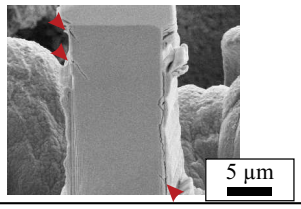	✓
1.6×10^{-2}	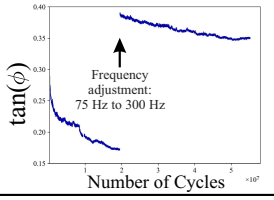	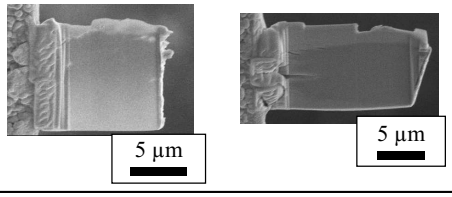	✗

Figure 4.21: Summary of hammerhead microsample fatigue experiments: resolved shear strain amplitude on the primary slip system, tan(ϕ) during cyclic loading, micrographs of samples after fatigue testing, and whether or not cracks were found during post-testing characterization.

where Stage I micro-cracks were observed in later stages of analysis. These cracks are difficult to observe during *in situ* analysis with only one viewing angle of the surface available during testing. These observations, along with the fact that cracks have been previously shown to correlate with increases in ϕ [149], it is reasonable to attribute these increase in $\tan(\phi)$ to crack initiation/growth events.

As mentioned previously, once an increase in $\tan(\phi)$ is observed, it does not always monotonically continue to increase for the samples in this chapter. For example, for the 4.5×10^{-3} strain amplitude experiment, there is an abrupt increase in $\tan(\phi)$ and then afterwards, $\tan(\phi)$ continues to decline. This indicates that the although a crack is present, it does not continuously grow and cyclic hardening mechanisms are still active in the meantime. The crack does not continuously grow in these experiments because they are all strain controlled. Once a crack is present, the sample stiffness reduces and the load amplitude must compensate for the increase in displacement amplitude by decreasing.

In future micro-fatigue experiments, $\tan(\phi)$ could be a useful indicator of changes in sample stiffness as compared to looking at the dynamic stiffness alone. This could be of significant importance when conducting experiments at frequencies so high that the damping from the actuator is too high to accurately determine the load on the sample, such as in Chapter 3.

4.3.8 Scatter in Dynamic Data During Crack Growth

Another interesting feature seen in the $\tan(\phi)$ signal during the later stages of fatigue is an increase in the scatter, most notably in the 6.3×10^{-3} shear strain amplitude sample after 0.5×10^{7} cycles. As can be seen in Figure 4.21, $\tan(\phi)$ during some fatigue tests exhibits more erratic behavior about the mean $\tan(\phi)$ value during later stages as compared to the early stages of fatigue. Although

only $\tan(\phi)$ is shown, this scatter is also seen in the load and displacement amplitude signals and is an artifact of the control loop of the cyclic loading methodology. It is surmised that once a crack is present, the displacement amplitude increases rapidly. In response, the load amplitude must rapidly decrease to maintain the strain or displacement amplitude. This tug-of-war behavior continues and likely stabilizes the crack growth. The larger scatter is thus believed to be caused by meta-stable crack growth and the time delay required for the control loop to stabilize the displacement amplitude at the target value. One point of interest is that for the 6.3×10^{-3} shear strain amplitude experiment shown in Figure 4.21, the scatter does not increase appreciably right after the increase in $\tan(\phi)$ is observed. This would seem to indicate that $\tan(\phi)$ is perhaps more sensitive to the presence of a crack than either the load or displacement amplitude signal since the crack(s) present at this point are likely too small have a significant impact on the elastic stiffness of the micro-sample.

4.3.9 Displacement Amplitude Bursts During Fatigue Crack Growth

In the experiment shown in Figure 4.14, once a crack $\sim$1μm in size is seen on the surface, the loading method is changed to displacement amplitude control to load amplitude control to drive the crack. This portion of the experiment starts at cycle 3.70×10^6 and the continues for another 10^4 cycles until complete fracture. The increase in the displacement amplitude as the crack grows is clear from the displacement signal (see Figure 4.15(c)).

The displacement amplitude is calculated in real time during the test by continuously performing an FFT over a moving window 1 cycle in length. The displacement amplitude for the same experiment in shown in Figure 4.22. The inset of Figure 4.22 reveals that the incremental increases in displacement

amplitude happen in an intermittent manner. There appear to be periods of steady increase with periods of constant amplitude in between. Since the load amplitude is constant during these events, it would seem that these increases in displacement amplitude must be a consequence of crack growth events. In other words, these events are physical and not an artifact of the actuator control script. When the crack grows, it grows continuously for several hundreds of cycles and then stops, as indicated by the leveling off of the displacement amplitude. This unstable equilibrium is maintained until the crack once again proceeds to propagate and the displacement amplitude again increases continuously. This process continues until the micro-sample completely fractures.

Although the crack size cannot be directly measured, it is clear that these intermittent increases in displacement amplitude are correlated with the crack size. Thus, the stair-step profile seen in the filtered displacement amplitude signal reveals that the micro-crack considered here grows in a discontinuous manner. Intermittent burst events are present in various other natural phenomena such as avalanches [257], earthquakes [258], and dislocation plasticity [18]. With these type of intermittent events, a statistical treatment is necessary to characterize their dynamical behavior.

A threshold-based data analysis method, as detailed in Section 2.5, is used to extract displacement amplitude bursts during the course of the experiment (see the right axis of Figure 4.22). After the burst size data is obtained, the data is then binned according to the burst magnitude using a logarithmic scale. The solid lines in Figure 4.23(a) represent the logarithmically binned probability distributions from the burst data. For the high burst sizes, a power-law probability distribution is used. The functional form for the power law probability distribution is given as follows:

$$p(x) = Cx^{-\alpha} \tag{4.5}$$

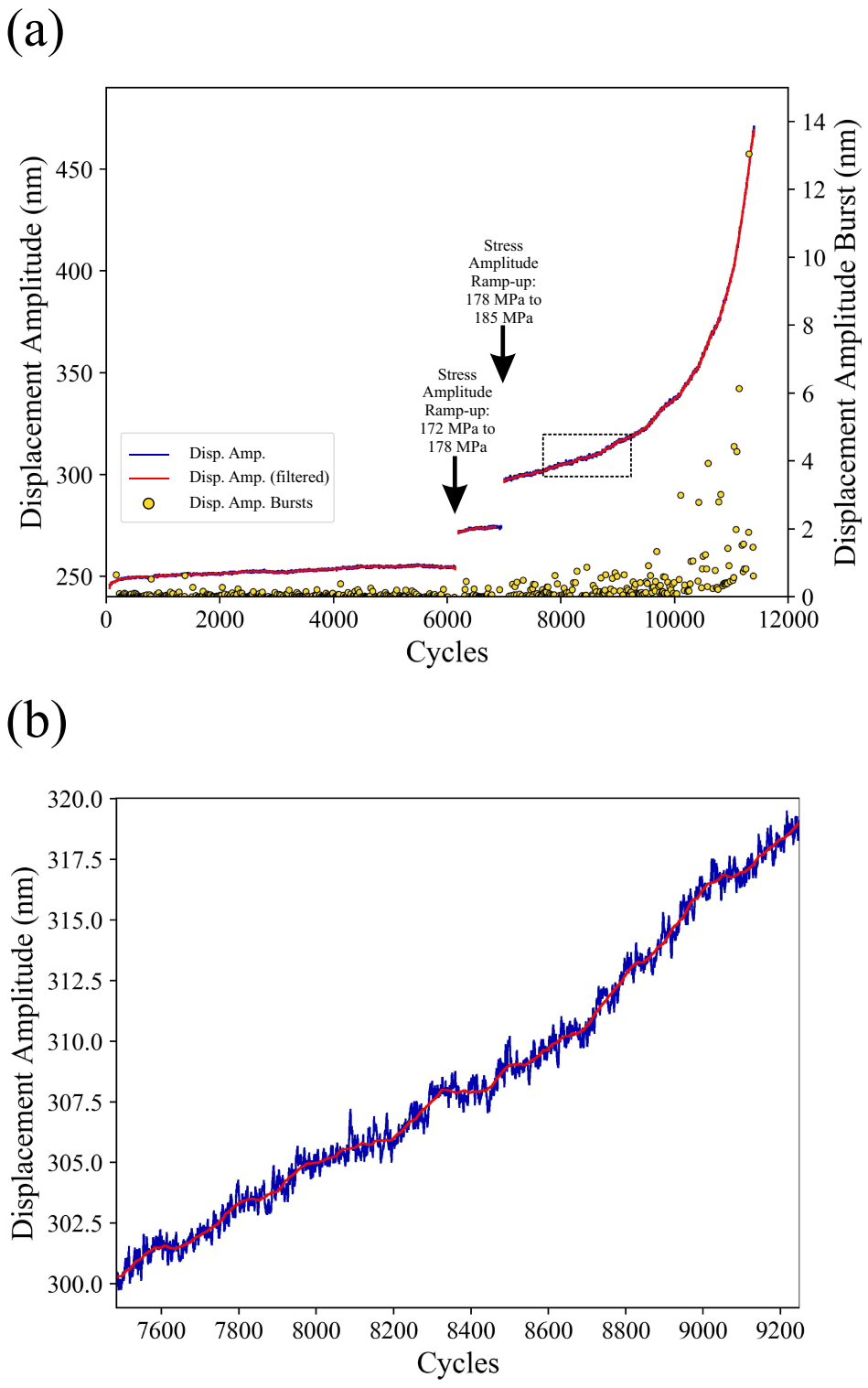

Figure 4.22: (a) Displacement amplitude and displacement amplitude bursts versus cycles for Ni hammerhead micro-fatigue experiment shown in Figure 4.14. (b) Dashed line inset from (a).

where C and α are fitting constants and x is the event size.

The binning, and thus the curve-fitting, is sensitive to the lower bound cutoff, x_{min}, above which data is used for subsequent analysis. It should be noted that applying a cutoff is reasonable since the test instrument has a limited amount of resolution (0.04 nm) in the displacement signal. Upon observing the binned data with no cutoff applied in Figure 4.23(a), it is clear that for smaller burst sizes, the probability distribution becomes flat, which is characteristic of a random uniform event distribution such as instrument noise. To avoid arbitrarily choosing this cutoff, a parametric study is performed whereby a range of values for x_{min} are considered and the resulting α, Kolmogorov-Smirnov distance (D), and standard error (SE) are reported in Figure 4.23(b).

Two local minima in D are found by parameterizing x_{min}. One minima results in the absolute lowest D but with a SE greater than 0.10. The other minima results in a higher D but a SE below 0.05. Both local minima are considered and the resulting curve-fit power law distributions are plotted as a dashed-line in Figure 4.23(a). Values for α obtained are 1.72 and 2.20. It should also be noted this analysis was performed on a similar fracture experiment and values for α of 1.54 and 1.70 were obtained, although the goodness-of-fit parameter was much larger ($D >$0.16) since less burst data was obtained in this experiment. In contrast, values for α in large crack growth of polycrystalline Cu were found to be 1.81 for an experiment in air and 1.33 in liquid (note that the present study is performed in vacuum) [259].

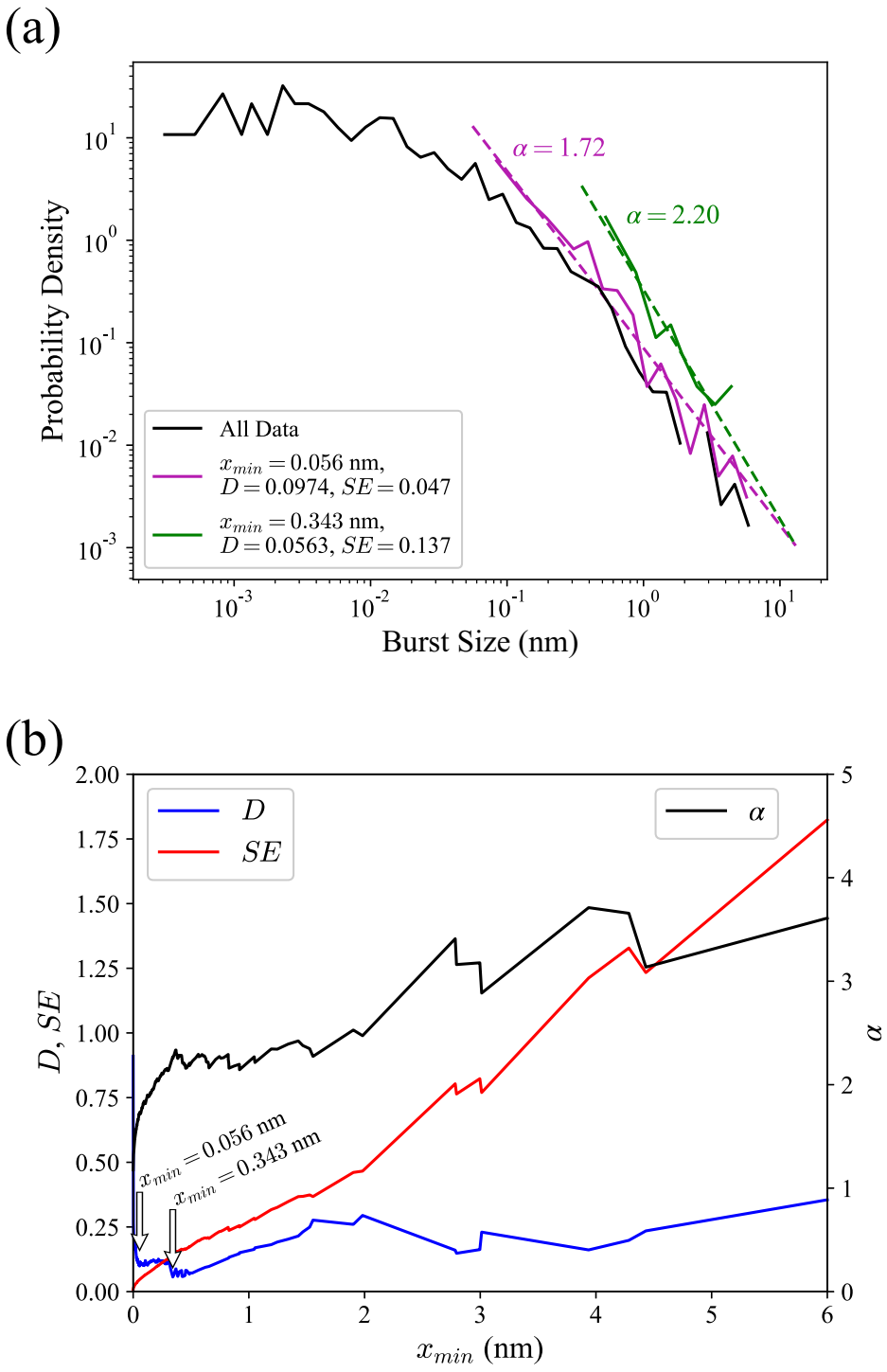

Figure 4.23: Burst probability distribution analysis: (a) logarithmically binned data (solid lines) and power-law curve fits (dashed lines); (b) parametric study on the effect of the lower cutoff, x_{min} on the Kolmogorov-Smirnov distance (D), the standard error (SE), and the power-law exponent (α). Local minima are denoted with arrows.

4.4 Conclusions

In this chapter, a novel small-scale, *in situ*, uniaxial micro-fatigue method was demonstrated on Ni microcrystals oriented for single slip. Using dynamic measurements, real-time SEM observations, and *post-mortem* characterization, unique observations of dislocation microstrucure evolution and fatigue fracture were obtained.

TEM characterization revealed that PSBs and dislocation tangles were observed at low shear strain amplitudes ($\leq 1.5\times10^{-2}$). Veins were also found but only sporadically and were markedly different from those found in bulk Ni. The lack of veins was believed to be a size effect related to the difficulty in accumulating dislocations with the high surface-to-volume ratio. Using *in situ* surface observations, PSMs were found to nucleate locally within microcrystal volumes and then propagate until they spanned the entire slip region. PSBs at low strain amplitudes took many more cycles ($>10^6$) to form than what is typically required in bulk single crystals. This is believed to be due to the fact that a smaller volume would have fewer PSB nucleation sources and a statistical model is proposed that captures this behavior. Slip traces formed within the first $\sim$10 cycles are found to be indicators of where PSMs, and thus cracks, will eventually form. This is of significance for non-destructive damage quantification (i.e., failure prediction) as well as to the physics-based modelling community since simulating microstructures in fatigue is usually too computationally expensive to perform simulations past 100 cycles. These low shear strain amplitude findings are important in understanding the early stages of PSB formation. This fundamental insight can be used to connect these microscale deformation mechanisms with fatigue failures at the bulk scale.

At high shear strain amplitudes (i.e., $>1.5\times10^{-2}$) cyclic hardening was also exhibited with a diminishing rate as the number of cycles was increased,

although true cyclic saturation was not always achieved. This was attributed to a size effect where the high surface-to-volume ratio made it difficult for the crystal to accumulate dislocations. Cellular dislocation microstructures, similar to those found in bulk single crystal fatigue, were observed in the fatigued micro-specimens. Very high numbers of cycles were reached ($>10^7$) without any signs of fracture. However, fabrication defects were found to occasionally lead to crack initiation and subsequent failure. This extreme fatigue life was attributed to the limited fracture mechanisms available with a cellular dislocation microstructure. This behavior at high strain amplitudes indicates that sample life in single crystals cyclically loaded at high strain amplitudes may be more sensitive to defects than dislocation microstructure.

For samples that did fracture, the displacement amplitude signal proved to be an indirect signature of crack size. Analysis of the displacement amplitude revealed an intermittent crack burst pattern that followed a "scale-free" power-law probability distribution. This finding may indicate that microscopically short cracks are self-organized critical in nature.

Chapter 5

Acoustic Emissions During Compression of Nickel Microcrystals

5.1 Introduction

In mechanical testing of materials, the far-field boundary conditions (e.g., stress and strain) are an ensemble average of local contributors throughout the sample volume. These physical sources can be any number of deformation and fracture events. In addition to affecting the mechanical response, these local sources also radiate elastic stress waves that travel through the material. These waves, known as acoustic emissions (AE), can be detected during mechanical testing with high temporal resolution as opposed to measuring the cumulative effects of each event (i.e., far-field measurements). The AE signal of an event is directly related to the physics of source, such as dislocation plasticity or crack propagation.

For dislocation plasticity, there are three dominant AE mechanisms [260]. One, the relaxation of a transient stress field induced by a dislocation in mo-

tion. Two, the sudden nucleation or annihilation of a dislocation, either from another dislocation or at the surface of the crystal, radiates an AE wave. Three, the acceleration or deceleration of a dislocation produces an acoustic Bremsstrahlung. For example, a Frank-Read source continuously produces dislocations and thus radiates AE energy upon activation. The Bremsstrahlung energy of the associated AE has been modeled using the Eshelby model for a vibrating screw dislocation [261, 262]:

$$E_B = \frac{\pi \mu b^2 l^2 \bar{v}^2 \omega_0^2}{5c^3} \tag{5.1}$$

where l is the dislocation length, ω_0 is the frequency of vibration, c is the transverse wave velocity, and $\bar{v}$ is the average dislocation velocity. It is important to note that the energy emitted by an individual dislocation motion is too small to be detected by modern AE equipment. Rather, collective motion of dislocation ensembles ($\sim$10's of dislocations) are detectable by AE. For multiple dislocations, $N = L/l$, where L is the total dislocation length. Thus, the total energy is [262]:

$$E_{tot} = Ll\frac{\pi \mu b^2 \bar{v}^2 \omega_0^2}{5c^3} \tag{5.2}$$

Equation 5.2 reveals that the AE energy from dislocation motion is related not only to the total dislocation density, L, but also the individual segment length, l. In other words, for a given total dislocation length L, more energy would be emitted from one long dislocation line than that from individual, coherently moving short dislocation segments, all else being equal.

While these elastic models are useful for comparing the AE energy released by different dislocation mechanisms, these parameters are not directly measured by AE. To compare physical dislocation models with AE data, the Fleischmann model was developed to predict the AE signal power detected by a dislocation segment initially at rest and then suddenly moving a distance, s,

at a velocity, v [263, 264]:

$$W = \frac{2}{\pi} Z b \dot{\varepsilon} l^2 V \sin^2 \left(\frac{\omega s}{2v} \right) M^2(\omega) \Delta\omega \tag{5.3}$$

where $\dot{\varepsilon}$ is the resulting strain rate, V is the sample volume, ω is the AE sensor frequency, $\Delta\omega$ is the AE sensor bandwidth, Z is the acoustic impedance of the material, and $M^2(\omega)$ is a transition function dependent on the sample geometry and ω. Several noteworthy items can be found by examining Equation 5.3. One in particular is the dependence of the AE power on the sensing frequency. The maximum in power (i.e., the maximum detectability) occurs when the AE sensor is detecting at $\omega = \pi v/s$. Also, longer dislocation segments, l, produce more AE power, consistent with Equation 5.2. Finally, larger sample volumes, V, result in larger AE signals.

Upon considering the sample volume term, V, in Equation 5.3, the idea of applying AE detection to micro-mechanical experiments is especially intriguing. Studies that have incorporated surface nanoindentation with AE have been able to detect pop-in events related to dislocation motion and cracking in small volumes (i.e., <1000μm) [265, 266]. However, there are relatively few studies that have detected AE during deformation and fracture of micro-samples. A recent proof-of-concept AE experiment was performed on an Al-5%Mg alloy micropillar where AE events were detected during the plastic region of the stress-strain curve [267]. However, it is not clear if the events were due to pinning and unpinning (i.e., a Portevin-Le Chatelier (PLC) effect) or dislocation avalanches, which is believed to have a smaller AE yield [268].

Another reason coupling AE measurements with small-scale experiments is of interest is to further characterize the intermittent nature of dislocation plasticity. One of the main contrasts between small-scale and bulk-scale mechanical experiments is that when a small volume of material is tested, a much

smaller number of sources contribute to the overall response of the sample. A consequence of this is that small volumes generally exhibit more variation in mechanical response among tested samples since the source distribution of each is less statistically representative of bulk. Also, the far-field response of a micro-scale sample is very sensitive to individual sources. In metals, this often results in an intermittent stress-strain response where strain burst events each occur one at a time. These bursts are associated with dislocation plasticity and have been studied in Ni extensively [269]. Correlating these strain bursts with individual AE events could provide more insight into the dislocation avalanche mechanisms occurring within the micro-sample volume.

Fitting the concept of AE into the broader scope of the present thesis, there is a demand to detect many of the local deformation and fracture events that occur during micro-fatigue experiments. For example, there is great interest in characterizing the crack growth behavior of physically small micro-cracks. Since the stress and strain levels are typically smaller for cyclic loading than monotonic loading, it would also be expected that the AE energies for the events would be correspondingly smaller. This chapter details results from applying AE detection to Ni micro-samples. As a first step in incorporating AE with the micro-fatigue setup developed in this thesis, monotonic compression of Ni micropillars is performed. Having shown the ability to detect AE at this size-scale, the methodology can then be used with micro-fatigue deformation and fracture.

5.2 Results

5.2.1 Monotonic Micro-compression with AE

The technical aspects of incorporating AE detection with the small-scale methodologies used in this thesis are detailed in Section 2.4. The experimental

design for this chapter is illustrated in Figure 5.1. During deformation of the single crystal Ni micropillar, the deformation events result in both an increase in cross-head displacement (i.e., a displacement burst) and an AE wave. The AE propagates from the surface of the crystal, through the bulk of the material, and then reaches the sensor located at the bottom surface of the material.

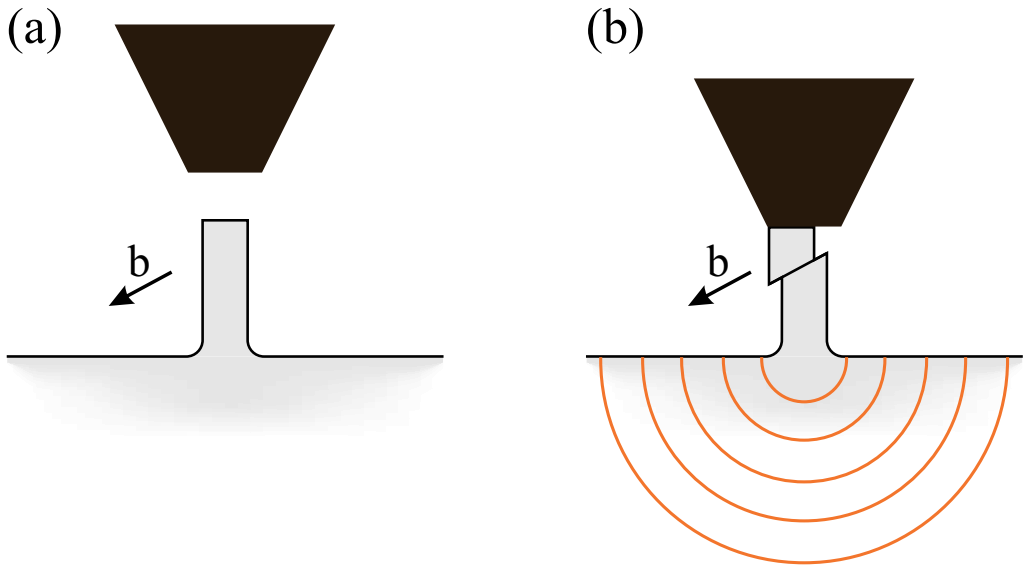

Figure 5.1: Schematic of single crystal Ni micropillar compression-AE experiment (a) before and (b) after compression. Orange waves illustrate the acoustic waves emitted as a result of the slip deformation.

Since the Ni micropillars in this study are pure and oriented for single slip ($[\bar{3}5\bar{2}]$ loading direction), the dominant source of AE is likely to be dislocation motion on a single slip plane. Also, because only a small, local region of the bulk material is being interrogated, the location of the source is approximately the same for the entirety of the micro-compression experiments. This is in contrast with bulk AE experiments where many events are detected with little certainty about their location of origin. All micropillars in this study had a nominal diameter of 10 μm. Details about the materials can be found in section 2.1.1.2. The micropillar fabrication process is detailed in Section 2.2.3. The micro-actuator loading methodology is detailed in Section 2.3.1.

The AE system is set up before compression with the settings shown in

Tables 5.1 and 5.2. Micro-compression experiments were performed while collecting AE data using a wideband HD2WD sensor (see Section 2.4.1) so that a broad range of frequencies could be detected. The micro-actuator was controlled using a simple constant force increase method with a rate of 0.16 mN/s. This way, the load on the sample increased monotonically so that displacement bursts were only a function of deformation physics, not actuator control loops. The threshold-based burst analysis method, detailed in Section 2.5, was performed to identify the start and stop of strain bursts. Then, time correlation, as detailed in Section 2.4, was performed to correlate the strain bursts with the detected AE events.

Table 5.1: AE test settings for Ni compression experiments in Figure 5.2(a).

Thres.	Analog Filter	Digital Filter	Samp. Rate	PDT	HDT	HLT
26 dB	20 kHz - 3 MHz	None	5 MHz	200 µs	500 µs	250 µs

Table 5.2: AE test settings for Ni compression experiments in Figure 5.2(b) and (c).

Thres.	Analog Filter	Digital Filter	Samp. Rate	PDT	HDT	HLT
25 dB	20 kHz - 3 MHz	None	5 MHz	200 µs	900 µs	10 µs

Note that in Table 5.1, the threshold was set such that no noise events were detected during the baseline test. For the test settings in Table 5.2, the threshold was set 1 dB lower, and although noise events were detected, these were removed by filtering all events that had a duration or count value of zero. The latter method yielded more AE events at an amplitude of 25 dB.

The resulting compression-AE data is shown in Figures 5.2 and 5.3. The most prolific part of each experiment in terms of AE events is the very onset of plastic deformation. This is despite the fact that the largest strain bursts, in terms of displacement and velocity, occur at higher strains. Many strain bursts yield no AE detectable events, especially beyond 2.5% strain.

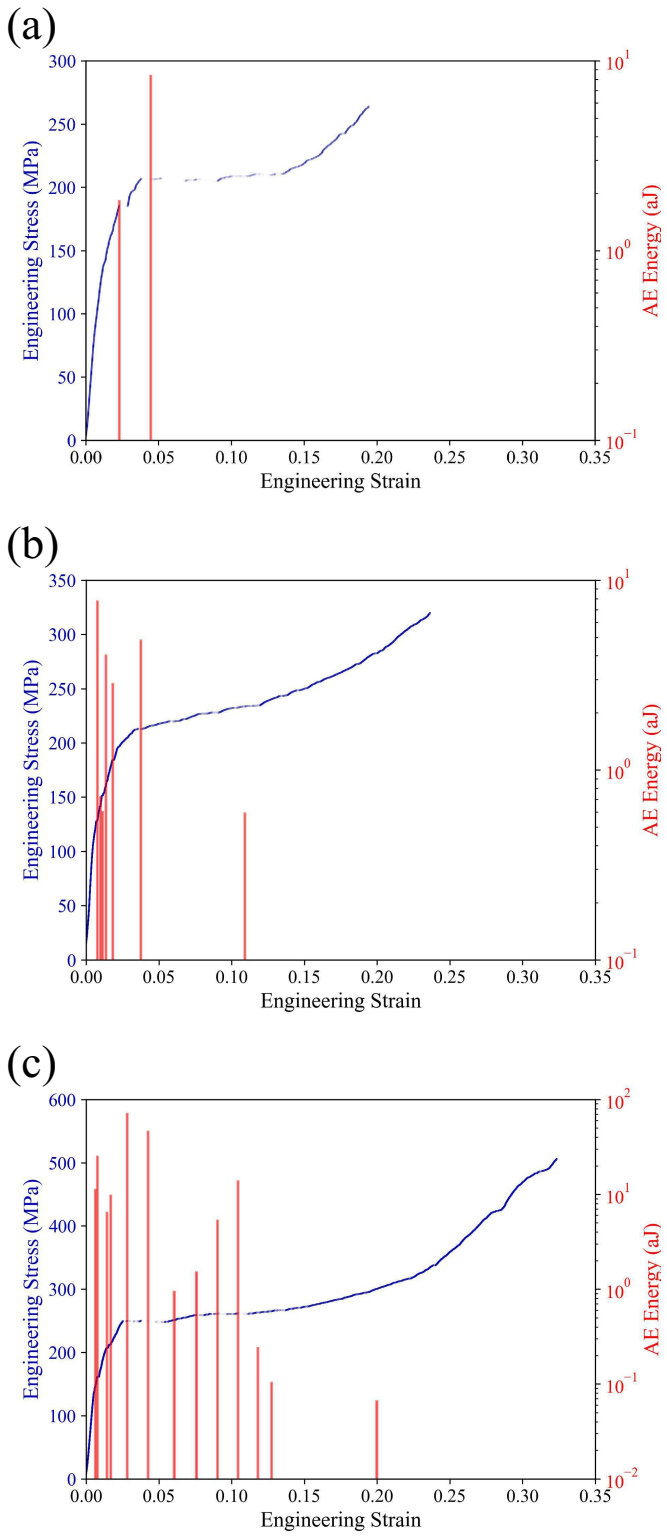

Figure 5.2: (a)-(c) Ni micropillar engineering stress versus engineering strain curves with associated AE absolute energies.

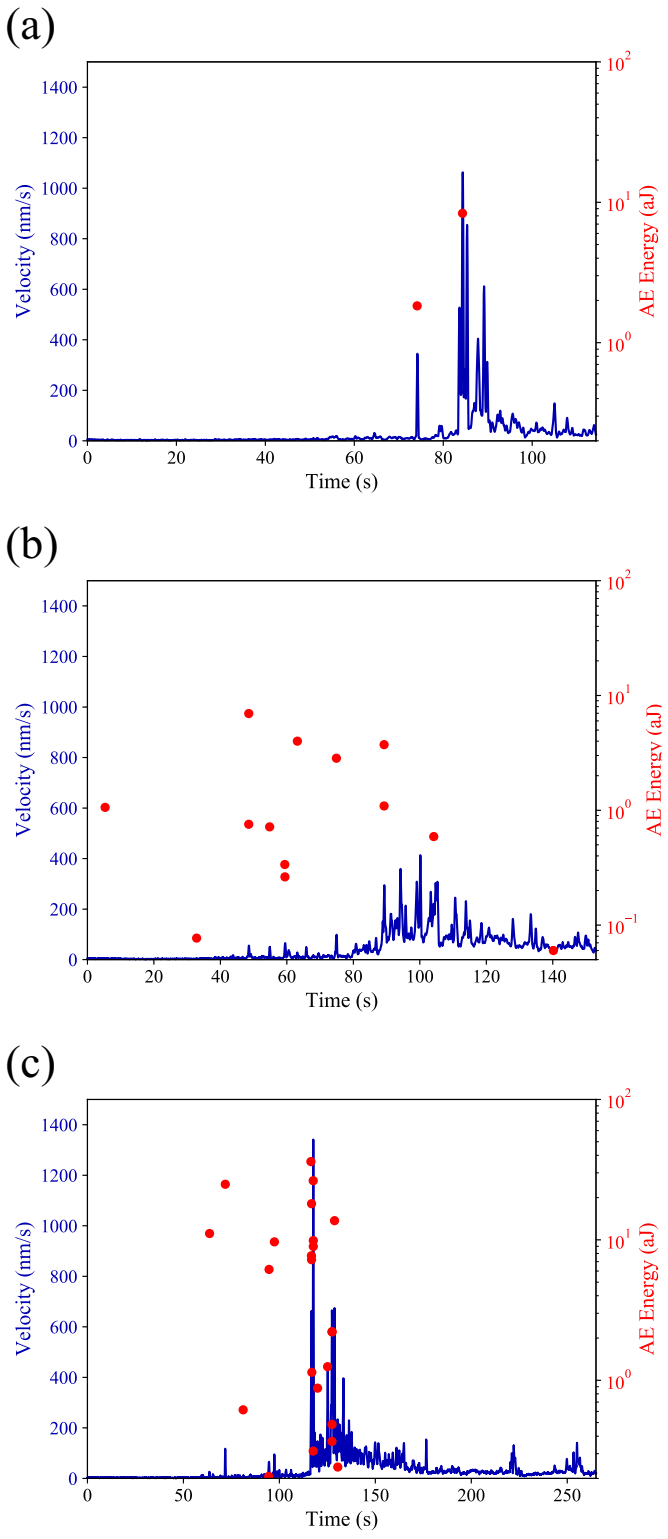

Figure 5.3: (a)-(c) Ni micropillar micro-actuator velocity versus time curves with AE event absolute energies. Subfigures correspond with stress strain subfigures shown in Figure 5.2.

During the experiments, *in situ* SEM micrographs were recorded in a video format. Snapshots of the experiments are shown in Figures 5.4 and 5.5. During the first signs of plastic deformation, slip traces form along the primary slip system and the micro-actuator probe lowers. Each burst in displacement seems to be accompanied by a newly created slip trace.

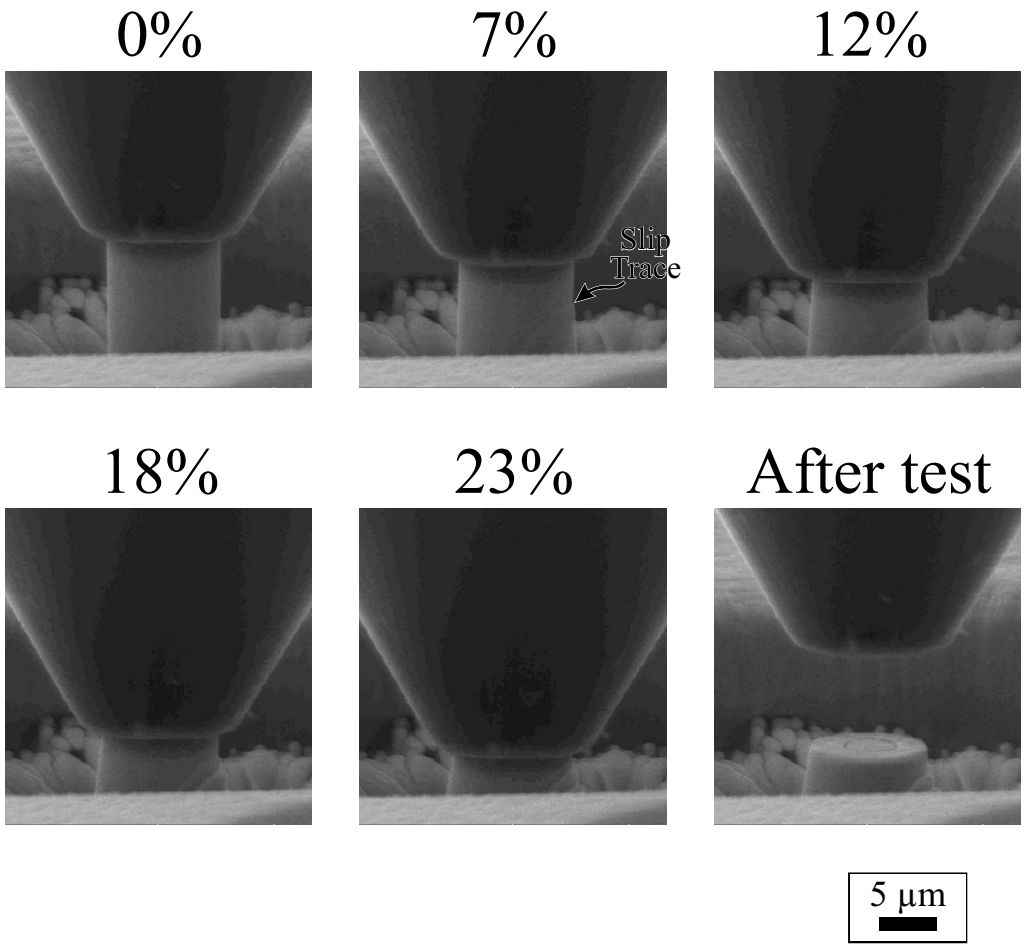

Figure 5.4: SEM micrographs during an *in situ* Ni micropillar experiment at different strain values. Stress-strain, velocity, and AE data is shown in Figures 5.2(b) and 5.3. Pre- and post-testing micrographs are shown in Figure 5.6(b).

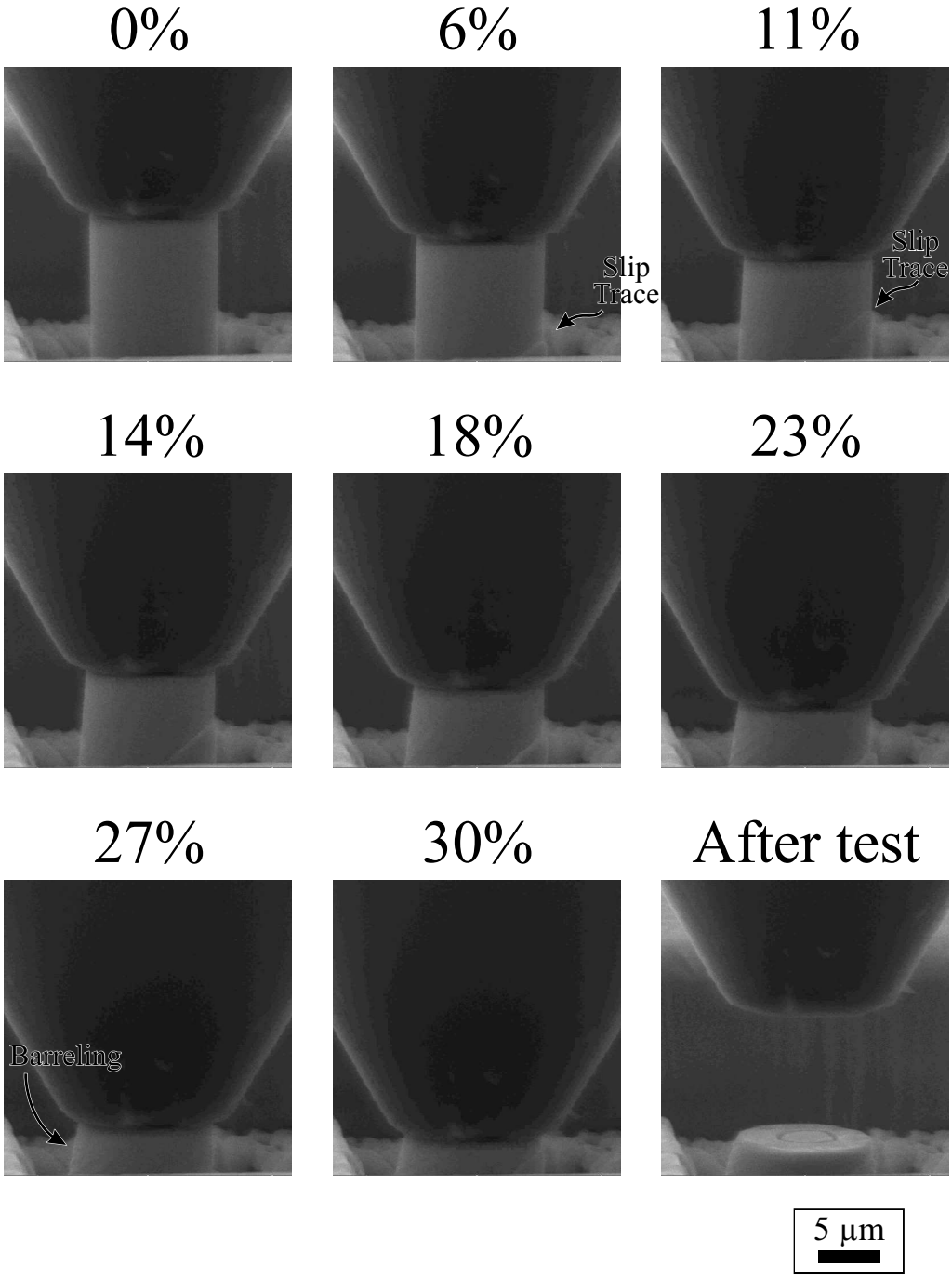

Figure 5.5: SEM micrographs during an *in situ* Ni micropillar experiment at different strain values. Stress-strain, velocity, and AE data is shown in Figures 5.2(c) and 5.3. Pre- and post-testing micrographs are shown in Figure 5.6(c).

The *in situ* micrographs also reveal the effects of tip friction in these experiments. This can be seem very clearly in Figure 5.5. The primary slip

displaces the top portion of the micropillar relative to the bottom; however, the tip friction does not allow the top of the micropillar to move laterally, as idealized in Figure 5.1. Also, by the time 27% strain is reached, it is clear that the micropillar gage region has widened considerable due to the Poisson effect. However, the top of the pillar is not allowed to expand and thus the sidewall forms a curved profile (i.e., barreling). A better look at the slip morphology is obtained using *post-mortem* analysis (see Figure 5.6).

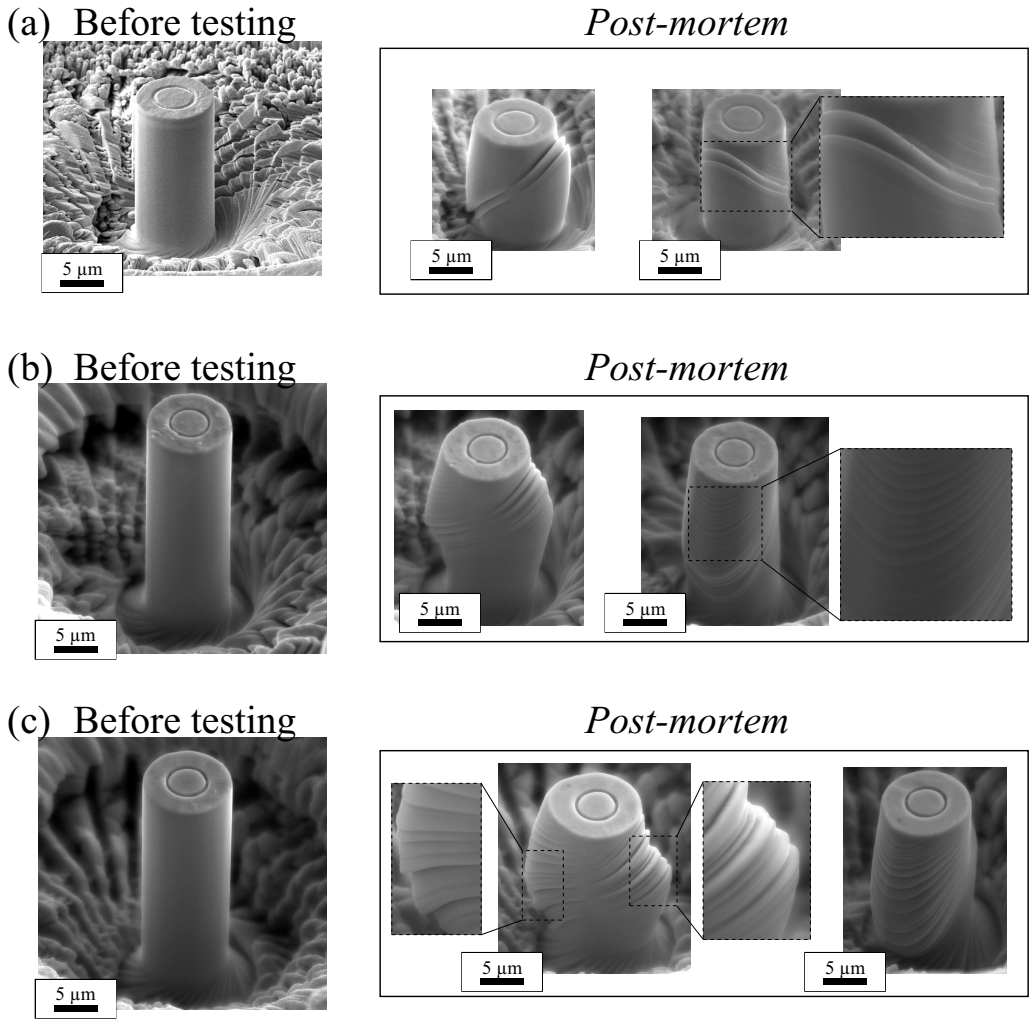

Figure 5.6: SEM micrographs before testing and after compression (i.e., *post-mortem*) of Ni micropillars with initial aspect ratios of (a) 2.2, (b) 3.1, and (c) 3.0.

The slip traces can clearly be seen in all tested micropillars. Interestingly,

the slip traces are not straight but curved. This is also likely a result of the tip friction during compression. The slip traces were likely straight upon nucleation, in line with the primary slip planes. Once the top of the micropillars moved laterally in response to shear deformation, secondary slip systems had to activate to accommodate the deformation. Further evidence for this is the dramatic increase in hardening seen in the stress-strain curves in Figure 5.6. The interaction of the secondary slip systems with the primary slip system causes the flow stress to continually increase with higher strain.

Also clear from Figure 5.6 is the effect of aspect ratio on the number of slip traces. The micropillar in Figure 5.6(a) had a relatively low aspect ratio of 2.2, while the micropillars in Figure 5.6(b) and (c) both had an aspect ratio greater than 3. The smaller volume clearly limited the amount of slip traces in the sample even though a comparable strain was reached for the higher aspect ratio sample in Figure 5.6(b). Instead, the fewer slip traces appear to have slipped farther in distance; whereas the other micropillars appear to have more slip traces with smaller slip distances. The highest strained sample (Figure 5.6(c)), clearly exhibits the most slip traces and the most pronounced secondary slip induced by tip friction.

5.2.2 Cyclic Micro-compression with AE

To determine if the AE behavior observed in the previous section was structure-dependent or stress-dependent, a cyclic compression experiment was performed on another 10 μm Ni micropillar. The loading for this experiments was still at a constant rate of force increase (0.16 mN/s); however, the direction of loading was varied such that three full load/unload cycles were performed. For this experiment, the sensor configuration was changed such that the sensing element was in direct contact with the Ni bulk material with no intermediate material as before. This was avoided in Section 5.2.1 because this resulted

in a significant increase in AE noise. While the physical origin of this is not clear, it may be related to the magnetic properties of Ni. Other materials, such as magnesium and Ni-base superalloy René-N5, did not exhibit this behavior when contacting the sensing element. Also, the frequency settings were adjusted, as tabulated in Table 5.3.

Table 5.3: AE test settings for Ni cyclic compression experiment.

Thres.	Analog Filter	Digital Filter	Samp. Rate	PDT	HDT	HLT
25 dB	100 kHz - 3 MHz	100 kHz - 2 MHz	10 MHz	200 µs	900 µs	10 µs

To filter the heightened level of noise during this experiment, cluster analysis on the AE data was performed after the experiment. Two datasets were obtained: one recorded during the experiment and the other as a noise baseline (i.e., identical conditions except no applied loading). Then, spectral analysis was performed on each AE waveform to obtain an FFT spectrum. By defining partial powers in certain frequency ranges, it was possible to distinguish the experimental data from the baseline data. This is shown in Figure 5.7.

The vast majority of AE events from the two datasets overlap, indicating that these are noise events common to both experiments. The dashed line in Figure 5.7(a) encompasses data points obtained during loading that are clearly separated from this noise cluster and are thus considered events induced by the micropillar deformation. The FFT spectrums for two data points are shown: one considered a deformation event and the other a noise event (Figure 5.7(b) and (c)). One clear contrast between the two spectra is a more pronounced spike in the 0-200 kHz range for the deformation event. However, the rest of the spectra for each event looks very similar, indicating the contribution from noise dominates the waveform even for deformation AE events.

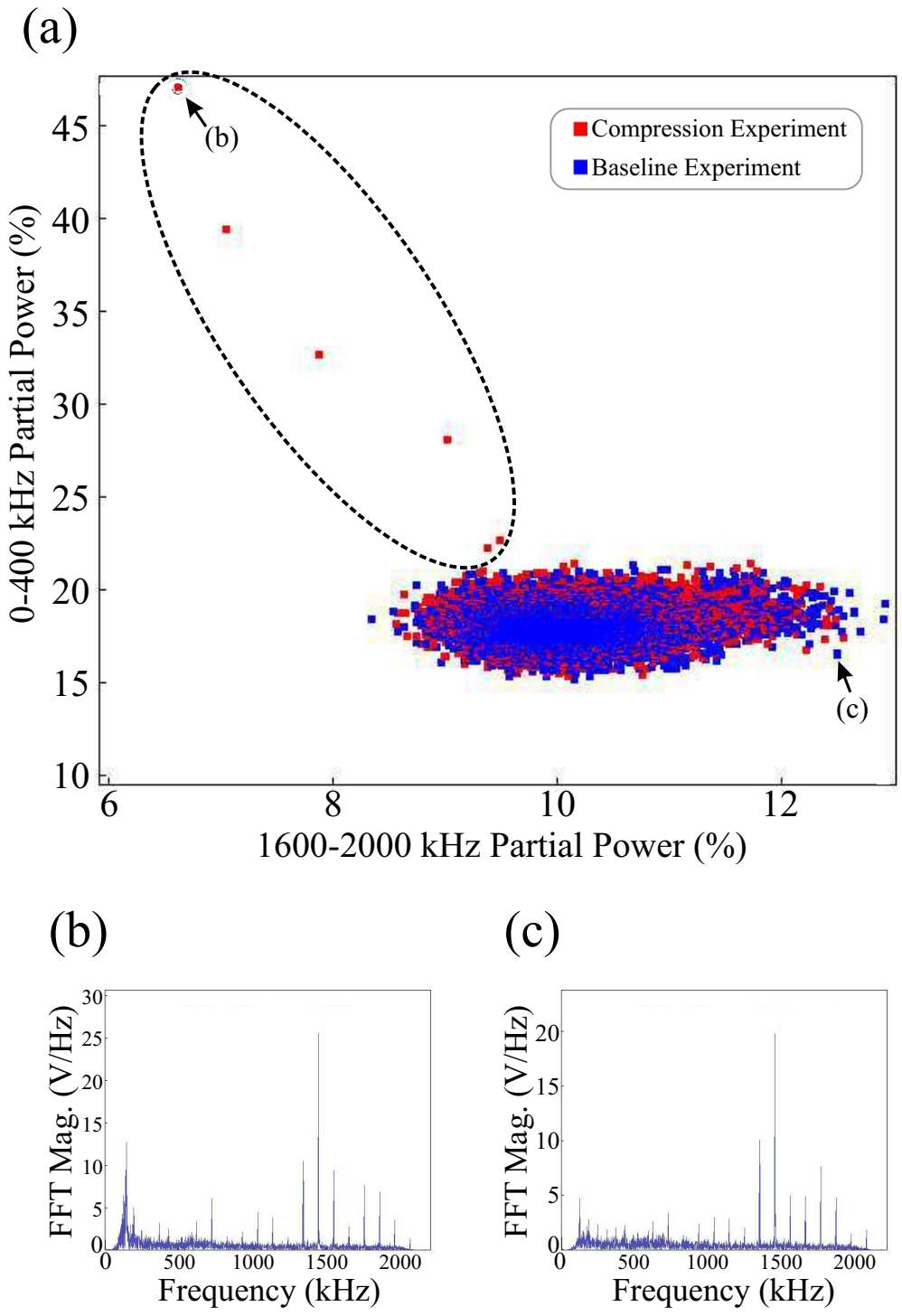

Figure 5.7: Ni micropillar spectral AE data for compression experiment and baseline: (a) Partial power clustering used to distinguish deformation events (in the dashed region) from noise events. (b)-(c) FFT magnitude versus frequency curves for a selected deformation event and noise event, respectively.

Using the filtered data (i.e., the dashed line points in Figure 5.7), the mechanical and AE data for cyclic compression experiment is summarized in Figure 5.8. SEM micrographs showing the micropillar before and after compression are shown in Figure 5.9.

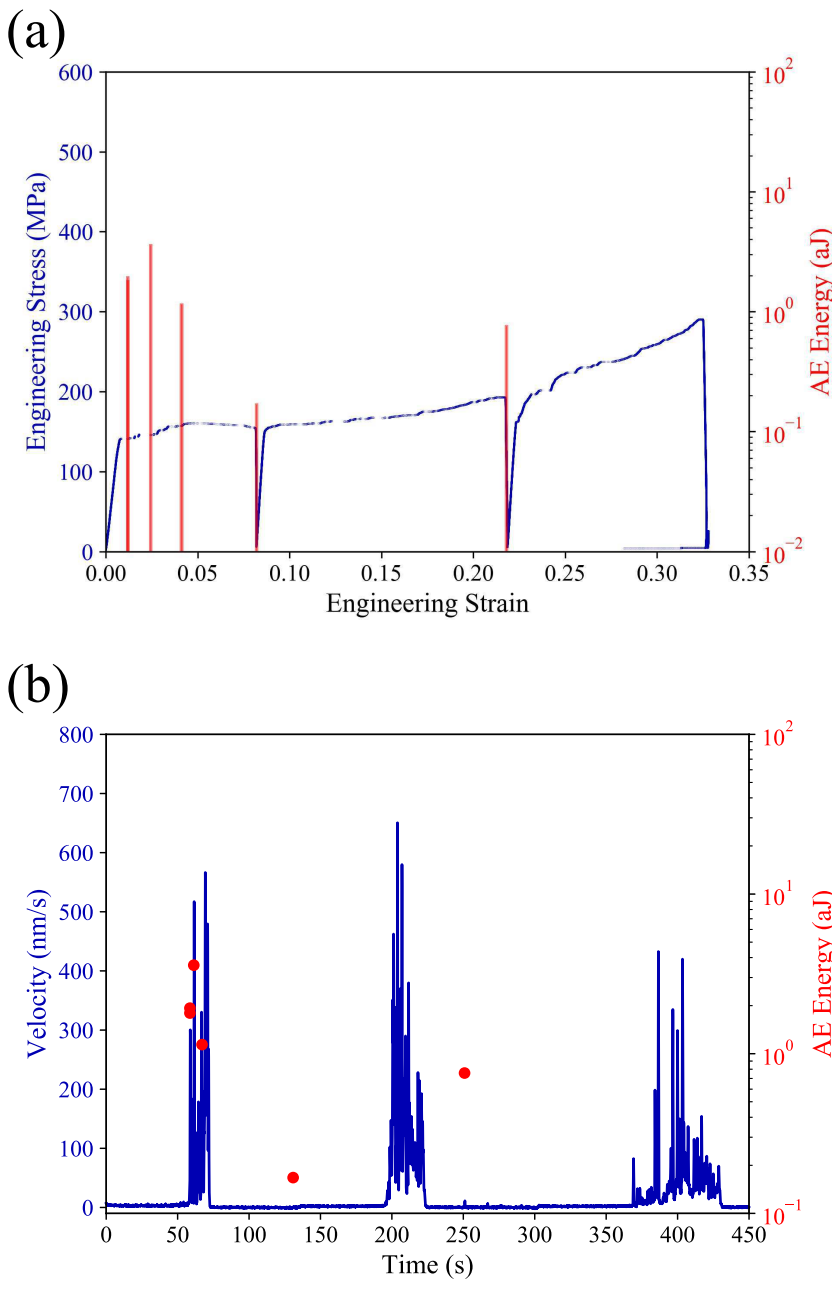

Figure 5.8: Ni micropillar (aspect ratio: 2.8) cyclic compression experiment: (a) Engineering stress versus engineering strain curve with AE event absolute energies. (b) Velocity versus time curve with AE event absolute energies.

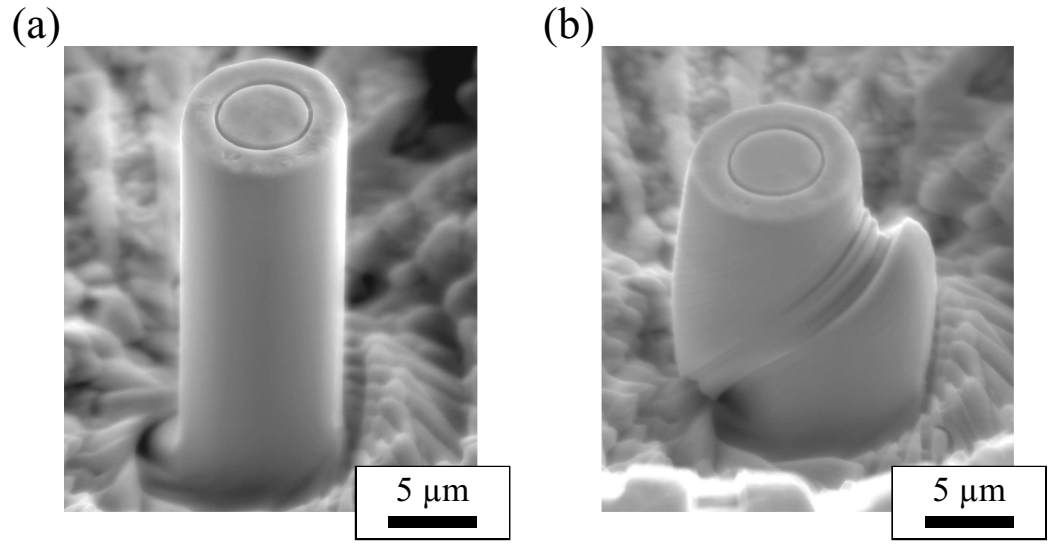

Figure 5.9: Ni micropillar (aspect ratio: 2.8) cyclic compression SEM micrographs (a) before testing and (b) *post-mortem*.

Note that in Figure 5.8(a), AE events are not binned according to strain burst data, as in Section 5.2.1, but instead simply plotted in time. Also, for this experiment, data from the micro-actuator and the AE system was synchronized by applying an external stimulus to signal both systems to begin data acquisition simultaneously. Thus, the need for post-processing synchronization was eliminated.

Once again, the onset of plasticity yielded the most AE events. Upon unloading and reloading, larger strain burst events occurred but with no associated AE, even though the strain bursts exhibited during the later cycles were often at the same stress levels as the initial compression cycle. Also, of note is the much lower flow stress levels for this experiment. While, the periodic unloading certainly may have helped relieve effects of tip friction hardening, even the initial strain bursts were at lower stress levels than the stress-strain responses shown in Figure 5.2. This level of variability in flow stress is not uncommon at this size scale [270], and indicates that this local region of the crystal had a higher initial dislocation density than the other tested micropillars.

Only two more events are recorded after the first loading cycle. One is recorded during the first unload (at ∼131 seconds), just as the tip reaches zero stress. No strain burst is correlated with this event, indicating that it is likely related to the loss of contact with the micro-probe. The final AE event is also recorded during unloading, this time the second unload at ∼251 seconds while a 126 MPa stress was applied. This AE event is correlated with a small strain burst as can be seen in Figure 5.8(b). It is interesting that a positive strain burst would occur while loading is being decreased. The stress that this event occurs at (126 MPa) is comparable to the stress during the initial yield of the micropillar (140 MPa). Therefore, it could be the case that the increase in flow stress may have been largely due to tip friction and this small burst is related not to plastic deformation but the relief of the friction. Upon lowering the stress on the sample, the top of the lateral friction would be relieved, and the top of the sample would slide laterally. This repositioning would be detected by the micro-actuator since motion of the top portion of the pillar would effect the micro-probe displacement. This friction from the tip sliding along the micro-probe surface may have been the AE source. Further evidence for this is that upon reloading, a lower flow stress is reached, indicating that some of the increase in the previous cycle was related to tip friction. The only counterargument that could explain this event is perhaps a dislocation creep event. Although a displacement burst with a maximum velocity of 11 nm/s was not detectable with the AE system in previous experiments at comparably high strain levels.

The *post-mortem* in micrograph Figure 5.9(b) reveals that a relatively small region of the crystal accommodated the plastic strain. There were relatively few slip traces as compared to other micropillars with similar aspect ratios (see Figure 5.6(b) and (c)) and the slip distances were much larger as well. Also, activity related to secondary slip systems was minimal as the top portion of the pillar was able to translate laterally much more than the other compressed

micropillars.

5.3 Statistical Analysis of Burst and Acoustic Emission Events

Using the burst displacement and AE absolute energy data, statistical analysis was performed to determine the event frequency as a function of its size. To do this, the powerlaw Python package was used [191] (see Section 2.5 for details). Different lower bound cutoffs, x_{min} were used tested to optimize the goodness of fit and standard error. The results of the analysis are shown in Figure 5.10.

For the displacement burst data (Figure 5.10(a)), the optimal goodness-of-fit (D) is shown for an x_{min} = 32 nm. A power law exponent of α = 2.16 is obtained, although the standard error is relatively high at 0.135. In comparison with a previous study on bursts in Ni microcrystals, power law exponents between 1.38 and 1.75 were obtained [269], although the crystals considered for this study had diameters between 18.0 and 21.2 μm [269]. Also, the nominal strain rate for these experiments was reported as 10^{-4} 1/s [269] whereas for plastic flow in the present study, nominal strain rates ranged from approximately 10^{-3}-10^{-2} 1/s.

For the AE absolute energy data (Figure 5.10(b)), power law fits are shown for the entire data set as well as the optimal goodness-of-fit data (x_{min} = 4.82 aJ), yielding power law exponents of 1.26 and 2.04, respectively. Neither fit is particularly convincing in terms of goodness-of-fit or standard error. Clearly, more AE data is required to improve the level of certainty in this analysis, as exemplified by the large gaps in the logarithmically binned data.

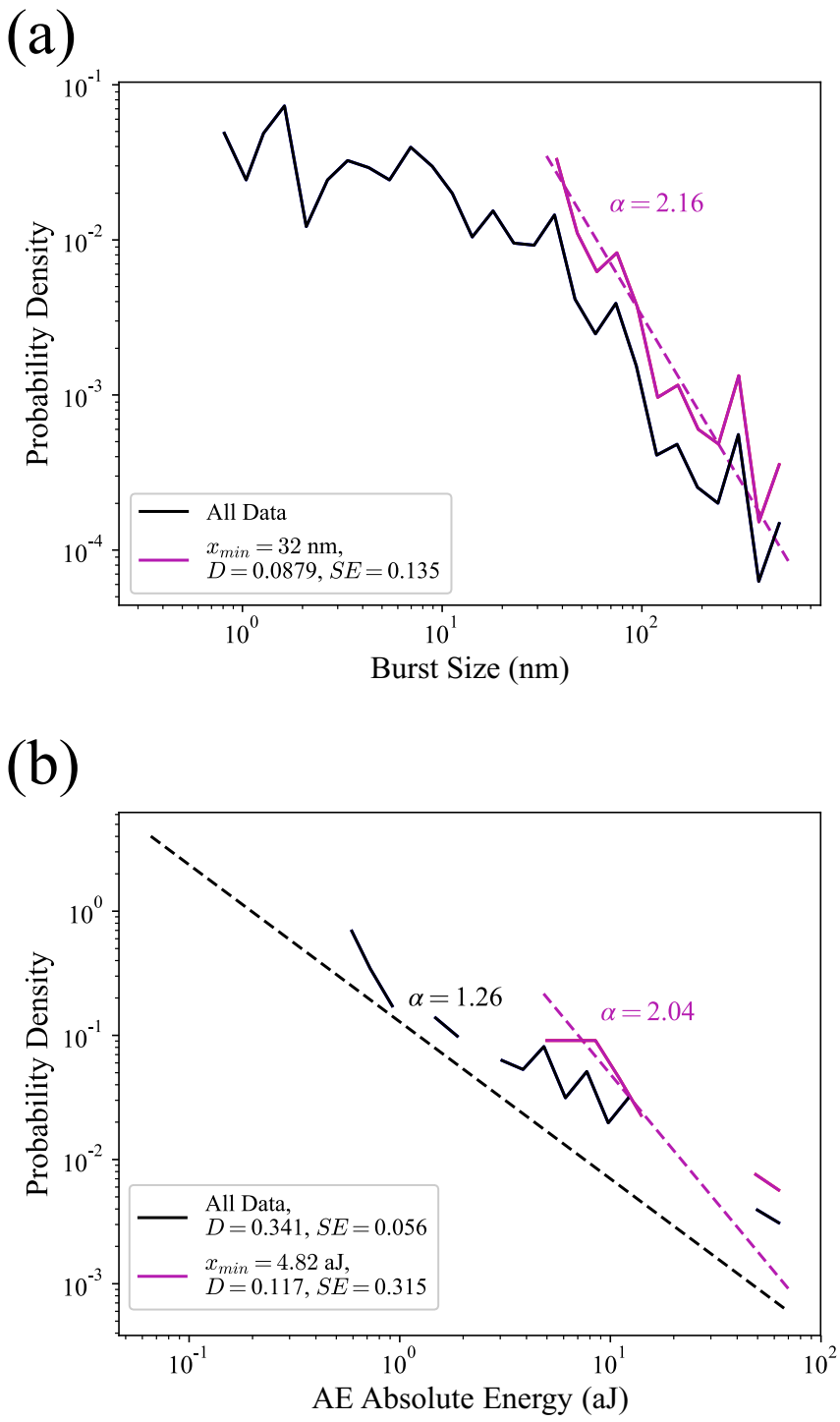

Figure 5.10: Probability distributions for (a) micro-actuator burst displacement data and (b) AE absolute energy data. Power law curve fits are shown using different lower cutoffs, x_{min}. Corresponding values for the Kolmogorov-Smirnov statistic, D, and the standard error, SE, are reported. Solid lines denote logarithmically binned data and dashed lines denote power law curve fits.

5.4 Discussion

5.4.1 Correlation Between Strain Bursts and AE

The strength of the experiments shown in this chapter is the ability to make one-to-one associations between strain bursts and AE events. It is desirable to develop a model that could predict the detected AE using only the burst parameters; however, the results of the present chapter suggest that the AE induced by plastic deformation is much more complex than this. Namely, it is clear that the AE amplitude, and thus the detectability, of a strain burst is dependent on the dislocation structure at the time of the event, among other things.

To further illustrate this, Figures 5.11 and 5.12 show the AE absolute energy and AE maximum amplitude with correlated strain burst displacement and velocity for the three monotonic compression-AE experiments performed in this chapter. While it could be argued that there is weak correlation for post-2.5% strain data, the pre-2.5% strain data does not appear to exhibit any clear trends. For the AE absolute energy, larger bursts occurring after 2.5% strain do appear to result in larger AE energy. However, the pre-2.5% strain data appears to deviate from this correlation with disproportionately large AE energy relative to the burst displacement and velocity. For AE maximum amplitude, it would appear that there is almost no correlation when considering the entire dataset.

It can clearly be seen that strain bursts were more detectable at early plastic strains, as compared to later stages of deformation. The detectability is related not to the energy emitted over the duration of an AE event but the maximum amplitude. Thus, it is possible to have a larger burst event with a lower maximum AE amplitude, as was often the case in this study. To understand this, one important thing to be conscious of is the relative time resolution of the micro-actuator and AE systems. The time between

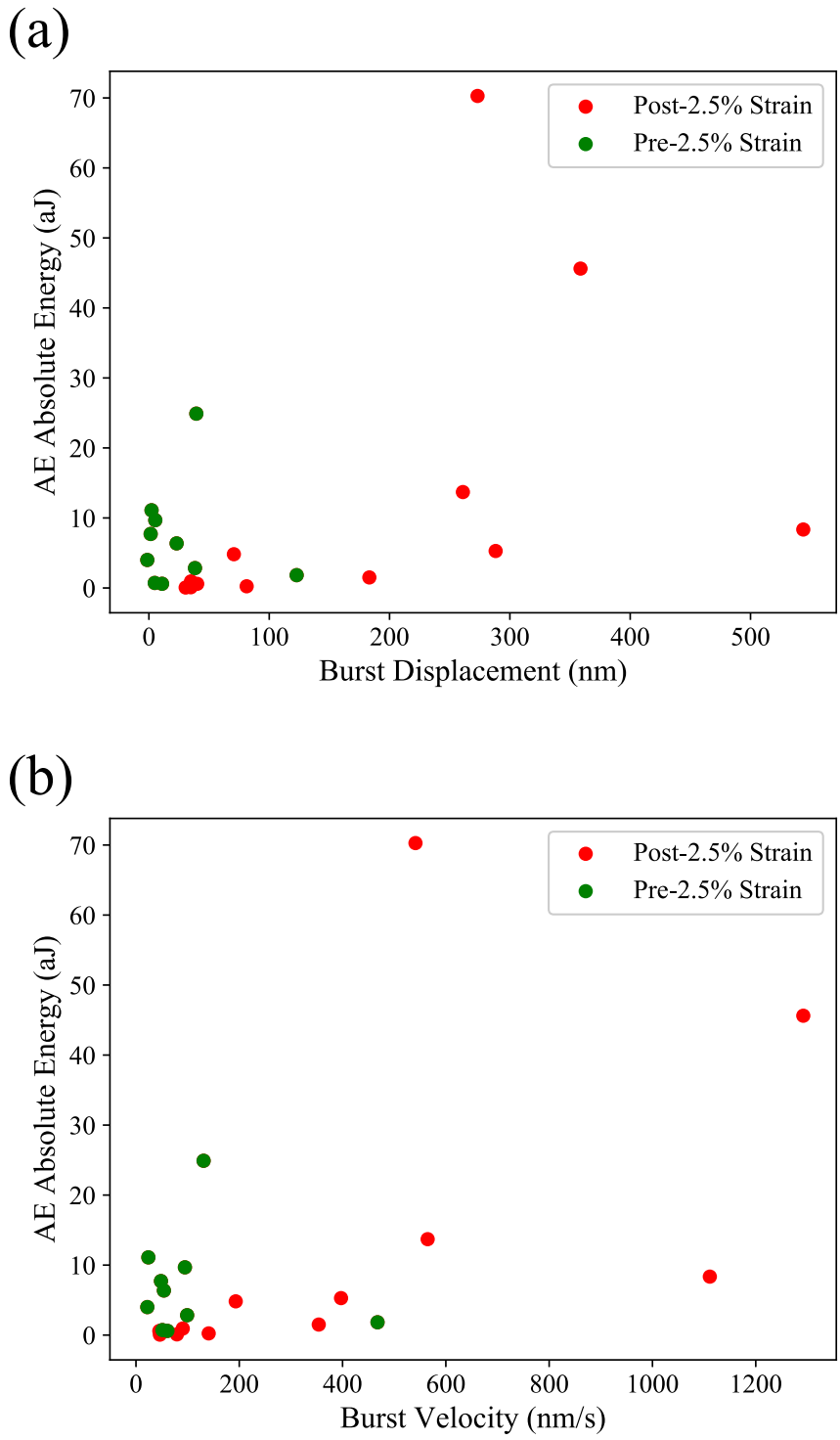

Figure 5.11: AE absolute energy versus associated micro-actuator (a) burst displacement and (b) burst maximum velocity for three Ni micropillar experiments. Note that only data where AE events and micro-actuator bursts were correlated in time are shown. Also, different colors are used to denote data before and after 2.5% strain.

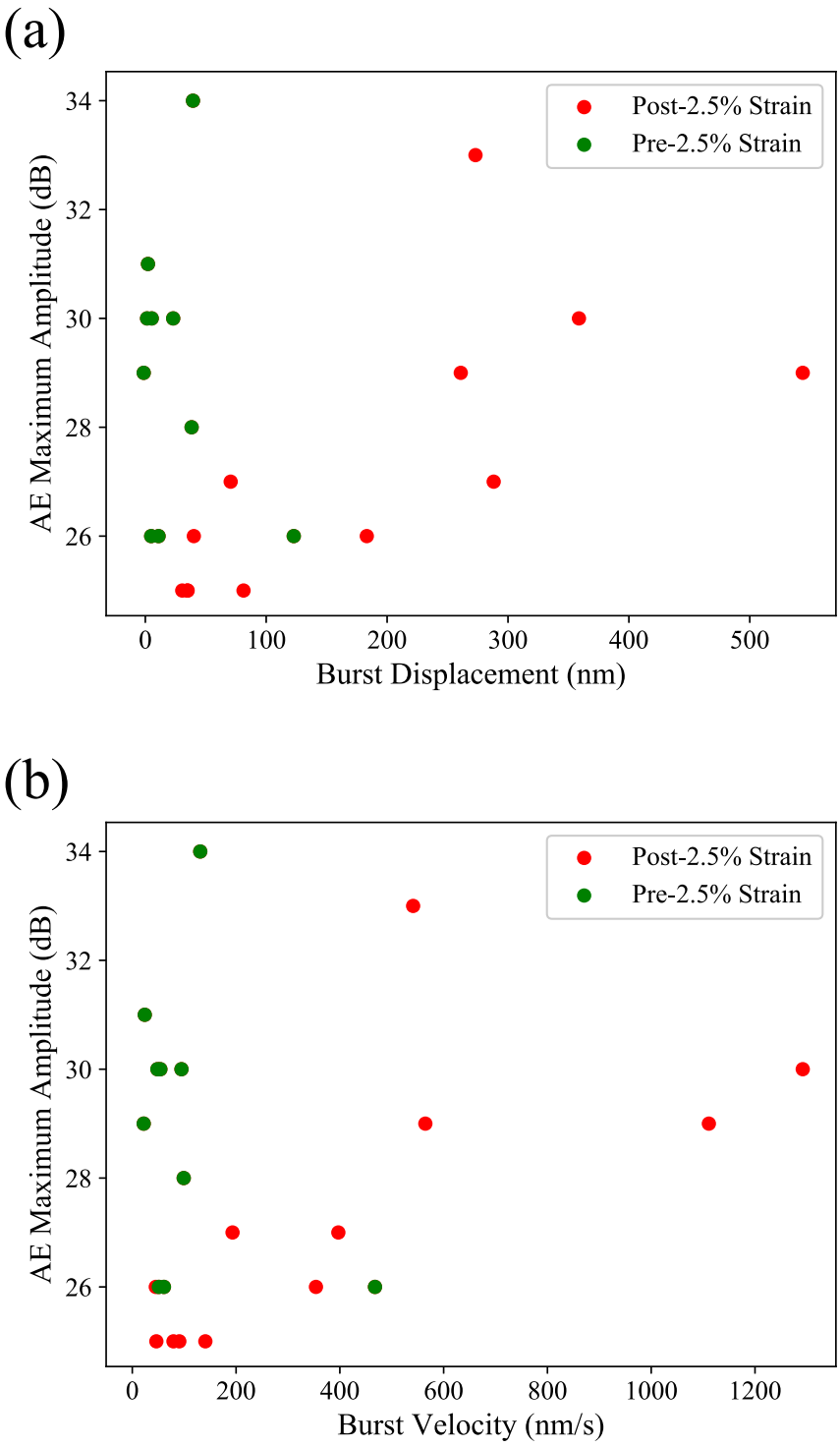

Figure 5.12: AE maximum amplitude versus associated micro-actuator (a) burst displacement and (b) burst maximum velocity for three Ni micropillar experiments. Note that only data where AE events and micro-actuator bursts were correlated in time are shown. Also, different colors are used to denote data before and after 2.5% strain.

datapoints in the micro-actuator displacement data is 1 millisecond. The resolution of the AE system is less than a microsecond and thus multiple AE events can be recorded during one displacement burst event.

Finally, to compare the AE energy to energy loss during strain bursts, the AE energies are plotted with the correlated strain burst energies in Figure 5.13. Once again, there is weak correlation between the energies, with early events yielding disproportionate AE energy relative to burst energy.

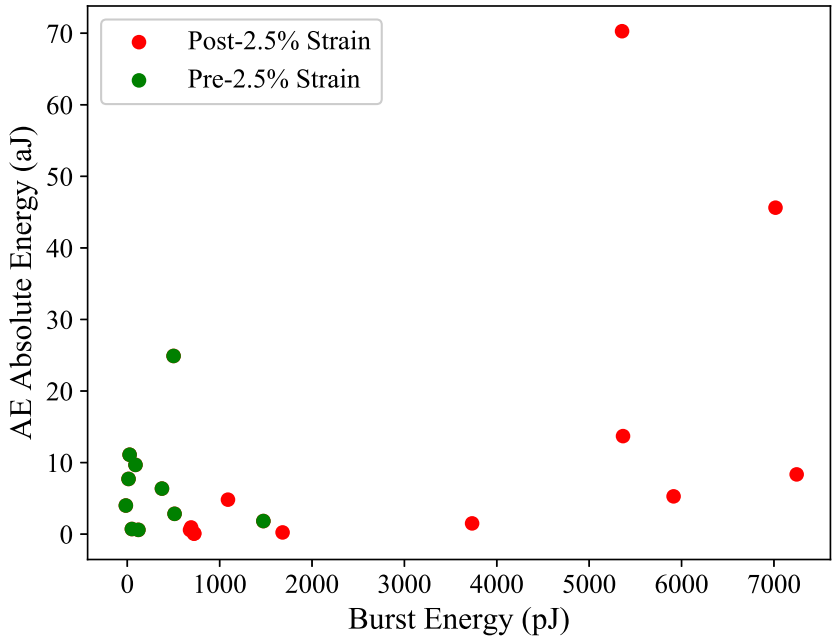

Figure 5.13: AE absolute energy versus associated micro-actuator energy during burst. The burst energy, $\int Pdh$, was approximated by computing the trapezoidal area of the load-displacement curve from the beginning to the end of the burst. Note that only data where AE events and micro-actuator bursts were correlated in time are shown. Also, different colors are used to denote data before and after 2.5% strain.

5.4.2 Mechanistic Explanations for Detected Acoustic Emissions

Having established that small, early strain bursts yield higher amplitude AE signals, the following attempts to explain this phenomenon using dislocation

mechanisms.

One observation that may shed light on this can be seen by examining the *post-mortem* micrographs in Figure 5.6. In Figure 5.6(a), there are two large slip traces that are correlated with the two detected AE events. For the micropillar in Figure 5.6(b), there are more slip traces and more AE events. Figure 5.6(c) exhibits the most slip traces and the most AE events. Thus, it would appear that the initial activation of a slip plane yields higher AE amplitudes as compared to repeated bursts on the same plane. One important caveat is that it cannot be said with certainty that more AE events would not have been recorded with the shorter sample had the AE threshold been 1 dB lower, as was the case for the taller micropillars. Since the amplitude of recorded events (25-34 dB) is so close to the level of noise ($\sim$24 dB), it is likely that many deformation-related events are missed by the AE system.

One possible explanation for the initial strain bursts yielding the most AE may be related to the dislocation annihilation at the surface of the sample. Since dislocation annihilation is a known AE source [271], it could perhaps be argued that dislocations leaving the surface yields a higher amplitude then dislocation motion and thus these events are more detectable. However, no noticeable difference in the AE spectrum for early versus later strain events could be discerned upon analyzing the FFT of each waveform. This would lead one to believe that the events are mechanistically the same, and only differ in magnitude.

An alternative explanation can be found by considering the evolution of the dislocation microstructure as the micro-sample is compressed. The number of Frank-Read sources activated continuously increases as higher stresses are reached. Correspondingly, the overall dislocation density increases and the overall line length of dislocations increases. Assuming that the rate of dislocation escape at the free surface is not enough to offset the rate of dislocation production, forest dislocations will interact and cause dislocations to become

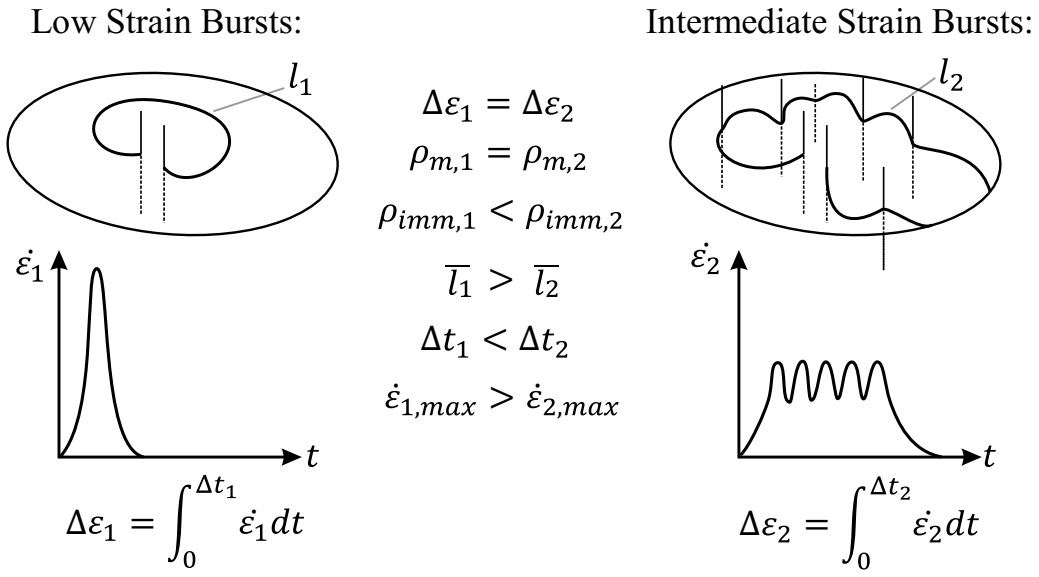

Figure 5.14: Schematic representation of the proposed dislocation motion on the primary slip plane occurring at low strains (subscript 1) versus intermediate strains (subscript 2) during micropillar compression in the present study. The strain burst increment, $\Delta\varepsilon$, is the integral of strain rate, $\dot{\varepsilon}$, over the duration of the event, Δt. For simplicity, it is assumed that $\Delta\varepsilon_1 = \Delta\varepsilon_2$ for the two bursts.

pinned. A schematic of the scenario is illustrated in Figure 5.14. Initially, the Frank-Read source generates dislocation that are able to reach the free surface with few interactions. Later, forest interactions induce the formation of junctions between primary and secondary dislocations. These are depicted as pinning points in the intermediate strain bursts. It is assumed that although the overall dislocation density is greater at intermediate strains, the mobile dislocation density on the primary slip plane, ρ_m, is taken to be the same for both low and intermediate strains. However, the overall immobile dislocation density, ρ_{imm}, is larger for the intermediate strains.

The pertinent points in Figure 5.14 with regards to AE can be seen by considering the individual segment lengths, l. For a single Frank-Read source to sweep the same area, and thus induce the same strain burst increment $\Delta\varepsilon$, the dislocation line must overcome many more pinning points at intermediate strains. Thus, at intermediate strains, the individual segments each move incoherently with a smaller average segment length, $\bar{l}$ over a longer time increment,

Δt. The resulting strain rate is given by Orowan's equation [272]:

$$\dot{\varepsilon} = \rho_m b \bar{v} \tag{5.4}$$

Since the dislocation velocity is a function of stress, it can be assumed that the velocity of each dislocation segment is approximately the same. Therefore, the strain rate at any given point in time is only related to the length of moving dislocation segments. Since all this happens at a time scale much shorter than the resolution of the micro-actuator (1 ms), the two events would be indistinguishable in both burst displacement and velocity. However, the AE system, with a sub-microsecond time resolution may be affected by the lower burst strain rates at intermediate strains. Namely, by looking at the energy emitted by the activation of a Frank-Read source (Equation 5.2), a smaller average dislocation segment length l, would result in a smaller AE signature. This can also be seen by observing Equation 5.3 which shows that the AE yield is proportional to $\dot{\varepsilon}$. The lower maximum strain amplitude would yield a less prominent AE signal according to this model. This also explains the observation that early strain events were lower in AE energy but approximately the same in amplitude as later events (see Figures 5.11 and 5.12). Later AE events were larger in energy because more sources were likely activated during the burst; however, the incoherent nature of the dislocation motion did not yield as high an instantaneous AE amplitude as compared to earlier strain bursts.

5.5 Conclusions

In this chapter, the incorporation of acoustic emission (AE) detection with micro-scale experiments was demonstrated on Ni micropillars. AE events from plastic deformation were detected even though the event amplitudes were very

close to noise levels during experiments. Strain bursts in the first 2.5% strain were found to yield the most AE events, even though these initial bursts had relatively small far-field displacement and velocity values. Based on *in situ* and *post-mortem* electron micrographs, these high amplitude acoustic events appear to be associated with the initial activation of dislocation motion on a slip plane. A model is proposed to explain the greater detectability (i.e., higher AE amplitude) of early burst events by considering the increase in dislocation forest interactions at higher strains. These results suggest that AE detection can reveal physical insight into dislocation mechanisms that micro-actuators cannot resolve in time.

Chapter 6

Summary and Future Directions

6.1 Summary

In this thesis, a novel micro-fatigue methodology was developed and utilized to provide unique insight into dislocation motion, micro-crack initiation, and micro-crack propagation in face-centered cubic (FCC) single crystal metals under cyclic loading. All tested samples were at a size scale of ∼10 μm. Cycle numbers greater than 10^7 were reached all while collecting real time surface micrographs. These experiments were performed on Ni superalloys micro-beams and pure Ni uniaxial micro-samples, both with fully reversed tension-compression loading profiles. The methodology was later expanded to incorporate acoustic emissions detection. This capability was demonstrated on monotonic compression and cyclic compression of Ni micropillars.

Using these methods, the effect of size on fatigue behavior was studied. For superalloy micro-beams, improved fatigue life was observed as compared to bulk. Cyclic hardening was observed in both superalloys and pure Ni while cyclic softening was only observed in superalloys at high fatigue amplitudes. This cyclic softening was shown to be a result of precipitate shearing by dislocations. For Ni, persistent slip bands were found to form at much later

cycle numbers than in bulk-scale crystals. Additionally, these *in situ* observations revealed that persistent slip bands nucleate and propagate in a way that has not been reported before. Cellular dislocation structures were also found to form in Ni microcrystals under fatigue. Fatigue fracture was observed at notches in superalloy micro-beams and along slip bands in both Ni-base superalloys and pure Ni. The *in situ* observations reveal that precursors to cracks (i.e., intrusions) sometimes form before extrusions, suggesting refinements are needed to conventional crack initiation models. Crack propagation bursts were also found in Ni. Statistical analysis reveals a scale-free avalanche-like behavior common in many other physical systems. In Ni compression, acoustic emission was found to be correlated with strain bursts, with the most prominent acoustic signals detected at the very earliest bursts. This phenomena appeared to be dislocation structure-dependent since subsequent loading cycles did not repeat this AE behavior. A dislocation model was proposed to explain this phenomenon.

The work presented in this thesis is useful to those that perform experiments and simulations at the micro-scale, as well as the broader mechanics and materials community. Experimentally, reaching these cycle numbers at this size scale with fully reversed loading was not previously possible. With the details of the setup outlined in this thesis, the methodology can be extended to investigate other materials. In terms of simulations, these experiments are well-suited to provide validation to mesoscale modeling methods, such as discrete dislocation dynamics (DDD). These experimental results can be used to directly validate the simulations, since both involve the same loading and boundary conditions, which is not always the case when comparing the DDD simulations with bulk experiments. Also, these simulation results can be used directly to interpret experimental observations. In terms of scientific impact, the findings of this thesis shed light on many fatigue mechanisms that contribute to eventual material failures in important FCC engineering materials.

Most notably, the dislocation plasticity that precedes fatigue crack initiation in single crystals is better understood with the mechanisms discussed in this thesis. With this insight, materials can be "designed" such that fatigue life of engineering components can be prolonged.

Finally, one other impact of this work is its contribution to the non-destructive evaluation (NDE) method for damage detection of materials in service. NDE methods typically obtain data from many sources located throughout a material while it is being cyclically loaded. The ability to isolate one location in a material, as was done in this thesis, makes it possible to associate individual AE events with discrete deformation and fracture events. This capability could lead to NDE systems that can automatically classify the physical source of detected AE events in engineering applications.

6.2 Future Directions

6.2.1 Experimental Improvements

While the micro-fatigue methodology developed in this thesis provides many new capabilities, there are still many aspects that can be improved upon.

For example, the temporal resolution and acquisition rate of the micro-actuator are factors that limit the amount of data that can be acquired in a single experiment. While the method is able to perform cyclic loading at high frequencies, much of the control unit displacement and load data is not recorded since it cannot be transferred to the control PC fast enough. As a result, each dynamic data point describes multiple fatigue cycles but does not provide intra-cycle data. One solution to this problem would be eliminating the bottleneck at the interface between the control unit and the control PC by controlling and storing data directly onto the control unit.

Another current limitation of the micro-actuation method is the inability to

directly control displacement. Relying on feedback loops to control displacement amplitude requires an assumption of an ideal sinusoidal displacement profile. With the current method, changes in the displacement profile affect the displacement amplitude, but there is no way to distinguish between changes in amplitude or changes in mean displacement. Displacement-controlled systems, such as piezo-electric actuators, may provide a solution to this difficulty.

The current bottleneck in obtaining data with this methodology is the micro-sample fabrication step. This thesis presents unique methods to efficiently fabricate micro-samples with high precision; however, a single sample can still take more than 12 hours to fabricate. Much of this time requires someone to be present to monitor the fabrication process. The combination of coarse femtosecond laser milling with fine FIB milling has at least made fabrication of multiple micro-samples possible but perhaps an intermediate scale milling technique would make the process even faster. In particular, plasma FIB has the capability of reaching beam currents of 2 μA [273] (approximately 100 times the maximum for most FIBs). This may be a good way to smooth this sidewalls after the laser milling step and get within ∼5-10 μm of the final geometry before Ga FIB. Finally, automated fabrication would free up the FIB/laser operator to work on other aspect of the experiments. Automated fabrication with FIB has proven to be an effective method for fabricating simple geometries, such as micropillars [167]. One current difficulty is that these methods entail significantly more ion exposure to image, locate, and center fiducial marks. This ion exposure may affect the mechanical response of these micro-samples [274]. Also, FIB computer systems are not currently able to assess sample surface quality as well as a human can. Once these difficulties in fabrication are overcome, data for small-scale experiments can be produced at a much higher rate.

Once samples can be fabricated more quickly, the next bottleneck in data output will be how quickly they can be tested. One of the advantages of the

micro-fatigue method developed in this thesis is that tests can be completed during a single SEM session; however, these sessions can be up to several days in length. Also, it is not typically known *a priori* how long a micro-fatigue test will last. Since the sample is glued to the micro-probe, dividing the test into segments is not an option because shutting down the experiment would destroy the micro-sample. This presents great challenges both during and after the experiment. During the course of an experiment, many things change such as SEM drift and sample failure. It is not always practical for someone to monitor the experiment during its entirety. Also, to obtain better quality micrographs, the high frequency loading has to be manually paused. After the experiment, very large and intractable data files are obtained. While lots of data is potentially useful, the vast majority of it is not of interest and slows down the data analysis process. This data is not only micro-actuator data but also SEM video files which are continuously recorded during the entire fatigue life of the samples. To avoid large file sizes, the video quality is compressed which is certainly not ideal. One potential solution would be to automate these experiments; however, this would require a better interface between the SEM and the micro-actuator control system. As of now, these systems are completely separate with no way for them to communicate. This limitation requires someone to manage both systems and makes automation of these experiments difficult. Once this is overcome, the experiment can be periodically stopped, the SEM can take a high resolution micrograph, and then the loading can be continued all without the need for a human in the loop. To reduce the SEM session time required for these experiments, the only solution would be to test at higher frequencies. The current limit is that the absolute maximum velocity the micro-actuator can reach is 130 mm/s. Making the sample size smaller would increase the maximum frequency for a given fatigue amplitude, but smaller size scales may not always be desirable. To increase this velocity limit micro-actuators with lower damping levels would have to be

explored.

A smaller actuator damping coefficient would also improve the control loop for high frequency fatigue. With negligible damping, the actuator force would always be equal to the load on the sample without the need to make any assumptions. Also, since the sample would be the only contributor to damping, this would provide a way to directly measure plasticity or other sources of energy dissipation in the micro-sample.

In terms of the *in situ* test setup, modifications could be made to make more of the micro-sample visible during experiments. At this point, the primary factor that is limiting SEM viewing angles and image quality is the size of the setup relative to the SEM chamber. Clearance issues with other instruments in the SEM greatly limit the range of tilts that can be achieved. This also requires large SEM working distances during experiments which reduces micrograph resolution. Finally, an extra tilt axis about the loading direction would provide the degrees of freedom necessary to image a micro-sample from all possible angles.

Adhering the micro-sample to the micro-probe opened up a wide range of micro-fatigue experiments, as exhibited in this thesis. Still, the difficulty in consistently getting a consistent glue bond remains one of the biggest variables in the success of each experiment. A more consistent method may be the incorporation of micro-tweezer grip probes that allow samples to be put into compression and tension without slipping between the grips. Doing so may also increase the loads, and thus size scales, that can be tested in fully reversed fatigue. Also, a gripper probe would likely result in more uniform stress state for tension-compression fatigue.

It is clear that these micro-fatigue experiments are very expensive and time consuming. Thus, it is desirable to obtain as much data from as many different sources as possible for each test. The method developed in this thesis accomplishes that to an extent; having incorporated micro-actuator data, SEM

micrographs, acoustic emissions, and *post-mortem* characterization methods. However, currently, many inferences must be made about the dislocation microstructure evolution based on micro-mechanical data and surface observations. One idea would be to incorporate *in situ* electron channeling contrast imaging (ECCI) to obtain near-surface dislocation microstructure data during micro-fatigue experiments. However, this would require a wider range of motion for the experimental setup, as previously discussed. Another instrument that could be used during *in situ* micro-fatigue of alloys is an energy dispersive spectroscopy (EDS) detector. This could provide chemical segregation information at different stages of fatigue experiments. However, a number of methods that potentially can be used to provide real-time, although not 3D, dislocation microstructure information during fatigue loading. Transmission SEM (TSEM) also holds the potential to provide directly comparable dislocation dynamics observations [275] although it has not yet been applied to fatigue and is currently limited to thin foil sample geometries. In terms of *post-mortem* analysis, various cutting-edge characterization techniques, such as 3D x-ray reconstructions of crack surfaces [276] and DIC detection of microcracks [277], also hold great potential for non-destructively quantifying the evolution of dislocation plasticity and other micro-structural defects in micro-scale experiments. Miniaturized fatigue samples are also useful since they allow for *in situ* observations within microscopes as opposed to destructive methods. Also, with small volumes there is little uncertainty about where failure will occur so experimentalists can focus on why and how failure occurs and observe it in real time.

The AE small-scale testing apparatus could also be refined to increase the detection sensitivity. One area for improvement is limiting the noise so that more physical events can be detected. An alternative approach would be to increase the sample volume so that the level of AE is better separated from the noise. There is also the idea that traditional threshold-based methods

of AE detection are not appropriate for this application. Thus, they could be abandoned, and instead a constant stream of AE signals could be recorded during experiments. From these raw signals, filters could be applied to reduce the noise in real time. Since it would be impractical to save all the signals obtained during an entire fatigue experiment, only segments associated with physical deformation and fracture events would be stored. This process could be automated using a signal classification model on the front-end of the AE system. Finally, although synchronization between the AE and micro-actuation systems was able to correlate strain bursts with AE events ($\sim$1-10 ms precision), even higher precision to within $\sim$1 μs of delay may be desirable.

6.2.2 Future Potential Research Endeavors

In terms of future scientific directions, there are many potential research projects that this work opens the door to.

For one, it would be interesting to investigate a broader range of sizes. Smaller, perhaps even submicron size scales, are very rare in fatigue studies and are usually limited to polycrystalline thin films. It would be interesting to investigate crack initiation mechanisms in nano-crystals. Since persistent slip bands would not be expected to be active at such a small size scale, other mechanisms would have to be dominant.

Larger size scales would be useful for investigating more intermediate size scales to better evaluate the transition to bulk fatigue responses. Also, it would be interesting to perform a systematic study on size effects in fatigue life. To date, most data on this top is a combination of various studies each using different experimental techniques and materials.

While the present work provides some insight on micro-crack propagation, more data is needed to fully characterize the nature of short crack growth. The acoustic emission detection system shown here has the potential to quantify

fatigue crack propagation events. This could be an improvement over the threshold-based analysis on micro-actuator displacement amplitude performed in this thesis. Also, with the high temporal resolution of AE, short burst events could be detected that were not obtainable from micro-actuation. Additionally, fracture mechanics could be incorporated with these fatigue methods to better quantify fatigue crack growth behavior. Namely, using compliance changes in the micro-samples under cyclic loading, the crack size could be quantified and then compared against Paris law.

While uniaxial loading is perhaps the most important stress state for micro-fatigue testing, it may be desirable to look into other loading methodologies. For examples, pure shear and torsional loading may yield interesting results. Also, the incorporation of biaxial stress states is a relatively unexplored area in micro-fatigue.

To build on the AE during plasticity work in this thesis, it would be very interesting to apply dislocation dynamics simulations. With these small-scale experiments being a parallel to mesoscale simulations, one could obtain an acoustic signature from dislocation motion. This would entail incorporating dynamic stress wave propagation using finite elements, and then measuring the resulting surface displacement. This project has the potential to characterize AE dislocation mechanisms occurring within the sample volume that cannot be observed experimentally.

Finally, in light of the recent surge in data science and artificial intelligence (AI), it would make sense to apply these methods to the vast quantities of data compiled during these micro-fatigue experiments. In particular, to classify acoustic events based on their AE signatures would likely be too complex to perform with conventional methods. Machine learning models could be developed to classify AE events based on their physical source. With the methods developed in this thesis, each AE event can be correlated with a deformation or fracture mechanism. By assigning these labels manually, the

model could be trained and once enough training data is acquired, this model could classify event labels automatically. Additionally, unsupervised clustering algorithms, such as support vector machines (SVMs), could be used to identify unique AE waveforms that are too complex for a human to distinguish. Another application for data science would be in identifying *in situ* features, such as slip bands and cracks. Since most micrograph findings rely on human interpretation, many findings may be mis-characterized or go unnoticed. As has been performed in radiology analysis [278], AI and deep learning could be used to better reduce SEM image noise as well as assist in recognizing features associated with deformation and fracture.

Bibliography

[1] S. Lavenstein and J.A. El-Awady. Micro-scale fatigue mechanisms in metals: Insights gained from small-scale experiments and discrete dislocation dynamics simulations. *Curr. Opin. Solid State Mater. Sci.*, 23(5):100765, 2019.

[2] R.I. Stephens, A. Fatemi, R.R. Stephens, and H.O. Fuchs. *Metal Fatigue in Engineering, 2nd Ed.* Wiley, 2000.

[3] J. Schijve. Fatigue damage in aircraft structures not wanted but tolerated. *Int. J. Fatigue*, 31:998–1011, 2009.

[4] S. Suresh. *Fatigue of Materials, 2nd Ed.* Cambridge University Press, 1998.

[5] H. Mughrabi. Fatigue, an everlasting materials problem - still en vogue. *Proc. Engineering*, 2:3–26, 2010.

[6] J. Schijve. *Fatigue of Structures and Materials, 2nd Ed.* Springer, 2009.

[7] M.D. Sangid. The physics of fatigue crack initiation. *Int. J. Fatigue*, 57:58–72, 2013.

[8] N. Thompson, N. Wadsworth, and N. Louat. XI. The origin of fatigue fracture in copper. *Philos. Mag.*, 1(2):113–126, 1956.

[9] P.J.E. Forsyth. Exudation of Material from Slip Bands at the Surface of Fatigued Crystals of an Aluminium-Copper Alloy. *Nature*, 171:172–173, 1953.

[10] E.E. Laufer and W.N. Roberts. Dislocations and persistent slip bands in fatigued copper. *Philos. Mag.*, 14(127):65–78, 1966.

[11] P. Lukas, M. Klesnil, J. Krejci, and P. Rys. Substructure of Persistent Slip Bands in Cyclically Deformed Copper. *Phys. Stat. Sol.*, 15(71):71–82, 1966.

[12] F. Ackermann, L.P. Kubin, J. Lepinoux, and H. Mughrabi. The Dependence OF Dislocation on Plastic Strain Ampltiude in Cyclically Strained Copper Single Crystals. 32(5):715–725, 1984.

[13] H. Mughbrabi, F. Ackermann, and K. Herz. Persistent Slipbands in Fatigued Face-Centered and Body-Centered Cubic Metals. *Fatigue Mech.*, ASTM STP 6:69–105, 1979.

[14] C. Laird. Low Energy Dislocation Structures Produced by Cyclic Deformation. *Mater. Sci. Eng.*, 81:433–450, 1986.

[15] J. Polák. Electrical resistivity of cyclically deformed copper. *Czechoslov. J. Phys.*, 19(3):315–322, 1969.

[16] M.D. Uchic, P.A. Shade, and D.M. Dimiduk. Plasticity of micrometer-scale single crystals in compression: a critical review. *Annu. Rev. Mater. Res.*, 39(1):361–386, 2009.

[17] M.D. Uchic, D.M. Dimiduk, J.N. Florando, and W.D. Nix. Sample dimensions influence strength and crystal plasticity. *Science (80-.).*, 305(5686):986–989, 2004.

[18] D.M. Dimiduk, C. Woodward, R. LeSar, and M.D. Uchic. Scale-Free Intermittent Flow in Crystal Plasticity. 1188(2006):318–320, 2011.

[19] J.R. Greer, W.C. Oliver, and W.D. Nix. Size dependence of mechanical properties of gold at the micron scale in the absence of strain gradients. *Acta Mater.*, 53(6):1821–1830, 2005.

[20] H. Bei, S. Shim, G. M. Pharr, and E.P. George. Effects of pre-strain on the compressive stress-strain response of Mo-alloy single-crystal micropillars. *Acta Mater.*, 56(17):4762–4770, 2008.

[21] F. Briffod, T. Shiraiwa, and M. Enoki. Microstructure modeling and crystal plasticity simulations for the evaluation of fatigue crack initiation in α-iron specimen including an elliptic defect. *Mater. Sci. Eng. A*, 695:165–177, 2017.

[22] K. Kirane and S. Ghosh. A cold dwell fatigue crack nucleation criterion for polycrystalline Ti-6242 using grain-level crystal plasticity FE Model. *Int. J. Fatigue*, 30(12):2127–2139, 2008.

[23] S. Sinha and S. Ghosh. Modeling cyclic ratcheting based fatigue life of HSLA steels using crystal plasticity FEM simulations and experiments. *Int. J. Fatigue*, 28(12):1690–1704, 2006.

[24] F.P.E. Dunne, D. Rugg, and A. Walker. Lengthscale-dependent, elastically anisotropic, physically-based hcp crystal plasticity: Application to cold-dwell fatigue in Ti alloys. *Int. J. Plast.*, 23(6):1061–1083, 2007.

[25] G.M. Castelluccio and D.L. McDowell. Microstructure and mesh sensitivities of mesoscale surrogate driving force measures for transgranular fatigue cracks in polycrystals. *Mater. Sci. Eng. A*, 639:626–639, 2015.

[26] G.M. Castelluccio, W.D. Musinski, and D.L. McDowell. Recent developments in assessing microstructure-sensitive early stage fatigue of polycrystals. *Curr. Opin. Solid State Mater. Sci.*, 18(4):180–187, 2014.

[27] G.M. Castelluccio and D.L. Mcdowell. A mesoscale approach for growth of 3D microstructurally small fatigue cracks in polycrystals. *Int. J. Damage Mech.*, 23(6):791–818, 2014.

[28] K. Nishimura and N. Miyazaki. Molecular dynamics simulation of crack growth under cyclic loading. *Comput. Mater. Sci.*, 31(3-4):269–278, 2004.

[29] T. Tang, S. Kim, and M.F. Horstemeyer. Fatigue crack growth in magnesium single crystals under cyclic loading: Molecular dynamics simulation. *Comput. Mater. Sci.*, 48(2):426–439, 2010.

[30] G. Sainath, P. Rohith, and B.K. Choudhary. Fatigue Deformation of Polycrystalline Cu Using Molecular Dynamics Simulations. *Trans. Indian Inst. Met.*, 69(2):489–493, 2016.

[31] M. Hommel, O. Kraft, and E. Arzt. A new method to study cyclic deformation of thin films in tension and compression. *J. Mater. Res.*, 14(6):2373–2376, 1999.

[32] C.L. Muhlstein, S.B. Brown, and R.O. Ritchie. High-Cycle Fatigue of Polycrystalline Silicon Thin Films in Laboratory Air. *Mater. Res.*, 657(4):1–6, 2001.

[33] A. Barrios, S. Gupta, G.M. Castelluccio, and O.N. Pierron. Quantitative in Situ SEM High Cycle Fatigue: The Critical Role of Oxygen on Nanoscale-Void-Controlled Nucleation and Propagation of Small Cracks in Ni Microbeams. *Nano Lett.*, 18(4):2595–2602, 2018.

[34] H. Zhang, C. Jiang, and Y. Lu. Low-Cycle Fatigue Testing of Ni Nanowires Based on a Micro-Mechanical Device. *Exp. Mech.*, 57(3):495–500, 2017.

[35] M. Qi, Z. Liu, and X. Yan. A low cycle fatigue test device for micro-cantilevers based on self-excited vibration principle. *Rev. Sci. Instrum.*, 85(10):1–6, 2014.

[36] C.J. Szczepanski, S.K. Jha, P.A. Shade, R. Wheeler, and J.M. Larsen. Demonstration of an in situ microscale fatigue testing technique on a titanium alloy. *Int. J. Fatigue*, 57:131–139, 2013.

[37] Z.-J. Wang, Q.-J. Li, Y.-N. Cui, Z.-L. Liu, E. Ma, J. Li, J. Sun, Z. Zhuang, M. Dao, Z.-W. Shan, and S. Suresh. Cyclic deformation leads to defect healing and strengthening of small-volume metal crystals. *PNAS*, 112(44):13502–13507, 2015.

[38] D. Kiener, C. Motz, W. Grosinger, D. Weygand, and R. Pippan. Cyclic response of copper single crystal micro-beams. *Scr. Mater.*, 63(5):500–503, 2010.

[39] C. Kirchlechner, P.J. Imrich, W. Liegl, J. Pörnbacher, J.-S. Micha, O. Ulrich, and C. Motz. On the reversibility of dislocation slip during small scale low cycle fatigue. *Acta Mater.*, 94:69–77, 2015.

[40] Y. Yang, H.H. Ruan, J. Lu, N. Yao, W.L. Shan, and W.O. Soboyejo. Development of a Micro-beam Method to Investigate the Fatigue Crack Growth Mechanisms of Submicron-scale Cracks. *Exp. Mech.*, 49:731–742, 2009.

[41] J. Gong and A. Wilkinson. Ultra small scale high cycle fatigue testing by micro-cantilevers. *Nanomechanical Test. Mater. Res. Dev. V*, (2009):1–2, 2015.

[42] C. Howard, R. Fritz, M. Alfreider, D. Kiener, and P. Hosemann. The influence of microstructure on the cyclic deformation and damage of copper and an oxide dispersion strengthened steel studied via in-situ micro-beam bending. *Mater. Sci. Eng. A*, 687:313–322, feb 2017.

[43] L. Eisenhut, F. Schaefer, P. Gruenewald, L. Weiter, M. Marx, and C. Motz. Effect of a dislocation pile-up at the neutral axis on transcrystalline crack growth for micro-bending fatigue. *Int. J. Fatigue*, 94:131–139, 2017.

[44] M. Schamel, J. M. Wheeler, C. Niederberger, J. Michler, A. Sologubenko, and R. Spolenak. Cyclic loading for the characterisation of strain hardening during in situ microcompression experiments. *Philos. Mag.*, 96(32-34):3479–3501, 2016.

[45] B. Merle and H.W. Hoppel. Microscale High-Cycle Fatigue Testing by Dynamic Micropillar Compression Using Continuous Stiffness Measurement. *Exp. Mech.*, 58:7–9, 2018.

[46] R. Hofbeck, K. Hausmann, B. Ilschner, and H. U. Künzi. Fatigue of very thin copper and gold wires. *Scr. Metall.*, 20(11):1601–1605, 1986.

[47] M. Judelewicz, H.U. Kiinzi, N. Merk, and B. Ilschner. Microstructural development during fatigue of copper foils 20-100 μm thick. *Mater. Sci. Eng. A*, 186(1-2):135–142, 1994.

[48] Y. Higo, K. Takashima, M. Shimojo, S. Sugiura, and M. V. Swain. Fatigue testing machine of micro-sized specimens for MEMS applications. *Symp. MM - Mater. Sci. Microelectromechanical Syst. Devices II*, 605:241–246, 1999.

[49] J.B. Pethica and W.C. Oliver. Tip Surface Interactions in STM and AFM. *Phys. Scr.*, 19:61–66, 1987.

[50] R. Schwaiger and O. Kraft. High Cycle Fatigue of Thin Silver Films Investigated by Dynamic Microbeam Deflection. *Scr. Mater.*, 41(8):823–829, 1999.

[51] X. Li and B. Bhushan. Fatigue studies of nanoscale structures for MEMS/NEMS applications using nanoindentation techniques. *Surf. Coat. Technol.*, 163-164:521–526, 2003.

[52] A. Wimmer, W. Heinz, T. Detzel, W. Robl, M. Nellessen, C. Kirchlechner, and G. Dehm. Cyclic bending experiments on free-standing Cu micron lines observed by electron backscatter diffraction. *Acta Mater.*, 83:460–469, 2015.

[53] T. Sumigawa, K. Byungwoon, Y. Mizuno, T. Morimura, and T. Kitamura. In situ observation on formation process of nanoscale cracking during tension-compression fatigue of single crystal copper micron-scale specimen. *Acta Mater.*, 153:270–278, 2018.

[54] T. Straub, M. F. Berwind, T. Kennerknecht, Y. Lapusta, and C. Eberl. Small-Scale Multiaxial Setup for Damage Detection Into the Very High Cycle Fatigue Regime. *Exp. Mech.*, 55(7):1285–1299, 2015.

[55] F. Sadeghi-Tohidi and O.N. Pierron. Extreme stress gradient effects on the fatigue behavior of Ni notched microbeams. *Acta Mater.*, 106:388–400, 2016.

[56] Y. Wang, T. Hoechbauer, J.G. Swadener, and A. Misra. Mechanical Fatigue Measurement via a Vibrating Cantilever Beam for Self-Supported Thin Solid Films. *Exp. Mech.*, 46:503–517, 2006.

[57] Z. Alam, D. Eastman, G. Weber, S. Ghosh, and K. Hemker. Microstructural Aspects of Fatigue Crack Initiation and Short Crack Growth in René 88Dt. In *Superalloys 2016 Proc. 13th Int. Symp. Superalloys*, pages 561–561, 2016.

[58] E.K. Baumert and O.N. Pierron. Fatigue Degradation Properties of LIGA Ni Films Using Kilohertz Microresonators. *J. Microelectromechanical Syst.*, 22(1):16–25, 2013.

[59] H. Van Swygenhoven, S. Van Petegem, N. Grilli, A. Bollhalder, S. Brandstetter, and D. Grolimund. Following dislocation patterning during fatigue. *Acta Mater.*, 112:184–193, 2016.

[60] D.C. Bufford, D. Stauffer, W.M. Mook, S.A.S. Asif, B.L. Boyce, and K. Hattar. High Cycle Fatigue in the Transmission Electron Microscope. *Nano Lett.*, 16:4946–4953, 2016.

[61] C.J. Szczepanski, P.A. Shade, M.A. Groeber, J.M. Larsen, S.K. Jha, and R. Wheeler. Development of a Microscale Fatigue Testing Technique. *Adv. Mater. Process.*, 171(6):18–21, 2013.

[62] R. Schwaiger, G. Dehm, and O. Kraft. Cyclic deformation of polycrystalline Cu films. *Philos. Mag.*, 83(6):693–710, 2003.

[63] G.P. Zhang, C.A. Volkert, R. Schwaiger, E. Arzt, and O. Kraft. Damage behavior of 200-nm thin copper films under cyclic loading. *J. Mater. Res.*, 20(1):201–207, 2005.

[64] G.P. Zhang, C.A. Volkert, R. Schwaiger, P. Wellner, E. Arzt, and O. Kraft. Length-scale-controlled fatigue mechanisms in thin copper films. *Acta Mater.*, 54(11):3127–3139, 2006.

[65] M. Klein, A. Hadrboletz, B. Weiss, and G. Khatibi. The 'size effect' on the stress-strain, fatigue and fracture properties of thin metallic foils. *Mater. Sci. Eng.*, A319-321:924–928, 2001.

[66] A. Hadrboletz, B. Weiss, and G. Khatibi. Fatigue and fracture properties of thin metallic foils. *Int. J. Fract.*, 107:307–327, 2001.

[67] G. Khatibi, A. Betzwar-Kotas, V. Gröger, and B. Weiss. A study of the mechanical and fatigue properties of metallic microwires. *Fatigue Fract. Eng. Mater. Struct.*, 28(8):723–733, 2005.

[68] H. Mughrabi. Cyclic slip irreversibilities and the evolution of fatigue damage. *Met. Mater. Trans. A*, 40A(4):431–453, 2009.

[69] M.D. Sangid. The physics of fatigue crack initiation. *Int. J. Fatigue*, 57:58–72, 2013.

[70] D. Kuhlmann-Wilsdorf. Dislocation cells, redundant dislocations and the LEDS hypothesis. *Scr. Mater.*, 34(4):641–650, 1996.

[71] D. Kuhlmann-Wilsdorf. High-strain dislocation patterning, texture formation and shear banding of wavy glide materials in the LEDS theory. *Scr. Mater.*, 36(2):173–181, 1997.

[72] D. Kuhlmann-Wilsdorf. The theory of dislocation-based crystal plasticity. *Philos. Mag. A*, 79(4):955–1008, 1999.

[73] P. Neumann. Dislocation dynamics in fatigue. *Phys. Scr.*, 1987(T19B):537–543, 1987.

[74] C. Déprés, C.F. Robertson, and M.C. Fivel. Low-strain fatigue in AISI 316L steel surface grains: a three-dimensional discrete dislocation dynamics modelling of the early cycles I. Dislocation microstructures and mechanical behaviour. *Philos. Mag.*, 84(22):2257–2275, 2004.

[75] C. Erel, G. Po, T. Crosby, and N. Ghoniem. Generation and interaction mechanisms of prismatic dislocation loops in FCC metals. *Comput. Mater. Sci.*, 140:32–46, 2017.

[76] J. Kratochvíl and M. Saxlová. Sweeping mechanism of dislocation pattern formation. *Scr. Metall. Mater.*, 26(1):113–116, 1992.

[77] J. Huang, N.M. Ghoniem, and J. Kratochvíl. On the sweeping mechanism of dipolar dislocation loops under fatigue conditions. *Model. Simul. Mater. Sci. Eng.*, 12(5):917–928, 2004.

[78] T. Shimada, T. Kondo, and T. Kitamura. Critical Thickness for Formation of Fatigue Dislocation Structures: A Discrete Dislocation Dynamics Study. *Trans. Japan Soc. Mech. Eng.*, 78(793):1242–1249, 2012.

[79] T. Tabata, H. Fujita, M.A. Hiraoka, and K. Onishi. Dislocation behaviour and the formation of persistent slip bands in fatigued copper single crystals observed by high-voltage electron microscopy. *Philos. Mag. A*, 47(6):841–857, 1983.

[80] R.J. Amodeo and N.M. Ghoniem. Dislocation dynamics. II. Applications to the formation of persistent slip bands, planar arrays, and dislocation cells. *Phys. Rev. B*, 41(10):6968–6976, 1990.

[81] H. Mughrabi. Dislocation Wall and Cell Structures and Long-Range Internal Stress in Deformed Metal Crystals. *Acta Metall.*, 31(9):1367–1379, 1983.

[82] H. Mughrabi. The long-range internal stress field in the dislocation wall structure of persistent slip bands. *Phys. Stat. Sol. (a)*, 104:107–120, 1987.

[83] L.M. Brown. Dislocation plasticity in persistent slip bands. *Mater. Sci. Eng. A*, 285(1-2):35–42, 2000.

[84] H. Mughrabi and F. Pschenitzka. Constrained glide and interaction of bowed-out screw dislocations in confined channels. *Philos. Mag.*, 85(26-27 SPEC. ISS.):3029–3045, 2005.

[85] L. Brown. Dislocation bowing and passing in persistent slip bands. *Phil. Mag.*, 86:4055–4068, 2006.

[86] L. Kubin and M. Sauzay. Persistent slip bands: The bowing and passing model revisited. *Acta Mater.*, 132:517 – 524, 2017.

[87] K.W. Schwarz and H. Mughrabi. Interaction and passing stress of two threading dislocations of opposite sign in a confined channel. *Phil. Mag. Letters*, 86:773–785, 2006.

[88] J. Křišt'an and J. Kratochvíl. Interaction of glide dislocations in a channel of a persistent slip band. *Phil. Mag.*, 87:4593–4613, 2007.

[89] J.A. El-Awady, N. Ghoniem, and H. Mughrabi. Dislocation Modelling of Localized Plasticity in Persistent Slip Bands. In *Mater. Process. Manuf. Div. Symp. Mech. Mater.*, pages 23–35, 2007.

[90] P. Pauš, J. Kratochvíl, and M. Beneš. A dislocation dynamics analysis of the critical cross-slip annihilation distance and the cyclic saturation stress in fcc single crystals at different temperatures. *Acta Mater.*, 61(20):7917 – 7923, 2013.

[91] C. Erel, G. Po, and N. Ghoniem. Dependence of hardening and saturation stress in persistent slip bands on strain amplitude during cyclic fatigue loading. *Philos. Mag.*, 97(32):2947–2970, 2017.

[92] H. Mughrabi and F. Pschenitzka. Constrained glide and interaction of bowed-out screw dislcoations in confined channels. *Phil. Mag.*, 85:3029–3045, 2005.

[93] H. Mughrabi. The Cyclic Hardening and Saturation Behaviour of Copper Single Crystals. *Mater. Sci. Eng.*, 33:207–223, 1978.

[94] S.S. Shishvan, R.M. McMeeking, T.M. Pollock, and V.S. Deshpande. Discrete dislocation plasticity analysis of the high-temperature cyclic response of composites. *Mater. Sci. Eng. A*, 712:714–719, 2018.

[95] A.M. Hussein and J.A. El-Awady. Quantifying dislocation microstructure evolution and cyclic hardening in fatigued face-centered cubic single crystals. *J. Mech. Phys. Solids*, 91:126–144, 2016.

[96] G. Dehm, C. Motz, C. Scheu, H. Clemens, P.H. Mayrhofer, and C. Mitterer. Mechanical size-effects in miniaturized and bulk materials. *Adv. Eng. Mater.*, 8:1033–1045, 2006.

[97] O. Kraft, P.A. Gruber, R. Monig, and D. Weygand. Plasticity in confined dimensions. *Annu. Rev. Mater. Res.*, 40:293–317, 2010.

[98] G.M. Pharr, E.G. Herbert, and Y. Gao. The indentation size effect: A critical examination of experimental observations and mechanistic interpretations. *Annu. Rev. Mater. Res.*, 40:271–292, 2010.

[99] J.A. El-Awady. Unravelling the physics of size-dependent dislocation-mediated plasticity. *Nat. Commun.*, 6:5926, 2015.

[100] D. Wang, C. A. Volkert, and O. Kraft. Effect of length scale on fatigue life and damage formation in thin Cu films. *Mater. Sci. Eng. A*, 493(1-2):267–273, 2008.

[101] O. Kraft, P. Wellner, M. Hommel, R. Schwaiger, and E. Arzt. Fatigue behavior of polycrystalline thin copper films. *Zeitschrift für Met.*, 93(5):392–400, 2002.

[102] O. Kraft, R. Schwaiger, and P. Wellner. Fatigue in thin films: Lifetime and damage formation. *Mater. Sci. Eng. A*, 319-321:919–923, 2001.

[103] X.J. Sun, C.C. Wang, J. Zhang, G. Liu, G.J. Zhang, X.D. Ding, G.P. Zhang, and J. Sun. Thickness dependent fatigue life at microcrack nucleation for metal thin films on flexible substrates. *J. Phys. D. Appl. Phys.*, 41(19), 2008.

[104] P. Lukáš and L. Kunz. Effect of grain size on the high cycle fatigue behaviour of polycrystalline copper. *Mater. Sci. Eng.*, 85(C):67–75, 1987.

[105] K. Kammuri, M. Kitamura, T. Fujii, and M. Kato. Effects of Thickness and Crystallographic Orientation on Fatigue Life of Single-Crystalline Copper Foils. *Mater. Trans.*, 56(2):200–205, 2015.

[106] D.T. Read. Tension-tension fatigue of copper thin films. 20(3):203–209, 1998.

[107] S. Hong and R. Weil. Low cycle fatigue of thin copper foils. *Thin Solid Films*, 283:175–181, 1996.

[108] M. Korn, R. Lapovok, A. Bohner, H.W. Hoppel, and H. Mughrabi. Bimodal grain size distributions in UFG materials produced by SPD - their evolution and effect on the fatigue and monotonic strength properties. 88(1):43–53, 1982.

[109] B. Weiss, V. Gröger, G. Khatibi, A. Kotas, P. Zimprich, R. Stickler, and B. Zagar. Characterization of mechanical and thermal properties of thin Cu foils and wires. *Sensors Actuators, A Phys.*, 99(1-2):172–182, 2002.

[110] B. Yang, C. Motz, W. Grosinger, and G. Dehm. Stress-controlled fatigue behaviour of micro-sized polycrystalline copper wires. *Mater. Sci. Eng. A*, 515(1-2):71–78, 2009.

[111] C.Y. Dai, G.P. Zhang, and C. Yan. Size effects on tensile and fatigue behaviour of polycrystalline metal foils at the micrometer scale. *Philos. Mag.*, 91(6):932–945, 2011.

[112] S. Burger, C. Eberl, A. Siegel, A. Ludwig, and O. Kraft. A novel high-throughput fatigue testing method for metallic thin films. *Sci. Technol. Adv. Mater.*, 12(5):1–7, 2011.

[113] H. Conrad, J. White, W. D. Cao, X. P. Lu, and A. F. Sprecher. Effect of electric current pulses on fatigue characteristics of polycrystalline copper. *Mater. Sci. Eng. A*, 145(1):1–12, 1991.

[114] Y. Nakai, A. Hashimoto, and A. Taketani. Development of fatigue test method and size effect of fatigue strength in metallic thin wires. *Journal of the Society of Materials Science, Japan*, 54(3):284–289, 2005.

[115] H.D. Merchant, M.G. Minor, and Y.L. Liu. Mechanical fatigue of thin copper foil. *Journal of Electronic Materials*, 28(9):998–1007, 1999.

[116] G.P. Zhang, K. Takashima, and Y. Higo. Fatigue strength of small-scale type 304 stainless steel thin films. *Mater. Sci. Eng. A*, 426(1-2):95–100, 2006.

[117] G.P. Zhang, R. Schwaiger, C.A. Volkert, and O. Kraft. Effect of film thickness and grain size on fatigue-induced dislocation structures in Cu thin films. *Philos. Mag. Lett.*, 83(8):477–483, 2003.

[118] A.M. Hussein and J.A. El-Awady. Surface roughness evolution during early stages of mechanical cyclic loading. *Int. J. Fatigue*, 87:339–350, 2016.

[119] C. Motz, D. Weygand, J. Senger, and P. Gumbsch. Micro-bending tests: A comparison between three-dimensional discrete dislocation dynamics simulations and experiments. *Acta Mater.*, 56(9):1942–1955, 2008.

[120] J. Senger, D. Weygand, O. Kraft, and P. Gumbsch. Dislocation microstructure evolution in cyclically twisted microsamples: A discrete dislocation dynamics simulation. *Model. Simul. Mater. Sci. Eng.*, 19(7):074004, 2011.

[121] M. Stricker, D. Weygand, and P. Gumbsch. Irreversibility of dislocation motion under cyclic loading due to strain gradients. *Scr. Mater.*, 129:69–73, 2017.

[122] U. Essmann, U. Gösele, and H. Mughrabi. A model of extrusions and intrusions in fatigued metals I. Point-defect production and the growth of extrusions. *Philos. Mag. A Phys. Condens. Matter, Struct. Defects Mech. Prop.*, 44(2):405–426, 1981.

[123] J. Polák. On the Role of Point Defects in Fatigue Crack Initiation. *Mater. Sci. Eng.*, 92:71–80, 1987.

[124] J. Polák and J. Man. Mechanisms of extrusion and intrusion formation in fatigued crystalline materials. *Mater. Sci. Eng. A*, 596:15–24, 2014.

[125] C. Déprés, C.F. Robertson, and M.C. Fivel. Crack initiation in fatigue: experiments and three-dimensional dislocation simulations. *Mater. Sci. Eng. A*, 387-389:288–291, 2004.

[126] C. Déprés, G.V. Prasad Reddy, C. Robertson, and M. Fivel. An extensive 3D dislocation dynamics investigation of stage-I fatigue crack propagation An extensive 3D dislocation dynamics investigation of stage-I fatigue crack propagation. *Philos. Mag.*, 94(36):4115–4137, 2014.

[127] V.S. Deshpande, A. Needleman, and E. Van Der Giessen. A Discrete Dislocation Analysis of Near-Threshold Fatigue Crack Growth. *Acta Mater.*, 49:3189–3203, 2001.

[128] S. Brinckmann and E. Van der Giessen. A fatigue crack initiation model incorporating discrete dislocation plasticity and surface roughness. *Int. J Fract.*, 148(2):155–167, 2007.

[129] C. Déprés, C. Robertson, and M. Fivel. Discrete Dislocation Dynamics Investigations of Fatigue Crack Initiation and Propagation. *J. Aerosp. Lab*, (9), 2015.

[130] S. Suresh and R.O. Ritchie. Propagation of short fatigue cracks. *Int. Met. Rev.*, 29(6):445–475, 1984.

[131] F. Sadeghi-Tohidi and O.N. Pierron. Extreme stress gradient effects on microstructural fatigue crack propagation rates in Ni microbeams. *Appl. Phys. Lett*, 106:201904, 2015.

[132] F. Sadeghi-Tohidi and O.N. Pierron. Towards prediction of the fatigue life of Ni microbeams under extreme stress gradients. *Extrem. Mech. Lett.*, 9:97–107, 2016.

[133] K. Takashima, Y Higo, S. Sugiura, and M. Shimojo. Fatigue Crack Growth Behavior of Micro-Sized Specimens Prepared from an Electroless Plated Ni-P Amorphous Alloy Thin Film. *Mater. Trans.*, 42(1):68–73, 2000.

[134] J. Miao, T.M. Pollock, and J. Wayne Jones. Crystallographic fatigue crack initiation in nickel-based superalloy René 88DT at elevated temperature. *Acta Mater.*, 57(20):5964–5974, 2009.

[135] R. Schwaiger and O. Kraft. Size effects in the fatigue behavior of thin Ag films. *Acta Mater.*, 51(1):195–206, 2003.

[136] V.S. Deshpande, A. Needleman, and E. Van Der Giessen. Discrete dislocation modeling of fatigue crack propagation. *Acta Mater.*, 50:831–846, 2002.

[137] O. Kraft, R. Schwaiger, and P. Wellner. Fatigue in thin films: Lifetime and damage formation. *Mater. Sci. Eng. A*, 319-321:919–923, 2001.

[138] X. Li and B. Bhushan. Fatigue studies of nanoscale structures for MEMS/NEMS applications using nanoindentation techniques. *Surf. Coatings Technol.*, 163-164:521–526, 2003.

[139] D. Son, D.-J. Kim, T.W. Lim, and D. Kwon. Evaluation of fatigue strength of LIGA nickel film by microtensile tests. *Scr. Mater.*, 50(10):1265–1269, 2004.

[140] R. Mönig, R.R. Keller, and C.A. Volkert. Thermal fatigue testing of thin metal films. *Rev. Sci. Instrum.*, 75(11):4997–5004, 2004.

[141] S. Wiersma, F. Dolan, and D. Taylor. Fatigue and fracture in materials used for micro-scale biomedical components. *Biomed. Mater. Eng.*, 16(2):137–146, 2006.

[142] Y.C. Lin, H. Hocheng, W.L. Fang, and R. Chen. Fabrication and fatigue testing of an electrostatically driven microcantilever beam. *Mater. Manuf. Process.*, 21(1):75–80, 2006.

[143] Y. Yang, B.I. Imasogie, S.M. Allameh, B. Boyce, K. Lian, J. Lou, and W.O. Soboyejo. Mechanisms of fatigue in LIGA Ni MEMS thin films. *Mater. Sci. Eng. A*, 444(1-2):39–50, 2007.

[144] D. Liu, Y. He, D.J. Dunstan, B. Zhang, Z. Gan, P. Hu, and H. Ding. Anomalous Plasticity in the Cyclic Torsion of Micron Scale Metallic Wires. *Phys. Rev. Lett.*, 110:244301:1–5, 2013.

[145] D. Liu, Y. He, L. Shen, J. Lei, S. Guo, and K. Peng. Accounting for the recoverable plasticity and size effect in the cyclic torsion of thin metallic wires using strain gradient plasticity. *Mater. Sci. Eng. A*, 647:84–90, 2015.

[146] C.A. Sweeney, B. O'Brien, F.P.E. Dunne, P.E. McHugh, and S.B. Leen. Micro-scale testing and micromechanical modelling for high cycle fatigue of CoCr stent material. *J. Mech. Behav. Biomed. Mater.*, 46:244–260, 2015.

[147] Y.C. Shieh, H.Y. Lin, W. Hsu, and Y.H. Lin. A Rapid Fatigue Test Method on Micro Structures for High-Cycle Fatigue. *IEEE Trans. Device Mater. Reliab.*, 16(1):61–68, 2016.

[148] S. Fu, L. Wang, G. Chen, D. Yu, and X. Chen. A tension-torsional fatigue testing apparatus for micro-scale components. *Rev. Sci. Instrum.*, 87:15111, 2016.

[149] S. Lavenstein, B. Crawford, G.-D. Sim, P.A. Shade, C. Woodward, and J.A. El-Awady. High frequency in situ fatigue response of Ni-base superalloy René-N5 microcrystals. *Acta Mater.*, 144:154–163, 2018.

[150] B.L. Boyce, J.R. Michael, and P.G. Kotula. Fatigue of metallic microdevices and the role of fatigue-induced surface oxides q. *Acta Mater.*, 52:1609–1619, 2004.

[151] T. Kakiuchi, Y. Uematsu, S. Tamano, and S. Mizuno. Effect of Grain Orientation on Fatigue Behavior in Micro Cantilever of Magnesium Alloy AZ31. *Procedia Mater. Sci.*, 3:967–972, 2014.

[152] Y. Uematsu, T. Kakiuchi, S. Tamano, S. Mizuno, and K. Tamada. Fatigue behavior of AZ31 magnesium alloy evaluated using single crystal micro cantilever specimen. *Int. J. Fatigue*, 93:30–37, 2016.

[153] Nickel Development Institute. High-Temperature High-Strength Nickel Base Alloys, 1995.

[154] P.A. Shade, M.D. Uchic, D.M. Dimiduk, G.B. Viswanathan, R. Wheeler, and H.L. Fraser. Size-affected single-slip behavior of {Rene N5} microcrystals. *Mater. Sci. Eng., A*, 535:53–61, 2012.

[155] W. Zhou, R. Apkarian, Z.L. Wang, and D. Joy. Fundamentals of scanning electron microscopy (SEM). In *Scanning Microsc. Nanotechnol. Tech. Appl.*, pages 1–40. 2007.

[156] TESCAN. Scanning Electron Microscope Mira3 FEG-SEM Instructions for Use, 2011.

[157] O. Engler and V. Randle. *Introduction to texture analysis*. 2008.

[158] C.A. Volkert and A.M. Minor. Focused Ion Beam Microscopy and Micromachining. *MRS Bull.*, 32(5):389–399, 2007.

[159] N.I. Kato. Reducing focused ion beam damage to transmission electron microscopy samples. *J. Electron Microsc. (Tokyo).*, 53(5):451–458, 2004.

[160] W.J. Moberlychan, P. David, M.J. Aziz, G. Hobler, and T. Schenkel. Fundamentals of Focused Ion Beam Nanostructural Processing: Below, At, and Above the Surface. *MRS Bull.*, 32(May):424–433, 2007.

[161] R.D. Kelley, K. Song, B. Van Leer, D. Wall, and L. Kwakman. Xe+ FIB Milling and Measurement of Amorphous Silicon Damage. *Microsc. Microanal.*, 19(S2):862–863, 2013.

[162] J.A. El-Awady, C. Woodward, D.M. Dimiduk, and N.M. Ghoniem. Effects of focused ion beam induced damage on the plasticity of micropillars. *Phys. Rev. B*, 80(10):1–5, 2009.

[163] M.P. Echlin, A. Mottura, C.J. Torbet, and T.M. Pollock. A new TriBeam system for three-dimensional multimodal materials analysis. *Rev. Sci. Instrum.*, 83(2), 2012.

[164] E.G. Gamaly, A.V. Rode, V.T. Tikhonchuk, and B. Luther-Davies. Ablation of solids by femtosecond lasers: Ablation mechanism and ablation thresholds for metals and dielectrics. *Phys. Plasmas*, 9:949–957, 2002.

[165] D. Eastman. *Microscale Testing and Characterization Techniques for Benchmarking Crystal Plasticity Models*. PhD thesis, Johns Hopkins University, 2018.

[166] J.E. Sipe, J.F. Young, J.S. Preson, and H.M. van Driel. Laser-induced periodic surface structure. I . Theory. *Phys. Rev. B*, 27(2):1141–1154, 1983.

[167] M.D. Uchic and D.M. Dimiduk. A methodology to investigate size scale effects in crystalline plasticity using uniaxial compression testing. *Mater. Sci. Eng. A*, 400-401(1-2 SUPPL.):268–278, 2005.

[168] G.-D. Sim, G. Kim, S. Lavenstein, M.H. Hamza, H. Fan, and J.A. El-Awady. Anomalous hardening in magnesium driven by a size-dependent transition in deformation modes. *Acta Mater.*, 144, 2018.

[169] Core Technology. http://nanomechanicsinc.com/products/.

[170] P.S. Phani, B.A. Crawford, and W.C Oliver. Performing accurate and precise nanoindentation measurements. Technical report.

[171] W. Bonin. High-performance drive circuitry for capacitive transducers, 2005.

[172] D.J. Inman. *Engineering Vibration*. Pearson, 2007.

[173] P.A. Shade, R. Wheeler, Y.S. Choi, M.D. Uchic, D.M. Dimiduk, and H.L. Fraser. A combined experimental and simulation study to examine lateral constraint effects on microcompression of single-slip oriented single crystals. *Acta Mater.*, 57(15):4580–4587, 2009.

[174] Kleindiek Nanotechnik. SEMGLU. nanotechnik.com/semglu.html, 2017.

[175] C. Kirchlechner, P.J. Imrich, W. Liegl, J. Pombacher, J.-S. Mich, O. Ulrich, and C. Motz. On the reversibility of dislocation slip during small scale low cycle fatigue. *Acta Mater.*, 94:69–77, 2015.

[176] Simulia. ABAQUS 6.13 Documentation, 2013.

[177] K. Ono. Acoustic Emission. In *Handb. Acoust.* 2014.

[178] D. Li, K.S.C. Kuang, and C.G. Koh. Fatigue crack sizing in rail steel using crack closure-induced acoustic emission waves. *Meas. Sci. Technol.*, 28(6), 2017.

[179] N. Kiesewetter and P. Schiller. The acoustic emission from moving dislocations in aluminium. *Phys. Status Solidi*, 38(2):569–576, 1976.

[180] J. Weiss, W.B. Rhouma, S. Deschanel, and L. Truskinovsky. Plastic intermittency during cyclic loading: From dislocation patterning to microcrack initiation. *Phys. Rev. Mater.*, 3:23603, 2019.

[181] B.I. Voronenko. Acoustic emission during phase transformations in alloys. *Met. Sci. Heat Treat.*, 24(8):545–553, 1982.

[182] C. Mo, B. Wisner, M. Cabal, K. Hazeli, K.T. Ramesh, H. El Kadiri, T. Al-Samman, K.D. Molodov, D.A. Molodov, and A. Kontsos. Acoustic Emission of Deformation Twinning in Magnesium. *Materials (Basel).*, 9(8):662, aug 2016.

[183] H. Aburatani. Acoustic Emission Measurements on Piezoelectric/Ferroelectric Materials. *J. Acoust. Emiss.*, 29:149–159, 2011.

[184] A. Terchi and Y.H.J. Au. Acoustic emission signal processing. *Meas. Control*, 34(8):240–244, 2001.

[185] S. Gholizadeh, Z. Lemana, and B. T.H.T. Baharudinb. A review of the application of acoustic emission technique in engineering. *Struct. Eng. Mech.*, 54(6):1075–1095, 2015.

[186] S.Y. Liang and D.A. Dornfield. Characterization of sheet metal forming using acoustic emission. *J. Eng. Mater. Technol.*, 112:44–51, 1990.

[187] C.L. Pekeris and H. Lifson. Motion of the Surface of a Uniform Elastic Half-Space Produced by a Buried Pulse. *J. Acoust. Soc. Am.*, 29:1233, 1957.

[188] D.L. Polla and L.F. Francis. Processing and characterization of piezoelectric materials and integration into microelectromechanical systems. *Ann. Rev. Mater. Sci.*, 28(1):563–597, 1998.

[189] ASTM. *ASTM Volume 03.03 Nondestructive Testing (I): B594 - E2373.*

[190] *SciPy Reference Guide.*

[191] J. Alstott, E. Bullmore, and D. Plenz. Powerlaw: A python package for analysis of heavy-tailed distributions. *PLoS One*, 9(1):1–18, 2014.

[192] A. Clauset, C.R. Shalizi, and M.E.J. Newman. Power-law distributions in empirical data. *SIAM Rev.*, 51(4):661–703, 2009.

[193] T.M. Pollock and S. Tin. Nickel-based superalloys for advanced turbine engines: chemistry, microstructure, and properties. *J. Propuls. Power*, 22:361–374, 2006.

[194] S. Raman and K.A. Padmanabhan. Room-temperature low-cycle fatigue behavior of a Ni-base superalloy. *Int. J. Fatigue*, 16:209–215, 1994.

[195] C. Calabrese and C. Laird. Cyclic stress-strain response of two-phase alloys. *Mater. Sci. Eng.*, 13, 1974.

[196] J.H. Zhang, Y.B. Xu, Z.G. Wang, and Z.Q. Hu. Fatigue Behavior of a Single Crystal Nickel-Base Superalloy. *Scr. Met. Mater.*, 32(12):2093–2098, 1995.

[197] N.K. Arakere and G. Swanson. Fretting Stresses in Single Crystal Superalloy Turbine Blade Attachments. *J. Tribol.*, 123(2), 2001.

[198] N.K. Arakere and J. Moroso. Fatigue failure in high-temperature single crystal superalloy turbine blades. *High Temp. Mater. Process.*, 20(2):117–136, 2001.

[199] B.A. Lerch and V. Gerold. Cyclic hardening mechanisms in {NIMONIC 80A}. *Met. Trans. A*, 18(12):2135–2141, 1987.

[200] L. Eisenhut, F. Schaefer, P. Gruenewald, L. Weiter, M. Marx, and C. Motz. Effect of a dislocation pile-up at the neutral axis on transcrystalline crack growth for micro-bending fatigue. *Int. J. Fatigue*, 94:131–139, 2017.

[201] R. Schwaiger and O. Kraft. High Cycle Fatigue of Thin Silver Films Investigated by Dynamic Microbeam Deflection. *Scr. Mater.*, 41(8):823–829, 1999.

[202] M. Schamel, J.M. Wheeler, C. Niederberger, J. Michler, A. Soogubenko, and R. Spolenak. Cyclic loading for the characterisation of strain hardening during in situ microcompression experiments. *Philos. Mag.*, 96(32-34):3479–3501, 2016.

[203] C.J. Szczepanski, S.K. Jha, P.A. Shade, R. Wheeler, and J.M. Larsen. Demonstration of an in situ microscale fatigue testing technique on a titanium alloy. *Int. J. Fatigue*, 57:131–139, 2013.

[204] P.A. Shade, R. Wheeler, Y.S. Choi, M.D. Uchic, D.M. Dimiduk, and H.L. Fraser. A combined experimental and simulation study to examine lateral constraint effects on microcompression of single-slip oriented single crystals. *Acta Mater.*, 57, 2009.

[205] A.M. Hussein and J.A. El-Awady. Quantifying dislocation microstructure evolution and cyclic hardening in fatigued face-centered cubic single crystals. *J. Mech. Phys. Solids*, 91:126–144, 2016.

[206] A.M. Hussein and J.A. El-Awady. Surface roughness evolution during early stages of mechanical cyclic loading. *Int. J. Fatigue*, 87:339–350, 2016.

[207] J. Miao, T.M. Pollock, and J.W. Jones. Crystallographic fatigue crack initiation in nickel-base superalloy {Rene 88DT} at elevated temperature. *Acta Mater.*, 57:5964–5974, 2009.

[208] Z.J. Zhang and Z.G. Wang. Comparison of fatigue cracking possibility along large- and low-angle grain boundaries. *Mater. Sci. Eng., A*, pages 285–291, 2000.

[209] J. Polak and J. Man. Initiation of stage {I} fatigue cracks - experiments and models. *Procedia Eng.*, 101:386–394, 2015.

[210] G.P. Zhang, C.A. Volkert, R. Schwaiger, E. Arzt, and O. Kraft. Damage behavior of 200-nm thin copper films under cyclic loading. *J. Mater. Res.*, 20(1):201–207, 2005.

[211] G.P. Zhang, C.A. Volkert, R. Schwaiger, P. Wellner, E. Arzt, and O. Kraft. Length-scale-controlled fatigue mechanisms in thin copper films. *Acta Mater.*, 54:3127–3139, 2006.

[212] H. Mughrabi. Fatigue, an everlasting materials problem - still en vogue. *Proc. Eng.*, 2:3–26, 2010.

[213] R. Schwaiger and O. Kraft. Size effects in the fatigue behavior of thin {Ag} films. *Acta Mater.*, 51:195–206, 2003.

[214] F. Ellyin. *Fatigue Damage, Crack Growth and Life Prediction*. Chapman & Hall, 1997.

[215] E.M. Orozco-Smith. Analysis of Low Cycle Fatigue Properties of Single Crystal Nickel-Base Turbine Blade Superalloys. Master's thesis, University of Florida, 2006.

[216] B. Yang, C. Motz, W. Grosinger, and G. Dehm. Stress-controlled fatigue behaviour of micro-sized polycrystalline copper wires. *Mater. Sci. Eng., A*, 515:71–78, 2009.

[217] G. Khatibi, A. Betzwar-Kotas, V. Groger, and B. Weiss. A study of the mechanical and fatigue properties of metal microwires. *Fatigue Fract. Eng. Mater. Struct.*, 28:723–733, 2005.

[218] L. Kunz, P. Lukáša, R. Konečná, and S. Fintová. Casting defects and high temperature fatigue life of IN 713LC superalloy. *Int. J. Fatigue*, 41:47–51, 2012.

[219] P.A. Shade, M.D. Uchic, D.M. Dimiduk, G.B. Viswanathan, R. Wheeler, and H.L. Fraser. Size-affected single-slip behavior of René N5 microcrystals. *Mater. Sci. Eng. A*, 535:53–61, 2012.

[220] R.E. Stoltz and A.G. Pineau. Dislocation-Precipitate Interaction and Cyclic Stress-Strain Behavior of Gamma-prime Strengthened Superalloy. *Mater. Sci. Eng.*, 34:275–284, 1978.

[221] B. Décamps, S. Raujol, A. Coujou, F. Pettinari-Sturmel, N. Clément, D. Locq, and P. Caron. On the shearing mechanism of γ' precipitates by a single (a/6)112 Shockley partial in Ni-based superalloys. *Philos. Mag.*, 84:91–107, 2004.

[222] A.M. Hussein, S.I. Rao, M.D. Uchic, T.A. Parthasarathy, and J.A. El-Awady. The strength and dislocation microstructure evolution in superalloy microcrystals. *J. Mech. Phys. Solids*, 99:146–162, 2017.

[223] T. Kruml, E. Conforto, B.Lo. Piccolo, D. Caillard, and J.L. Martin. From dislocation cores to strength and work hardening: a study of binary {Ni_3Al}. *Acta Mater.*, 50:5091–5101, 2002.

[224] H.P. Karnthaler, E.Th. Muhlbacher, and C. Rentenberger. The influence of the fault energies on the anomalous mechanical behaviour of Ni3Al alloys. *Acta Mater.*, 44:547–560, 1996.

[225] M. Petrenec, K. Obrtlik, and J. Polák. Inhomogeneous dislocation structure in fatigued INCONEL 713 LC superalloy at room and elevated temperatures. *Mater. Sci. Eng., A*, 400-401:485–488, 2005.

[226] M. McLean. Nickel-base superalloys: current status and potential. In *High-temperature Struct. Mater.*, chapter 1, pages 1–15. Springer, 1996.

[227] H. Kawazoe, M. Yoshida, Z.S. Basinski, and M. Niewczas. Dislocation microstructures in fine-grained Cu polycrystals fatigued at low amplitude. *Scr. Mater.*, 40(5):639–644, 1999.

[228] P. Lukáš and L. Kunz. Role of persistent slip bands in fatigue. *Philos. Mag.*, 84(3-5):317–330, 2004.

[229] U. Essmann, U. Gösele, and H. Mughrabi. A model of extrusions and intrusions in fatigued metals I. Point-defect production and the growth of extrusions. *Philos. Mag. A*, 44(2):405–426, aug 1981.

[230] G. Khatibi, A. Betzwar-Kotas, V. Gröger, and B. Weiss. A study of the mechanical and fatigue properties of metallic microwires. *Fatigue Fract. Eng. Mater. Struct.*, 28(8):723–733, 2005.

[231] H.W. Höppel, P. Goik, C. Krechel, and M. Göken. Ex and in situ investigations on the role of persistent slip bands and grain boundaries in fatigue crack initiation. 2019.

[232] F. Ackermann, L.P. Kubin, J. Lepinoux, and H. Mughrabi. The Dependence of Dislocation Microstructure on Plastic Strain Ampltiude in Cyclically Strained Copper Single Crystals. *Acta. Met.*, 32(5):715–725, 1984.

[233] P. Li, S. X. Li, Z.G. Wang, and Z.F. Zhang. Fundamental factors on formation mechanism of dislocation arrangements in cyclically deformed fcc single crystals. *Prog. Mater. Sci.*, 56(3):328–377, 2011.

[234] P. Peralta and C. Laird. Fatigue of Metals. In *Phys. Metall. Fifth Ed.*, pages 1765–1880. Elsevier, 5th edition, 2014.

[235] A. Schwab, J. Bretschneider, C. Buque, C. Blochwitz, and C. Holste. Application of electron channelling contrast to the investigation of strain localization effects in cyclically deformed fcc crystals. *Philos. Mag. Lett.*, 74(6):449–454, dec 1996.

[236] C. Buque. Persistent slip bands in cyclically deformed nickel polycrystals. Technical report, 2001.

[237] H. Mughbrabi, F. Ackermann, and K. Herz. Persistent Slipbands in Fatigued Face-Centered and Body-Centered Cubic Metals. In *Fatigue Mech.*, pages 69–69–37. ASTM International, 1979.

[238] J. Bretschneider, C. Holste, and B. Tippelt. Cyclic plasticity of Nickel single crystals at elevated temperatures. *Acta Mater.*, 45(9):3775–3783, 1997.

[239] B.-T. Ma and C. Laird. Dislocation Structures of Copper Single Crystals for Fatigue Tests under Variable Amplitudes. *Mater. Sci. Eng. A*, 102:247–258, 1988.

[240] PSB-Image-Analysis. *Github Repos. https//github.com/cemel-jhu/PSM-Image-Processing*, 2019.

[241] N. Otsu. A Threshold Selection Method from Gray-Level Histograms. *IEEE Trans. Syst. Man, Cybern.*, SMC-9(1):62–66, 1979.

[242] C. Blochwitz and U. Veit. Plateau Behaviour of Fatigued FCC Single Crystals. *Cryst. Res. Technol.*, 17(5):529–551, 1982.

[243] C.D. Liu and M.N. Bassim. Relationship between Stress and Dislocation Structure of Fatigued Polycrystalline Copper. Technical report, 1995.

[244] J. Polák, T. Lepistö, and P. Kettunen. Surface topography and crack initiation in emerging persistent slip bands in copper single crystals. *Mater. Sci. Eng.*, 74(1):85–91, sep 1985.

[245] J. Polák, V. Mazánová, M. Heczko, R. Petráš, I. Kuběna, L. Casalena, and J. Man. The role of extrusions and intrusions in fatigue crack initiation. *Eng. Fract. Mech.*, 185:46–60, nov 2017.

[246] H. Mughrabi. Fatigue, an everlasting materials problem - Still en vogue. *Procedia Eng.*, 2(1):3–26, 2010.

[247] Z.F. Zhang, Z.G. Wang, and H.H. Su. Observations on persistent slip bands transferring through a grain boundary in a copper bicrystal by the electron channelling contrast in scanning electron microscopy technique. Technical Report 5, 1999.

[248] C. Déprés, C.F. Robertson, M. Fivel, and S. Degallaix. A Three Dimensional Discrete Dislocation Dynamics Analysis of Cyclic Straining in 316L Stainless Steel. *Mater. Sci. Forum*, 482(February 2015):163–166, 2005.

[249] J. Ahmed, A. J. Wilkinson, and S. G. Roberts. Electron channelling contrast imaging characterization of dislocation structures associated with extrusion and intrusion systems and fatigue cracks in copper single crystals. *Philos. Mag. A Phys. Condens. Matter, Struct. Defects Mech. Prop.*, 81(6):1473–1488, 2001.

[250] L. Llanes and C. Laird. The role of annealing twin boundaries in the cyclic deformation of f.c.c. materials. *Mater. Sci. Eng.*, A157(21-27):1–7, 1992.

[251] P. Peralta, L. Llanes, J. Bassani, and C. Laird. Deformation from twin-boundary stresses and the role of texture: Application to fatigue. *Philos. Mag. A Phys. Condens. Matter, Struct. Defects Mech. Prop.*, 70(1):219–232, 1994.

[252] H. Kawazoe, M. Yoshida, Z.S. Basinski, and M. Niewczas. Dislocation microstructures in fine-grained Cu polycrystals fatigued at low amplitude. *Scr. Mater.*, 40(5):639–644, 1999.

[253] Z.S. Basinski and S.J. Basinski. Fundamental aspects of low amplitude cyclic deformation in face-centred cubic crystals. Technical report, 1992.

[254] J.F. Sola, R. Kelton, E.I. Meletis, and H. Huang. Predicting crack initiation site in polycrystalline nickel through surface topography changes. *Int. J. Fatigue*, 124:70–81, 2019.

[255] K. Mecke and C. Blochwitz. Saturation Dislocation Structures in Cyclically Deformed Nickel Single Crystals of Different Orientations. *Cryst. Res. Technol.*, 17(6):743–758, 1982.

[256] R. Wang, H. Mughrabi, S. McGovern, and M. Rapp. Fatigue of Copper Single Crystals in Vacuum and in Air I: Persistent Slip Bands and Dislocation Microstructures. *Mater. Sci. Eng.*, 65:219–233, 1984.

[257] V.A. Golyk. Self-organized criticality. 2012.

[258] A. Sornette and D. Sornette. Self-organized criticality and earthquakes. *Europhys. Lett.*, 9(3):197–202, 1989.

[259] R. Kokkoniemi, A. Miksic, M. Ovaska, L. Laurson, and M.J. Alava. Intermittent crack growth in fatigue. *J. Stat. Mech. Theory Exp.*, 073401:1–12, 2017.

[260] P. Dobro{\v{n}}. *An acoustic emission study of plasticity in crystalline materials*. PhD thesis, Charles University, 2016.

[261] J.D. Eshelby. The interaction of kinks and elastic waves. *Proc. Roy. Soc.*, 266(1325), 1962.

[262] N. Kiesewetter and P. Schiller. The Acoustic Emission from Moving Dislocations in Aluminium. Technical report, 1976.

[263] D. Rouby, P. Fleischmann, and C. Duvergier. Un modéle de sources d'émission acoustique pour l'analyse de lémission continue et de lémission par salves ii. Vérifications expérimentales. *Philos. Mag. B Phys. Condens. Matter; Stat. Mech. Electron. Opt. Magn. Prop.*, 47(5):689–705, 1983.

[264] W. Schaarwächter and H. Ebener. Acoustic emission: A probe into dislocation dynamics in plasticity. *Acta Metall. Mater.*, 38(2):195–205, 1990.

[265] T.P. Weihs, C.W. Lawrence, B. Derby, C.B. Scruby, and J.B. Pethica. Acoustic Emissions During Indentation Tests. In *Mat. Res. Soc. Symp. Proc.*, volume 239, pages 361–366, 1992.

[266] D.F. Bahr and W.W. Gerberich. Relationships between acoustic emission signals and physical phenomena during indentation. *J. Mater. Res.*, 13(4):1065–1074, 1998.

[267] Á.I. Hegyi, P.D. Ispánovity, M. Knapek, D. Tüzes, K. Máthis, F. Chmelík, Z. Dankházi, G. Varga, and I. Groma. Micron-Scale Deformation: A Coupled In Situ Study of Strain Bursts and Acoustic Emission. *Microsc. Microanal.*, 23(6):1076–1081, 2017.

[268] W.F. Hartman. Acoustic emission and the Portevin-Le Chatelier effect. *Exp. Mech.*, 14(1):19–23, 1974.

[269] D.M. Dimiduk, E.M. Nadgorny, C. Woodward, M.D. Uchic, and P.A. Shade. An experimental investigation of intermittent flow and strain burst scaling behavior in LiF crystals during microcompression testing. *Philos. Mag.*, 90(27-28):3621–3649, 2010.

[270] D.M. Dimiduk, M.D. Uchic, and T.A. Parthasarathy. Size-affected single-slip behavior of pure nickel microcrystals. *Acta Mater.*, 53(15):4065–4077, 2005.

[271] A. Pawelek, W. Stryjewski, H. Dybiec, and W. Bochniak. Acoustic emission during tensile deformation of copper single crystals and dislocation annihilation processes. *Arch. Acoust.*, 15(1-2):211–226, 1990.

[272] D. Hull and D.J. Bacon. *Introduction to Dislocations*. 1965.

[273] TESCAN. High-Resolution Xe Plasma FIB. tescan.com/en-us/hr-plasma-fib.

[274] J. Hütsch and E.T. Lilleodden. The influence of focused-ion beam preparation technique on microcompression investigations: Lathe vs. annular milling. *Scr. Mater.*, 77:49–51, 2014.

[275] J.C. Stinville, E.R. Yao, P.G. Callahan, J. Shin, F. Wang, M.P. Echlin, T.M. Pollock, and D.S. Gianola. Dislocation dynamics in a nickel-based superalloy via in-situ transmission scanning electron microscopy. *Acta Mater.*, 168:152–166, 2019.

[276] J.-Y. Buffiere. Fatigue Crack Initiation And Propagation From Defects In Metals: Is 3D Characterization Important? *Procedia Struct. Integr.*, 7:27–32, 2017.

[277] M. Mostafavi and T.J. Marrow. Quantitative in situ study of short crack propagation in polygranular graphite by digital image correlation. *Fatigue Fract. Eng. Mater. Struct.*, 35(8):695–707, 2012.

[278] S. Chan and E.L. Siegel. Will machine learning end the viability of radiology as a thriving medical specialty? *Br J Radiol*, 92(1094), 2019.

Vita

Steven Lavenstein was born in Baltimore, Maryland on March 22, 1991 to Randy and Janis Lavenstein. He obtained a Bachelor of Science in Mechanical Engineering in 2014 at the University of Maryland, Baltimore County (UMBC). His first research experience was from 2013 to 2014 as an intern at the Innovation Lab at Under Armour. Concurrently, he worked on the Hyper-Angular Rainbow Polarimeter (HARP) cubesat at the Joint Center for Earth Systems Technology at UMBC (the HARP cubesat was launched in 2019). Steven started graduate school at the Mechanical Engineering Department at Johns Hopkins University in 2014 and was advised by Professor Jaafar El-Awady. His research focused on micro-scale fatigue of metals and the associated physical deformation and fracture mechanisms. He obtained his Masters of Science and Engineering degree in 2015. During a brief hiatus in his graduate studies in the summer of 2019, Steven participated in The Data Incubator program in Washington, DC where he learned the fundamentals of data science and machine learning. In November 2019, he defended his dissertation and completed the requirements for the degree of Doctor of Philosophy in Mechanical Engineering at Johns Hopkins University.

List of Publications

- S. Lavenstein and J.A. El-Awady. Micro-scale fatigue mechanisms in metals: Insights gained from small-scale experiments and discrete dislocation dynamics simulations. *Current Opinion in Solid State & Materials Science*, 23(5):100765, 2019.

- R. Plamthottam, S. Lavenstein, J.A. El-Awady. Effect of temperature on the suppresion of twinning in textured magnesium. *MRS Communications*, 9(3):1093-1097, 2019.

- S. Lavenstein, B. Crawford, G.-D. Sim, P.A. Shade, C. Woodward, and J.A. El-Awady. High frequency *in situ* fatigue response of Ni-base superalloy René-N5 microcrystals. *Acta Materialia*, 144:154-163, 2018.

- G.-D. Sim, G. Kim, S. Lavenstein, M.H. Hamza, H. Fan, and J.A. El-Awady. Anomalous hardening in magnesium driven by a size-dependent transition in deformation modes. *Acta Materialia*, 144:11-20, 2018.

- S. Lavenstein, Y. Gu, D. Madisetti, and J.A. El-Awady. The heterogeneity of persistent slip band evolution in micro-scale metal crystals. *In preparation.*

- S. Lavenstein and J.A. El-Awady. The fatigue response of Ni microcrystals at high strain amplitudes. *In preparation.*

- S. Lavenstein and J.A. El-Awady. Acoustic emissions during compression of Ni microcrystals. *In preparation.*

- S.E. Prameela, P. Yi, S. Lavenstein, R. Plamthottam, J.A. El-Awady, M.L. Falk, and T.P. Weihs. Heterogeneous nucleation and growth of precipitates in Mg-9Al (wt%) alloy during hot compression. *In preparation.*